

Department of Electrical and Computer Engineering

**Power Management of Autonomous Microgrids
with Distributed Generations and Energy
Storage Systems**

Tahoura Hosseinimehr

This thesis is presented for the Degree of
Doctor of Philosophy
of
Curtin University

August 2017

To the best of my knowledge and belief this thesis contains no material previously published by any other person except where due acknowledgment has been made. This thesis contains no material which has been accepted for the award of any other degree or diploma in any university.

Tahoura Hosseinimehr
07/08/2017

*“To my dearest and my beloved family for their unconditional love and support
during this journey”*

Acknowledgments

I would like to express my deepest gratitude to my supervisor Professor Arindam Ghosh for his unwavering support, collegiality, and mentorship throughout this project from inception to completion.

I gratefully acknowledge the scholarship and funding received towards my Ph.D. studies from the Department of Electrical and Computer Engineering at Curtin University, Perth, Western Australia, Australia.

I would like to express my special thanks to my dearest, Alireza, for never once wavering in the complete support and encouragement. Last but not least, I would like to thank my beloved parents and my one and only sister; without whom none of this would indeed be possible.

Abstract

With increasing use of distributed generations (DGs) and the tendency to supply loads by localized grouping of DGs in the form of microgrids (MGs), the architecture of the existent grid is expected to drastically change in the near future. MGs are small-scale power networks capable of providing power to a small community, such as a suburban locality, a university, a commercial or industrial area, etc. The micro-sources employed in an MG are mainly renewable energy sources (RESs) which are integrated to generate power at the distribution level. To ensure that an MG can operate as a single aggregated system, and to maintain the power balance of this system, the MG DERs should be equipped with power-electronic interfaces and well-designed flexible control strategies. It is worth noting that the control strategies of stand-alone MGs have a greater degree of complexity compared to the inter-connected systems as voltage and frequency regulations are required to ensure that these parameters are kept within their reliable ranges. Moreover, to maintain the system power balance at any given moment, incorporation of energy storage systems (ESSs) in the stand-alone MGs is necessary. Thereby, a reliable power management strategy is needed to efficiently coordinate ESSs and DGs without interfering with the smooth performance of the system.

This thesis is mainly focused on the development of reliable power management strategies for islanded MGs. The main objectives of the proposed strategies are to provide accurate active and reactive power sharing, maintain system power balance, coordinate energy storage systems with distributed energy resources, enhance the lifetime of the batteries by controlling their state of charge, and efficiently employ renewable energy sources such as photovoltaic (PV) systems, etc. The proposed power sharing techniques and power management strategies in this thesis are;

- A new virtual impedance-based power sharing technique designed to mitigate reactive power sharing errors among distributed energy resources;

- An alternative virtual impedance-based power sharing technique designed and implemented based on the small-signal stability analysis of the microgrid;
- A new hierarchical (centralized) control strategy to coordinate distributed battery storage systems in an autonomous microgrid aiming to consider batteries state of charge (available capacity) instead of their maximum capacity in the droop characteristic of these units;
- A new reactive power control strategy to utilize the available capacity of the distributed batteries converters and to avoid overloading of the other units;
- A new autonomous (decentralized) power management strategy for a stand-alone droop controlled microgrid with multiple batteries based on comprehensive control of batteries in charge and discharge mode;
- A new decentralized power management strategy for a typical stand alone microgrid with a PV, a diesel generator and an energy storage system developed based on bus-signalling methods aiming to avoid the battery overcharge and over-discharge and to maintain the system power balance by providing a float charge characteristic for the battery.

Contents

Acknowledgments	iv
Abstract	v
List of Figures	xii
List of Tables	xvi
Abbreviations	xviii
List of Roman Symbols	xx
List of Greek Symbols	xxv
1 Introduction	1
1.1 Background	1
1.2 Distributed Generation	3
1.2.1 Micro-turbines	4
1.2.2 Wind Turbines	4
1.2.3 Fuel Cells	5
1.2.4 Photovoltaic Systems	5
1.2.5 Energy Storage Systems	6
1.2.6 Other DG Sources	6
1.3 Microgrids	6
1.4 Stand-alone Microgrids	7
1.5 Microgrid Structure	8
1.6 Applications of Energy Storage Systems in Microgrid	9

1.7	Energy Storage Technologies	10
1.7.1	Electrochemical Battery Storage Systems	12
1.8	Power Management of Islanded Microgrids	13
1.8.1	Hierarchical Control of Microgrids	15
1.8.2	Different Power Management Strategies for Islanded Microgrids	18
1.9	Thesis Objectives	22
1.10	Specific Contributions of the Thesis	23
1.11	Thesis Outline	24
2	Power Sharing Techniques for Converter-Interfaced DERs	27
2.1	Introduction	27
2.2	Microgrid Structure and Control	29
2.2.1	MG Hierarchical Control System	30
2.2.2	DER Converter Structure	31
2.2.3	Droop Control	31
2.3	Different Power Sharing Techniques	34
2.3.1	Power Sharing by Coupling Inductance Design	34
2.3.2	Power Sharing by Droop Coefficients Design	35
2.3.3	Power Sharing by Virtual Impedance Design	37
2.4	Simulation Results	41
2.4.1	Case-1: Power Sharing by Coupling Inductance Design	42
2.4.2	Case-2: Power Sharing by Droop Coefficients Design	43
2.4.3	Case-3: Power Sharing by Virtual Impedance-based Droop	44
2.4.4	Case-4: Power Sharing by Simple Droop	47
2.5	Conclusions	49
3	Small Signal Stability Analysis of Autonomous Microgrid	50
3.1	Introduction	50
3.2	Microgrid Structure and Control	52
3.2.1	Converter Structure and Control	52
3.2.2	Power Flow of the DERs	54

3.2.3	Reference Generation of the DERs	55
3.3	Dynamic Power Sharing by Analyzing Eigenvalues	55
3.4	Small Signal Stability Analysis	58
3.4.1	Voltage Source Converter Model	59
3.4.2	Load and Lines Model	60
3.4.3	Combined Model of the VSC, Load, and Lines	61
3.4.4	Droop Controller Model	61
3.4.5	The Overall Model of the MG	62
3.5	Study Cases and Simulation Results	66
3.5.1	Case-1: Simulation Results for $P_{ratio} = 3$	67
3.5.2	Case-2: Simulation Results for $P_{ratio} = 6$	70
3.5.3	Case-3: Dynamic Variation of the Power Ratio	73
3.6	Conclusions	75
4	Hierarchical Control of Battery Energy Storage Systems in Au-	
	tonomous Microgrids	76
4.1	Introduction	76
4.2	Microgrid Structure and Control	79
4.3	Proposed Cooperative Control of BES Units	81
4.3.1	BES Discharge Control Strategy	81
4.3.2	BES Charge Control Strategy	84
4.4	Determining BES Operation Mode	86
4.5	Performance Evaluation	87
4.5.1	Case-1: Normal Operation of the System	88
4.5.2	Case-2: Comparison of SoC-based Droop and Conventional Droop	92
4.5.3	Case-3: BES Switching from Discharge to Charge	92
4.5.4	Case-4: BES Switching from Charge to Discharge	95
4.5.5	Case-5: Comparison of Different Power-SoC characteristics	97
4.6	Conclusions	99

5	Autonomous Power Management of Islanded Microgrids with Multiple Energy Storage Systems	101
5.1	Introduction	101
5.2	System Structure and Control	103
5.2.1	Energy Storage System	103
5.2.2	Photovoltaic System	105
5.2.3	Distributed Energy Resource	105
5.3	Proposed Autonomous Power Management Strategy	107
5.3.1	ESS Reference Power Generation	107
5.3.2	Proposed Algorithm to Decide the ESS Operation Mode	110
5.4	Simulation Results	111
5.4.1	Case-1: Overall Performance of the System	111
5.4.2	Case-2: ESS Switching from Charge to Discharge	114
5.4.3	Case-3: Solar Radiation Mitigation	116
5.4.4	Case-4: Demand Lower than the PV Generation and ESS Disruption	118
5.5	Conclusions	118
6	Decentralized Power Management of an Islanded PV-Diesel Microgrid with Battery Energy Storage	122
6.1	Introduction	122
6.2	System Structure and Control	125
6.2.1	Battery Energy Storage System	126
6.2.2	Photovoltaic System	127
6.2.3	Diesel Generator System	128
6.3	Proposed Power Management Strategy	128
6.3.1	BES Comprehensive Charge and Discharge Control	129
6.3.2	PV Power Curtailment Control	133
6.4	Simulation results	135
6.4.1	Scenario I: Normal Operation of BES	135
6.4.2	Scenario II: Overcharge Operation of BES	138
6.4.3	Scenario III: Over-discharge Operation of BES	141

6.5	Conclusions	143
7	Conclusions	145
7.1	Thesis Summary and Conclusions	145
7.2	Future Work	149
Appendix A	Chapter 3 System Technical Data	150
Appendix B	Chapter 4 System Technical Data	151
Appendix C	Chapter 5 System Technical Data	152
Appendix D	Chapter 6 System Technical Data	153
Appendix E	Publications Incorporated in Thesis	154
	Bibliography	156

List of Figures

1.1	Different types of distributed generation technologies [19].	3
1.2	Schematic diagram of an example microgrid; (a) AC coupled, (b) DC coupled.	8
1.3	Hierarchical control of the microgrid [57].	15
1.4	DG incorporation in voltage control mode [63].	16
1.5	DG incorporation in current control mode [63].	17
1.6	Classification of microgrid power management strategies [57]. . . .	18
2.1	Schematic diagram of an example microgrid incorporated with hierarchical control structure.	29
2.2	DER unit including the primary source, VSC, filter, and coupling inductance; (a) three-phase schematic, (b) single-phase schematic.	31
2.3	Simplified diagram of the microgrid structure with two DERs. . . .	33
2.4	(a) $P - f$ and $Q - V$ droop characteristics of the MG DERs, (b) droop characteristics adjustment to satisfy the dynamic power ratio variations.	36
2.5	Simplified diagram of the microgrid with the measurement signals.	37
2.6	VSC control structure in presence of AVI.	38
2.7	DER control structure with the proposed adaptive virtual impedance.	40
2.8	DER control structure with the proposed adaptive virtual impedance.	41
2.9	Case-1 results: power sharing based on coupling inductance design.	44
2.10	Case-2 results: power sharing based on droop coefficient design.	45
2.11	Case-3 results: power sharing based on virtual impedance design.	46
2.12	Case-4 results: power sharing based on simple droop.	48
3.1	Schematic diagram of an example MG with n DERs.	51
3.2	(a) Converter structure, (b) equivalent circuit of phase- a	52

3.3	(a) Deployed algorithm by the MG central controller to determine the VI for each DER, (b) selecting the optimum inductance (L_{VI-opt}).	57
3.4	Closed-loop control of the voltage source converter.	58
3.5	Schematic diagram of an example MG with n DERs.	59
3.6	Case 1: (a) DERs active power, (b) DERs reactive power for L_{VI} variations from zero to 110 [mH].	66
3.7	Case 1: (a) Power ratio errors, (b) Objective functions.	67
3.8	Case 1: Root locus diagram for L_{VI} variations from zero to 110 [mH] and $P_{ratio} = 3$	68
3.9	Case 1: Dominant eigenvalues locus for L_{VI} variations from zero to 110 [mH] and $P_{ratio} = 3$	68
3.10	Case 1: (a) DERs active powers, (a) DERs reactive powers for L_{VI-opt} selection based on OF_1	69
3.11	Case 1: (a) DERs active powers, (a) DERs reactive powers for L_{VI-opt} selection based on OF_4	70
3.12	Case 2: (a) DERs active power, (b) DERs reactive power for L_{VI} variations from zero to 50 [mH].	71
3.13	Case 2: (a) Power ratio errors, (b) Objective functions.	71
3.14	Case 2: Root locus diagram for L_{VI} variations from zero to 50 [mH] and $P_{ratio} = 6$	72
3.15	Case 2: Dominant eigenvalues locus for L_{VI} variations from zero to 50 [mH].	72
3.16	Case 2: (a) DERs active powers, (b) DERs reactive powers for L_{VI-opt} selection based on OF_1	73
3.17	Case 2: (a) DERs active powers, (b) DERs reactive powers for L_{VI-opt} selection based on OF_4	74
3.18	Case 3: (a) DERs active powers, (a) DERs reactive powers when P_{ratio} varies dynamically.	75
4.1	Schematic diagram of an example microgrid with distributed BESs, DERs, and Loads.	77
4.2	Simplified diagram of the microgrid structure with one DER and one BES unit.	80
4.3	Dynamic $P - \delta$ droop coefficient modification for a BES system.	82

4.4	Dynamic $P - \delta$ droop coefficient modification for BES and RES system.	83
4.5	BES converter control structure in charge mode.	85
4.6	Proposed coordinated control of BES systems in discharge mode.	86
4.7	Proposed coordinated control of BES systems in charge mode.	87
4.8	Proposed algorithm to decide the BES mode of operation.	88
4.9	Schematic diagram of the investigated MG network.	89
4.10	Simulation results of Case-1: normal operation of the system.	90
4.11	Simulation results of Case-2: comparison of SoC-based droop and conventional droop.	93
4.12	Simulation results of Case-3: BES switching from discharge to charge	95
4.13	Simulation results of Case-4: BES switching from charge to discharge	96
4.14	Simulation results of Case-5.1	97
4.15	Simulation results of Case-5.2	98
4.16	Simulation results of Case-5.3	99
5.1	Stand-alone microgrid configuration with multiple ESSs, PV, DER and loads.	104
5.2	Energy storage system configuration and its control structure.	105
5.3	Photovoltaic system configuration and its control structure.	106
5.4	ESS reference power generation in association with the ESS SoC level and the system frequency.	107
5.5	Proposed algorithm to decide the ESS operation mode.	109
5.6	Case 1 results: overall performance of the system.	113
5.7	Case 2 results: switching from charge to discharge.	115
5.8	Case 3 results: solar radiation mitigation.	117
5.9	Case 4 results: demand lower than the PV generation and ESS disruption.	119
6.1	Stand-alone microgrid structure with BES, PV array, diesel generator and loads.	125
6.2	Battery energy storage system control structure.	126
6.3	Photovoltaic system control structure.	127
6.4	Diesel generator configuration; (a) speed control system, (b) droop control and governor control blocks.	128
6.5	Frequency regulation based on SoC.	129

6.6	BES reference power generation in association with the system frequency and SoC.	130
6.7	Active power reference modification to provide float charge characteristic for BES.	132
6.8	Proposed power curtailment technique for PV.	133
6.9	Simulation results of the proposed power curtailment technique. .	134
6.10	Case 1 results: BES discharge operation.	136
6.11	Case 2 results: BES charge operation.	137
6.12	Case 3 results: BES switching from charge to discharge.	139
6.13	Case 4 results: PV power curtailment.	140
6.14	Case 5 results: BES switching from discharge to charge.	141
6.15	Case 6 results: Demand lower than the PV generation.	142

List of Tables

1.1	Different types of energy storage systems and their applications [51].	11
2.1	Technical data of the considered MG.	42
2.2	DERs Specifications.	43
2.3	Active power ratio errors of Case-3 (virtual-impedance based droop).	47
2.4	Reactive power ratio errors of Case-3 (virtual-impedance based droop).	47
2.5	Active power ratio errors of Case-4 (simple droop).	47
2.6	Reactive power ratio errors of Case-4 (simple droop).	47
3.1	Optimum L_{VI} for Case-1 and Case-2.	70
3.2	Summary of results for Case-3.	74
4.1	Percentage of SoC drop for Case-1.	91
4.2	Active power ratio errors for Case-1.	91
4.3	Reactive power ratio errors for Case-1.	91
4.4	Active power ratio errors for Case-2 (SoC-based droop control).	94
4.5	Reactive power ratio errors for Case-2 (SoC-based droop control).	94
5.1	ESSs operation conditions for Case 1 and Case 2	120
5.2	ESSs operation conditions for Case 3 and Case 4	120
6.1	Possible scenarios in the islanded MG of Fig. 6.1	131
A.1	Technical data of the considered MG in Chapter 3.	150
B.1	Technical data of the investigated MG in Chapter 4.	151
C.1	Technical Data of the MG Elements in Chapter 5.	152

D.1 Technical data of the investigated system in Chapter 6. 153

Abbreviations

AC	Alternating Current
AVI	Adaptive Virtual Impedance
AWEC	Alta Wind Energy Centre
BES	Bater Energy Storage
CAES	Compressed Air Energy Storage
CCM	Current Control Mode
DC	Direct Current
DER	Distributed Energy Resources
DG	Distributed Generation
DOE	Department of Energy
DQ	Direct Quadrature
DSO	Distribution System Operator
DSP	Digital Signal Processor
EMF	ElectroMotive Force
ESS	Energy Storage Systems
IEA	International Energy Agency
IGBT	Insulated Gate Bipolar Transistors
LBC	Low Bandwidth Communication Channels
LPF	low pass Filter
LQR	Linear Quadratic Regulator
MEG	Microgrid Exchange Group
MG	Microgrid

MGCC	Microgrid Central Controller
MPP	Maximum Power Point
MPPT	Maximum Power Point Tracking
Ni/Cd	Nickle-Cadmium
Ni/MH	Nickel/Metal Hydride
OF	Objective Function
PCC	Point of Common Coupling
PI	Proportional Integral
PV	Photovoltaic
RES	Renewable Energy Sources
SoC	State of Charge
TI	Time Interval
VCM	Voltage Control Mode
VI	Virtual Impedance
VR	Virtual Resistance
VSC	Voltage Source Converter
WT	Wind Turbine

List of Roman Symbols

C_{ESS}	ESS capacity
C_f	Filter capacitance
E_{BES}^k	Stored energy of BES- k
$E_{BES-initial}^k$	Initial stored energy of BES- k
$E_{BES-max}^k$	Maximum energy capacity of BES- k
f_{max}	Maximum frequency limit
f_{min}	Minimum frequency limit
f_r	Rated frequency
f_{rated}	Rated frequency of the PCC
i_c	Filter capacitance current
i_{c-ref}	Reference current of filter capacitance
i_{ESS}	ESS current
i_{o-ref}	Reference current of coupling inductance
I_{o-ref}	Reference current magnitude of coupling inductance
$\angle I_{o-ref}$	Reference current angle of coupling inductance
i_f	Filter inductance current
i_{fd}, i_{fq}	dq components of filter inductance current
I_k	Phase- a output current magnitude for DER- k
i_o	Coupling inductance current
i_{od}, i_{oq}	dq components of coupling inductance current
J	Objective function of discrete LQR problem
$J(\infty)$	Objective function at infinite time

k	Coupling inductance ratio of DER-1 and DER-2
k_1, k_2, k_3	LQR gains
k_p	Active power ratio of DER-1 and DER-2
k_q	Reactive power ratio of DER-1 and DER-2
$L_{AVI-DER}^k$	Virtual inductance of DER- k
LC	Inductive-capacitive filter
L_c	Coupling inductance
L_{c-1}	Coupling inductance of DER-1
L_{c-2}	Coupling inductance of DER-2
L_f	Filter inductance
L_{line-1}	Feeder-1 inductance
L_{line-2}	Feeder-2 inductance
L_{VI}	Virtual inductance
L_{VI-1}	Virtual inductance of DER-1
L_{VI-2}	Virtual inductance of DER-2
L_{VI-opt}	Selected optimum virtual inductance
m	Frequency droop coefficient
m_0	Global droop coefficient
m_{BES}^k	Frequency droop coefficient of BES- k
m_{RES}^l	Frequency droop coefficient of RES- l
N	Number of BES units
n_{BES}^k	Voltage droop coefficient of BES- k
n_{RES}^l	Voltage droop coefficient of RES- l
OF	Objective function
P	Average output active power of DER
p	Output active power of DER
P_{BES}^k	Active power of BES- k
$P_{BES}^k(t)$	Average output active power of BES- k
P_{Demand}	Demand power

P_{max}	ESS maximum capacity
P_r	Maximum discharge capacity in float condition
P_{rated}	Rated active power of DER
$P_{rated,1}$	Rated active power of DER-1
$P_{rated,2}$	Rated active power of DER-2
$P_{rat-BES}$	Maximum capacity of BES
P_{ratio}^{actual}	Actual active power ratio of any two desired DERs
$P_{ratio}^{desired}$	Desired active power ratio of any two desired DERs
$P_{ref-ESS}$	ESS reference power
$P_{ref-BES}^{Ch}$	BES active power reference in charge mode
$P_{ref-BES}^{Dis}$	BES active power reference in discharge mode
$P_{RES-max}$	Maximum available power from RESs
Q	Average output reactive power of DER
q	Output reactive power of DER
Q_{actual}^k	Actual reactive power of DER- k
Q_{BES}^k	Reactive power of BES- k
$Q_{desired}^k$	Desired reactive power of DER- k
Q_{max}	Maximum available reactive power of VSC
Q_{rated}	Rated reactive power of DER
$Q_{rated,1}$	Rated reactive power of DER-1
$Q_{rated,2}$	Rated reactive power of DER-2
Q_{rated}^l	Rated reactive power of DER- l
Q_{rated}^k	Rated reactive power of DER- k
Q_{ratio}^{actual}	Actual reactive power ratio of any two desired DERs
$Q_{ratio}^{desired}$	Desired active power ratio of any two desired DERs
Q_{RES}^l	Reactive power of RES- l
R_f	Filter resistance
R_{line}	Feeder resistance
R_{line-1}	Feeder-1 resistance

R_{line-2}	Feeder-2 resistance
R_{load}	Load resistance
S_{max}	Maximum VSC capacity
$SoC_{BES}^k(t)$	instantaneous state of charge of BES- k
SoC_{BES-d}^k	Discretized SoC level of BES- k
SoC_{crit}	Critical SoC
SoC_{init}	Initial SoC level
SoC_{max}	Maximum SoC limit
SoC_{min}	Minimum SoC limit
SoC_{nom}	Nominal SoC
T_s	Sampling time
u	Switching function
u_c	Continuous-time approximation of the switching function
$ V_1 $	Voltage magnitude at VSC terminal of DER-1
$ V_2 $	Voltage magnitude at VSC terminal of DER-2
$v_a^k, v_b^k, v_c^k,$	Instantaneous voltage reference across the filter capacitance of DER- k
$v_{c-a}, v_{c-b}, v_{c-c},$	Three-phase instantaneous reference voltage of filter capacitor
v_c	Filter capacitance voltage
v_{cd}, v_{cq}	dq components of filter capacitance voltage
v_{c-ref}	Reference voltage of filter capacitance
V_{cm}	Reference voltage magnitude of filter capacitor
V_{dc}	DC link voltage
v_{droop}^k	Original droop voltage of DER- k
V_{droop}^k	Original droop voltage magnitude for DER- k
v_{droop}^k	Voltage drop across the AVI of DER- k
$ V_i $	Voltage magnitude at the output of VSC
$ V_j $	Voltage magnitude at the PCC side

V_{LL}	Rated voltage of PCC
V_{max}	Maximum allowable voltage of MG
v_o	Output voltage of DER
v_{od}, v_{oq}	dq components of DER output voltage
$ V_{pcc} $	Voltage magnitude at PCC
V_{rated}	Rated voltage of the PCC
v_{ref}^k	Voltage reference of DER- k considering the voltage drop across AVI
V_{ref}^k	Reference voltage magnitude for DER- k
$X_{AVI-DER}^l$	Virtual impedance of DER- l
$X_{AVI-DER}^k$	Virtual impedance of DER- k
X_{c-DER}^l	Coupling impedance of DER- l
X_{c-DER}^k	Coupling impedance of DER- k
\dot{x}_{DER}	State-space description of DER
X_{line}	Feeder reactance
X_{line-1}	Feeder-1 reactance
X_{line-2}	Feeder-2 reactance
X_{load}	Load reactance
\dot{x}_{MG}	State-space description of MG
Z_{line}	Feeder impedance
$z_{ref}(k)$	Desired state vector in discrete-time domain

List of Greek Symbols

α	Weighting coefficient of Active power ratio error
β	Weighting coefficient of reactive power ratio error
δ_1	Voltage angle at VSC terminal of DER-1
δ_2	Voltage angle at VSC terminal of DER-2
δ_i	Voltage angle at the output of VSC
δ_j	Voltage angle at the PCC side
δ_{pcc}	Voltage angle at PCC
δ_{droop}^k	Original droop voltage angle for DER- k
δ_{ref}^k	Reference voltage angle for DER- k
ΔL_{VI}	Virtual inductance step variations
ΔD	Duty ratio step variations
ΔP	Linearized output active power of DER
ΔQ	Linearized output reactive power of DER
Δf	Frequency band
ΔV	Voltage band
$\Delta i_{o,DQ}$	Linearized DQ DER currents
$\Delta v_{pcc,DQ}$	Linearized DQ PCC voltages
$\Delta i_{Load,DQ}$	Linearized DQ load currents
Δv_{c-ref}	Linearized reference voltage magnitude of filter capacitor
$\Delta \delta_{c-ref}$	Linearized reference voltage angle of filter capacitor
Δv_{c-ref}^{new}	Linearized reference voltage magnitude of filter capacitor considering virtual impedance

$\Delta\delta_{c-ref}^{new}$	Linearized reference voltage angle of filter capacitor considering virtual impedance
η_{ESS}	Charge/discharge efficiency
$\Delta\omega$	Microgrid frequency variation
$\Delta\omega_1$	DER-1 frequency variation
$\Delta\omega_2$	DER-2 frequency variation
ΔV	Microgrid voltage variation
ΔV_1	DER-1 voltage variation
ΔV_2	DER-2 voltage variation
ϵ_P	Active power ratio error
ϵ_Q	Reactive power ratio error
ω_{act}	Diesel generator actual frequency
ω_{load}	Low pass filter cut-off frequency
ω_{rat}	Diesel generator rated frequency
ω_{ref}	Diesel generator reference frequency
θ_k	Phase- <i>a</i> output current magnitude for DER- <i>k</i>

Chapter 1

Introduction

1.1 Background

Nowadays the face of electricity generation and transmission is changing due to economic factors, technological breakthroughs, and environmental concerns. There is a growing trend of connecting smaller generating sources that are distributed throughout distribution systems. This obviates the need for expansion in the traditional centralized generations and power networks. Distributed generation (DG) encompasses different types of resources, such as micro-turbines, gas turbines, wind turbines, fuel cells, and photovoltaics. These emerging resources are more cost-effective, and at the same time have lower emissions compared to the traditional generations. Different applications of these technologies can be categorized as substations power support, suspension of transmission and distribution upgrades and remote generations [1].

DGs penetration across the traditional power network is increasing rapidly and therefore; it is necessary to investigate the issues related to the high penetration of DGs within the distribution network. Although applying individual DGs may solve some existent problems of the distribution network, indiscriminate application of these units may introduce some other problems to the power system. To realize the emerging potential of the DGs, it is better to consider the DG and the incorporated loads as an autonomous subsystem or a microgrid (MG) [1]. By employing a DG in association with MGs, local control of the DG becomes feasible, and the need for central dispatch would be eliminated. Moreover, in case of any disturbance, the entire MG including the DG primary source and the constituent loads can be isolated from the distribution network without interfering with the integrity of the grid. Thus, deliberately isolating of the MG provides a

higher local reliability compared to the one provided by the entire power system. Moreover, due to the smaller size of MGs, it is possible to optimally place them close to the heat loads, such that waste heat can be utilized, especially in colder climates [2].

The main issue of the MGs is the technical difficulties in coordinating their several constituent DGs. As an example, for California, approximately 120000 of 100 [kW] generators are required to meet the power demand. Therefore, providing a complex control from a central point may create more problems than solutions. To avoid this, it is required for the MGs to be capable of responding to the system contingencies in an autonomous manner using local information. Thereby, it is necessary for the MG to switch to the stand-alone mode if the system faces a voltage drop, faults, blackouts, etc. This also, requires the DGs to switch their output power control to provide voltage and frequency regulation to the isolated MG [3]-[5].

Different strategies are introduced to control the MGs and to coordinate their associated DGs, in which the most important insights are obtained from the basic power system concepts that are utilized in the traditional operations of power systems [5]-[11]. As an example, frequency and voltage droop controls, which were originally deployed for the large generators of a power system, are extensively used to provide active and reactive power control to the DGs of an MG. The major difference between an isolated MG and the utility grid is the possibility that inverter-based DGs are not capable of providing instantaneous power requirements due to the lack of inertia. Therefore, in the stand-alone operation mode, load tracking problems may appear. Hence, adding some form of energy storage devices to MGs where several DGs are designed to perform in the stand-alone mode is indispensable. This is to ensure that the MG power balance is maintained specifically during load variations.

As mentioned previously, local control of DGs as an incorporated unit in an MG can increase the system reliability and power quality if the MG is designed to operate in autonomous mode as well as grid-connected mode. This way, in case of any contingencies in the system, the MG can continue to its operation in a seamless manner in islanded mode [12]. Hence, from the utility point of view, the MG can be considered as a controllable load which can meet the transmission system requirements by its fast response. Thereby, the need of secondary on-site power backup would be less or perhaps avoided completely. On the other hand, from the customer point of view, the MG can provide local voltage support, reliability improvement, feeder loss reduction, efficiency enhancement (by using the

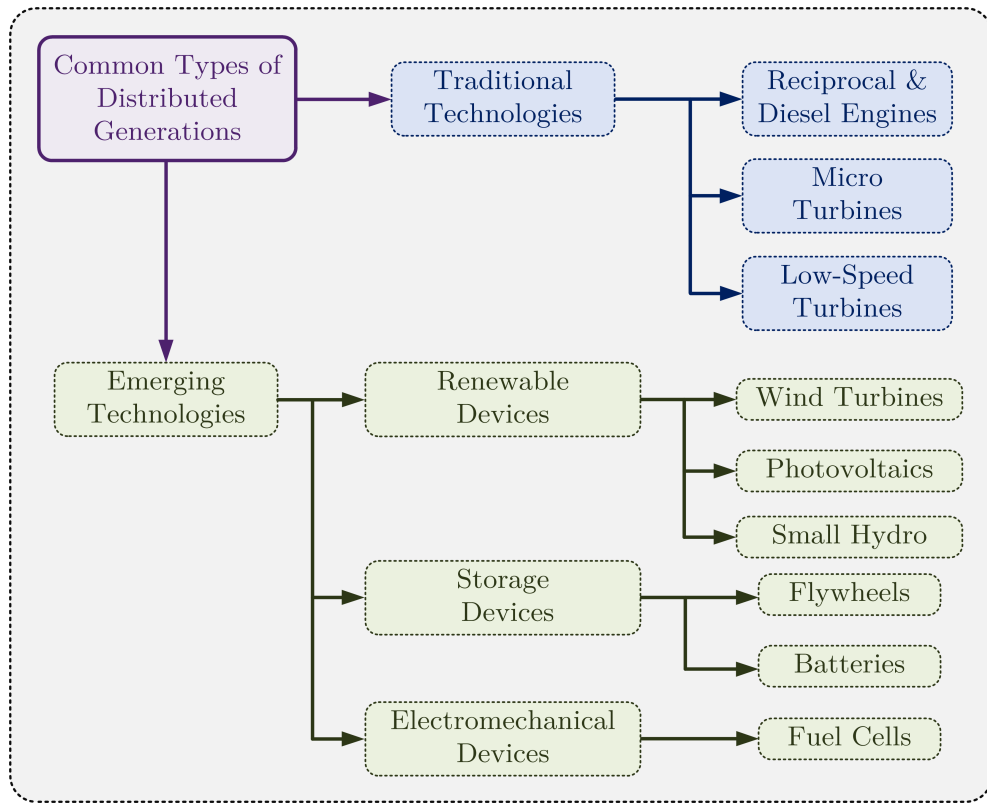


Figure 1.1: Different types of distributed generation technologies [19].

waste heat), voltage sag correction, etc. [1]. MG reliability, economic operation and planning are investigated in [13]-[15].

1.2 Distributed Generation

The traditional power generation network is unidirectional in nature. With the existing network, only one-third of fuel energy is converted to electricity and the waste heat is not recovered [16]. As an example, almost 8% of electricity production in the European electricity grid is wasted along the transmission lines while only 20% of its generation capacity is utilized to meet the peak demand [16]. High environmental pollution, transmission and distribution losses, and gradual depletion of fossil fuels have led to a new form of power generation which is called distributed generation (DG). Distributed generation can be considered as local power generation at the distribution level. Different types of sources which are included in distributed generation are summarized in Fig. 1.1 and are termed as distributed energy resources (DERs) [17].

There are several economical and technical benefits of implementation of DGs

in a power system; to name a few, cost reduction for installation of new transmission lines, variety of energy sources, power loss reduction, flexibility in the placement of the power plant, improvement of system reliability, etc.

The following subsections briefly introduce the main features of different types of DERs.

1.2.1 Micro-turbines

Micro-turbines are combustion turbines with small capacity, which are fueled by natural gas, propane or other types of fuels. Different components of the micro-turbines in a simple form could be combustor, compressor, recuperator, small turbine, and generator [18]-[20]. In some micro-turbines, only one moving shaft is utilized while air and oil are used as lubricants. A remarkable advantage of micro-turbines is their small scale compared to their size (i.e. 0.4-1.0 [m^3] for 20-500 [kW]). Micro-turbines run at less temperature and pressure and faster speed (up to 150,000 [rpm]) compared to the traditional combustion turbines. Low price of natural gas, low installation cost, and low maintenance cost are the main motivations which make micro-turbines one of the most promising DG energy resources today. A back-to-back power electronic converter system, mainly voltage source converter, is required to interface a micro-turbine with an AC grid or an MG [21]. Micro-turbines are dispatchable and do not suffer from intermittent generation problems.

1.2.2 Wind Turbines

Wind Energy has been used in electrical energy generation for decades. A wind turbine (WT) consists of a rotor, generator, turbine blades, drive, shaft, and gearbox. Wind turbines can be deployed in the power system individually or as a wind farm. For the wind plants installed in windy areas, the electrical efficiency of 20%-40% is expected, while the expected power sizes are in the range of 0.3 [kW] to 7.5 [MW] [22]-[29].

Wind turbines are classified into different types of A, B, C, and D [30]. The first three types are connected to the grid or load through a rotary machine, mainly an induction generator. While, for type D a full-scale power electronic converter (i.e. voltage source converter) is utilized for grid interfacing [30].

Wind farms may be designed in different scales. Currently, Alta Wind Energy Centre (AWEC) in Tehachapi, Kern County, California, is the largest wind farm

in the world with an operational capacity of 1,548 [MW] [31]. Due to the high penetration of wind farms and the chaotic nature of wind power, the impact of this distributed generation on the power system is remarkable. Hence, addressing the impact of wind turbines on system operation, such as stability, planning, power quality, pricing, market, etc., are extensively investigated in many studies [24],[26, 27].

1.2.3 Fuel Cells

Fuel cells use electrochemical processes to generate electricity and emit thermal energy. Fuel cells can be considered as batteries which generate electricity as long as they are being supplied by the required fuels [32]-[34]. The capacity of fuel cells is in the range of 1 [kW] for portable units and a few [MW] for stationary units. Fuel cells generate clean power and heat by consuming gaseous and liquid fuels. Operating at different pressures and temperatures, fuel cells can be supplied by different types of hydrogen-rich fuels, such as gas, biogas, gasoline, and propane [32]-[34]. Similar to micro-turbines, fuel cells require a power electronic converter as an interface for grid or load connection [21].

1.2.4 Photovoltaic Systems

The direct conversion of sunlight into electricity without any heat engine is named photovoltaic (PV) conversion. Photovoltaic devices are robust and can be simply designed while requiring very little maintenance. The greatest advantage of PVs is their stand-alone construction which makes them ideal for applications, such as water pumping, solar home systems, remote buildings, communications, satellites, etc.

A photovoltaic array consists of several square or round shape cells which are made of doped silicon crystal. A PV array contains a number of PV modules where each module itself contains strings of cells that are connected in series or parallel.

PV arrays are mostly rated between 0.3 [kW] and a few [MW]. However, there are some limitations for the design of photovoltaic plants, such as high land cost, weak solar intensity in many areas, climate changes leading to unpredictable sun exposure, etc [1], [35]-[38]. As an example, to provide 150 [kW] of electricity, one acre of land is approximately required [1].

An advantage of PV generation is that its impact on the power system, such

as voltage fluctuations and possible harmonic injection, is not as problematic as wind generation. Thereby, injecting a controlled-reactive power to the inverter of the PV would be enough to mitigate the fluctuations and harmonics. Hence, study of internal control of PV generation systems and development of more exotic solar cell technology are of interest in many researches [39],[40]. DC/DC and DC/AC converters are mainly utilized to interface PVs with the grid or the AC loads.

1.2.5 Energy Storage Systems

Different types of energy storage systems (ESSs) are commonly used today, such as batteries, super-capacitors, super-conducting magnetic energy storage and flywheels [41]. Different applications of energy storage systems in MGs can be summarized as fast load pick-up enabling, reliability enhancement, smooth power generation for non-dispatchable sources [41]-[43]. Similar to PVs, ESSs are interfaced with the grid or AC loads through voltage source converters.

1.2.6 Other DG Sources

Other types of distributed generation sources can also be utilized in micro-grids; to name a few, micro-hydro power, bio-energy, geothermal power, ocean thermal power, and ocean wave power.

1.3 Microgrids

With the increasing use of DERs and the tendency to supply the load by localized grouping of the DERs in the form of microgrids (MGs), the architecture of the existent grid is expected to change drastically in the near future. Microgrids are small-scale power networks capable of providing power to a small community, such as a university, a residential, commercial, or industrial area, etc. The micro-sources deployed in an MG are mainly renewable DERs which are coordinated to supply power at the distribution level. To ensure that an MG can maintain its power balance while performing as a single aggregated system, it is required for the DERs of an MG to be equipped with power electronic interfaces and well-designed flexible control strategies. Combination of these control strategies forms the MG power management which allows the MG to operate as a single controllable unit from the utility point of view [44].

Being able to operate in grid-connected and islanded mode, integrating MGs in the power system can enhance the system reliability since the MG can seamlessly continue to operate in islanded mode during network faults or lack of power quality [44]. Another advantage of MG integration in the power system is reduction of transmission and distribution losses by providing local distributed generations to the loads. There are several technical issues related to the stand-alone operation of the MGs which needs to be investigated in the design of their power management strategies. Some of these are as follows:

- Frequency and voltage reference design;
- A reliable and accurate active and reactive power sharing technique;
- An energy storage system to balance the system power in the case of generation and consumption mismatch.

1.4 Stand-alone Microgrids

Based on International Energy Agency (IEA) records, more than one billion people do not have access to electricity across the world [45]. Hence, it is necessary to investigate different available options, such as grid-connected and stand-alone configurations, which can be used to alleviate this critical problems. Also, to avoid expensive grid extensions, decentralized configurations can be considered as a suitable, cost-effective option. Moreover, in the case of supplying remote areas, stand-alone microgrids are considered as an ultimate solution from both economic and environmental points of view.

Designing stand-alone microgrids can be distinguished from inter-connected networks from two different aspects; accurate sizing of the DERs to ensure complete coverage of the local loads and to have sufficient reserve capacity to deal with probable contingencies [42]. Stand-alone microgrids equipped with renewable energy sources (RESs) are free from fossil fuel consumption, pollution, and greenhouse gas emissions. Hence, they are more cost-effective and environment friendly compared to the stand-alone fossil fuel based power systems. However, RESs such as PVs and wind turbines suffer from fluctuations in the output power due to the intermittent nature of their primary sources. Thus, to ensure a smooth and reliable output power, energy storage systems are required for stand-alone operations of microgrids.

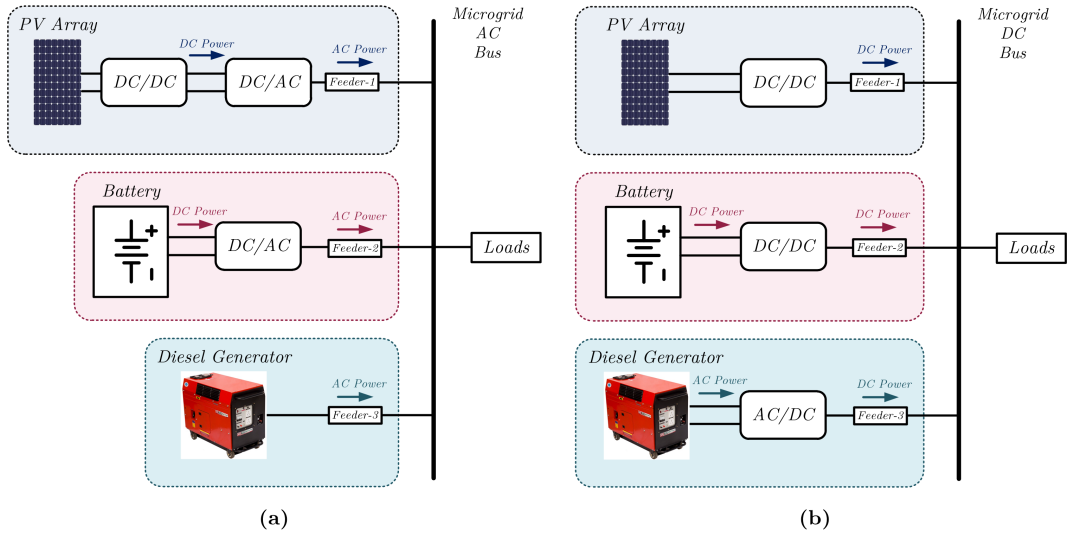


Figure 1.2: Schematic diagram of an example microgrid; (a) AC coupled, (b) DC coupled.

Additionally, the control strategy of stand-alone microgrids has a greater degree of complexity compared to the inter-connected systems. This is due to the requirement of voltage and frequency regulations to ensure these parameters are kept within their reliable range. Moreover, to maintain the system power balance at any given moment, a reliable power management is needed to efficiently coordinate the energy storage systems and the DGs without interfering with the smooth performance of the system [44],[46].

1.5 Microgrid Structure

Microgrid components including DERs and their power electronic interfaces and the end user are either AC coupled, or DC coupled as shown in Fig. 1.2. Fig. 1.2(a) shows a typical configuration of an AC-coupled microgrid. In this topology, all DERs with AC output (e.g. wind turbines, biogas engines, wave turbines, hydro turbines) are directly connected to an AC bus, and the AC bus itself may be connected to the utility system through a converter for grid-connected operation. On the other hand, DC output DERs (e.g. PVs, batteries, fuel cells) are connected to the main system via DC/AC converters.

A typical configuration of a DC coupled microgrid is shown in Fig. 1.2(b). In this topology all the DC output DERs are connected to the DC bus via DC/DC converters to ensure their output voltage is adjusted to the DC bus voltage.

Moreover, storage and DC loads can also be directly connected to the network, whereas the AC output DERs are connected to the DC bus through AC/DC converters [47, 48].

1.6 Applications of Energy Storage Systems in Microgrid

It is well-known that storing electrical energy without its conversion into a different form of energy (i.e. chemical, electromagnetic, electrostatic, or mechanical) is impossible. Hence, different types of energy storage systems (ESSs) are designed to convert different forms of energy into electricity.

The main roles of energy storage systems in the microgrids with RESs can be summarized as; providing reliable energy supply (by producing reserve capacity), reducing energy losses, and improving the operation of the microgrid (by allowing the RESs to operate based on maximum power point tracking strategies). Enhanced utilization of RESs is only possible with the coordination of ESSs in both stand-alone MGs and large-scale RES systems. Nonetheless, including ESSs in the microgrids may have some drawbacks which are described below.

In an AC coupled microgrid, an inverter is required for some sorts of ESSs such as batteries to supply the AC loads during the lack of generation. Moreover, to store the surplus power of the AC output RES units (e.g. wind turbines) in the ESS an AC/DC converter (i.e. rectifier) is needed. Altogether, it can be concluded that including ESSs in the MG imposes some extra costs to the system. Another disadvantage of ESSs would be the energy transformation and conversion losses.

It is well-known that ESSs are supposed to store the surplus power during the periods of off-peak demand (i.e. surplus generation) and to inject their stored energy during the periods of peak demand (i.e. lack of generation). However, the generation and consumption patterns vary differently, during a day, month or season. As an example, peak generation of PVs is usually presented in the middle of a day, while their output power drops to zero during the evenings. On the other hand, the peak demand usually occurs in the evening, whereas during the night the demand significantly becomes low. Moreover, the power consumption pattern is different throughout the year, as there is more requirement for heating during winter and for air conditioning during summer. Meanwhile, the RES generation varies significantly during a year. As an example, in Canberra, the average daily

irradiation per square meter in June is at its lowest where the PV generation drops by 30%, compared to January which has the highest PV generation [49]. Hence, maintaining the power balance of the system relies on well-tailored design of the system storage capacity.

Based on the storage duration, the ESSs are classified as [50];

- **Short-term storage:** Including this type of storage in the system is necessary in order to deal with the short-time transients, and to avoid oscillations and instability in the system. Moreover, in the case of high reactive power demands, voltage instability may occur, which may result in a sudden voltage drop of the system. The most suitable option to overcome the short-term transients is the flywheel system due to its prompt response characteristic. Other options could be batteries and super-capacitors.
- **Medium-term storage:** These storage systems are required for peak load shaving and smoothing the daily variations of the RESs. These storage systems are prone to frequent charge and discharge. Hence, the main factor in choosing the storage systems for such an application is the maximum number of cycles. The most popular types of storage systems which are suitable for this purpose are hydrogen storage systems and compressed air energy storage (CAES).
- **Long-term storage:** These storage systems contain large installations which are required to store a large amount of energy. Hence, their storage capacity is much higher compared to the short-term and medium-term ESSs. As an example, Tesla is installing a long-term storage including a 100 [MW] lithium-ion battery system that will provide the South Australia with 129 [MW-h] of energy.

Table 1.1 summarizes different types of energy storage technologies and their applications based on the storage duration [51].

1.7 Energy Storage Technologies

As mentioned previously, it is possible to store electricity by the conversion of electrical energy into another form of energy such as chemical, mechanical, etc. Batteries are the most popular energy storage systems which store electrical energy in the form of chemical energy. Hence, they are categorized as electrochemical storage systems, whereas compressed air energy storage (CAES) systems,

Table 1.1: Different types of energy storage systems and their applications [51].

Full Power Duration of Storage	Applications and Possible Replacement of Conventional Electricity System Control	Biomass	Large Hydro	CAES	Pumped Hydro	Batteries	Flywheel	Super-capacitor
4 Months	Annual Smoothing of Loads, PV, Wind, Small Hydro	✓	✓					
3 Weeks	Smoothing weather effects: load, PV, wind, small hydro	✓	✓					
3 Days	Weekly smoothing of loads and most weather variations	✓	✓	✓	✓			
8 h	Daily load cycle, PV, wind, transmission line repair	✓	✓	✓	✓	✓		
2 h	Peak load looping, standing reserve, wind power smoothing	✓	✓	✓	✓	✓		
20 min	Spinning reserve, wind power smoothing, clouds on PV	✓	✓	✓	✓	✓	✓	
3 min	Spinning reserve, wind power smoothing of gusts	✓	✓	✓	✓	✓	✓	
20 secs	Line or local faults, voltage and frequency control	✓	✓	✓	✓	✓	✓	✓

CAES=Compressed Air Energy Storage

hydro-power and flywheels are mechanical ESSs. Additionally, capacitors and super-capacitors are considered as electrical storage systems. Different storage technologies may be selected for different systems, depending on the application of the storage and the system requirements from the technical and economical points of view [51].

In this thesis, chemical conversion of electrical energy in particular electro-chemical batteries are considered as a single or distributed energy storage systems in the microgrids, which will be described in the following subsection. This work is mainly focused on providing a reliable power management strategy for a stand-alone microgrid in order to efficiently coordinate the RES systems and the ESS technologies.

1.7.1 Electrochemical Battery Storage Systems

Electrochemical batteries are one of the most popular technologies for the storage of electrical energy. Batteries include several series and/or parallel connected electrolytic cells where each cell consists of two half-cells. Each half-cell is in series with a conductive electrolyte including anions and cations which are the negatively charged ions and positively charged ions, respectively. The half-cell connected to the positive electrode is cathode, whereas the half-cell connected to the negative electrode is anode. Anions move toward the cathode, while cations are absorbed by the anode. During the redox reaction, anions are oxidized, which means the electrons are removed at the anode. Whereas, cations are reduced, which means the electrons are added at the cathode. The required electrical connection for redox reaction is provided by the conductive electrolyte [50].

Batteries are classified as electrochemical energy accumulators. Lead-acid, lithium-ion, and nickel based are among the most popular types of the batteries. Low cost of lead-acid batteries and their energy characteristic, with an energy density of almost 30 [kW/kg] and roundtrip efficiency of 80%-85%, makes them one of the most common options for electrochemical storage. High reliability, simple technology, and wide availability are the other features of lead-acid batteries. However, they have several drawbacks, such as relatively short lifetime, large size, ventilation requirement due to their hydrogen production during charging. Another disadvantage of lead-acid batteries is the complexity of their state of charge (SoC) estimation, which may complicate the power management design if included in the stand-alone MGs. The lead-acid electrolytic cell has a nominal electromotive force (EMF) of 2 [V]. However, this value is affected by various external factors, such as ambient temperature, electrolyte density, circulating current, and state of charge. Self-discharge phenomenon is another aspect to be considered which occurs due to different side reactions. In normal conditions, the state of charge of the lead-acid batteries reduces by 2%-3% per month [50].

Nickel-cadmium (Ni/Cd) and nickel/metal hydride (Ni/MH) are among the most popular types of nickel-based batteries. Ni/Cd batteries have some advantages compared to lead-acid batteries including robustness, higher life time, reliability, and better performance at low temperatures. However, since these batteries contain cadmium, their disposal is problematic. Hence, due to the environmental problems and some economic issues, nowadays the use of Ni/Cd batteries is on the decline [43],[50].

Ni/MH batteries are introduced by substituting cadmium with a mixture of

metal hydrides. These batteries were developed to replace Ni/Cd batteries. The energy density of Ni/MH batteries is about 40%-85%, which is higher than that of Ni/Cd. The round-trip efficiency is approximately 65%. The self-discharge of these batteries is almost 20% per month at the ambient temperature. In portable applications, Ni/MH batteries are widely replaced by lithium-ion batteries. However, hybrid vehicles mostly operate with Ni/MH batteries, due to their robustness and safer performance in comparison to lithium-ion batteries [43],[50]-[52].

One of the most promising electrochemical storage systems are lithium batteries. Two different types of lithium batteries are available in the market. Among these, lithium-ion batteries with liquid electrolyte are the most technically mature. The second type is the lithium-ion polymer battery, with solid polymeric electrolyte [52].

The energy capacity of lithium-ion batteries is 130-180 [kW/kg], which is the highest among all the electrochemical storage systems. Their efficiency is also very high and is usually in the range of 95%-98%. These batteries are considered as flexible and universal storage technologies since a discharge-time of seconds to weeks can be realized for them. Standard cells with 5000 full cycles and a 100% depth of discharge can be found in the market. Lithium-ion battery technology is still progressing, and there is a potential for further development [52].

1.8 Power Management of Islanded Microgrids

As mentioned previously, introducing distributed generation (DG) to the traditional centralized power system, has emerged the concept of microgrids (MGs). MGs are able to efficiently coordinate several distributed energy resources (DERs) by providing local power managements. Microgrid Exchange Group (MEG) of the U.S. Department of Energy (DOE) defines a microgrid as [53];

“a group of interconnected loads and distributed energy resources within clearly defined electrical boundaries that acts as a single controllable entity with respect to the grid. A microgrid can connect and disconnect from the grid to enable it to operate in both grid-connected or islanded mode.”

In the grid-connected mode, due to the presence of large synchronous generators in the power system and their rotating mass inertia, a relatively robust frequency regulation is provided to the microgrid. Moreover, the utility grid

provides the required voltage regulation of the MG [54]. The power mismatch between the generation and consumption in this mode can also be easily compensated by the grid. However, power management of the MG in the stand-alone mode is quite more challenging than the grid-connected mode. There are two main aspects to be considered in the design of power management strategies for stand-alone microgrids:

- **System Voltage and Frequency Regulation:** Since the large synchronous generators in the conventional power system have large rotating mass inertia, a stiff frequency regulation is offered by the grid in grid-connected mode. To achieve this, the system frequency is slightly increased/decreased during the transients and the grid supplies/absorbs the power mismatch between the generation and consumption in the MG. However, in the stand-alone operation mode, it is necessary to provide voltage and frequency regulation to the MG at least by one of the DG units.

Prompt acting energy storage technologies, such as batteries, flywheels, or super-capacitors can be utilized in the islanded mode in order to mimic the effect of the large generators in the conventional power systems [55, 56]. There are two different ways to connect these energy storage systems in a microgrid. They can be connected to either the DC link of the DG units or the microgrid bus as a distributed storage. In either connection, any power mismatch between the generation and consumption can be compensated by the fast response of the storage unit, while the voltage and frequency are also regulated by the storage device.

In this study, battery storage is chosen as the storage element of the microgrid, because of its high energy density compared to super-capacitors and flywheels.

- **System Power Balance:** Maintaining the system power balance in stand-alone mode, requires a control strategy, which coordinates the energy storage systems with the other DER units, specifically the renewable energy sources. To achieve this, the storage device should be able to absorb the surplus power of the renewable sources during the off-peak periods. On the other hand, during the peak periods, the deficit of power should be supplied by the storage units. Moreover, in the steady state, where there is no mismatch between the generation and consumption, the battery neither should absorb nor should deliver power from/to the microgrid.

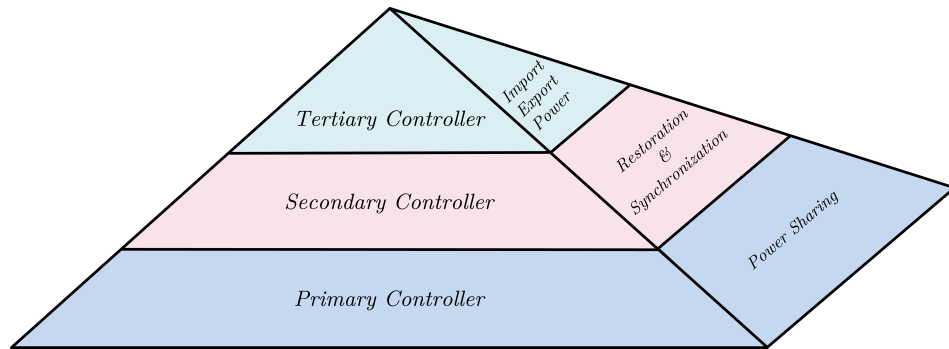


Figure 1.3: Hierarchical control of the microgrid [57].

To realize the above objectives for the global control of a stand-alone microgrid, it is necessary to design a specific control strategy for each unit based on its primary source characteristic. This control layer is referred as the primary control. Moreover, a centralized controller may be required to enhance the performance of the primary controllers. This control layer is referred as the secondary control.

1.8.1 Hierarchical Control of Microgrids

Hierarchical control of microgrids can be divided into three layers as shown in Fig. 1.3. Different layers of the MGs hierarchical control are briefly described below [57],[56, 58];

Primary Control Layer

Primary controllers are the locally implemented control strategies at the converter of each DG unit. These controllers usually contain inner control loops such as voltage and power control loops, aiming to adjust the DG output voltage and power with their desired references. The voltage and power references could be generated either internally using local measurements or externally (i.e. from a central controller) [55]. In this study, the output of the voltage source converter (VSC) is referred as the output of the DG unit. The VSC can be controlled either in voltage control mode (VCM) or current control mode (CCM), depending on its primary source characteristic and its role in the microgrid system. These control modes are briefly described below.

- **Voltage Control Mode:** In voltage control mode (VCM), the VSC control strategy aims to regulate the magnitude and the frequency of the output

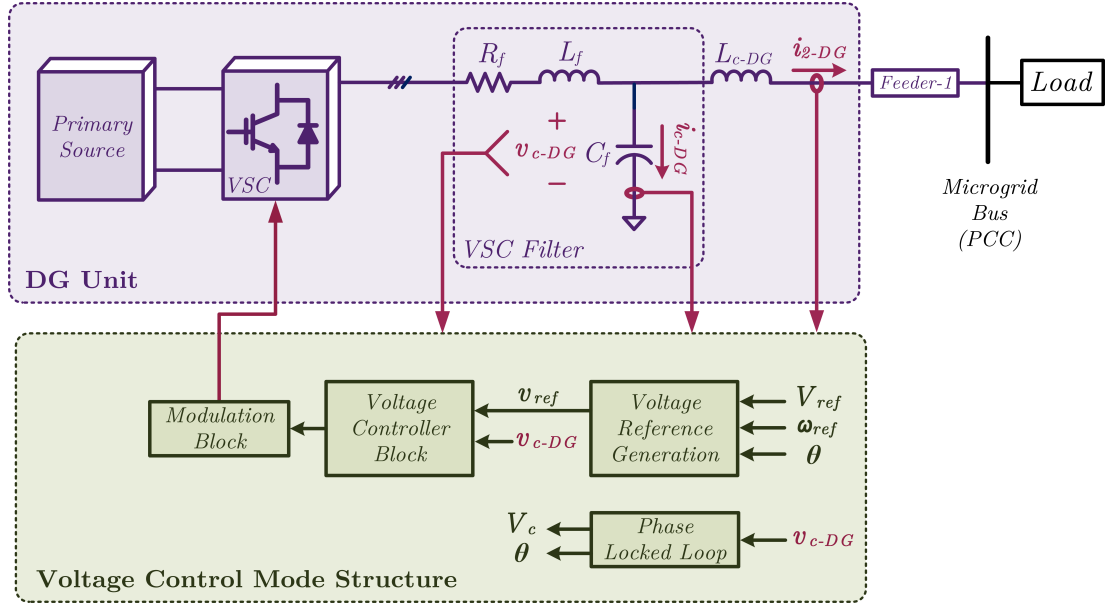


Figure 1.4: DG incorporation in voltage control mode [63].

voltage. Hence, the DG units which are incorporated in voltage control mode form the MG bus voltage and are referred as master unit or grid-forming unit [54],[59]-[62]. Fig. 1.4 shows a DG unit which is employed in the MG in voltage control mode [63], [61],[64]-[68]. In single-master microgrids, where only one DG unit regulates the voltage and frequency, nominal voltage (V_{rated}) and nominal frequency (f_{rated}) are chosen as the voltage (V_{ref}) and frequency (f_{ref}) references, respectively. However, in multi-master microgrids, where more than one unit is responsible for regulating the system voltage and frequency, droop controls are usually used to duplicate the mass inertia effect of the large synchronous generators as in conventional power systems [62],[69, 70].

- **Current Control Mode:** Fig. 1.5 shows a typical control structure of a DG unit in current control mode (CCM) [63],[61],[66]. The main objective of incorporating the DG units in current control mode is to set their output active and reactive powers based on specified references. In this sense, the MG voltage and frequency are assumed to be formed by another unit or units. The control strategies which are designed in current control mode are mostly suitable for non-dispatchable DGs, such as renewable sources (e.g. PV systems and wind turbines) as their output power is determined according to the maximum available power of their primary source (e.g. solar radiation, wind generation). However, in the case of dispatchable

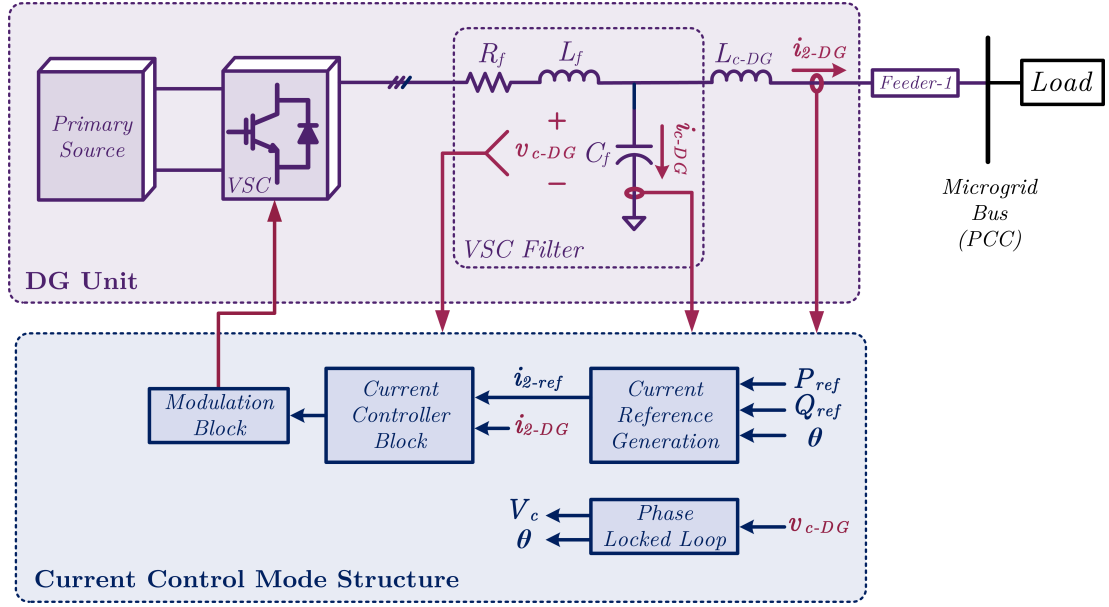


Figure 1.5: DG incorporation in current control mode [63].

sources, such as fuel cells or micro-turbines the power reference should be decided by a supervisory controller.

The power management strategies in islanded microgrids are mainly formed based on the above control modes (i.e. voltage and current control modes). The primary source characteristics and the role of the DG unit in the MG are the main factors to be considered when deciding the control mode of the DG unit.

Secondary Control Layer

Secondary controllers are responsible for achieving general objectives, such as power management, voltage and frequency restoration, cost reduction, or providing accurate reactive power sharing to the DGs [55],[58],[71]-[78]. However, the primary controllers are still utilized to attain the aforementioned general goals. The secondary control layer is slower compared to the primary control layer. This is due to the band-width of the secondary control layer, which is limited by the throughput rate of its communication technology.

Tertiary Control Layer

Tertiary controllers are responsible for regulating the power exchange between the microgrid and the utility grid. Tertiary control layer communicates with the distribution system operator (DSO). After processing the received data, the

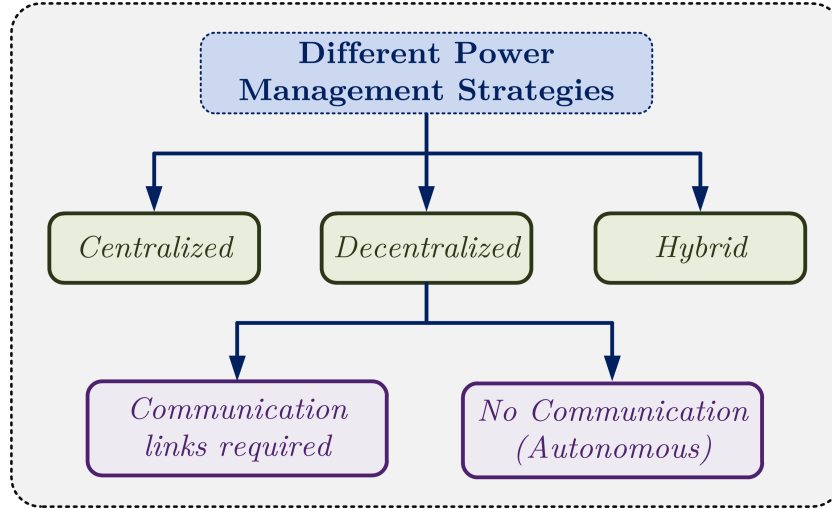


Figure 1.6: Classification of microgrid power management strategies [57].

power exchange between the main grid and the microgrid is scheduled. Amongst the three controllers, the primary controller is the fastest and the tertiary is the slowest. The speed of response of the secondary controller is in between these two.

1.8.2 Different Power Management Strategies for Islanded Microgrids

The main objective of power management strategies in islanded microgrids is to balance the power amongst the DGs, energy storage systems, and loads [79]-[82]. Most power management strategies are designed according to the hierarchical control structure explained in the previous subsection. Depending on the implementation of their secondary controller, the power management strategies can be divided into three main categories; centralized, decentralized and hybrid strategies. Fig. 1.6 indicates this classification [57]. Note that the decentralized strategies include two different sub-categories; non-autonomous (i.e. with communication links) and autonomous (i.e. without communication links). Each category is discussed below [57].

Centralized Control

Centralized control is one of the most popular paradigms of coordinated power management strategies [83]-[86]. In these strategies, in addition to the primary control of the MG elements a central or supervisory controller is designed in order

to coordinate all the constituent units of the MG in a reliable and efficient manner [55]. The central controller is responsible for collecting the required measurement signals from the primary controllers, processing the received data and sending the provided commands such as the reference power or the reference voltage to the primary controllers of the DERs [87, 88].

In [58], a centralized control approach is proposed that uses low-bandwidth communication (LBC) channels in order to restore the voltage level. The voltage level of the point of common coupling (PCC) is compared with the reference voltage, and the error is sent to all the constituent units of the microgrid, after processing by a compensator. This provides the required output voltage restoration to the system.

In [84], a supervisory (centralized) control is applied to the MG to avoid voltage deviations. In this study, two batteries are connected to the MG common bus as distributed storage units. The supervisory control modifies the batteries virtual resistance (VR) so that their state of charge (SoC) vary similarly. The value of the virtual resistance is determined based on the available SoC of the batteries; i.e. a higher virtual resistance results into a lower charge or discharge rate. As an example, in charge mode, a higher VR is applied to the battery with a higher SoC. On the contrary, in discharge mode, a higher VR is applied to the battery with a lower SoC.

An intelligent multi-layer centralized control is proposed in [88] which is specifically designed to realize the power balance in the MG of a tertiary building. The set points of the DGs and load shedding actions are decided by the supervisory control according to the end-user demand, energy cost management, PV generation, load forecast, etc.

The main drawback of the aforementioned centralized control strategies is that they are subject to failure, especially if the system includes several distributed units where the computational burden becomes excessive. To overcome this limitation, decentralized control strategies are proposed as explained below.

Decentralized Control

These control strategies, are further categorized as; (1) with communication (2) without communication (autonomous control).

- **Decentralized Approaches with Communication:** In these approaches, the centralized control is removed, but the communication links are still required to transfer data between some optional DGs. The substantial differ-

ence between the centralized and decentralized controls is that the operative decisions are taken in a decentralized manner.

In [89], a low band-width communication (LBC) channel is used to transfer the current and the DC voltage of the converters, while all the calculations and operational decisions are accomplished in the local (primary) controllers. The proposed control strategy aims to enhance the voltage deviations and poor power sharing which are introduced by the primary controllers. The droop equations of the primary controllers are affected by two locally generated signals. The first signal is formed by processing the error of the reference voltage and the average of the actual voltage by a compensator. This is to restore the MG bus voltage. The second signal is generated by passing the current error through a compensator aiming to provide accurate power sharing to the DGs.

Reference [90] presents a decentralized control strategy to enhance the primary control voltage deviation. This approach shifts the voltage-current droop characteristic by adding a small voltage signal. Using an LBC, the local controllers of the DGs transfer their current magnitude (in per unit) with one another. Then the average current, which should be supplied by each DG, is calculated at their local controllers. Finally, the required signal for voltage control is generated.

Reference [91] also introduces a distributed control technique where a common information bus is used to transfer data among the local controllers. Using a specific resistance, the measured current at the output of each DG is transformed to voltage and is added to the droop equation. The objective of this control approach is to provide equal load sharing among the DGs and to adjust the common bus voltage. The main drawback of this scheme is that the required bus for current sharing needs to be allocated next to the power lines, which may cause significant noises in the bus.

The proposed control method in [92], also performs based on power-line signalling. In this, the communication channel is provided by the power network, where the required data is directly received from the VSC primary controllers and is transferred as power-line signals. The local controller of each DG receives the signal and applies the required variations to its reference voltage.

In conclusion, for the systems with several distributed DGs, utilizing de-

centralized approaches with communication may result into communication network complexity, physical location problems, and plug and play limitations [93].

- **Autonomous Approaches:** In the autonomous power management strategies, the power balance of the microgrid is maintained solely by the primary controller of the DERs, and there is no need for a central controller, external references and/or external communications. Hence, these strategies are the most reliable and robust option for power management of stand-alone microgrids. Nonetheless, the secondary control can still be implemented to provide voltage/frequency restoration or to provide accurate reactive power sharing [58],[71],[74].

Droop control is one of the most promising methods which is extensively deployed in the power management of isolated microgrids [55],[58],[61],[71]. However, since droop control methods use the voltage control mode (VCM), they are not a suitable option for renewable energy sources such as photovoltaic (PV) systems. This is due to the intermittent nature of the RESs that makes them operate more efficiently when deployed in current control mode (CCM), by which they are able to deliver their maximum available power. Another aspect to be considered here is that droop control methods determine the output power of the units based on their maximum capacity which is not a practical solution in the case of energy storage systems. This is due to the variations of the batteries state of charge (i.e. available capacity) as they supply power. Hence, the batteries available capacity plays more important role compared to their maximum capacity and should be given priority when determining their reference power.

Another control method, which is extensively used in this sense is the bus-signalling technique, where different thresholds of the common bus voltage or frequency trigger the mode-changing actions for coordination of the DERs and the ESSs. In [94] a new bus-signalling approach is utilized for power management of an MG with a PV and a storage device. This study only considers the extreme conditions of the stand-alone mode, such as full-charge or full-discharge of the batteries. Another bus-signalling based power sharing is introduced in [95] which aims to limit the influence of the diverse loads. This scheme is implemented on a laboratory MG consisting of a PV, a fuel cell, and multiple batteries. Reference [96] presents a novel bus-signalling approach for a MG with several storage devices. In this

method, the batteries switch their operation mode accordingly in order to maintain the common bus voltage within its allowable range.

Another autonomous approach is presented in [97] for an MG composed of a PV and a battery storage. During charge process, where the battery voltage increases, the VSC of this unit reduces the bus frequency below the anti-islanding frequency limit of the PV. Subsequently, the PV unit becomes disconnected. The main problem of the proposed technique in [97] is that it can only be applied to the microgrids where only one battery storage is responsible for voltage and frequency regulation.

Hybrid Control

Hybrid control structures are a combination of the above structures at different levels to enhance the microgrid performance. References [98]-[100] propose a control scheme for a hybrid system including a PV and a battery storage. An advantage of these approaches is that the PV unit has direct access to the state of charge (SoC) of the battery and external communication is not required in this sense. However, the proposed strategy in [100] still requires a central controller to transfer data between the PV and the diesel generator. Moreover, the control strategies of [98, 99] contain one hybrid source and load which causes the system to operate more like a stand-alone power supply from the control point of view. Hence, these control structures are not useful for an isolated MG with several distributed units.

1.9 Thesis Objectives

The overall objective of the thesis is to develop reliable power management strategies considering practical constraints such as state of charge of battery energy storage systems and distributed energy generation capacities. More detailed objectives of the research presented in this thesis are as follows;

- To enhance the reactive power sharing among inverter-interfaced distributed energy resources (DERs) of an autonomous microgrid.
- To coordinate multiple distributed battery storage systems (BESs) with the distributed energy resources (DERs) of an autonomous microgrid based on a hierarchical (centralized) SoC-based droop control ;

- To propose a new decentralized-autonomous power management strategy for a stand-alone microgrid with multiple distributed energy storage systems (ESSs), maximum power point tracking (MPPT) controlled photovoltaic (PV) system, and a droop controlled DER;
- To propose a new decentralized power management technique, based on bus-signalling approach, for an autonomous microgrid composed of an MPPT controlled PV, a diesel generator and a battery storage system.

1.10 Specific Contributions of the Thesis

The specific contributions of this thesis are highlighted below.

Chapter 2 In this chapter, the existing power sharing techniques are introduced, and their advantages and disadvantages are discussed. Then a new virtual impedance-based power sharing technique is proposed which is specifically designed to adaptively mitigate the reactive power sharing errors among distributed energy resources.

Chapter 3 An alternative power sharing technique is proposed in this chapter which designs and implements a virtual impedance based on eigenvalue analysis of the autonomous microgrid. This strategy provides more reliable response to the system as it is developed based on small-signal model of the microgrid and the microgrid transients as well as the steady state errors are considered.

Chapter 4 In this chapter, a new hierarchical (centralized) control strategy is proposed to coordinate distributed battery storage systems in an autonomous microgrid. Moreover, a new reactive power sharing strategy is proposed which aims to utilize the unused capacity of the BES converters.

Chapter 5 In this chapter, a new decentralized-autonomous power management strategy is proposed for a stand-alone microgrid with a PV, a droop controlled DER, and multiple energy storage systems. Being independent from communication links, proposed strategy provides a more reliable power management to the system compared to the centralized strategy developed in Chapter 4.

Chapter 6 In this chapter, a new decentralized power management strategy is proposed for a typical stand alone microgrid with a PV, a diesel generator, and a battery energy storage system. The proposed strategy performs based on bus-signalling approaches to avoid the battery overcharge and over-discharge. To achieve this, the battery energy storage (BES) unit alarms the other units about its status via regulating the system frequency to predefined values. Also, the required voltage support of the system is always provided with the proposed control of the BES and the PV system.

The publications incorporated in this thesis are given in Appendix E.

1.11 Thesis Outline

The remaining parts of this thesis consists of the following chapters.

Chapter 2 discusses different techniques which can be used for power sharing control and adjustment among parallel converter-interfaced distributed energy resources (DERs) in an autonomous microgrid. The desired power sharing ratio among the DERs is decided by the secondary controller of the distribution network. The MG central controller (MGCC) is responsible for sending the processed data to the primary controller of the DERs. This chapter initially presents the restrictions of the first two methods, then the proposed (third) method is introduced which overcomes the limitations of the other two methods. To minimize the reactive power sharing error among the DERs, in the proposed technique, an adaptive virtual impedance calculation loop is included in the control structure of the DER which imposes the required voltage drop at the output of the converters to attain the desired reactive power sharing. The amount of virtual impedance is adaptively changed to ensure the system disturbances are considered and the power ratio errors are kept below 5%.

Chapter 3 introduces an alternative approach for virtual impedance design, which decouples the active and reactive power sharing without compromising the system stability. To attain this, the virtual impedance is determined based on the stability analysis of the MG. Hence, the system transients and stability requirements are taken into account in addition to the steady state power ratio errors of the DERs. This strategy provides more reliable response to the system compared to the method introduced in Chapter 2 since it is developed based on the small-signal model of the microgrid.

Chapter 4 proposes a new dynamic control method for the BES units within an MG which is composed of two control subsystems. Each subsystem is applied to the BES units depending on their operation mode, i.e. charging or discharging mode. The main objective of the proposed control algorithm in discharge mode is to avoid premature depletion of the BES units as they contribute in supplying the load. Therefore, the BESs output active powers are modified accordingly with their SoC levels reduction. Additionally, in discharge mode, in order to use the BES converter capacity and to avoid overloading the RES units, the proposed control method employs a new reactive power sharing algorithm. Based on this algorithm, the BES units with a lower SoC or a higher unused converter capacity supply a higher amount of reactive power. To achieve this, virtual impedance method is included in the control structure of the BESs converters to facilitate the desired active and reactive power sharing ratios.

Chapter 5 proposes a new decentralized power management strategy which is capable of maintaining the power balance of the MGs including multiple distributed ESSs. The proposed control structure is independent from any global and/or local communication links and therefore, performs in an autonomous manner. With the proposed power management strategy, the RESs operate in current control mode, delivering their maximum available power, while the ESSs supply/absorb the generation and consumption mismatch. Furthermore, the proposed strategy always respects the ESS SoC level, when deciding its mode of operation, to avoid ESS overcharge and over-discharge. Also, the ESS control structure provides voltage regulation to the system in case of voltage sags/swells. Based on the proposed method, ESS operation mode is determined according to its SoC level and the system frequency. This implies that although the system frequency represents the generation and consumption mismatch, the priority is given to the ESS SoC level to decide the mode of operation, while the amount of active power reference for each ESS is determined based on the system frequency.

Chapter 6 proposes a new decentralized power management strategy based on frequency bus-signalling. In the proposed strategy, the BES unit regulates the system frequency according to its SoC, while the proposed comprehensive charge/discharge control, which facilitates a float charge characteristic for the BES, ensures the system power balance. Based on the proposed control, the BES unit is mainly charged by the PV to limit the operation of the diesel generator. Moreover, the PV unit may operate in maximum power point tracking (MPPT) mode or curtailment mode according to the BES status. Lastly, the proposed power management, which is realized in a decentralized manner, provides a robust

voltage regulation to the system under any circumstances. Several case studies are investigated to verify the system performance with the proposed strategy.

The thesis concludes in Chapter 7, where the concluding remarks derived from this research as well as the potential future work are presented.

Chapter 2

Power Sharing Techniques for Converter-Interfaced DERs

2.1 Introduction

Microgrids (MGs) are becoming more popular as an alternative to the expansion of the conventional distribution networks. This is due to the fast development of distributed generations (DGs) and power electronic technologies [101, 102]. MGs could be considered as local grids with several distributed energy resources (DERs) including energy storage systems (ESSs) operating either in grid-connected mode or autonomous mode. In grid-connected operation, the power mismatch within the MG can be compensated by the grid. However, in the autonomous operation, it is necessary to deploy a reliable power sharing technique to integrate all the constituent units of the MG. Moreover, this technique should be capable of responding to the variations of the system without compromising the power balance of the MG [103]. References [104, 105] introduce the MG concept, including the MG protection and power management. Also, [106]-[110] investigate different power management strategies and control algorithms for autonomous MGs.

Three-level hierarchical control is one of the most popular structures for the MGs power management as is shown in Fig. 2.1 [106]. As described in Chapter 1, the MG tertiary controller is responsible for collecting the required data; such as load/weather forecast, economic dispatch, and electricity market and passes the processed data to the MG secondary (central) controller. The MG central controller also receives some other required information from the primary controller of each DER unit and after analyzing the received data determines the reference

power of all the constituent units based on a specific power sharing technique. These reference powers are then sent to the primary controller of each DER where a particular control structure matches the DER output power with its reference power.

Among the existent power management strategies, droop control is widely accepted and deployed in the MG secondary controller. Droop control utilizes the frequency and voltage deviations to decide the DERs output active and reactive powers, respectively [111]-[115]. To determine power ratio among the DERs, it is necessary to design the frequency and voltage droop coefficients properly [114]. This chapter introduces three different power sharing techniques that can be utilized to adjust the output active and reactive powers of the DERs within a droop controlled autonomous MG.

It is well known that in droop controlled converter interfaced MGs; the DERs reactive power is affected by the coupling inductance of the DERs. Therefore, one of the promising power sharing techniques, which is extensively utilized in the MGs, is to design the coupling inductance of any two DERs to be inversely proportional to the desired ratio of the DERs output powers. The main drawback of this technique is that the output power ratio between any two constituent unit is predefined and cannot be modified dynamically. Moreover, in practice, selecting an specified value for DERs coupling inductance is a challenging issue.

The second technique, proposed in [116], simply adjusts the DERs output active power by dynamically modifying the droop control coefficients. With this technique, any desired output active power ratio among the DERs is feasible, regardless of their coupling inductance ratio. However, the main limitation of this technique is that it is only capable of controlling the active power sharing and no control is provided to the DERs reactive power sharing. Hence, this technique is not suitable for the MGs, where the accuracy of reactive power ratio is of interest.

Finally, in this chapter, a different power sharing technique is proposed which combines the advantages of both the aforementioned techniques. This technique aims to adjust the output active and reactive powers of the DERs with respect to their desired ratios and without identifying their coupling inductance ratio. To achieve this, a small virtual inductance is imposed to the converter of each DER in order to realize the desired reactive power ratios. The main advantage of this method is that the desired reactive power ratios are always accomplished as the virtual impedance value is dynamically modified considering the network variations. Different case studies are investigated in PSCAD/EMTDC, in order to

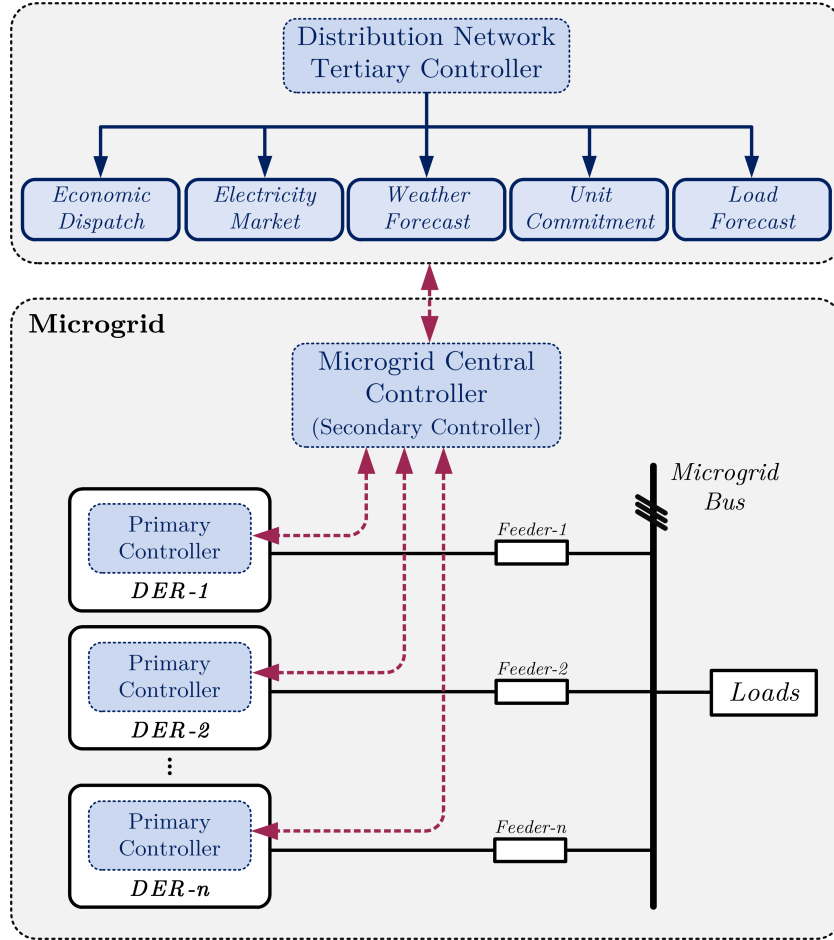


Figure 2.1: Schematic diagram of an example microgrid incorporated with hierarchical control structure.

evaluate and compare the performance of the discussed power sharing techniques.

2.2 Microgrid Structure and Control

Fig. 2.1 shows the stand-alone microgrid (MG) configuration which is investigated in this chapter. The considered MG network consists of n converter-interfaced DERs where each DER includes a primary controller. In Fig. 2.1, a centralized load is indicated. However, the loads can be distributed throughout the MG. Moreover, three levels of the MG hierarchical control structure and the communication links are also shown in Fig. 2.1. It is to be noted that the considered DER units in this chapter are operating in voltage control mode (VCM) and their instantaneous output powers are limited to their maximum capacity.

2.2.1 MG Hierarchical Control System

To achieve a reliable power management and to ensure that the MG power balance is maintained in the autonomous mode, a three-level hierarchical control system can be utilized as shown in Fig. 2.1. This hierarchical control structure consists of the DERs primary controllers, the MG central (secondary) controller.

An optional tertiary controller can be used in an isolated microgrid to provide optimal power flow within the system considering different factors which may affect the system power balance [116]. For this, the network tertiary controller collects different signals such as load/weather forecast, economic dispatch, and electricity market as shown in 2.1. These data are initially processed by the analyzing algorithm of the tertiary controller, and the results are then sent to the MG secondary controller.

The secondary or the central controller of the MG is responsible for maintaining the power balance of the system. To attain this, the secondary controller continuously communicates with the primary and tertiary controllers to ensure that the system variations are taken into account. After receiving the required data from the primary and tertiary controllers, the MG secondary controller determines the active and reactive reference powers and sends them to the primary controller of the DERs. It is worth noting that in the autonomous mode the reference signals are sent to the DERs in the form of voltage magnitude and frequency as the DERs are operating in VCM. Moreover, the secondary control is run in a slower time frame in comparison to the primary control [117].

The primary controller of each DER is responsible for matching the DERs actual output powers with their references. This controller consists of two control loops. The outer control loop aims to produce the output active and reactive power references according to the reference voltage magnitude and frequency received from the secondary controller. Whereas, the inner control loop ensures the proper tracking of the generated references by controlling the switching signals of the converter.

This chapter introduces different power sharing techniques which can be applied to an existing droop controlled MG. To achieve this, some modifications are applied to the MG secondary controller and the DERs primary controller. As a result, the share of output active and reactive powers will be different when applying different techniques.

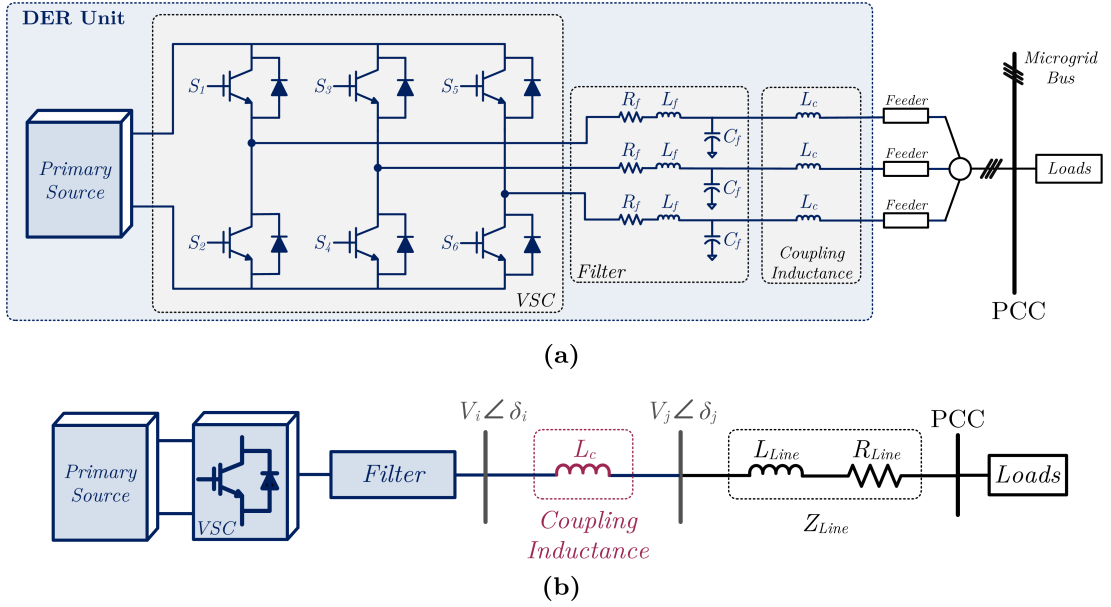


Figure 2.2: DER unit including the primary source, VSC, filter, and coupling inductance; (a) three-phase schematic, (b) single-phase schematic.

2.2.2 DER Converter Structure

Fig. 2.2(a) shows different components of the DER units. As shown in this figure, the DER units considered in this chapter consist of a primary source, voltage source converter (VSC) and VSC filter. The VSC structure includes a three phase converter which utilizes insulated gate bipolar transistors (IGBT), as indicated in Fig. 2.2(a). IGBTs are equipped with anti-parallel diodes and snubber circuits. As the converters are performed in voltage control mode (VCM), an LC filter is considered for each phase at the outputs of the VSC. Also, the output terminals of the VSC filters are connected to the feeders through the coupling inductance (L_c) of the DER. It is worth noting that the output reactive power of the DERs is highly dependent to this coupling inductance. Hence, considering this inductance in the power sharing techniques is necessary.

2.2.3 Droop Control

Fig. 2.2(b) shows the single-phase connection of the DER unit to the point of common coupling (PCC). The voltage magnitude and angles across the coupling inductance of L_c are also specified in this figure. Based on Fig. 2.2(b), the active power (p) and reactive power (q) supplied by the DER systems to the MG can

be calculated as [118];

$$s = p + jq = |V_j| \left(\frac{|V_i| \angle \delta_i - |V_j| \angle \delta_j}{\omega L_c} \right)^* \quad (2.1)$$

where, $|V_i|$ and δ_i are the voltage magnitude and angle at the output of the VSC filter whereas $|V_j|$ and δ_j are the voltage magnitude and angle at the PCC side.

Based on frequency droop control in the autonomous mode, it is assumed that for the the DER output active power variations between zero and the rated value (P_{rated}), the MG system frequency varies by $\Delta\omega$. The slope of this variation is referred to as frequency droop coefficient (m) and is calculated as;

$$m = \frac{\Delta\omega}{P_{rated}} = 2\pi\Delta f \quad (2.2)$$

In the considered MG of Fig. 2.1, $\Delta\omega$ is constant for all the associated units of the MG (i.e. $\Delta\omega_1 = \Delta\omega_2$ for any two DERs with different capacity). Hence, the ratio of P - f droop coefficient (m) between these two DER systems can be expressed as;

$$m_1 P_{rated,1} = m_2 P_{rated,2} \implies \frac{m_1}{m_2} = \frac{P_{rated,2}}{P_{rated,1}} \quad (2.3)$$

Similarly, based on voltage droop control, it is assumed that for the DER output reactive power variations between zero and the rated value (Q_{rated}), the MG voltage varies by ΔV . The slope of this variation is referred to as voltage droop coefficient (n) and is calculated as [118];

$$n = \frac{\Delta V}{Q_{rated}} \quad (2.4)$$

In the considered MG of Fig. 2.1, for any two DERs with different capacity, ΔV is constant (i.e. $\Delta V_1 = \Delta V_2$). Hence, the ratio of Q - V droop coefficient (n) between these two DER units can be expressed as;

$$n_1 Q_{rated,1} = n_2 Q_{rated,2} \implies \frac{n_1}{n_2} = \frac{Q_{rated,2}}{Q_{rated,1}} \quad (2.5)$$

Therefore, utilizing the conventional droop control facilitates decentralized power sharing control of the MG units by controlling the voltage magnitude and angle at the output of the DERs converters. This can be expressed for the DER of Fig. 2.2(b) as [118];

$$f_j = f_{rated} + m \left(\frac{X_{Line}}{Z_{Line}} (P_{rated} - P) - \frac{R_{Line}}{Z_{Line}} (Q_{rated} - Q) \right) \quad (2.6)$$

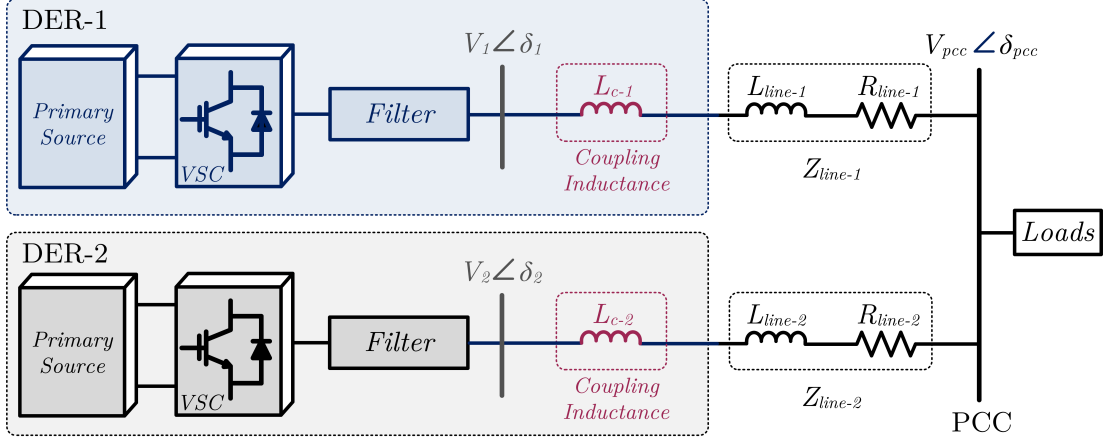


Figure 2.3: Simplified diagram of the microgrid structure with two DERs.

$$V_j = V_{rated} + n \left(\frac{R_{Line}}{Z_{Line}} (P_{rated} - P) + \frac{X_{Line}}{Z_{Line}} (Q_{rated} - Q) \right) \quad (2.7)$$

where, $Z_{line} = R_{line} + jX_{line}$ is the feeder equivalent impedance as shown in Fig. 2.2(b). If the MG feeders are considered to be mostly inductive (i.e. with a higher X_{line}/R_{line} ratio), the active and reactive powers can be decoupled. Therefore, (2.4) can be further simplified as;

$$f_j = f_{rated} + m(P_{rated} - P) \quad (2.8)$$

$$V_j = V_{rated} + n(Q_{rated} - Q) \quad (2.9)$$

where, V_{rated} and f_{rated} are the same for all the associated DERs of the system. Also, m , n , P_{rated} and Q_{rated} are specified based on (2.2) and (2.4). Hence, the average output active and reactive power ratios among DER-1 and DER-2 can be expressed as;

$$\frac{P_1}{P_2} = \frac{m_2}{m_1} \quad (2.10)$$

$$\frac{Q_1}{Q_2} = \frac{n_2}{n_1} \quad (2.11)$$

In the MG structure shown in Fig. 2.3, it is assumed that the line impedance is mostly inductive (i.e. $X_{Line} \gg R_{Line}$) and the two DER units are supplying a common load. In Fig. 2.3, the coupling inductance of DER-1 is shown as L_{c-1} while that of DER-2 is shown as L_{c-2} . Also, the feeder impedance of DER-1 and DER-2 are considered to be jX_{line-1} and jX_{line-2} , respectively. Assuming the PCC voltage magnitude and angle to be V_{pcc} and δ_{pcc} , respectively, the active power supplied by each DER to the load can be calculated based on (2.1) as;

$$P_1 = \frac{|V_{pcc}| |V_1| \sin(\delta_1 - \delta_{pcc})}{\omega L_{c-1} + \omega L_{line-1}} \quad (2.12)$$

$$P_2 = \frac{|V_{pcc}||V_2|\sin(\delta_2 - \delta_{pcc})}{\omega L_{c-2} + \omega L_{line-2}} \quad (2.13)$$

Similarly, the reactive power supplied by each DER to the load can be calculated based on (2.1) as;

$$Q_1 = \frac{|V_1|^2 - |V_1||V_{pcc}|\cos(\delta_1 - \delta_{pcc})}{\omega L_{c-1} + \omega L_{line-1}} \quad (2.14)$$

$$Q_2 = \frac{|V_2|^2 - |V_2||V_{pcc}|\cos(\delta_2 - \delta_{pcc})}{\omega L_{c-2} + \omega L_{line-2}} \quad (2.15)$$

where, $|V_1|$ and $|V_2|$ are the voltage magnitude at the output of DER-1 and DER-2, respectively, and δ_1 and δ_2 are the voltage angle at the output of DER-1 and DER-2, respectively. As the line impedance is chosen to be negligible compared to the coupling inductance of the DERs (i.e. $X_{line} \ll X_c = \omega L_c$), the active/reactive power delivered by the DER system to the load is mainly affected by the coupling inductance at the output of the DER system and is independent of the MG line reactance. Therefore, (2.12)-(2.15) can be simplified as;

$$P_1 = \frac{|V_{pcc}||V_1|\sin\delta_1}{\omega L_{c-1}} \quad (2.16)$$

$$P_2 = \frac{|V_{pcc}||V_2|\sin\delta_2}{\omega L_{c-2}} \quad (2.17)$$

$$Q_1 = \frac{|V_1|^2 - |V_1||V_{pcc}|\cos\delta_1}{\omega L_{c-1}} \quad (2.18)$$

$$Q_2 = \frac{|V_2|^2 - |V_2||V_{pcc}|\cos\delta_2}{\omega L_{c-2}} \quad (2.19)$$

2.3 Different Power Sharing Techniques

In this section, three different power sharing techniques are introduced which can be used to control the output active and reactive powers of parallel connected DERs in an autonomous MG. Each technique has several advantages and disadvantages which are explained in detail in the following subsections.

2.3.1 Power Sharing by Coupling Inductance Design

Considering Eqs. (2.16)-(2.19), the average active/reactive power ratio for any two DER units within the example MG of Fig. 2.1 can be given as;

$$\frac{P_1}{P_2} = \frac{L_{c-2} |V_1| \sin\delta_1}{L_{c-1} |V_2| \sin\delta_2} \quad (2.20)$$

$$\frac{Q_1}{Q_2} = \frac{L_{c-2} |V_1| - |V_{pcc}| \cos \delta_1}{L_{c-1} |V_2| - |V_{pcc}| \cos \delta_2} \quad (2.21)$$

For simplicity, many researches such as [103, 110] design the DERs coupling inductance such that their ratio is inversely proportional to the desired ratio of the DERs output active and reactive powers;

$$\frac{P_1}{P_2} = \frac{L_{c-2}}{L_{c-1}} = \frac{m_2}{m_1} \quad (2.22)$$

$$\frac{Q_1}{Q_2} = \frac{L_{c-2}}{L_{c-1}} = \frac{n_2}{n_1} \quad (2.23)$$

In other words, the higher the DER share of power the smaller the coupling inductance should be selected. To achieve (2.22) and (2.23), the following equations must be satisfied:

$$|V_1| \sin \delta_1 = |V_2| \sin \delta_2 \quad (2.24)$$

$$|V_1| \cos \delta_1 = |V_2| \cos \delta_2 \quad (2.25)$$

This is the most popular technique to realize the desired output power ratio among parallel connected DERs in an MG. An advantage of the above technique is that it ensures the desired ratio for both active and reactive output powers. Nonetheless, the main restriction of this technique is that a constant power ratio should be chosen for both active and reactive powers of the DERs and the ratios cannot be changed under any circumstances. Otherwise, the desired ratio cannot be facilitated as the coupling inductance ratio cannot be redesigned. Moreover, designing a specified ratio for the DERs coupling inductance is a challenging issue as these inductances are predefined.

It is to be noted that some assumptions are taken into account in this technique. As an example, the voltage angle difference on two sides of the coupling inductance (δ_{ij}) is assumed to be negligible. Hence, the operating point is placed on the linear section of the sinusoidal $P - \delta$ characteristic of (2.1). Similarly, it is assumed that the voltage drop across the coupling inductance ($|V_1| - |V_{pcc}|$) is ignorable (i.e. 1%-2%).

2.3.2 Power Sharing by Droop Coefficients Design

In this technique, it is assumed that the ratio of the DERs coupling inductance (i.e. $k > 0$) is chosen regardless of the active and reactive power ratios. Thus, based on this technique to realize the desired output active power ratio between any two DERs, it is suggested to adjust the reference power (P_{ref}) and $P - f$

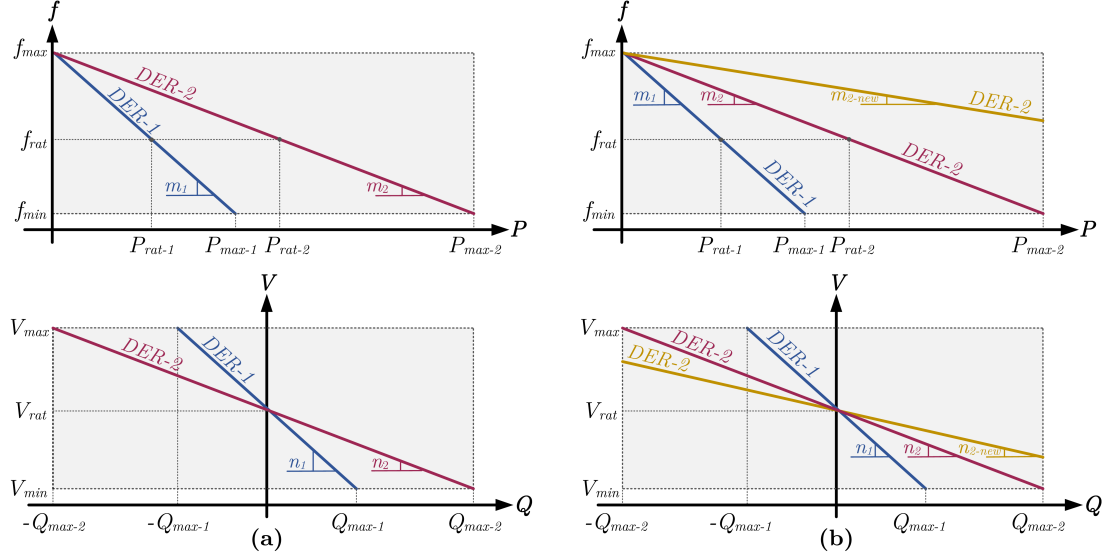


Figure 2.4: (a) $P - f$ and $Q - V$ droop characteristics of the MG DERs, (b) droop characteristics adjustment to satisfy the dynamic power ratio variations.

droop coefficient (m) for one DER according to the predefined parameters of the other DER. Reference [119] indicates that by changing P_{rated} , Q_{rated} , m , and n to P_{rated}^{new} , Q_{rated}^{new} , m^{new} , and n^{new} for one DER while assuming a constant predefined P_{rated} , Q_{rated} , m and n for the other DER, the output active power ratio of the DERs can be adjusted. The schematic of this procedure is shown in Fig. 2.4. Considering the above conditions [119];

$$\begin{cases} P_1/P_2 = k_p \\ L_{c-2}/L_{c-1} = k \end{cases} \implies |V_1| \sin \delta_1 = (k_p/k) |V_2| \sin \delta_2 = k' |V_2| \sin \delta_2 \quad (2.26)$$

where $k' = k_p/k$. From (2.22), it is evident that under the above conditions, The output voltages of both DER units are correlated by a factor of k' . Similarly, with the above conditions, the reactive power ratio of the two DER units can be expressed as [119];

$$\begin{cases} Q_1/Q_2 = k_q \\ L_{c-2}/L_{c-1} = k \end{cases} \implies |V_1| - |V_{pcc}| \cos \delta_1 = (k_q/k) (|V_2| - |V_{pcc}| \cos \delta_2) \quad (2.27)$$

Hence, from (2.26) and (2.27), it is evident that in general $k_p \neq k_q$. Therefore, the active output power of the two DER systems can be controlled to be equal to the desired value of k_p while the ratio of the reactive power outputs among these two DER systems will not be equal to k_p . In [119], a detailed analysis presents the limits of k_p and k_q .

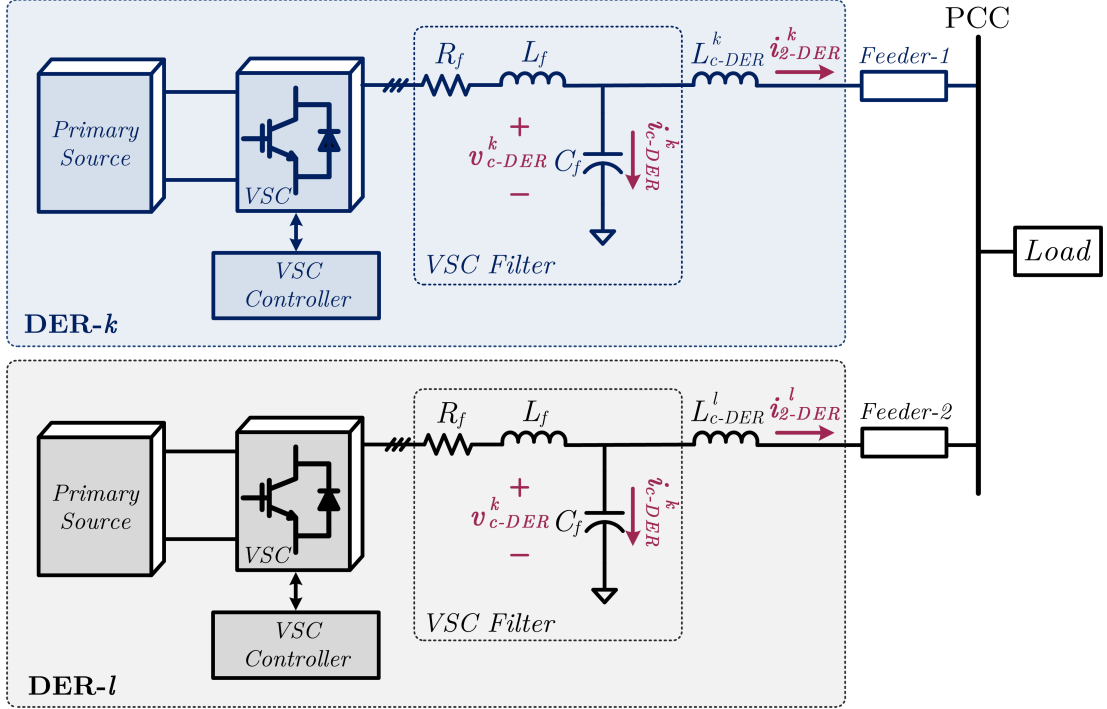


Figure 2.5: Simplified diagram of the microgrid with the measurement signals.

It can be concluded that by applying this second technique, the DERs output active power ratio can be modified dynamically irrespective of the DERs coupling inductance ratios. This is achieved by adaptively adjusting the droop control parameters (i.e. P_{ref} , Q_{ref} , m and n). However, the introduced technique is not able to control the DERs output reactive power ratios at the same time.

2.3.3 Power Sharing by Virtual Impedance Design

As mentioned previously, the reactive power sharing among the DERs in a droop controlled MG is extremely affected by the coupling inductance of the DERs whereas, the active power sharing can be controlled regardless of the L_c ratios. Therefore, coupling inductance mismatches always result in poor reactive power sharing between the DERs. Considering X_{c-DER}^l and X_{c-DER}^k as the output coupling impedance of DER- l and DER- k , respectively (see Fig. 2.5), based on (2.1), reactive power ratio among these units is proportional to;

$$\frac{Q_{DER}^l}{Q_{DER}^k} \propto \frac{X_{c-DER}^k}{X_{c-DER}^l} \quad (2.28)$$

Since designing the coupling inductance ratio is problematic, imposing a virtual impedance in series with the coupling inductance is proposed instead. To ac-

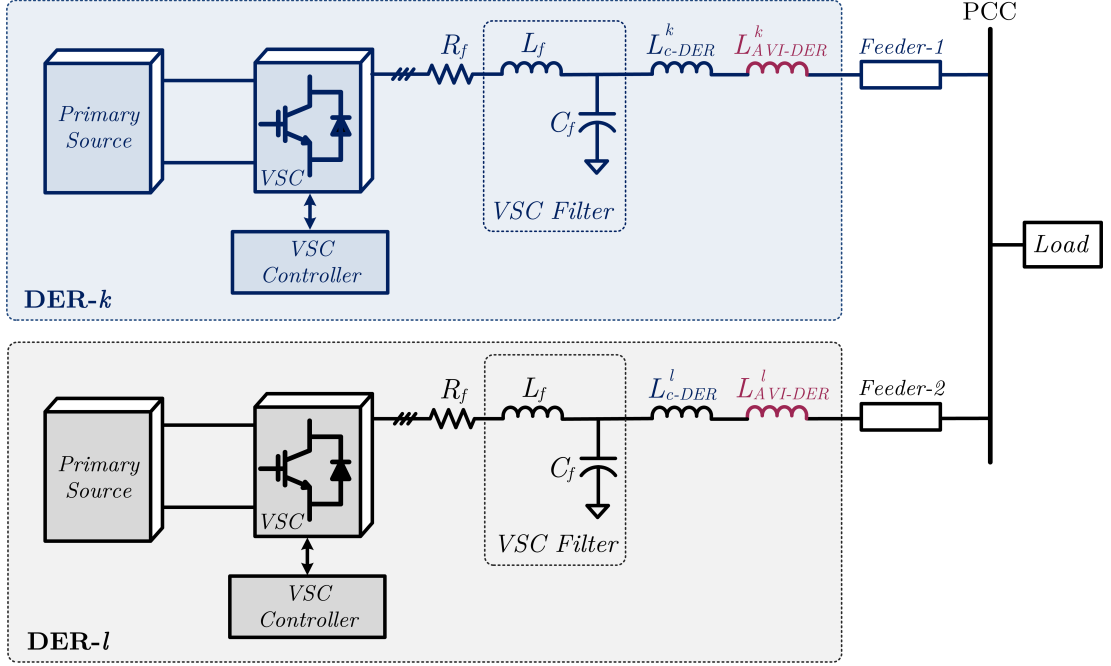


Figure 2.6: VSC control structure in presence of AVI.

comply the desired reactive power sharing among the DERs with the proposed method, it is necessary to carefully design and implement the virtual impedance for the converter of each unit in order to compensate the impedance mismatch between the units. For this, a new technique is developed and is described in detail below.

Proposed Adaptive Virtual Impedance Design and Implementation

In Fig. 2.6, two DER units are connected to the point of common coupling (PCC). Assuming the virtual inductances of $L_{AVI-DER}^l$ and $L_{AVI-DER}^k$ are connected in series with the coupling inductances of each unit (i.e. L_{c-DER}^l and L_{c-DER}^k) as shown in Fig. 2.6, the reactive power ratio between these two units can be expressed as,

$$\frac{Q_{DER}^l}{Q_{DER}^k} \propto \frac{X_{c-DER}^k + X_{AVI-DER}^k}{X_{c-DER}^l + X_{AVI-DER}^l} \quad (2.29)$$

where, X_{c-DER}^l and $X_{AVI-DER}^l$ are the coupling impedance and virtual impedance of DER- l , respectively. Also, X_{c-DER}^k and $X_{AVI-DER}^k$ are the coupling impedance and virtual impedance of DER- k , respectively.

The same approach can be considered for the reactive output power of each DER with and without the virtual impedance. Based on (2.29), the ratio of actual

and desired reactive power for DER- k of the MG can be expressed as;

$$\frac{Q_{actual}^k}{Q_{desired}^k} = \frac{X_{c-DER}^k + X_{AVI-DER}^k}{X_{c-DER}^k} \quad (2.30)$$

where, Q_{actual}^k and $Q_{desired}^k$ are the actual and desired reactive power values for DER- k and X_{c-DER}^k and $X_{AVI-DER}^k$ are the coupling and virtual impedance of the same DER, respectively. Eq. (2.30) is achieved based on the fact that the actual reactive power is delivered by the DER without the virtual impedance and the desired reactive power can be drawn from the DER if $X_{AVI-DER}^k$ was in series with the coupling inductance of X_{c-DER}^k . Note that the desired reactive power for each DER is determined based on the demand and the reactive power ratios. Hence, from (2.30) the virtual impedance value of DER- k can be calculated as;

$$x_{AVI-DER}^k = \left(\frac{Q_{actual}^k}{Q_{desired}^k} - 1 \right) X_{c-DER}^k \quad (2.31)$$

To minimize the reactive power sharing error among the DERs in the proposed method, the reactive power ratio errors are calculated and monitored continuously as;

$$Q_{ratio-err} \% = \left(\frac{Q_{desired}^k}{Q_{desired}^l} - \frac{Q_{actual}^k}{Q_{actual}^l} \right) / \left(\frac{Q_{desired}^k}{Q_{desired}^l} \right) \times 100 \quad (2.32)$$

where, $Q_{actual}^{k/l}$ and $Q_{desired}^{k/l}$ are the measured and desired reactive power of DER- k/l and the latter is decided by the MG secondary controller. If the errors are more than five percent, the control system continues to calculate a new adaptive virtual impedance (AVI) value by re-measurement of actual reactive power and adding the new $X_{AVI-DER}^k$ to the previous value to reduce the reactive power ratio error dynamically. In fact, the process of AVI calculation is flexible, and hence, it adaptively updates the AVI following any variations within the system. The minimum limit of the ratio error can be modified according to the system requirements. To define the AVI for each DER in the MG, a new module is developed and located within the DER primary controller as shown in Fig. 2.7 which calculates $L_{AVI-DER}$ for each DER based on (2.31). Moreover, the desired reactive power in (2.31) is determined by the secondary controller of the MG and transmitted to the primary controller of the DERs.

Converters Voltage Reference Generation in the Presence of AVI

The proposed control structure for each converter-interfaced DER contains two inner control loops as shown in Fig. 2.7:

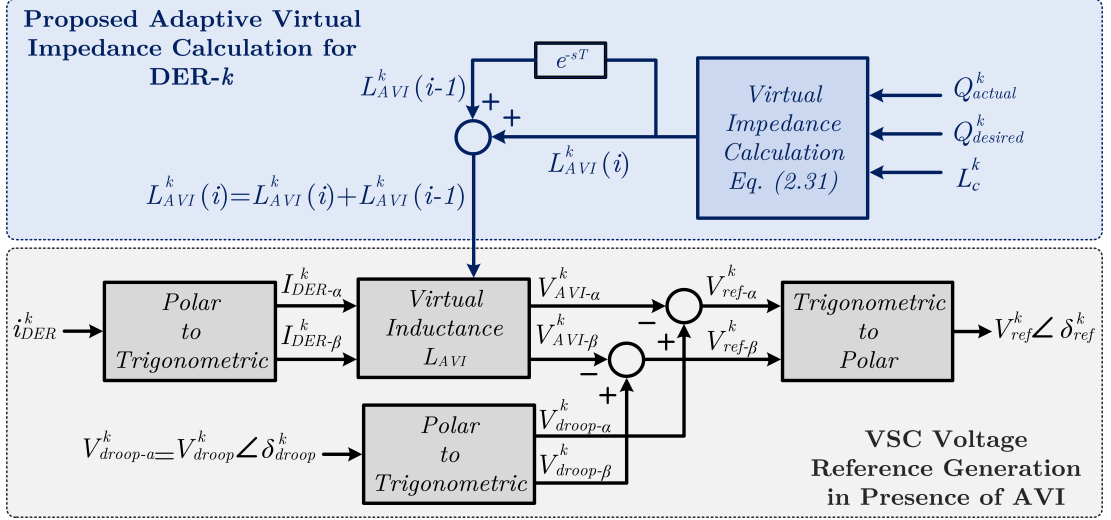


Figure 2.7: DER control structure with the proposed adaptive virtual impedance.

- Adaptive virtual impedance calculation loop based on (2.31), in order to establish reactive power sharing;
- VSC voltage reference generation loop as explained below, to provide the switching signals of the converters.

To generate voltage references, first, it is necessary to calculate the phase voltages at the output of the VSCs by applying the voltage drop across the AVI. This is calculated for DER- k as [120],

$$v_{ref}^k = v_{droop}^k - v_{AVI}^k \quad (2.33)$$

where, $v_{droop}^k = V_{droop}^k \angle \delta_{droop}^k$ is the original droop voltage calculated from (2.9) and v_{AVI}^k is the voltage drop across the AVI. Eq. (2.33) can be expressed in $\alpha\beta$ coordinates as;

$$\begin{aligned} V_{ref-\alpha}^k &= v_{droop}^k \cos(\delta_{droop}^k) + X_{AVI-DER}^k I^k \sin(\theta^k) \\ V_{ref-\beta}^k &= v_{droop}^k \sin(\delta_{droop}^k) - X_{AVI-DER}^k I^k \cos(\theta^k) \end{aligned} \quad (2.34)$$

where, $X_{AVI-DER}^k = \omega L_{AVI-DER}^k$ and $I^k \angle \theta^k$ is the phase- a current of the coupling inductance for DER- k . The reference voltage for the VSC output of DER- k is then calculated as [120];

$$\begin{aligned} V_{ref}^k &= \sqrt{(V_{ref-\alpha}^k)^2 + (V_{ref-\beta}^k)^2} \\ \delta_{ref}^k &= \tan^{-1}\left(\frac{V_{ref-\beta}^k}{V_{ref-\alpha}^k}\right) \end{aligned} \quad (2.35)$$

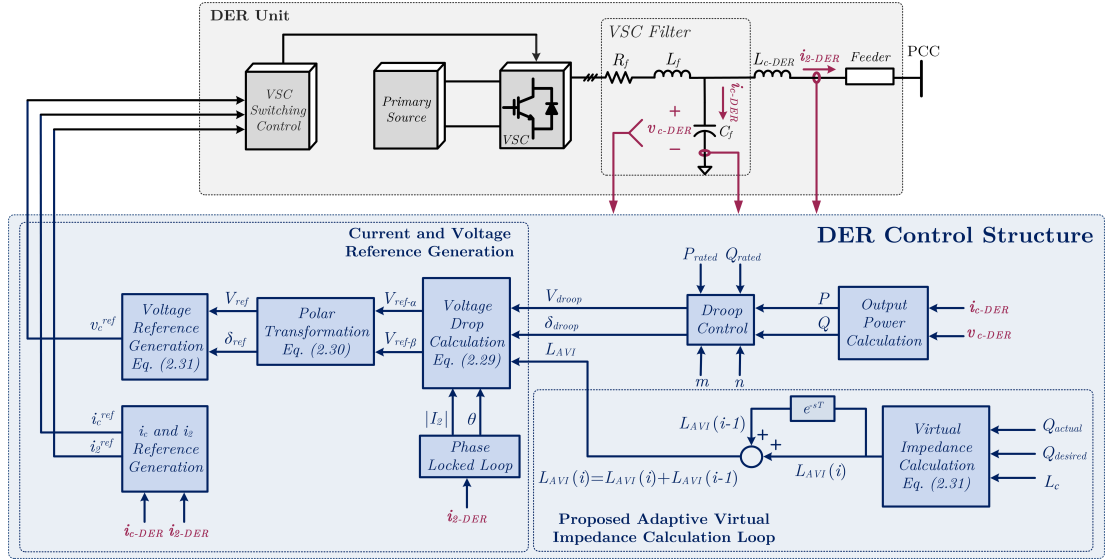


Figure 2.8: DER control structure with the proposed adaptive virtual impedance.

Finally, the instantaneous voltage reference across the filter capacitance (C_f) of DER- k is generated as;

$$\begin{aligned}
 v_a^k &= \sqrt{2}V_{ref}^k \sin(\omega t + \delta_{ref}^k) \\
 v_b^k &= \sqrt{2}V_{ref}^k \sin(\omega t + \delta_{ref}^k - 120) \\
 v_c^k &= \sqrt{2}V_{ref}^k \sin(\omega t + \delta_{ref}^k + 120)
 \end{aligned} \tag{2.36}$$

Fig. 2.8 illustrates the proposed DER control structure with the adaptive virtual impedance calculation loop.

2.4 Simulation Results

To evaluate the performance of the discussed power sharing techniques, the MG system shown in Fig. 2.1 is simulated in PSCAD/EMTDC. Four different case studies are investigated here, where two DERs are considered in Case-1 and Case-2 and four DERs are considered in the last two cases. The parameters of the network, DER converters and filters are given in the Table 2.1. Also, Table 2.2 specifies the DERs coupling inductance and droop coefficients for each case study.

Table 2.1: Technical data of the considered MG.

Parameter	Description
<i>Microgrid Parameters</i>	
Rated PCC Voltage	$V_{LL} = 220 V$
Rated Frequency	$f_r = 50 Hz$
Feeder Resistance	$R_{line} = 0.5 \Omega$
Feeder Inductance	$L_{line} = 3.2 mH$
<i>Voltage Source Converters</i>	
Filter Resistance	$R_f = 0.1 \Omega$
Filter Inductance	$L_f = 0.1 mH$
Filter Capacitance	$C_f = 50 \mu$
DC Link Voltage	$V_{dc} = 350 V$
Rated Power	$P_{rat} = 3 \text{ kW}, Q_{rat} = 1 \text{ kVar}$

2.4.1 Case-1: Power Sharing by Coupling Inductance Design

In this case, it is assumed that the coupling inductance ratio of the DERs is inversely proportional to the ratio of the droop coefficients. Hence, (2.22) and (2.23) are satisfied as follows;

$$\frac{P_1}{P_2} = \frac{L_{c-2}}{L_{c-1}} = \frac{m_2}{m_1} = 2 \quad (2.37)$$

$$\frac{Q_1}{Q_2} = \frac{L_{c-2}}{L_{c-1}} = \frac{n_2}{n_1} = 2 \quad (2.38)$$

Fig. 2.9 shows the simulation results of this case study. Initially, a constant load of 5.8 [kW] and 1.9 [kVar] is applied to the system. As indicated in Fig. 2.9(a), two step variations are applied to the load. At $t = t_1$, load is decreased to 4.8 [kW] and 1.5 [kVar] and at $t = t_2$, it is increased to 6.4 [kW] and 2.9 [kVar].

Fig. 2.9(b) shows the active power variations of the two DERs. It is evident that during all three time intervals the active output power of DER-1 is almost twice as that of DER-2. The results of reactive power outputs are shown in Fig. 2.9(c). From this figure, it is obvious that DER-1 delivers twice more reactive power compared to DER-2.

Based on the above results, it can be concluded that the errors of active and reactive power ratios are negligible if the droop coefficient and the coupling inductance ratios are designed to be inversely proportional to the desired active and reactive power ratios.

Table 2.2: DERs Specifications.

Parameter	Description		
<i>Coupling Inductances</i>			
<i>DER</i>	<i>Case-1</i>	<i>Case-2</i>	<i>Case-3</i>
DER-1	$L_c = 30 \text{ mH}$	$L_c = 30 \text{ mH}$	$L_c = 30 \text{ mH}$
DER-2	$L_c = 60 \text{ mH}$	$L_c = 30 \text{ mH}$	$L_c = 30 \text{ mH}$
DER-3	-	-	$L_c = 30 \text{ mH}$
DER-4	-	-	$L_c = 30 \text{ mH}$
<i>Frequency Droop Coefficients</i>			
<i>DER</i>	<i>Case-1</i>	<i>Case-2</i>	<i>Case-3</i>
DER-1	$m = 1500$	$m = 1500$	$m = 897.6$
DER-2	$m = 3000$	$m = 3000$	$m = 1795.2$
DER-3	-	-	$m = 448.8$
DER-4	-	-	$m = 897.6$
<i>Voltage Droop Coefficients</i>			
<i>DER</i>	<i>Case-1</i>	<i>Case-2</i>	<i>Case-3</i>
DER-1	$n = 0.9$	$n = 0.9$	$n = 24$
DER-2	$n = 1.8$	$n = 1.8$	$n = 12$
DER-3	-	-	$n = 48$
DER-4	-	-	$n = 24$

2.4.2 Case-2: Power Sharing by Droop Coefficients Design

In this case study it is assumed that both DERs have the same coupling inductance, as specified in Table 2.1 while $P_1/P_2 = k_p = 2$. Hence, in (2.26) and (2.27), $k_p \neq k_q$. The related simulation results of this case study are depicted in Fig. 2.10. Fig. 2.10(a), indicates the load variations for this case study. For $t < t_1$, a constant load of 6.2 [kW] and 2.0 [kVar] is applied to the system. At $t = t_1$, the load is increased to 7.2 [kW] and 3.3 [kVar] and at $t = t_1$, the load is increased further to 5.0 [kW] and 1.5 [kVar].

The active power variations of the two DERs are shown in Fig. 2.10(b). It is visible from this figure that the desired active power ratio of $P_1/P_2 = 2$ is validated during all three time intervals. However, the results are not the same for the reactive power ratios. Based on Fig. 2.10(c) for three time intervals of $t < t_1$, $t_1 < t < t_2$ and $t_2 < t < t_3$, the ratio of Q_1/Q_2 is equal to 0.84, 0.8 and

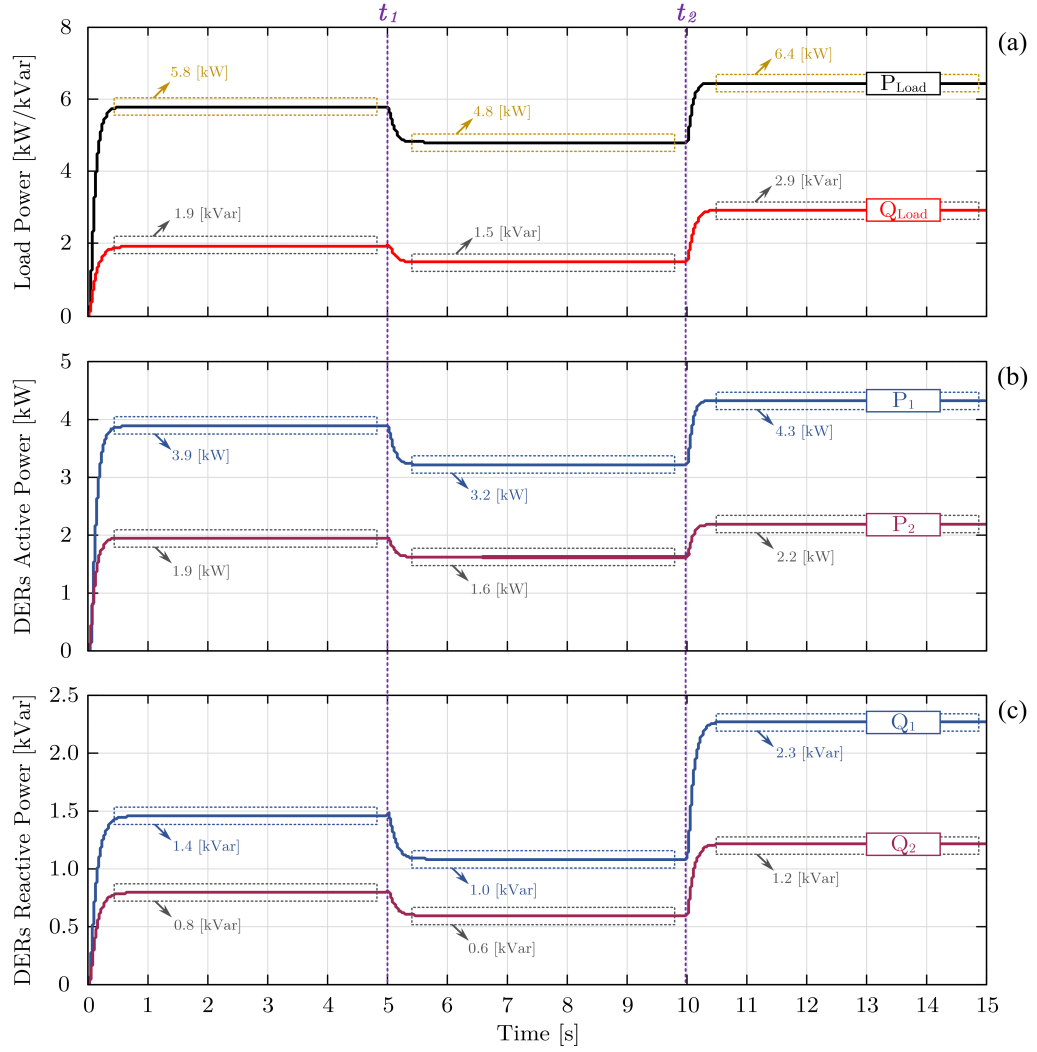


Figure 2.9: Case-1 results: power sharing based on coupling inductance design.

0.88, respectively. Hence, the second power sharing technique is not suitable for the MG systems where the accuracy of the reactive power ratios are of interest.

2.4.3 Case-3: Power Sharing by Virtual Impedance-based Droop

In this case study, four DERs are considered in the MG configuration shown in Fig. 2.1 and the adaptive virtual impedance (AVI) calculation loop, shown in Fig. 2.7 is applied to the primary controller of each DER. It is also assumed that all the DERs have the same coupling inductance as specified in Table 2.2. Moreover, the desired reactive power ratios are assumed to be reciprocal with

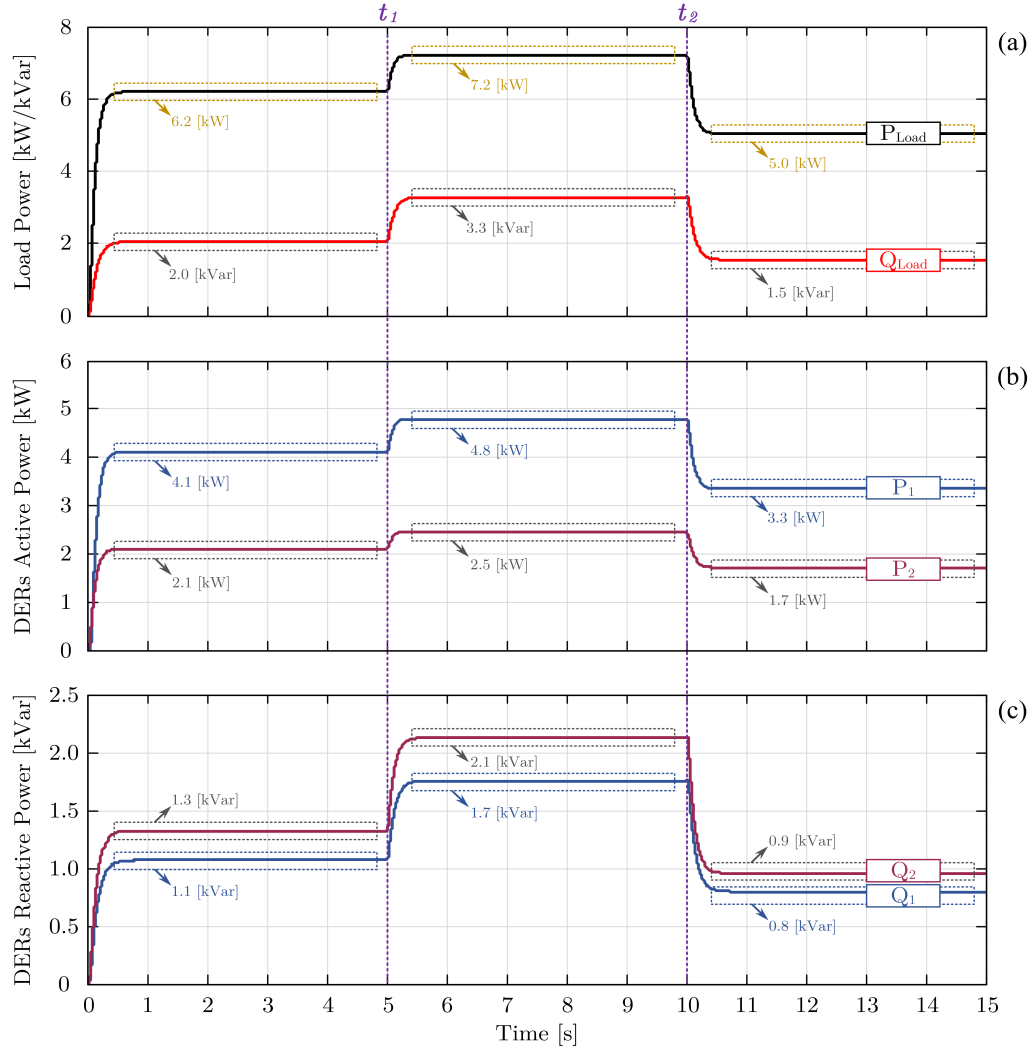


Figure 2.10: Case-2 results: power sharing based on droop coefficient design.

the desired active power ratios. It is worth noting that the reactive power ratios can be varied to any values considering the system requirements. Initially, a constant load of 7.5 [kW] and 2.5 [kVar] is applied to the system. As indicated in Fig. 2.11(a), two step variations are applied to the load. At $t = t_1$, the load is decreased to 5.8 [kW] and 1.8 [kVar] and at $t = t_2$, it is increased to 8.5 [kW] and 3.9 [kVar].

Figs. 2.11(b) and 2.11(c) depict the active and reactive power variations of the four DERs. From these figures DER-1 and DER-4 have the same output active and reactive powers which is expected according to their m and n ratios (see Table 2.2).

Table 2.3 summarizes the desired active power ratios and the errors of these

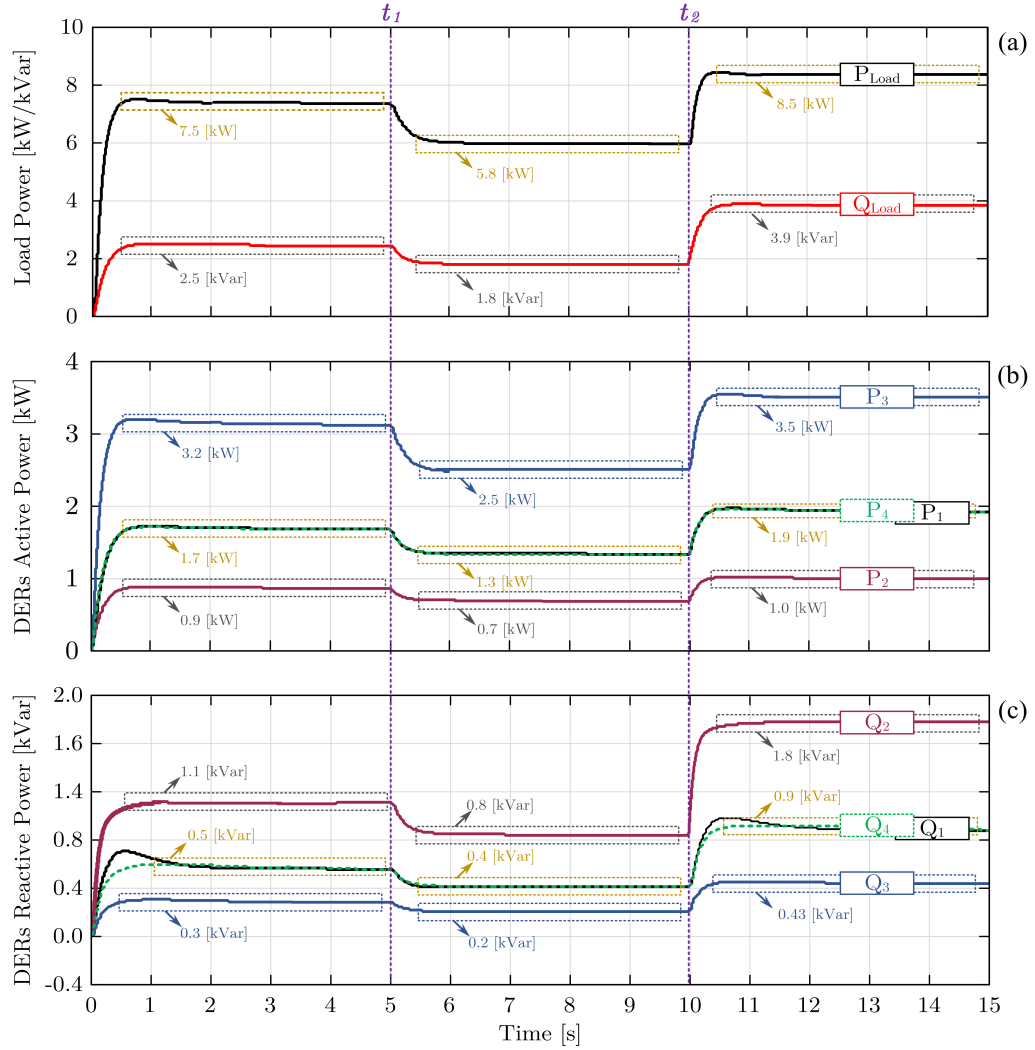


Figure 2.11: Case-3 results: power sharing based on virtual impedance design.

ratios during all three time intervals. It is evident from this table that the errors are kept below 10%, regardless of the coupling inductance ratios.

Table 2.4 indicates the results for the desired reactive power ratios and their errors during all three time intervals. It is evident from this table that the steady state errors for the reactive power ratios are kept below 3%. This is achieved by including the AVI calculation loop in the primary controller of the DERs which dynamically calculates and applies the AVI to their output terminals.

Moreover, from Fig. 2.11 and Table 2.4 it can be concluded that the load variations are also considered by the virtual impedance calculation loop as a new AVI is calculated for each time interval of the load changes. Thus, the proposed power sharing technique adaptively varies the virtual impedance without inter-

Table 2.3: Active power ratio errors of Case-3 (virtual-impedance based droop).

Time Intervals	Active Power Ratios and Errors for Fig. 2.10(b)					
	P_1/P_2	Error [%]	P_1/P_3	Error [%]	P_1/P_4	Error [%]
$0 < t < t_1$	2	2.4	0.5	2.8	1.0	3.0
$t_1 < t < t_2$	2	6.7	0.5	6.5	1.0	8.4
$t_2 < t < t_3$	2	0.01	0.5	0.03	1.0	0.12

Table 2.4: Reactive power ratio errors of Case-3 (virtual-impedance based droop).

Time Intervals	Reactive Power Ratios and Errors for Fig. 2.10(c)					
	Q_1/Q_2	Error [%]	Q_1/Q_3	Error [%]	Q_1/Q_4	Error [%]
$0 < t < t_1$	0.5	1.3	2.0	2.4	1.0	1.6
$t_1 < t < t_2$	0.5	0.6	2.0	1.2	1.0	0.8
$t_2 < t < t_3$	0.5	2.2	2.0	0.05	1.0	1.5

Table 2.5: Active power ratio errors of Case-4 (simple droop).

Time Intervals	Active Power Ratios and Errors for Fig. 2.11(b)					
	P_1/P_2	Error [%]	P_1/P_3	Error [%]	P_1/P_4	Error [%]
$0 < t < t_1$	2.0	3.0	0.5	2.9	1.0	3.3
$t_1 < t < t_2$	2.0	6.3	0.5	5.9	1.0	7.0
$t_2 < t < t_3$	2.0	0.11	0.5	0.09	1.0	0.22

Table 2.6: Reactive power ratio errors of Case-4 (simple droop).

Time Intervals	Reactive Power Ratios and Errors for Fig. 2.11(c)					
	Q_1/Q_2	Error [%]	Q_1/Q_3	Error [%]	Q_1/Q_4	Error [%]
$0 < t < t_1$	0.5	80	2.0	81	1.0	83
$t_1 < t < t_2$	0.5	48	2.0	47	1.0	52
$t_2 < t < t_3$	0.5	38	2.0	39	1.0	38

fering with the smooth performance of the system.

2.4.4 Case-4: Power Sharing by Simple Droop

This case study investigates the active and reactive power ratio errors for the same system as considered in Case-3 without applying the adaptive virtual impedance to the DERs. Fig. 2.12 shows the simulation results of this case study where the load variations are similar to Case-3 (see Fig. 2.12(a)). Fig. 2.12(b),

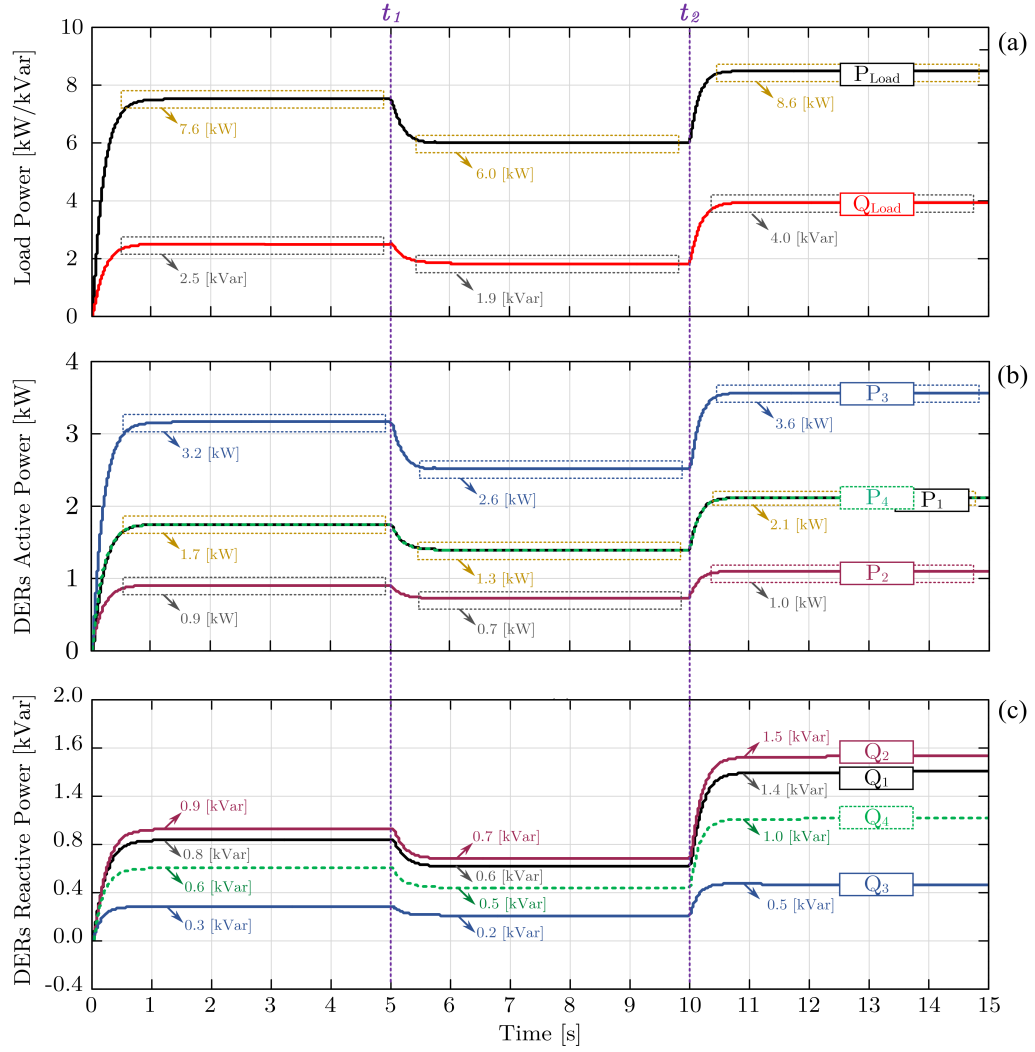


Figure 2.12: Case-4 results: power sharing based on simple droop.

indicates the active power variations of the DERs. It is visible from this figure that the active power output of each DER is almost the same as in Case-3. This is also evident in Table 2.5 as the errors are kept below 10% even though the virtual impedance is not applied to the DERs. Reactive power outputs for this case study are illustrated in Fig. 2.12(c). It is obvious from this figure that the reactive output powers are not similar to the ones in Case-3. For instance, DER-1 and DER-4 reactive powers are not the same. The results for the desired reactive power ratios and their errors are summarized in Table 2.6. This table confirms that without imposing the virtual impedance to the DERs, reactive power ratio errors are significant. Hence, it can be concluded that the proposed adaptive virtual impedance technique effectively reduces these errors while maintaining

the system power balance as described in Case-3.

2.5 Conclusions

Different techniques which can be used for power sharing control and adjustment of parallel converter-interfaced distributed energy resources (DERs) in an autonomous microgrid are discussed in this chapter. Initially, restrictions of the existing methods are discussed. Then, the proposed (third) method is introduced which overcomes the limitations of the other two methods. The main disadvantage of power sharing using the first method is that the coupling inductance of the distributed energy resources needs to be designed and implemented physically which is an expensive process. Moreover, the coupling inductances can only be designed for a specific power sharing ratio. Hence, this method is not suitable for the systems where the power ratio among the microgrid units modifies dynamically. Also, the main limitation of the second method is that it is not able to provide accurate reactive power sharing. However, the proposed (third) method overcomes these drawbacks by adaptively modifying the virtual impedance value considering the system disturbances and maintaining the reactive power ratio error below 5%.

Chapter 3

Small Signal Stability Analysis of Autonomous Microgrid

3.1 Introduction

Increased integration of renewable energy sources and micro-sources such as photovoltaic panels, wind turbines and fuel cells in the form of distributed generations (DGs) has proposed the concept of microgrids (MGs) [121, 122]. MGs operation in both grid-connected mode and autonomous mode enhances their reliability and power quality in comparison to the conventional power distribution systems. However, providing smooth and seamless transitions between different operation modes is a challenging issue. One of the most promising techniques to control distributed energy resources (DERs) of an MG, is to provide voltage control for their converters [123]-[130].

A centralized control scheme can be adopted to facilitate the required voltage control for the interfacing converters of the DERs as studied in [127]. On the other hand, it is possible to control the MG in a decentralized manner by only local measurements of signals. In this sense, droop control is one of the most popular methods which regulates the active and reactive power of the DERs based on the frequency and voltage deviations, respectively [131]-[146]. However, considering the fact that the DERs interfacing converters are connected to the point of common coupling (PCC) through their coupling inductances and feeders, conventional droop control is prone to several problems such as [127];

- Active and reactive powers coupling and their steady state error is an issue if the coupling inductance is presented;

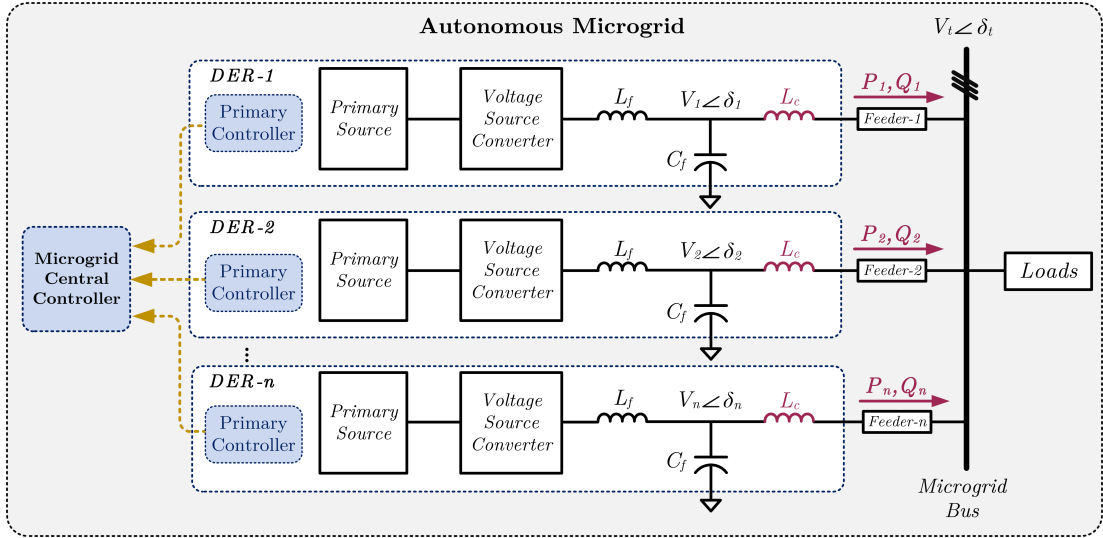


Figure 3.1: Schematic diagram of an example MG with n DERs.

- The MG stability may be affected by the feeder impedance if no coupling inductance is presented at the output terminals.

To address active and reactive power coupling issues, the virtual active and reactive power method is proposed in [131], and the virtual voltage and frequency frame method is utilized in [147]. However, with these methods enhancement of the steady state error is not achievable. Another approach to suppress the coupling issue is to impose a virtual inductance at the terminal of the DERs [127], as explained in Chapter 2. References [133, 134] show that proper design and implementation of the virtual impedance can improve the power sharing accuracy (i.e. steady state results) as well as the transient performance of the DERs. However, poor design of the virtual impedance may adversely affect the system stability and dynamic performance.

This chapter introduces a new approach for virtual impedance design which provides the active and reactive powers decoupling without compromising the system stability. To attain this, the virtual impedance is determined based on the developed small-signal model of the overall MG. Hence, the system transients and stability requirements are taken into account in the virtual impedance design in addition to the steady state power ratio errors of the DERs.

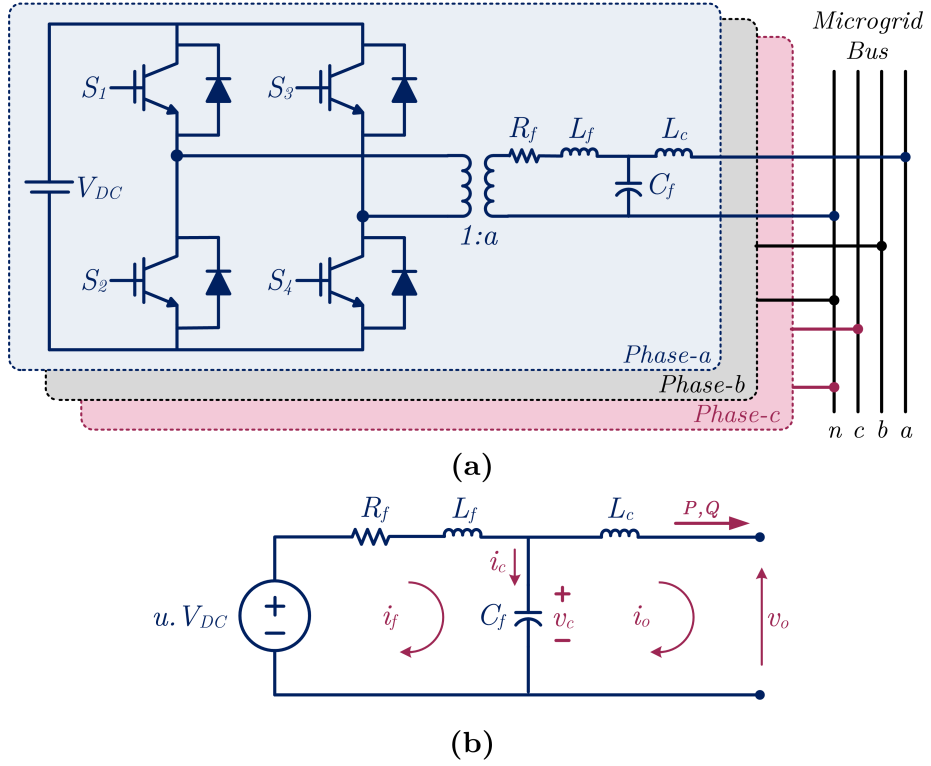


Figure 3.2: (a) Converter structure, (b) equivalent circuit of phase- a .

3.2 Microgrid Structure and Control

An example MG is shown in Fig. 3.1 with a central load and n converter interfaced DERs where the DERs are connected to the MG bus through their coupling inductance and distribution feeders. Each DER consists of a primary source a voltage source converter (VSC) and an LC filter. The DERs converter structure and power flow equations are explained in detail in the following subsections.

3.2.1 Converter Structure and Control

The voltage source converter (VSC) structure is shown in Fig. 3.2(a) which is composed of three H-bridges that are supplied from the battery. The output terminals of each H-bridge are connected to a single-phase transformer, and the transformers secondary windings are star-connected. Switching and transformer losses are represented by resistance R_f , while the leakage reactance of the transformers are represented by L_f . The filter capacitor C_f bypasses the switching harmonics. The VSC and its filter system are connected to the PCC through a coupling inductance of L_c [148].

For the converter structure of Fig. 3.2(a), voltage control technique is utilized in abc frame in order to track the desired voltage at the output of each VSC [149]. Equivalent circuit of the converter for one phase is shown in Fig. 3.2(b). In this figure, uaV_{dc} represents the output voltage of the transformer, where u is the switching function. For a bipolar switching, u takes on ± 1 . The converter control mainly aims to generate u . From Fig. 3.2(b), the state vector of $z(t) = [i_o(t) \ i_c(t) \ v_c(t)]^T$ is chosen for each phase of the VSC and filter system where i_o is the current of L_c and v_c and i_c represent the voltage and current of C_f , respectively. Thus, the state-space description of the system can be expressed as [148],[149];

$$\dot{z}(t) = [\mathbf{A}]_{\mathbf{z}} z(t) + [\mathbf{B}]_{\mathbf{z}} u_c(t) + [\mathbf{C}]_{\mathbf{z}} v_z(t) \quad (3.1)$$

where, u_c is the continuous-time approximation of the switching function u and v_o represents the network load change effects on this system; hence, it is considered as a disturbance for the controller. Eq. (3.1) is represented in discrete mode as;

$$z(k+1) = [\mathbf{F}]_{\mathbf{z}} z(k) + [\mathbf{G}]_{\mathbf{z}} u_c(k) + [\mathbf{H}]_{\mathbf{z}} v_o(k) \quad (3.2)$$

where,

$$\begin{aligned} [\mathbf{F}]_{\mathbf{z}} &= e^{[\mathbf{A}]_{\mathbf{z}} T_s}, \\ [\mathbf{G}]_{\mathbf{z}} &= \int_0^{T_s} e^{[\mathbf{A}]_{\mathbf{z}} t} [\mathbf{B}]_{\mathbf{z}} dt, \\ [\mathbf{H}]_{\mathbf{z}} &= \int_0^{T_s} e^{[\mathbf{A}]_{\mathbf{z}} t} [\mathbf{C}]_{\mathbf{z}} dt, \end{aligned}$$

and T_s is the sampling time [150]. Using state feedback control law, $u_c(k)$ can be calculated as;

$$u_c(k) = -[k_1 \ k_2 \ k_3][z(k) - z_{ref}(k)]^T \quad (3.3)$$

where, $[k_1 \ k_2 \ k_3]$ is a gain vector and $z_{ref}(k)$ is the desired state vector in discrete-time domain.

As the system behavior in steady-state is interested and assuming a full control over $u_c(k)$, an infinite-time linear quadratic regulator (LQR) can be designed for this problem to define $[k_1 \ k_2 \ k_3]$. In a discrete LQR problem, an objective function J is chosen as [151].

$$J(k) = \sum_0^{\infty} [z(k) - z_{ref}(k)]^T \mathbf{Q}(\mathbf{k}) [z(k) - z_{ref}(k)] + u_c(k)^T \mathbf{R}(\mathbf{k}) u_c(k) \quad (3.4)$$

where, \mathbf{R} is the control cost matrix, \mathbf{Q} is the state weighting matrix that reflects the importance of each controlling parameter in z , and $J(\infty)$ represents the objective function at infinite time (steady-state condition). Eq. (3.4) is then minimized

to obtain the optimal values for $u_c(k)$ through solution of Riccati equations while satisfying system constraints in (3.2) [148].

Eq. (3.3) shows the total tracking error of each DER converter. The tracking error is minimized by limiting this error within a very small bandwidth (e.g. $h = 10^{-4}$). Thus, using a hysteresis control, the switching function (u) is generated as [148];

$$u = \begin{cases} +1, & \text{if } u_c(k) > +h \\ u(k-1), & \text{if } -h \leq u_c(k) \leq +h \\ -1, & \text{if } u_c(k) \leq -h \end{cases} \quad (3.5)$$

The above control approach provides perfect tracking of the references [152].

3.2.2 Power Flow of the DERs

The average active (P) and reactive (Q) power flows from each DER unit to PCC are expressed as;

$$P = \frac{|V||V_{pcc}|\sin(\delta - \delta_{pcc})}{\omega L_c} \quad (3.6)$$

$$Q = \frac{|V|^2 - |V||V_{pcc}|\cos(\delta - \delta_{pcc})}{\omega L_c} \quad (3.7)$$

where, V and δ are respectively the magnitude and angle of the voltage across the filter capacitor (C_f) of each DER, ω is the nominal angular frequency of the system, and V_{pcc} and δ_{pcc} are the magnitude and angle of the voltage at PCC, respectively. The average powers are calculated by passing instantaneous active (p) and reactive powers (q) through low-pass filters with a cut-off frequency of ω_c . With a mainly inductive feeder and small $\delta - \delta_{pcc}$, the active power can be controlled by δ_{pcc} while the reactive power can be controlled by the voltage magnitude of V . Thus, power sharing among the DERs can be achieved using the angle and voltage droop instead of the conventional frequency and voltage droop equations as [153];

$$\delta_{droop} = \delta_{rated} - m(P - P_{rated}) \quad (3.8)$$

$$V_{droop} = V_{droop} - n(Q - Q_{rated}) \quad (3.9)$$

In (3.8) and (3.9), the rated subscript shows the rated values for each DER while m and n are the $P - \delta$ and $Q - V$ droop coefficients, respectively. Therefore, the ratio of the average output active and reactive power among every two DERs in an MG can be expressed as [148];

$$\frac{P_1}{P_2} = \frac{m_2}{m_1} \quad (3.10)$$

$$\frac{Q_1}{Q_2} = \frac{n_2}{n_1} \quad (3.11)$$

3.2.3 Reference Generation of the DERs

The single-phase equivalent circuit of the VSC is shown in Fig. 3.2(b). In this figure the reference voltage and current of the capacitor are defined as [153];

$$v_{c-ref} = V \cos(\omega t + \delta) \quad (3.12)$$

$$i_{c-ref} = V \omega C_f \sin(\omega t + \delta) \quad (3.13)$$

and the reference current of i_{o-ref} is calculated as;

$$i_{o-ref} = v_c - v_{pcc} j \omega L_c \quad (3.14)$$

To calculate the instantaneous current reference a phase shifter is required for (3.14) which is not desirable. Therefore, the measured average active and reactive powers of the VSC are used to calculate the magnitude and the phase angle of the reference current [153]. From Fig. 3.2(b), it is visible that,

$$\begin{aligned} |I_{o-ref}| &= \frac{\sqrt{P^2 + Q^2}}{V_c} \\ \angle I_{o-ref} &= \delta - \tan^{-1}(Q/P) \end{aligned} \quad (3.15)$$

Thus, the current reference can be expressed as;

$$i_{o-ref} = |I_{o-ref}| \cos(\omega t + \angle I_{o-ref}) \quad (3.16)$$

3.3 Dynamic Power Sharing by Analyzing Eigenvalues

As mentioned previously, the desired active power ratio can be achieved by designing the angle droop coefficient (m) based on (3.10). Whereas, the reactive power ratio is extremely affected by the coupling inductance of the DERs; and hence, cannot be achieved by only designing the voltage droop coefficients. Since it is not possible to vary the coupling inductance of the DERs, imposing a virtual impedance (VI) to the output terminals of the VSC filters is suggested instead, as mentioned in Chapter 2. The main objective of this approach is to create a voltage drop across the virtual impedance. Thus, imposing a virtual impedance causes the voltage across the filter capacitor (C_f) to be slightly lower or higher

than the value which is determined by the droop control. This in turn facilitates a desired active/reactive power ratio at the output of the DER units, irrespective of the coupling inductance ratios. To ensure that active and reactive powers are decoupled, and the power ratio errors are negligible, the following constraints should be satisfied in the design of L_{VI} [148];

$$\frac{m_2}{m_1} = \frac{L_{c-2} + L_{VI-2}}{L_{c-1} + L_{VI-1}} \quad (3.17)$$

$$\frac{n_2}{n_1} = \frac{L_{c-2} + L_{VI-2}}{L_{c-1} + L_{VI-1}} \quad (3.18)$$

Fig. 3.3(a) indicates the utilized flowchart which determines the optimal VI for each DER. Based on this flowchart, initially, the MG central controller receives the desired power ratio of all the DERs from the network secondary controller. Then the DER with the highest power ratio which is designated to have the lowest VI is identified. Following this, the optimal L_{VI} for the selected DER is determined based on the second flowchart shown in Fig. 3.3(b). Finally, after calculating the optimum inductance L_{VI-opt} for all the MG constituent units based on (3.17) and (3.18), the final values are transferred to the primary controller of each DER [148]. To identify the optimal VI for the DER with the highest power ratio an objective function of OF is considered in the flowchart of Fig. 3.3(b) as;

$$OF = \alpha\epsilon_P + \beta\epsilon_Q \quad (3.19)$$

where, ϵ_P and ϵ_Q represent the errors of active and reactive power ratios, respectively and are defined as;

$$\epsilon_P = \frac{P_{ratio}^{actual} - P_{ratio}^{desired}}{P_{ratio}^{desired}} \quad (3.20)$$

$$\epsilon_Q = \frac{Q_{ratio}^{actual} - Q_{ratio}^{desired}}{Q_{ratio}^{desired}} \quad (3.21)$$

also, α and β are the weighting coefficients of these errors. It is worth noting that the α and β coefficients can be simply varied according to the system requirements and the importance of the active and reactive power ratio accuracy.

Based on the flowchart shown in Fig. 3.3(b), the system is initially run in the time domain for $L_{VI} = 0$, and then L_{VI} is increased in predefined steps of ΔL_{VI} . In each step, the system operating point and the eigenvalues are calculated. Then the algorithm monitors the eigenvalue results to ensure if the system stability is

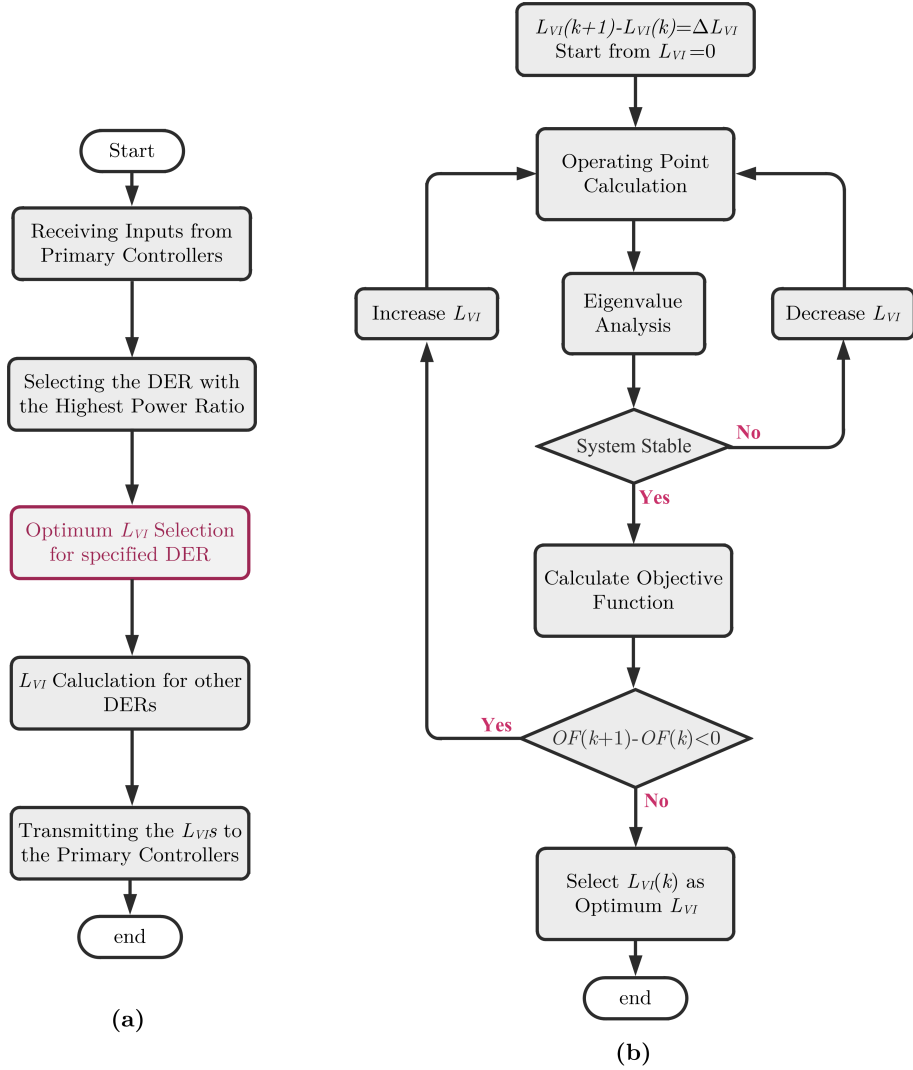


Figure 3.3: (a) Deployed algorithm by the MG central controller to determine the VI for each DER, (b) selecting the optimum inductance (L_{VI-opt}).

realized. If the system remains stable, the objective function is calculated and compared with its previous value. This process is repeated as long as increasing the VI with the predefined steps reduces the OF , and in turn, the active and reactive power errors are decreased. The small signal stability analysis utilized in this flowchart is discussed in detail in the following section. It is worth noting that the introduced objective function properly recognizes the VIs which may result into system oscillations as the steady state errors become relatively high for these VIs. Based on the determined VI for each DER system, the reference voltage at the output of the VSC (v_{ref}) can be calculated from (2.36).

Fig. 3.4 shows the closed-loop control of the VSC where the proposed dynamic

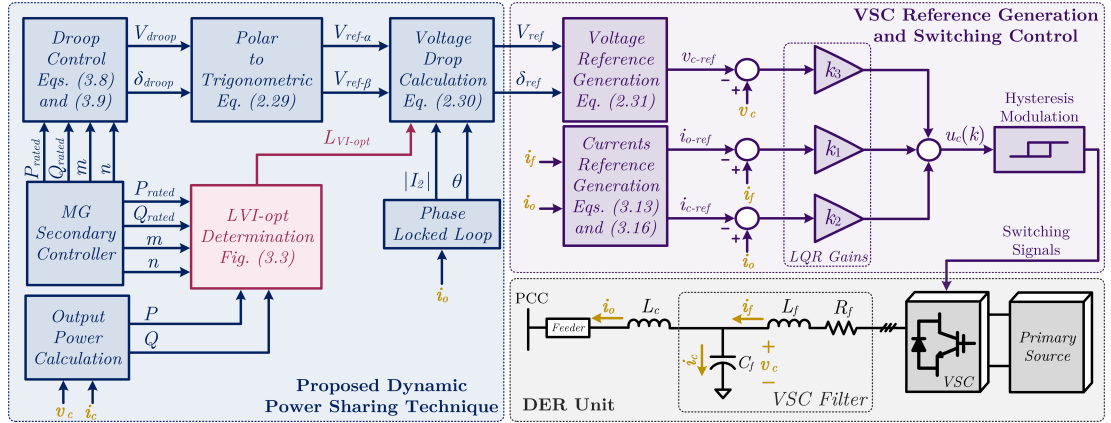


Figure 3.4: Closed-loop control of the voltage source converter.

power sharing technique with consideration of the virtual impedance is shown in detail.

3.4 Small Signal Stability Analysis

To investigate the MG stability, analysis of the state-space models are required. For this, it is necessary to model the converters in the same manner as the models of rotating machine are established. Similar to the machine models which include automatic voltage regulators and wash-out functions, the VSC models should also consider the internal control loops [154]. In an autonomous MG with only converter interfaced DERs, the network dynamics may be affected by the fast switching action [155]. Thus, modeling the MG by differential equations is mandatory for stability investigations. The single-phase control of the VSCs was presented in the previous section. However, to investigate the total MG behavior, it is required to define a common reference frame and convert all the system voltages and currents to this frame [156].

Fig. 3.5 shows the schematic diagram of the investigated MG with two DERs. The DER models are assumed to be the same consisting converter model, droop controller model, virtual impedance model and the conversion block model for converting all the inputs/outputs from direct-quadratic (dq) reference frame to the common reference frame and vice versa. To perform the eigenvalue analysis, it is required to linearize all the system equations. Thus, in the following section the prefix Δ represents the linear quantities. From Fig. 3.5, the measured output powers of the VSC ($\Delta P, \Delta Q$) are fed to the droop control block where the voltage reference magnitude and angle ($\Delta V_{c-ref}, \Delta \delta_{c-ref}$) for the filter capacitor

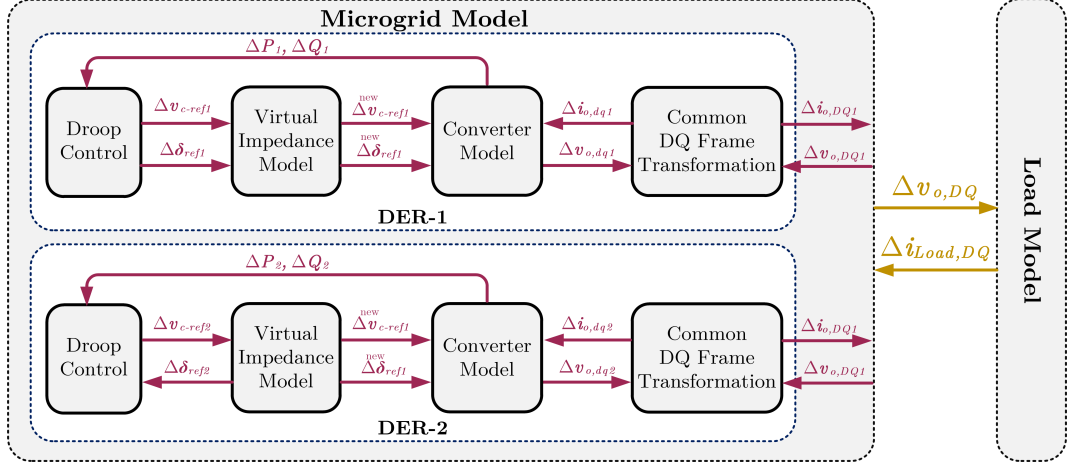


Figure 3.5: Schematic diagram of an example MG with n DERs.

is calculated and fed to the virtual impedance block. In the VI block the voltage drop across the L_{VI} is calculated which results into the reference voltage of $(\Delta V_{c-ref}^{new}, \Delta \delta_{c-ref}^{new})$. Then, this reference is fed to the VSC. Finally, the VSC outputs are sent to the conversion block where they are transferred to the common reference frame. The outputs of each DER are the currents of $(\Delta i_{o,D}, \Delta i_{o,Q})$, and the inputs are the voltages of and $(\Delta v_{pcc,D}, \Delta v_{pcc,Q})$. Similarly, the load model inputs are the PCC DQ voltages $(\Delta v_{pcc,D}, \Delta v_{pcc,Q})$, whereas its outputs are the load DQ currents of $(\Delta i_{Load,D}, \Delta i_{Load,Q})$. In the following subsections, first, the state-space equation of each component will be derived separately. Then, the MG overall model will be obtained by combining all these models.

3.4.1 Voltage Source Converter Model

Mesh analysis for the equivalent circuit of the VSC, shown in Fig. 3.2(b), results in the following equations for each phase;

$$\frac{di_f}{dt} = -\frac{R_f}{L_f}i_f + \frac{(-v_c + u\dot{V}_{dc})}{L_f} \quad (3.22)$$

$$\frac{dv_c}{dt} = \frac{i_f - i_o}{C_f} \quad (3.23)$$

$$v_c - v_{pcc} = L_c \frac{di_o}{dt} \quad (3.24)$$

Transferring (3.22)-(3.24) to dq frame and combining them yields the following state-space description for each DER in the MG network of Fig. 3.1;

$$\dot{x}_{DER} = [\mathbf{A}]x_{DER} + [\mathbf{B}]u_{DER} + [\mathbf{C}]v_{DER} \quad (3.25)$$

which is expanded as;

$$\frac{d}{dt} \begin{bmatrix} i_{fd} \\ i_{fq} \\ i_{od} \\ i_{oq} \\ v_{cd} \\ v_{cq} \end{bmatrix} = \begin{bmatrix} -R_f/L_f & \omega & 0 & 0 & -1/L_f & 0 \\ -\omega & -R_f/L_f & 0 & 0 & 0 & -1/L_f \\ 0 & 0 & 0 & \omega & 1/L_c & 0 \\ 0 & 0 & -\omega & 0 & 0 & 1/L_c \\ 1/C_f & 0 & -1/C_f & 0 & 0 & \omega \\ 0 & 1/C_f & 0 & -1/C_f & -\omega & 0 \end{bmatrix} \cdot \begin{bmatrix} i_{fd} \\ i_{fq} \\ i_{od} \\ i_{oq} \\ v_{cd} \\ v_{cq} \end{bmatrix} + a \frac{V_{dc}}{L_f} \begin{bmatrix} 1 & 0 \\ 0 & 1 \\ 0 & 0 \\ 0 & 0 \\ 0 & 0 \\ 0 & 0 \end{bmatrix} \cdot \begin{bmatrix} u_d \\ u_q \end{bmatrix} - \frac{1}{L_c} \begin{bmatrix} 0 & 0 \\ 0 & 0 \\ 1 & 0 \\ 0 & 1 \\ 0 & 0 \\ 0 & 0 \end{bmatrix} \cdot \begin{bmatrix} v_{od} \\ v_{oq} \end{bmatrix}_{DER} \quad (3.26)$$

Assuming a perfect tracking [152], u can be represented by u_c . Hence, considering a state-feedback control in the form of,

$$\begin{aligned} u_{DER} &= -[k_1 \ k_2 \ k_3][z_{DER} - z_{DER}^{ref}] \\ &= [\mathbf{G}]x_{DER} + [\mathbf{H}]z_{DER}^{ref} \end{aligned} \quad (3.27)$$

where,

$$\begin{aligned} z_{DER} &= [i_{fd} \ i_{fq} \ i_{od} \ i_{oq} \ v_{cd} \ v_{cq}]^T \\ \mathbf{G} &= \begin{bmatrix} -k_1 & 0 & k_1 - k_2 & 0 & -k_3 & 0 \\ 0 & -k_1 & 0 & k_1 - k_2 & 0 & -k_3 \end{bmatrix} \\ \mathbf{H} &= \begin{bmatrix} k_1 & 0 & k_2 & 0 & k_3 & 0 \\ 0 & k_1 & 0 & k_2 & 0 & k_3 \end{bmatrix} \end{aligned}$$

the state-space equation of the DERs become;

$$\dot{x}_{DER} = [\mathbf{A}]_{DER} x_{DER} + [\mathbf{B}]_{DER} z_{DER}^{ref} + [\mathbf{C}]_{DER} v_{DER} \quad (3.28)$$

where, $[\mathbf{A}]_{DER} = [\mathbf{A}] + [\mathbf{B}][\mathbf{G}]$ and $[\mathbf{B}]_{DER} = [\mathbf{B}][\mathbf{H}]$.

3.4.2 Load and Lines Model

The state-space equation of the centralized load and each line of the MG in dq frame are [148],[149];

$$\dot{x}_{load} = [\mathbf{A}]_{load} x_{load} + [\mathbf{C}]_{load} v_{load} \quad (3.29)$$

$$\dot{x}_{line} = [\mathbf{A}]_{line} x_{line} + [\mathbf{C}]_{line} v_{MG} \quad (3.30)$$

and are expanded respectively as;

$$\frac{d}{dt} \begin{bmatrix} i_d \\ i_q \end{bmatrix} = \begin{bmatrix} R_{load}/L_{load} & \omega \\ -\omega & R_{load}/L_{load} \end{bmatrix} \cdot \begin{bmatrix} i_d \\ i_q \end{bmatrix} + \frac{1}{L_{load}} \cdot \begin{bmatrix} v_{od} \\ v_{oq} \end{bmatrix} \quad (3.31)$$

$$\begin{aligned} \frac{d}{dt} \begin{bmatrix} i_d \\ i_q \end{bmatrix} &= \begin{bmatrix} R_{line}/L_{line} & \omega \\ -\omega & R_{line}/L_{line} \end{bmatrix} \cdot \begin{bmatrix} i_d \\ i_q \end{bmatrix} + \\ &\frac{1}{L_{line}} C_{line} \cdot \begin{bmatrix} v_{od}^1 & v_{oq}^1 & v_{od}^2 & v_{oq}^2 & v_{od}^3 & v_{oq}^3 \end{bmatrix}^T \end{aligned} \quad (3.32)$$

3.4.3 Combined Model of the VSC, Load, and Lines

Combining (3.28), (3.29) and (3.30) the equivalent state-space equation of the MG becomes;

$$\dot{x}_{MG} = [\mathbf{A}]_{MG} x_{MG} + [\mathbf{B}]_{MG} z_{MG}^{ref} + [\mathbf{C}]_{MG} v_{MG} \quad (3.33)$$

where,

$$\begin{aligned} x_{MG} &= \begin{bmatrix} x_{DER-1} & x_{DER-2} & x_{load} & x_{line-1} & x_{line-2} \end{bmatrix}^T \\ z_{MG}^{ref} &= \begin{bmatrix} z_{DER-1}^{ref} & z_{DER-2}^{ref} & \mathbf{O}_{6 \times 1} \end{bmatrix}^T \\ \mathbf{A}_{MG} &= \text{diag}(\mathbf{A}_{DER-1} \ \mathbf{A}_{DER-2} \ \mathbf{A}_{load} \ \mathbf{A}_{line-1} \ \mathbf{A}_{line-2}) \\ \mathbf{B}_{MG} &= \text{diag}(\mathbf{B}_{DER-1} \ \mathbf{B}_{DER-2} \ \mathbf{O}_{6 \times 6}) \\ \mathbf{C}_{MG} &= \begin{bmatrix} \text{diag}(\mathbf{C}_{DER-1} \ \mathbf{C}_{DER-2} \ \mathbf{C}_{load}) \\ \mathbf{C}_{line-1} \\ \mathbf{C}_{line-2} \end{bmatrix} \end{aligned}$$

where, $\text{diag}()$ represents a diagonal matrix and \mathbf{O} represents a zeros matrix [148].

3.4.4 Droop Controller Model

The references of the converter output voltage and magnitude are set by the droop controller where the output voltage of the converter is equal to the filter capacitor (C_f) voltage, as shown in Fig. 3.2(b). The instantaneous output active and reactive powers of each converter and filter in direct-quadratic (dq) frame is expressed based on its output voltage and current as [153];

$$\begin{bmatrix} p \\ q \end{bmatrix} = \frac{3}{2} \begin{bmatrix} i_{od} & i_{oq} \\ -i_{oq} & i_{od} \end{bmatrix} \cdot \begin{bmatrix} v_{cd} \\ v_{cq} \end{bmatrix} \quad (3.34)$$

The average values of active and reactive powers are obtained by passing their instantaneous (i.e. measured) values through low pass filters (LPFs) as;

$$\begin{aligned} P &= \frac{\omega_c}{s + \omega_c} p = \frac{\omega_c}{s + \omega_c} (v_{cd} i_{od} + v_{cq} i_{oq}) \\ Q &= \frac{\omega_c}{s + \omega_c} q = \frac{\omega_c}{s + \omega_c} (v_{cd} i_{oq} + v_{cq} i_{od}) \end{aligned} \quad (3.35)$$

where, ω_c is the filter cut-off frequency. Linearizing (3.35) around the operating point yields;

$$\begin{aligned} \Delta \begin{bmatrix} \dot{P} \\ \dot{Q} \end{bmatrix} &= \begin{bmatrix} -\omega_c & 0 \\ 0 & -\omega_c \end{bmatrix} \cdot \Delta \begin{bmatrix} P \\ Q \end{bmatrix} + \\ &\begin{bmatrix} 0 & 0 & v_{cd0} & v_{cq0} & i_{od0} & i_{oq0} \\ 0 & 0 & v_{cq0} & -v_{cd0} & -i_{oq0} & i_{od0} \end{bmatrix} \cdot \Delta \begin{bmatrix} i_{fd} & i_{fq} & i_{od} & i_{oq} & v_{cd} & v_{cq} \end{bmatrix}^T \end{aligned} \quad (3.36)$$

where, subscript 0 represents the nominal values. Defining a vector for active and reactive powers as;

$$\begin{bmatrix} P_{DER-1} & Q_{DER-1} & P_{DER-2} & Q_{DER-2} \end{bmatrix}^T \quad (3.37)$$

Eq. (3.36) can be rewritten as;

$$\Delta \dot{x}_{PQ} = [\mathbf{A}]_{PQ} \Delta x_{PQ} + [\mathbf{B}]_{PQ} \Delta x_{DER} \quad (3.38)$$

3.4.5 The Overall Model of the MG

To obtain the overall state-space equation of the MG, it is required to eliminate the reference vector represented in (3.28) by linearizing the droop equations. For this, it is assumed that the three-phase reference voltage of the filter capacitor can be expressed as [156];

$$\begin{aligned} v_{c-a} &= V_{cm} \sin(\omega t) \\ v_{c-b} &= V_{cm} \sin(\omega t - 2\frac{\pi}{3}) \\ v_{c-c} &= V_{cm} \sin(\omega t + 2\frac{\pi}{3}) \end{aligned} \quad (3.39)$$

From (3.39), the reference voltage of the capacitor in dq form becomes,

$$\begin{aligned} v_{c-ref,d} &= 0 \\ v_{c-ref,q} &= -V_{cm} \end{aligned} \quad (3.40)$$

As the converter output voltage and the capacitor voltage are the same, the voltage droop equation of (3.9) can be rewritten as;

$$v_{c-ref,d} = V_{c-ref} = V_{rated} - n(Q - Q_{rated}) \quad (3.41)$$

Linearizing and combining (3.8) and (3.41), results in the droop controller model as;

$$\begin{bmatrix} \Delta\delta_{ref} \\ \Delta v_{c-ref,d} \\ \Delta v_{c-ref,q} \end{bmatrix} = \begin{bmatrix} 0 & -m & 0 \\ 0 & 0 & -n \\ 0 & 0 & 0 \end{bmatrix} \begin{bmatrix} \Delta\delta \\ \Delta P \\ \Delta Q \end{bmatrix} \quad (3.42)$$

Similarly, the capacitor reference currents which lead the corresponding voltages by 90° are calculated as;

$$\begin{aligned} i_{c-ref,d} &= V_{cm}\omega C_f \\ i_{c-ref,q} &= 0 \end{aligned} \quad (3.43)$$

Since the active and reactive powers based on dq components are defined as;

$$\begin{aligned} P &= \frac{3}{2}(v_d i_d + v_q i_q) \\ Q &= \frac{3}{2}(v_q i_d - v_d i_q) \end{aligned} \quad (3.44)$$

substituting (3.40) into (3.44) yields the reference output current of the VSC (i_o) as;

$$\begin{bmatrix} i_{o-ref,d} \\ i_{o-ref,q} \end{bmatrix} = -\frac{2}{3V_{cm}} \begin{bmatrix} Q_{ref} \\ P_{ref} \end{bmatrix} \quad (3.45)$$

It is to be noted that all the parameters need to be transferred to the common direct-quadratic reference frame (DQ) by [149];

$$\begin{bmatrix} \Delta f_D \\ \Delta f_Q \end{bmatrix} = \begin{bmatrix} \cos\delta & -\sin\delta \\ \sin\delta & \cos\delta \end{bmatrix} \cdot \begin{bmatrix} \Delta f_d \\ \Delta f_q \end{bmatrix} \quad (3.46)$$

In (3.46), the common DQ frame is assumed to be the PCC voltage frame and δ is the angle difference between the PCC voltage and the VSC output voltage (i.e. δ is the angle difference between the two frames). Therefore, the filter capacitor reference voltage should be transferred to the common reference frame as;

$$\begin{bmatrix} \Delta v_{c-ref,D} \\ \Delta v_{c-ref,Q} \end{bmatrix} = \begin{bmatrix} \cos\delta & -\sin\delta \\ \sin\delta & \cos\delta \end{bmatrix} \begin{bmatrix} 0 \\ -V_{cm} \end{bmatrix} \quad (3.47)$$

Linearizing the above equation and substituting it in (3.42) results;

$$\begin{bmatrix} \Delta v_{c-ref,D} \\ \Delta v_{c-ref,Q} \end{bmatrix} = \begin{bmatrix} -mV_{cm0}\cos\delta_0 & -n\sin\delta_0 \\ -mV_{cm0}\sin\delta_0 & n\cos\delta_0 \end{bmatrix} \begin{bmatrix} \Delta P \\ \Delta Q \end{bmatrix} \quad (3.48)$$

where, subscript 0 represents the operating point values of each state. Similarly, the capacitor reference current is calculated as;

$$\begin{bmatrix} \Delta i_{c-ref,D} \\ \Delta i_{c-ref,Q} \end{bmatrix} = \begin{bmatrix} \lambda_1 \sin \delta_0 & -\lambda_2 \cos \delta_0 \\ -\lambda_1 \cos \delta_0 & -\lambda_2 \sin \delta_0 \end{bmatrix} \begin{bmatrix} \Delta P \\ \Delta Q \end{bmatrix} \quad (3.49)$$

where,

$$\lambda_1 = m\omega C_f V_{cm0}$$

$$\lambda_2 = n\omega C_f$$

Finally, replacing P_{ref} and Q_{ref} by P and Q in (3.45), results the linearized output current of the VSC as;

$$\begin{bmatrix} \Delta i_{o-ref,D} \\ \Delta i_{o-ref,Q} \end{bmatrix} = \frac{1}{V_{cm0}} \begin{bmatrix} \beta_{11} & \beta_{12} \\ \beta_{21} & \beta_{22} \end{bmatrix} \begin{bmatrix} \Delta P \\ \Delta Q \end{bmatrix} \quad (3.50)$$

where,

$$\beta_{11} = -(2/3)(mQ_0 \sin \delta_0 + mP_0 \cos_0 - \sin \delta_0)$$

$$\beta_{12} = -(2/3) \cos \delta_0 + ni_{2,D0}$$

$$\beta_{21} = -(2/3)(mP_0 \sin \delta_0 + \cos_0 - mQ_0 \cos \delta_0)$$

$$\beta_{22} = -(2/3) \sin \delta_0 + ni_{2,Q0}$$

Hence, the reference vector for each DER in (3.28) can be rewritten as;

$$\Delta z_{DER}^{ref} = [\mathbf{M}]_c \Delta x_{PQ} \quad (3.51)$$

where, $[\mathbf{M}]_c$ is obtained from (3.48), (3.49) and (3.50). Finally, for the example MG shown in Fig. 3.1, with two converter-interfaced DERs, the reference vector in (3.28) can be expressed as;

$$\Delta z_{MG}^{ref} = [\mathbf{M}]_c^{MG} \Delta x_{PQ}^{MG} \quad (3.52)$$

where,

$$[\mathbf{M}]_c = \text{diag}([\mathbf{M}]_c^{\text{DER-1}} [\mathbf{M}]_c^{\text{DER-2}})$$

Also, the total equivalent state-space equation representing the power and voltage angles in the MG is expressed as;

$$\Delta \dot{x}_{PQ}^{MG} = [\mathbf{A}]_{PQ}^{MG} \Delta x_{PQ}^{MG} + [\mathbf{B}]_{PQ}^{MG} \Delta x_{MG} \quad (3.53)$$

where,

$$x_{PQ}^{MG} = \begin{bmatrix} x_{PQ}^{\text{DER-1}} & x_{PQ}^{\text{DER-2}} \end{bmatrix}^T$$

$$[\mathbf{A}]_{\text{PQ}}^{\text{MG}} = \text{diag}([\mathbf{A}]_{\text{PQ}}^{\text{DER-1}} \quad [\mathbf{A}]_{\text{PQ}}^{\text{DER-2}})$$

$$[\mathbf{B}]_{\text{PQ}}^{\text{MG}} = \left[\text{diag}([\mathbf{B}]_{\text{PQ}}^{\text{DER-1}} \quad [\mathbf{B}]_{\text{PQ}}^{\text{DER-2}}) \quad \mathbf{O}_{4 \times 6} \right]$$

Thus, the homogenous state-space description of the complete network can be obtained by combining (3.33), (3.52) and (3.53) as;

$$\Delta \dot{x}_{\text{MG}}^{\text{Final}} = [\mathbf{A}]'_{\text{MG}} \cdot \Delta x_{\text{MG}}^{\text{Final}} + [\mathbf{C}]'_{\text{MG}} \cdot \Delta v_{\text{MG}} \quad (3.54)$$

which is expanded as;

$$\begin{bmatrix} \Delta \dot{x}_{\text{MG}} \\ \Delta \dot{x}_{\text{PQ}}^{\text{MG}} \end{bmatrix} = \begin{bmatrix} \mathbf{A}_{\text{MG}} & \mathbf{B}_{\text{MG}} \cdot \mathbf{M}_{\text{c}} \\ \mathbf{B}_{\text{PQ}}^{\text{MG}} & \mathbf{A}_{\text{PQ}}^{\text{MG}} \end{bmatrix} \cdot \begin{bmatrix} \Delta x_{\text{MG}} \\ \Delta x_{\text{PQ}}^{\text{MG}} \end{bmatrix} + \begin{bmatrix} \mathbf{C}_{\text{MG}} \\ \mathbf{O}_{4 \times 6} \end{bmatrix} \cdot \Delta v_{\text{MG}} \quad (3.55)$$

Assuming a large virtual resistor (e.g. $R_v = 10^4$) between each bus and ground [155], the voltage of each bus can be written as;

$$v = R_v \left(i_2 + \sum_{k=1}^n (\mu^k i_{\text{line}}^k - i_{\text{load}}) \right) \quad (3.56)$$

where, n is the number of MG buses and μ^k is either +1 for entering lines to the bus or -1 for exiting lines from the bus. Thus, δv_{MG} can be expressed as a function of Δx_{MG} as;

$$\Delta v_{\text{MG}} = [\mathbf{M}]_{\text{v}} \cdot \Delta x_{\text{MG}}^{\text{Final}} \quad (3.57)$$

Assuming,

$$[\mathbf{A}]_{\text{MG}}^{\text{H}} = [\mathbf{A}]'_{\text{MG}} + [\mathbf{C}]'_{\text{MG}} [\mathbf{M}]_{\text{v}}$$

Eq. (3.32) is expressed as;

$$\Delta \dot{x}_{\text{MG}}^{\text{Final}} = [\mathbf{A}]_{\text{MG}}^{\text{H}} \cdot \Delta x_{\text{MG}}^{\text{Final}} \quad (3.58)$$

The eigenvalues of the MG system (λ) are then calculated as the roots of [148];

$$\det(\lambda \mathbf{I}_{22 \times 22} - [\mathbf{A}]_{\text{MG}}^{\text{H}}) \quad (3.59)$$

where, \mathbf{I} is the identity matrix and $\det()$ is the determinant function. The closest eigenvalues to the imaginary axis in s -plane are the dominant eigenvalues. Any changes in the VI of the DERs may result into MG instability. Hence, their effect on the variations of the dominant eigenvalues should be carefully investigated [148].

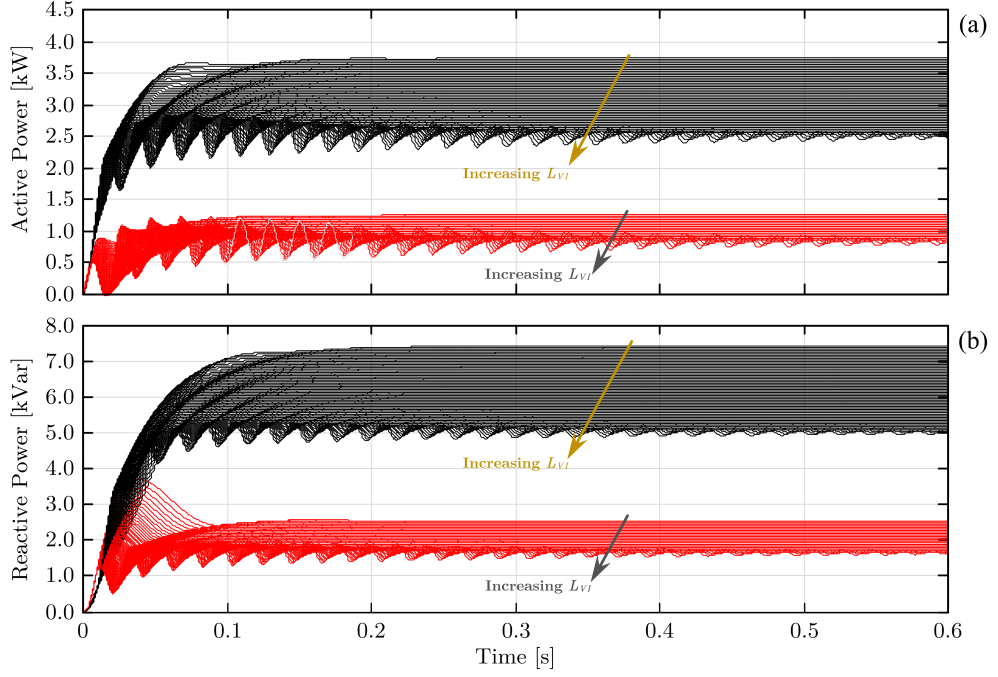


Figure 3.6: Case 1: (a) DERs active power, (b) DERs reactive power for L_{VI} variations from zero to 110 [mH].

3.5 Study Cases and Simulation Results

In this section the MG system of Fig. 3.1 with two converter-interfaced DERs and one central load is considered. To evaluate the performance of the system with different power sharing ratios, several case studies are first modeled in PSCAD/EMTDC and then numerically analyzed in MATLAB using the developed small signal stability model of the MG. For simplicity, the converter, coupling inductance and ratings of both DERs are assumed to be the same [148]. The parameters of the MG, VSCs, and filters are given in Appendix A Table A.1. Four different objective functions with different coefficients for the active and reactive power ratio errors are considered in the first two case studies. Table 3.1 summarizes the error coefficients of these OFs. From this table it is visible that for OF_1 , α and β coefficients are the same which means that the accuracy of active and reactive power ratios are similarly important. For OF_2 and OF_3 , reactive power ratio error and active power ratio errors are given the main priority, respectively. Finally, in OF_4 only the reactive power ratio errors are of interest.

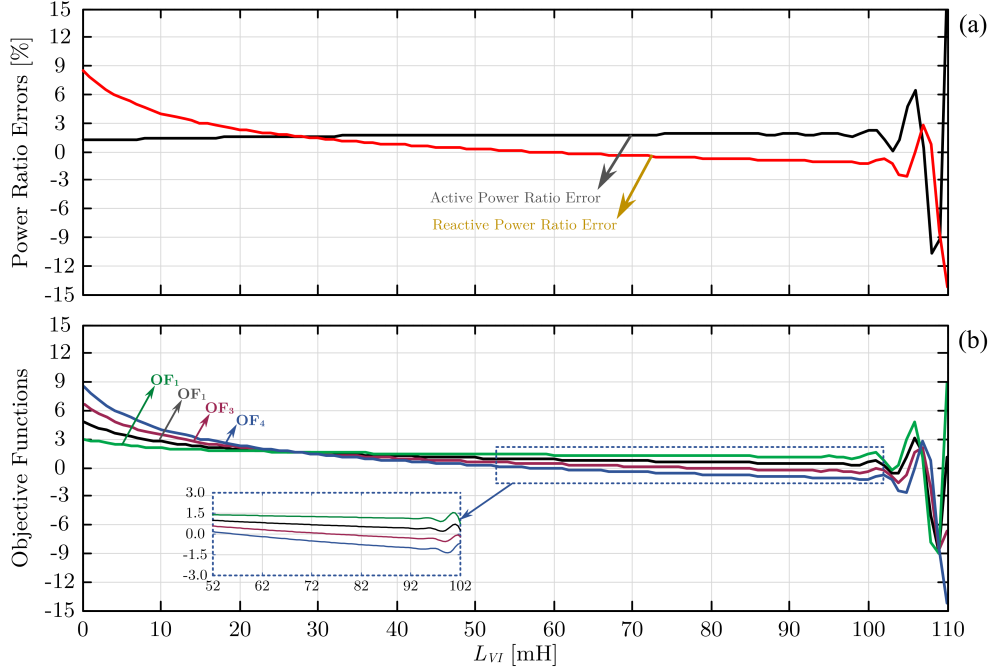


Figure 3.7: Case 1: (a) Power ratio errors, (b) Objective functions.

3.5.1 Case-1: Simulation Results for $P_{ratio} = 3$

In this case study, the power ratio of the two DERs is assumed to be $P_1/P_2 = 3$. Fig. 3.6(a) and Fig. 3.6(b) show the time domain results of the DERs active and reactive power outputs, respectively for L_{VI} variations from zero to 110 [mH]. From this figure, it is visible that the output powers become oscillatory as L_{VI} increases above some specific values. This implies that the proper design and implementation of the virtual impedance plays an important role in the stability of the overall system.

Fig. 3.7(a) shows the active and reactive power ratio errors of the two DERs for $0 < L_{VI} < 110$ [mH]. It is shown in this figure that for $L_{VI} < 102$ [mH], the active power ratio error is not changing significantly with the variation of VI, whereas the reactive power ratio error is obviously decreasing with the increase of L_{VI} . Moreover, for $L_{VI} > 102$ [mH], it is visible that both active and reactive power ratio errors increase significantly as the system becomes oscillatory. The objective function results shown in Fig. 3.7(b), also confirm the above statements. The OF variations for $52 \text{ [mH]} < L_{VI} < 102 \text{ [mH]}$ are indicated separately in a smaller frame in Fig. 3.7(b). The selected optimum L_{VI} based on different OFs are summarized in Table 3.1. From Fig. 3.7(b), for $L_{VI} = 56$ [mH], OF_4 becomes zero while increasing L_{VI} to the values above 56 [mH] results into negative values

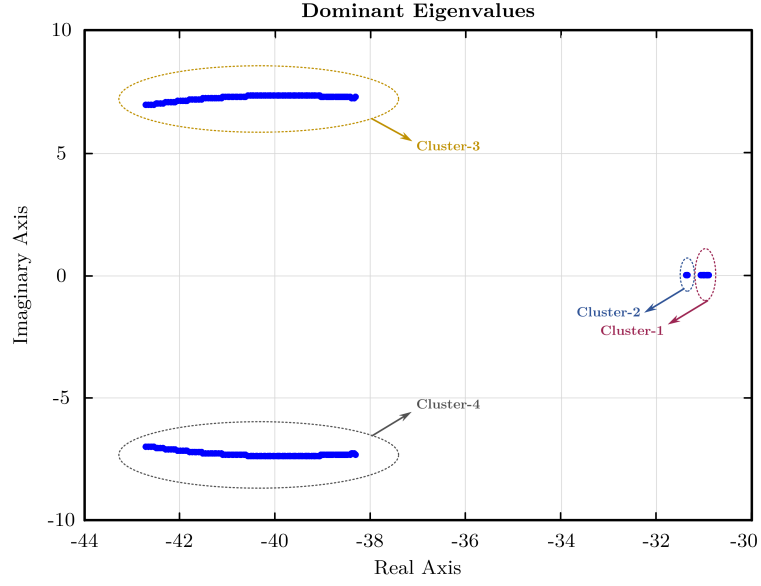


Figure 3.8: Case 1: Root locus diagram for L_{VI} variations from zero to 110 [mH] and $P_{ratio} = 3$.

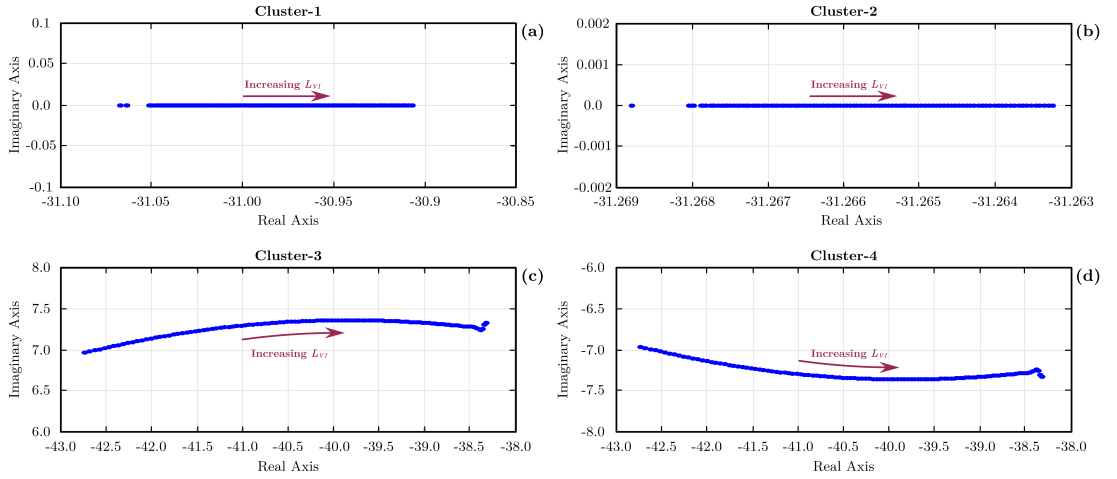


Figure 3.9: Case 1: Dominant eigenvalues locus for L_{VI} variations from zero to 110 [mH] and $P_{ratio} = 3$.

for OF_4 . Hence, based on the algorithm shown in Fig. 3.3(b), $L_{VI} = 56$ [mH] is selected as the optimum L_{VI} for OF_4 . The same procedure is considered for the other three OFs which results into different values of optimum L_{VI} for each OF as their trends are slightly different.

To investigate the system stability for different values of L_{VI} , the root locus diagram of the system including the MG dominant eigenvalues is shown in Fig. 3.8. Based on this figure, with the increment of L_{VI} , the MG dominant

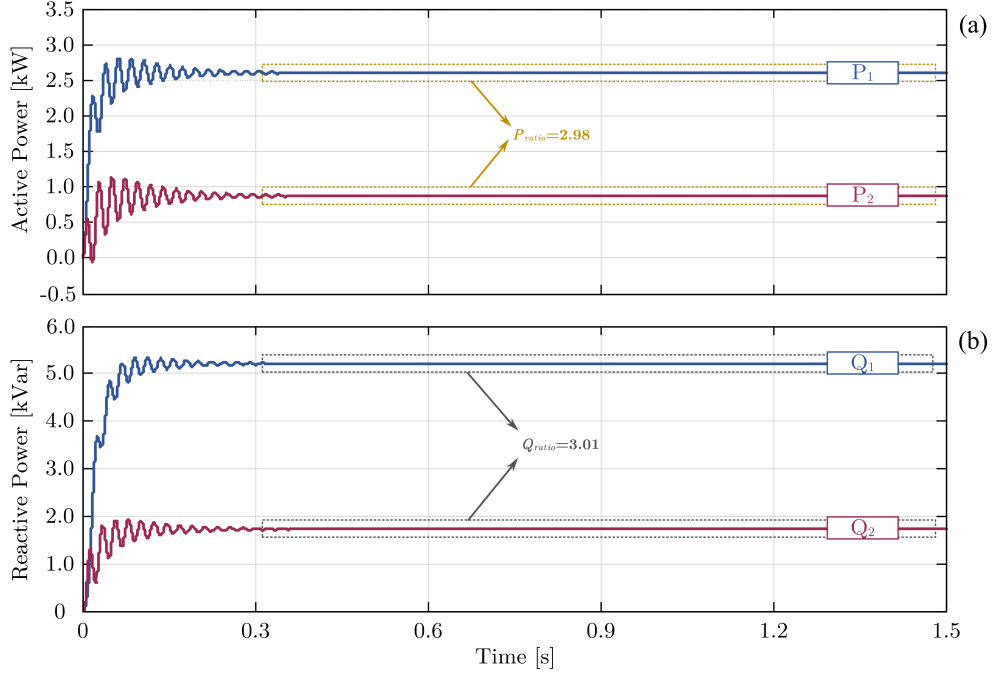


Figure 3.10: Case 1: (a) DERs active powers, (a) DERs reactive powers for L_{VI-opt} selection based on OF_1 .

eigenvalues are placed in four different clusters. The sensitivity of each cluster to the virtual impedance variations can be investigated through Fig. 3.9, where the locus of each pole cluster is shown separately. It is visible from this figure that all four clusters move toward the imaginary axis as L_{VI} varies from zero to 110 [mH] causing the system to become oscillatory. Moreover, it is evident that further increase of L_{VI} may cause the system to become unstable as expected.

Fig. 3.10(a) and Fig. 3.10(b) indicate the time domain results of the active and reactive power variations, respectively. The optimum L_{VI} is 98.4 [mH] which is selected based on OF_1 . From these figures, the active and reactive power ratios in the steady state are 2.98 and 3.01, respectively. This results in negligible errors of 0.6% and 0.3% for the active and reactive powers, respectively. The same graphs are depicted in Fig. 3.11(a) and Fig. 3.11(b) where $L_{VI} = 56$ [mH] is selected as the optimum VI based on OF_4 . Figs. 3.11(a) and 3.11(b) show that for the new value of L_{VI} the active power error remains the same. However, the reactive power ratio error varies slightly and becomes 0.2%. Moreover, the system oscillations are damped faster by the decrease of L_{VI} as it was expected.

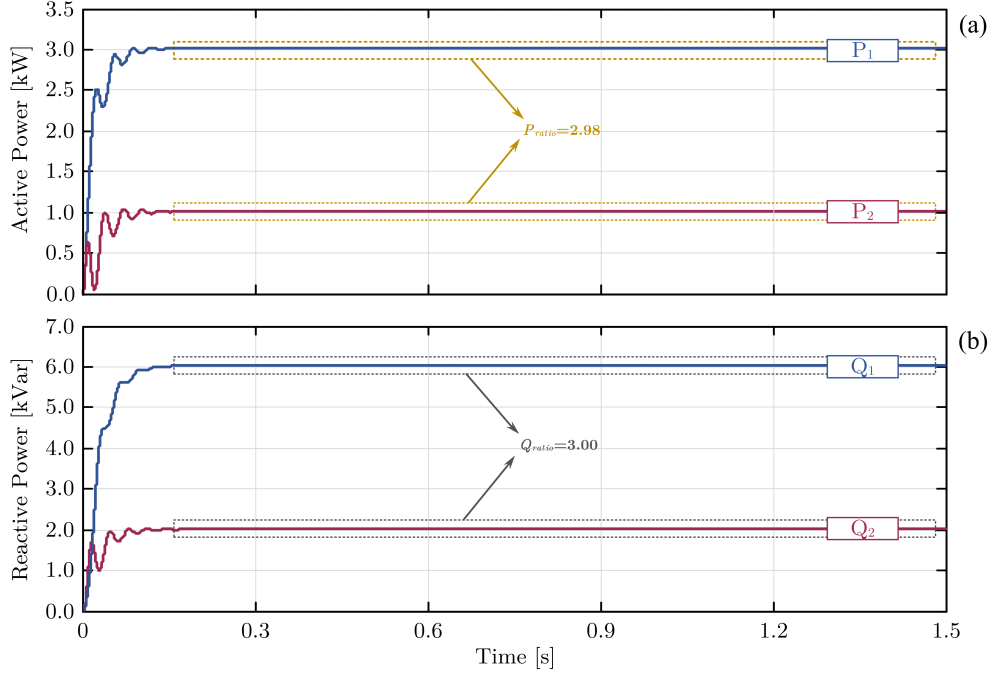


Figure 3.11: Case 1: (a) DERs active powers, (a) DERs reactive powers for L_{VI-opt} selection based on OF_4 .

Table 3.1: Optimum L_{VI} for Case-1 and Case-2.

Case	P_{ratio}	L_{VI-opt} [mH]			
		OF_1	OF_2	OF_3	OF_4
1	3	98.4	76	98.1	56
2	6	45.4	45.7	45.2	45.6

3.5.2 Case-2: Simulation Results for $P_{ratio} = 6$

In this case study, the DERs power ratio is assumed to be $P_1/P_2 = 6$. The time domain results of the DERs output powers are shown in Fig. 3.12. In this case study L_{VI} varies from zero to 50 [mH]. Similar to Case-1, the increase of L_{VI} above some specific values causes the system to become oscillatory as indicated in Fig. 3.12.

Fig. 3.13(a) indicates the power ratio errors for $0 < L_{VI} < 45$ [mH]. This figure shows that the active power ratio error almost remains unchanged (i.e. mainly below 4%) for $L_{VI} < 45$ [mH]. However, the reactive power ratio error significantly drops with the increase of L_{VI} from the initial value of 18%. Fig. 3.13(b) reveals the variations of the objective functions with the increment of L_{VI} . It is visible from this figure that the trend of OF variations is similar to Case-1.

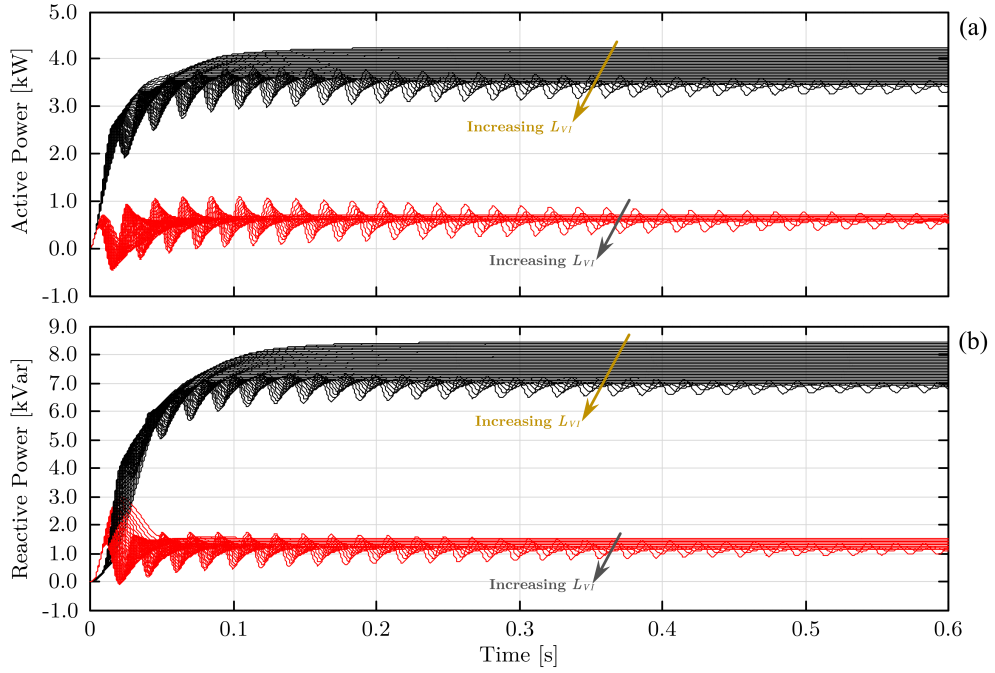


Figure 3.12: Case 2: (a) DERs active power, (b) DERs reactive power for L_{VI} variations from zero to 50 [mH].

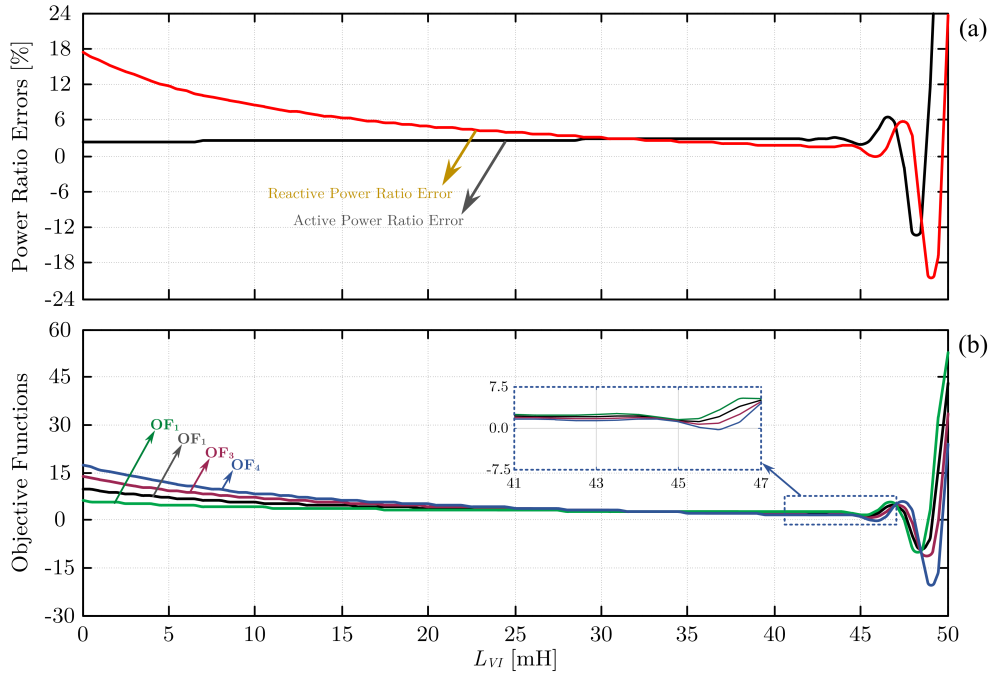


Figure 3.13: Case 2: (a) Power ratio errors, (b) Objective functions.

The selected optimum L_{VI} s for different OFs are summarized in Table 3.1. The smaller frame in Fig. 3.13(b) shows the OFs variations for $41 \text{ [mH]} < L_{VI} < 47$

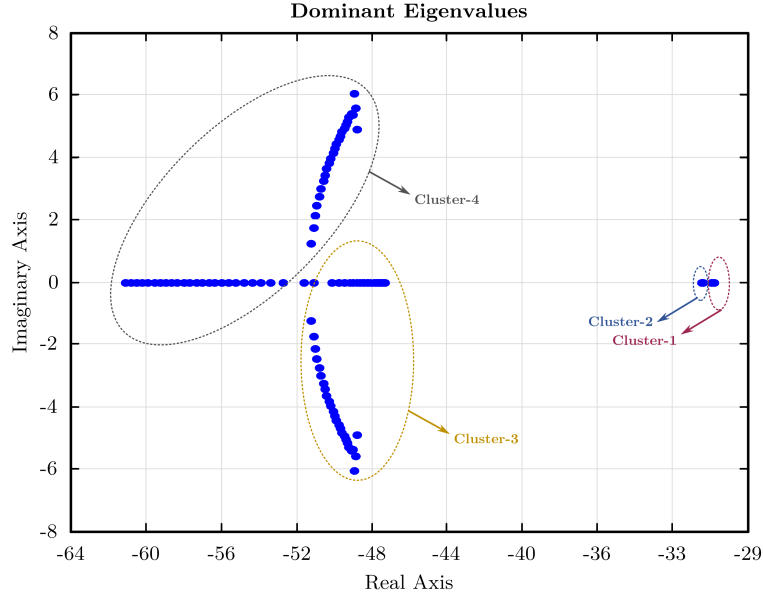


Figure 3.14: Case 2: Root locus diagram for L_{VI} variations from zero to 50 [mH] and $P_{ratio} = 6$.

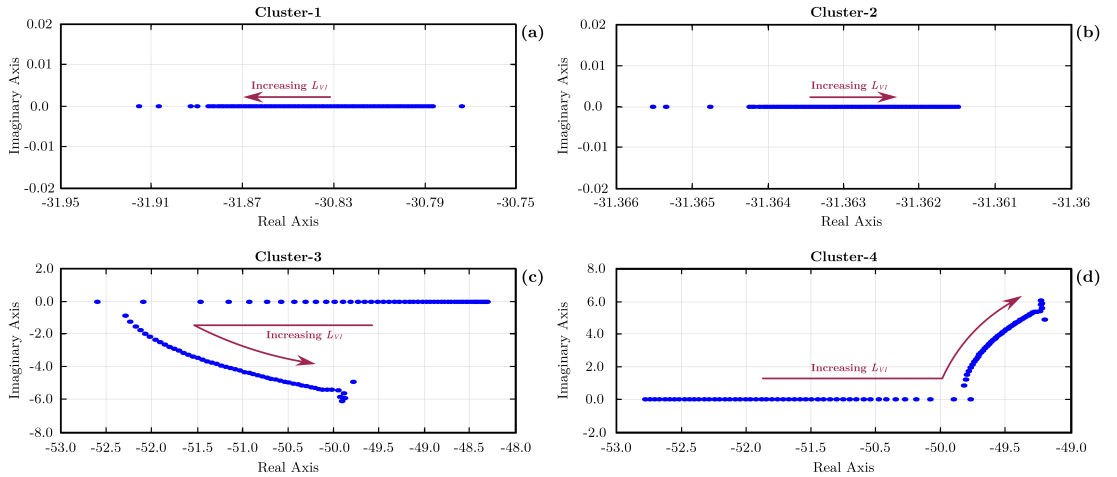


Figure 3.15: Case 2: Dominant eigenvalues locus for L_{VI} variations from zero to 50 [mH].

[mH]. From this figure, the optimum L_{VI} based on all four OFs, which minimizes the objective function and avoids oscillatory results is selected to be around 45.6 [mH] as indicated in Table 3.1.

Fig. 3.14 shows the root locus diagram of the MG network when L_{VI} varies from zero to 50 [mH]. Similar to Case-1, the dominant eigenvalues are mainly placed in four clusters. The sensitivity of each cluster to L_{VI} variations is investigated in Fig. 3.15. From this figure, cluster-1 moves along with the real

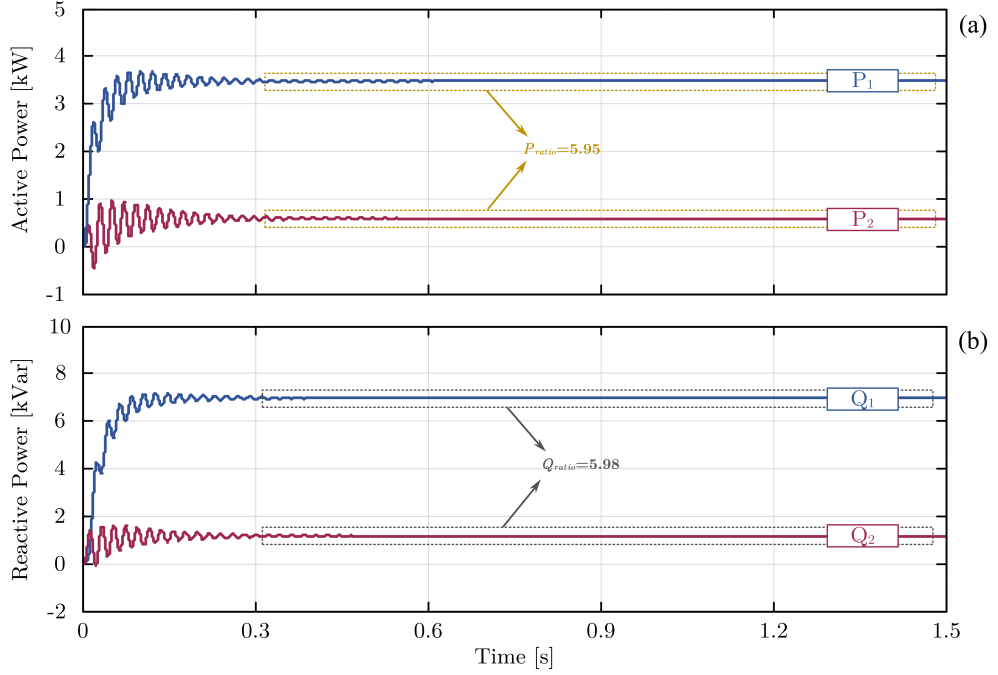


Figure 3.16: Case 2: (a) DERs active powers, (b) DERs reactive powers for L_{VI-opt} selection based on OF_1 .

axis (see Fig. 3.15(a)) whereas cluster-2 moves toward the imaginary axis (see Fig. 3.15(a)). Also Fig. 3.15(c) and Fig. 3.15(d) indicate that the poles of cluster-3 and cluster-4, which are placed on the real axis, become conjugate as L_{VI} increases. Also, with further increase of L_{VI} the conjugate poles grow apart causing the system damping ratio to reduce, and in turn, the system response will become slower.

The time domain variations of both active and reactive powers for two optimum L_{VI} s which are selected based on OF_1 and OF_4 are indicated in Fig. 3.16 and Fig. 3.17. From Fig. 3.16 (a), Fig. 3.17 (a) and Table 3.1, the ratio of active and reactive power for $L_{VI} = 45.6$ [mH] are 5.94 and 5.97, respectively. Hence, the active and reactive power ratio errors are 1% and 0.5%, respectively. Also, Fig. 3.16 (b) and Fig. 3.17 (b), indicate similar results for active and reactive power ratios as the selected optimum L_{VI} s for OF_1 and OF_4 are very close (see Table 3.2).

3.5.3 Case-3: Dynamic Variation of the Power Ratio

This case study investigates the system performance for the dynamic variations of the DERs power ratio. Fig. 3.18(a) and Fig. 3.18(b) reveal the time

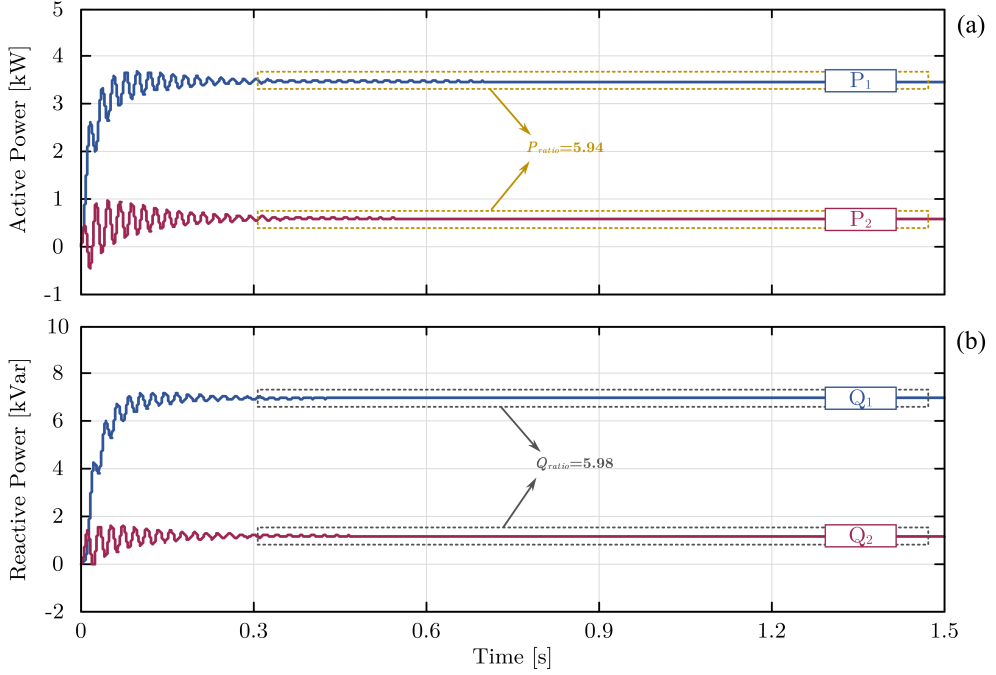


Figure 3.17: Case 2: (a) DERs active powers, (b) DERs reactive powers for L_{VI-opt} selection based on OF_4 .

Table 3.2: Summary of results for Case-3.

Time Intervals	L_{VI-opt} [mH]	Desired Ratios	Actual Ratios		Ratio Errors %	
			P	Q	P	Q
TI-1	44	2	1.99	2.0003	0.5	0.015
TI-2	60	4	3.97	4.0006	0.75	0.015
TI-3	56	5	4.96	5.0007	0.8	0.014

domain results of the DERs active and reactive powers, respectively. Three time intervals are defined in Fig. 3.18, as TI-1, TI-2 and TI-3. During TI-1 the power ratio of the DERs (i.e. P_1/P_2) is considered to be 2, whereas in TI-2 it increases to 4, and in TI-3 it increases further to 5. It can be seen from these figures that the system performance is smooth and seamless throughout the whole simulation although the power ratios are varied dynamically. Moreover, Table 3.2, summarizes the results of this case study giving the optimum VI (L_{VI-opt}), the desired active and reactive power ratios and the related errors. It is to be noted that to determine the optimum L_{VI} for this case study the fourth objective function (OF_4) of Appendix A Table A.1 is considered which aims to minimize the reactive power ratio error. Based on the results of Table 3.2, it can be concluded that

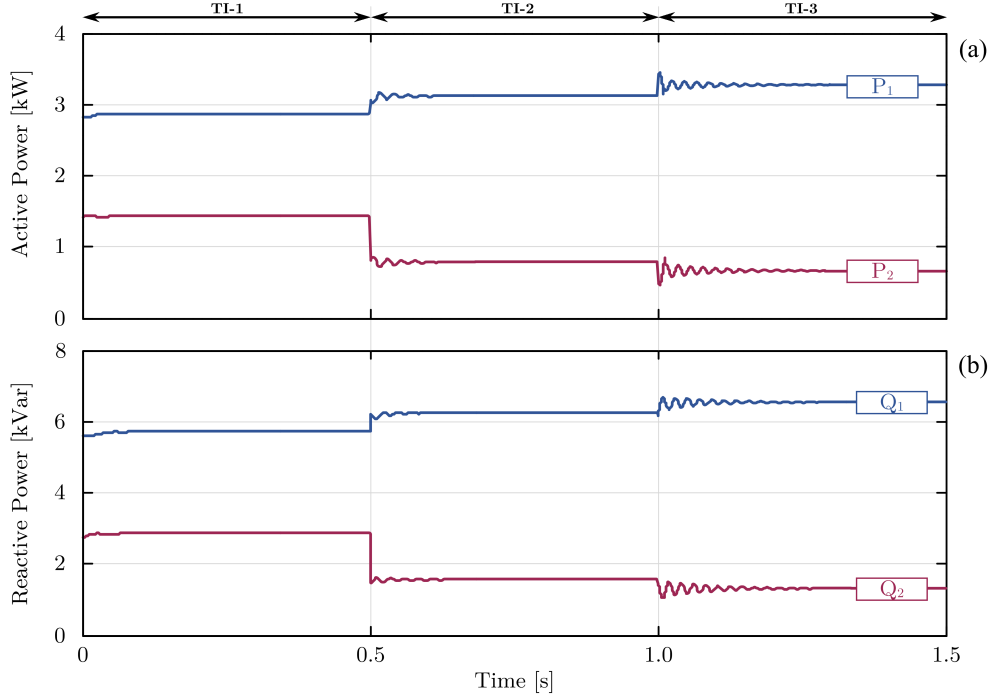


Figure 3.18: Case 3: (a) DERs active powers, (a) DERs reactive powers when P_{ratio} varies dynamically.

the control system properly varies the optimum L_{VI} such that the reactive power ratio errors are kept below 0.1%. Moreover, the active power ratio error is also kept below 1% however $\alpha = 0$ is chosen for the objective function.

3.6 Conclusions

An alternative approach for virtual impedance design is introduced in this chapter, which successfully decouples the active and reactive power sharing without compromising the system stability. To attain this, the virtual impedance is determined based on the stability analysis of the stand-alone MG. Hence, the system transients and stability requirements are taken into account in addition to the steady state power ratio errors of the DERs. This strategy provides a more reliable response to the system compared to the method introduced in Chapter 2 since it is developed based on the small-signal model of the microgrid.

Chapter 4

Hierarchical Control of Battery Energy Storage Systems in Autonomous Microgrids

4.1 Introduction

Due to the cost-effectiveness and lower emissions of renewable energy sources (RES) compared to the traditional generations, the conventional centralized power network is leading toward a smaller and more-distributed generation [157]. However, high penetration of RESs to the distribution systems introduces some problems that have hitherto not been seen. Investigating the issues presented by the chaotic nature of RESs has brought up the concept of microgrids as an ultimate solution [1].

Microgrids (MGs) are considered as a single controllable unit which consist of one or several distributed loads and renewable energy sources (RESs). Microgrids can operate in either grid-connected mode or autonomous mode, as shown in Fig. 4.1. In grid-connected mode, the grid is responsible for maintaining the power balance of the microgrid. However, in autonomous mode, the power management of the microgrid is a much more challenging issue. Energy storage systems (ESSs) such as batteries are widely used in the autonomous MGs in order to balance the generation and consumption mismatch [158]. This is achieved by charging/discharging the battery energy storage (BES) units during off-peak/peak periods.

Several studies have investigated the power management of autonomous microgrids consisting of RES and BES units. In [159], the frequency variations

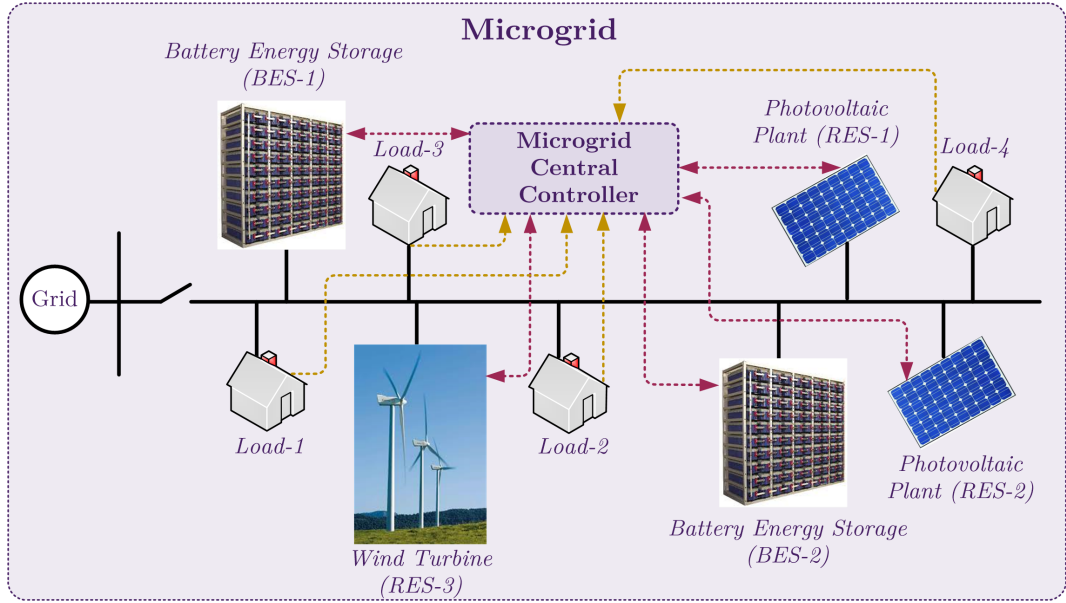


Figure 4.1: Schematic diagram of an example microgrid with distributed BESs, DERs, and Loads.

reflect the power imbalance within the MG, and the BES operation mode is decided, accordingly. Also, in [160] BES units are utilized to compensate the power fluctuations caused by the chaotic nature of the RES units. Moreover, the performance of different types of batteries has been investigated in several researches such as [161]-[164].

The well-known conventional droop control strategy can be utilized for battery energy storage (BES) units of an autonomous MG to duplicate the operation of huge synchronous generators in the traditional power system [58], [165]-[167]. In droop control strategies, the inverter active output power increases/decreases with the decrease/increase of the frequency till the supply and demand are in equilibrium [134]. An advantage of conventional droop control method is that it is independent of communication links. However, there are several limitations to this strategy when applied to BESs.

In conventional droop control strategies, power sharing among the constituent units of the MG is proportional to their maximum capacity. However, in the case of BESs, the available capacity (i.e. state of charge (SoC)) plays a more important role and needs to be given priority when determining the reference power of the battery. Hence, coordinating BES units with conventional droop control may result in premature depletion of BESs and those with lower initial SoC levels will rapidly run out of energy. Consequently, during peak periods the batteries may

not be available to restore the MG frequency.

To address this issue, one solution is to modify the conventional droop control of the BES units to correlate their power ratios with their state of charge (SoC) instead of their nominal capacity [168]-[169]. To achieve this, the droop coefficient of the BES unit needs to be modified dynamically according to its instantaneous SoC level. Based on this approach, the BES units with lower SoC levels, deliver less active power to sustain their available capacity. However, the main problem with the above modified droop control is that the output power of each BES unit is affected by the SoC of the other BES units, in addition to its own SoC level. To address this issue, in this chapter, a new dynamic control strategy is proposed, which updates the droop coefficients of the RES units according to the SoC variations of the BESs to ensure that the BES units perform independently.

The proposed strategy consists of two control subsystems, one for charge and the other for discharge operation of the BES unit. The discharge control strategy utilizes an SoC-based droop control to avoid premature depletion of the BES units. This is achieved by dedicating the highest priority to the available capacity of the BESs while respecting their maximum capacity. Therefore, the active output power of each BES unit is modified dynamically according to its SoC level variations (i.e. the lower the SoC level, the lower the output power). Moreover, with the proposed discharge control strategy the BES units operate independently from each other since a modified droop control is also applied to the RES units. Additionally, the proposed charge control strategy limits the power absorption of the BESs to the surplus power available from the RES units. This ensures that the MG power balance is maintained during charge operation of the BESs while RESs are deployed efficiently.

Active power sharing among the BES units within an MG has been thoroughly studied in the literature [93],[168]. However, reactive power sharing among the BES units has not been investigated as much. It is worth noting that the reactive power exchange of the BES units does not relate on their SoC level and is available due to their converters extra/unused capacity. Here, along with the SoC-based droop control for active power sharing of the BES units, a reactive power sharing strategy is proposed, in which the extra capacity of the BES converters is utilized. This strategy also aims to prevent overloading the RES units. Based on the proposed reactive power sharing algorithm, the BES unit with lower SoC (i.e. lower output active power) which reflects its higher unused converter capacity supplies a greater amount of reactive power. To attain this, the adaptive virtual impedance method, introduced in Chapter 2, is conducted in the discharge control

strategy of the BES units to ensure that the desired reactive power sharing ratios are achieved [120].

The main features of the proposed comprehensive control strategy of the BES units in charge and discharge modes are summarized below;

- The output powers of the BES units are decreased according to their SoC levels as they contribute in supplying the load. This avoids prompt depletion of the BES units, and as a result, they can operate in their nominal operation range for a longer time duration;
- The proposed reactive power sharing algorithm uses the maximum capacity of the BES converters and avoids overloading of the RES units;
- To implement the reactive power sharing algorithm, the adaptive virtual impedance method, introduced in Chapter 2, is conducted to ensure that the extra capacity of the BES converters is utilized;
- The BES units control in charge mode limits their absorbing power, to maintain the power balance of the MG. This implies that the BES absorbing power is limited to the available surplus power within the MG;
- To avoid overcharging of the BES units, when their SoC level reaches its maximum limit (SoC_{max}), BES is either disconnected or switched to discharge mode;

4.2 Microgrid Structure and Control

The structure of the considered MG is shown in Fig. 4.2, which consists of a BES unit and a RES unit. Note that the control strategy can be applied to the MG with multiple BES and RES units as investigated in the simulation results. Each distributed energy resource (DER) (i.e. BES/RES unit), is interfaced to the MG through a voltage source converter (VSC). The VSC and its filter system are connected to the point of common coupling (PCC) through a coupling inductance (L_c). The average active power (P) and reactive power (Q) supplied by each DER unit are expressed as;

$$P = \frac{|V||V_{pcc}|\sin(\delta - \delta_{pcc})}{\omega L_c} \quad (4.1)$$

$$Q = \frac{|V|^2 - |V||V_{pcc}|\cos(\delta - \delta_{pcc})}{\omega L_c} \quad (4.2)$$

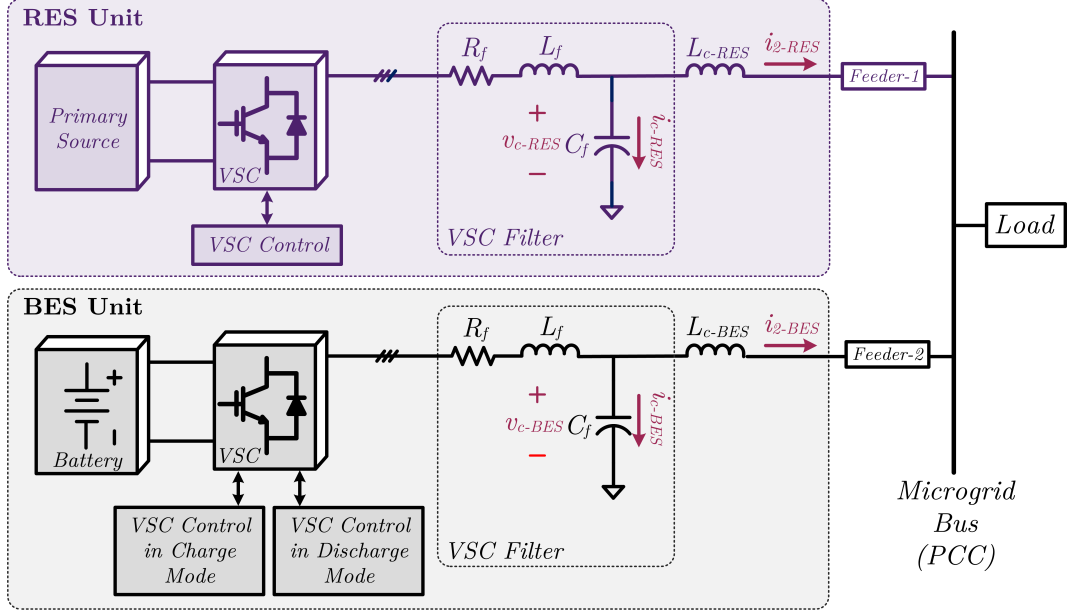


Figure 4.2: Simplified diagram of the microgrid structure with one DER and one BES unit.

where, V and δ are respectively the magnitude and angle of the voltage across the filter capacitor C_f of each DER, and X_c is the impedance of the coupling inductance at the nominal frequency. Also, V_{pcc} and δ_{pcc} are the magnitude and angle of the PCC voltage, respectively. The average powers are calculated by passing instantaneous active (p) and reactive powers (q) through low-pass filters with a cut-off frequency of ω_c . From the above equations, it is clear that for the small values of $\delta - \delta_{pcc}$, the active power can be controlled by δ , while the reactive power can be controlled by V [169]. Thus, power sharing among the DERs can be achieved using the angle and voltage droop instead of the conventional frequency and voltage droop equations as;

$$\delta_{droop} = -m(P - P_{rated}) \quad (4.3)$$

$$V_{droop} = V_{max} - nQ \quad (4.4)$$

where, P_{rated} represents the rated active power capacity of the DER and V_{max} denotes the maximum allowable voltage in the MG. Also, m and n are the slopes of the considered $\delta - P$ and $V - Q$ droop curves, respectively [169]. Hence, the ratio of average output active and reactive powers for any two DER units (e.g. RES- l and BES- k) in an MG are expressed as;

$$\frac{P_{BES}^k}{P_{RES}^l} = \frac{m_{RES}^l}{m_{BES}^k} \quad (4.5)$$

$$\frac{Q_{BES}^k}{Q_{RES}^l} = \frac{n_{RES}^l}{n_{BES}^k} \quad (4.6)$$

4.3 Proposed Cooperative Control of BES Units

To coordinate the operation of the BES units with the RESs within the MG, a new cooperative control is proposed here, which is divided into two subsystems. The first subsystem is dedicated to the SoC-based droop control of the BES units during discharge or nominal operation mode and the second subsystem is for the cooperative control of the BES units during charge mode.

4.3.1 BES Discharge Control Strategy

This control strategy is applied to the BES units, for $SoC_{min} \leq SoC \leq SoC_{max}$, where SoC_{min} is the minimum acceptable limit, and SoC_{max} is the maximum acceptable limit for the nominal operation of the BES unit. Based on the proposed control strategy, during discharge operation mode, the BES units deliver both active and reactive powers to the MG.

Active Power Sharing (SOC-Based Droop Control)

To respect the SoC level of the BES units, the proposed active power sharing method uses the BES available capacity (i.e. SoC) instead of the BES maximum capacity, in the power sharing equation of (4.3). To achieve this, it is necessary to calculate the stored energy of BES- k at a given time as;

$$E_{BES}^k = E_{BES-initial}^k - \int_0^t P_{BES}^k(t).dt \quad (4.7)$$

where, $E_{BES-initial}^k$ and $P_{BES}^k(t)$ are the initial stored energy and the average output active power of BES- k . Thus, the SoC level of BES- k can be expressed as;

$$SoC_{BES}^k(t) = \frac{E_{BES}^k(t)}{E_{BES-max}^k} \times 100 \quad (4.8)$$

where, $SoC_{BES}^k(t)$ and $E_{BES-max}^k$ represent the instantaneous SoC (i.e. available capacity) and the maximum energy capacity of BES- k , respectively. The objective of active power sharing control is to adjust the active output power of the BES units according to their SoC level. To achieve this, it is proposed to modify the $\delta - P$ droop coefficient to ensure that the BES unit with a lower SoC level provides a lower contribution in supplying the demand. The proposed approach

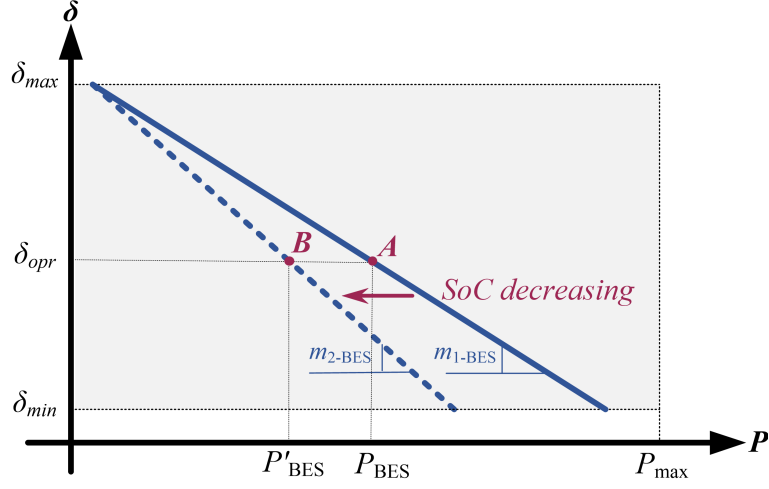


Figure 4.3: Dynamic $P - \delta$ droop coefficient modification for a BES system.

is shown in Fig. 4.3. This figure indicates that the modification of the $\delta - P$ droop coefficient results in moving the BES operating point from A to B . Hence, the BES active power output is reduced. Since the SoC level of BES changes dynamically, it is suggested to apply the changes to the $\delta - P$ droop coefficient over each 10% of variations in the SoC level in order to avoid system chattering. Therefore, the discretized SoC level SoC_{BES-d}^k is defined as follows;

$$SoC_{BES-d}^k = \begin{cases} 0.8, & \text{if } 80\% \leq SoC_{BES} \leq 90\% \\ 0.7, & \text{if } 70\% \leq SoC_{BES} \leq 80\% \\ 0.6, & \text{if } 60\% \leq SoC_{BES} \leq 70\% \\ 0.5, & \text{if } 50\% \leq SoC_{BES} \leq 60\% \\ 0.4, & \text{if } 40\% \leq SoC_{BES} \leq 50\% \end{cases} \quad (4.9)$$

SoC_{BES-d}^k can be used to modify the $\delta - P$ droop coefficient of BES- k as;

$$\frac{P_{BES}^k}{P_0} = \frac{SoC_{BES-d}^k}{SoC_0} = \frac{m_0}{m_{BES}^k} \quad (4.10)$$

where, m_0 is the global droop coefficient designed for P_0 and $SoC_0 = 1$. It is to be noted that in this chapter, the minimum and maximum acceptable limits for the SoC are 40% and 90% of $E_{BES-max}$, respectively. Thus, the nominal range of operation for the BES unit is $40\% \leq SoC \leq 90\%$, and (4.5) can be modified to;

$$\frac{P_{BES}^l}{P_{BES}^k} = \frac{SoC_{BES-d}^l}{SoC_{BES-d}^k} = \frac{m_{BES}^k}{m_{BES}^l} \quad (4.11)$$

The main problem of the above strategy is that the power sharing of each BES

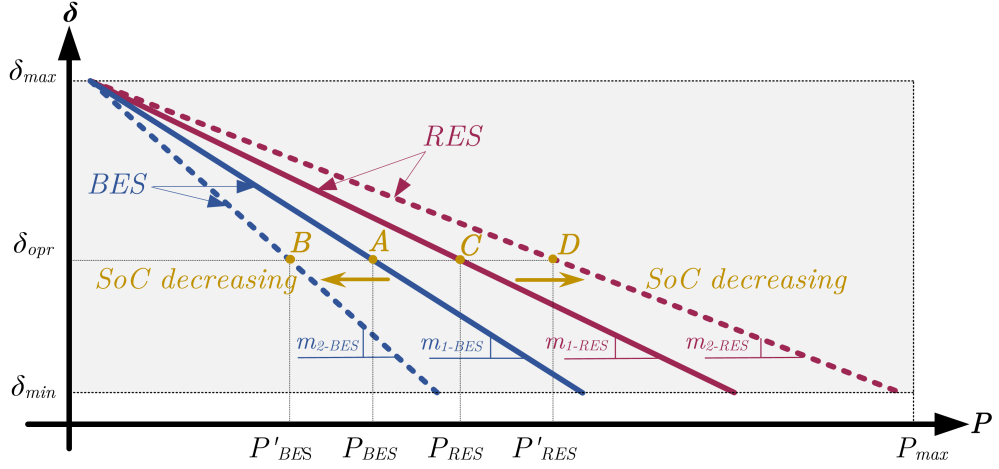


Figure 4.4: Dynamic $P - \delta$ droop coefficient modification for BES and RES system.

unit is affected by the SoC level of the other BES units. Therefore, with the decrease of BES output power due to its SoC reduction, the other BES units proceed to pick up the demand, and their SoC levels reduce drastically, despite the fact that the SoC control should avoid batteries unnecessary discharge. To address this issue, an alternative approach is proposed here, which compels the RES units to take over the power reduction of the BES unit. In this case, the other BES units continue to deliver the same amount of power, although they are operating in droop control. It is worth mentioning that the output powers of the RESs are limited to their ratings to avoid violating their maximum capacities.

The proposed alternative approach is shown in Fig. 4.4. From this figure, as the BES SoC level decreases and its operating point moves from point A to B, the RES operating point moves from C to D. This denotes that the output power of RES units should also variate adaptively with the SoC variation of all the constituent BES units. To achieve this, the droop coefficient of RES- l is defined as;

$$m_{RES}^l(t) = \frac{m_0}{\prod_{j=1}^N SoC_{BES-d}^j} \quad (4.12)$$

where, N represents the number of the BES units within the MG and SoC_{BES-d}^j represents the SoC level of the j th BES unit.

Reactive Power Sharing

Different approaches are considered for reactive power sharing among the RESs in an MG [170]-[172]. However, none of them investigates reactive power sharing among the BES units.

The purpose of reactive power sharing among the BES units is to utilize the unused power capacity of their VSCs. Considering a converter with the maximum capacity of S_{max} and the active power of P , the maximum available reactive power (Q_{max}) of converter can be expressed as;

$$Q_{max} = \sqrt{S_{max}^2 - P^2} \quad (4.13)$$

This implies that for two converters with the active power of P_1 and P_2 , where $P_1 < P_2$, the maximum available reactive power of the first converter is greater than that of the second one ($Q_{max-1} > Q_{max-2}$). Therefore, it is proposed here to set the reactive power sharing ratio among the BES units to be inversely proportional to the ratio of their active powers. Thus, the $V - Q$ droop coefficient ratios among BES- k and BES- l should be inversely proportional to their $\delta - P$ coefficient ratios as;

$$\frac{n_{BES}^k}{n_{BES}^l} = \frac{m_{BES}^l}{m_{BES}^k} \quad (4.14)$$

Based on the above approach, a BES unit which produces a lower amount of active power due to its lower SoC level is expected to produce a higher amount of reactive power. It is worth noting that the maximum capacity limit, based on (4.13), is applied to the system in order to avoid overloading the BES units.

It is well known that the reactive power sharing in droop control is affected by the coupling impedance of the DER, as discussed in Chapter 2 and Chapter 3 [173]. Therefore (4.14) is not satisfied, unless the impedance ratio between the DERs is in equilibrium with (4.14). This can be achieved by conducting the adaptive virtual impedance power sharing technique in the control structure of the BES converter, as discussed in Chapter 2.

4.3.2 BES Charge Control Strategy

This control strategy is applied to the BES units when $SoC < SoC_{min}$ and the BES units should switch to charge mode in order to avoid over-discharge. Based on this strategy, when the BES unit operates in charge mode, it only absorbs active power from the MG, and it neither absorbs nor injects reactive power. Therefore, the control strategy is only dedicated to the active power control.

During the discharge process, the BES unit operates in current control mode (CCM), as discussed in Chapter 1, to maintain the power balance of the MG. Two different scenarios can be considered here as below,

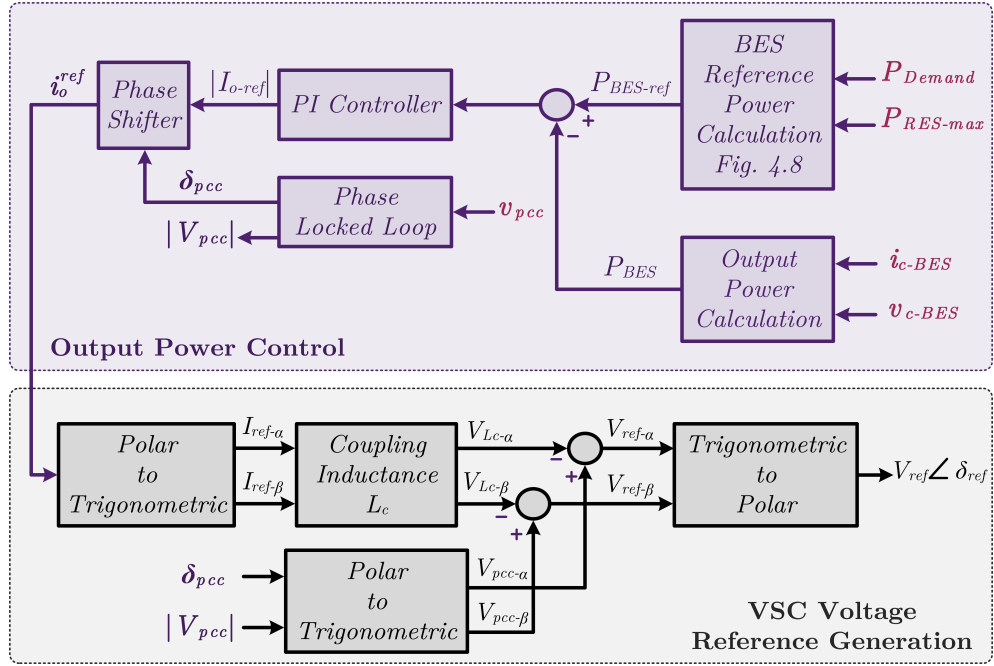


Figure 4.5: BES converter control structure in charge mode.

- The first scenario occurs when the surplus power from the RES units is higher than the maximum capacity of the BES unit, (i.e. $P_{RES-max} - P_{Demand} > P_{BES-max}$). In this scenario the BES unit is charged with its maximum rating ($P_{BES-max}$), as there is sufficient power available from the RES units to charge the battery and supply the load;
- The second scenario happens when the surplus power from the RES units is lower than the maximum rating of the BES unit, (i.e. $P_{RES-max} - P_{Demand} < P_{BES-max}$). In this case, the BES unit power absorption should be limited to $P_{RES-max} - P_{Demand}$, to ensure that the power balance of the system is unaffected.

The schematic of the control diagram of the BES unit in charge mode is shown in Fig. 4.5, where a proportional integral (PI) controller is used to set the active output powers as described in the above scenarios. As shown in Fig. 4.5, the reference current (i_{ref}) is generated by the power control block and is transferred to the voltage reference generation block, where the voltage reference is generated for the VSCs. Voltage reference generation for one phase is shown in Fig. 4.5. This voltage can be used for the other two phases after applying the required phase shifts.

Fig. 4.6 and Fig. 4.7 show the proposed coordinated control structure of the

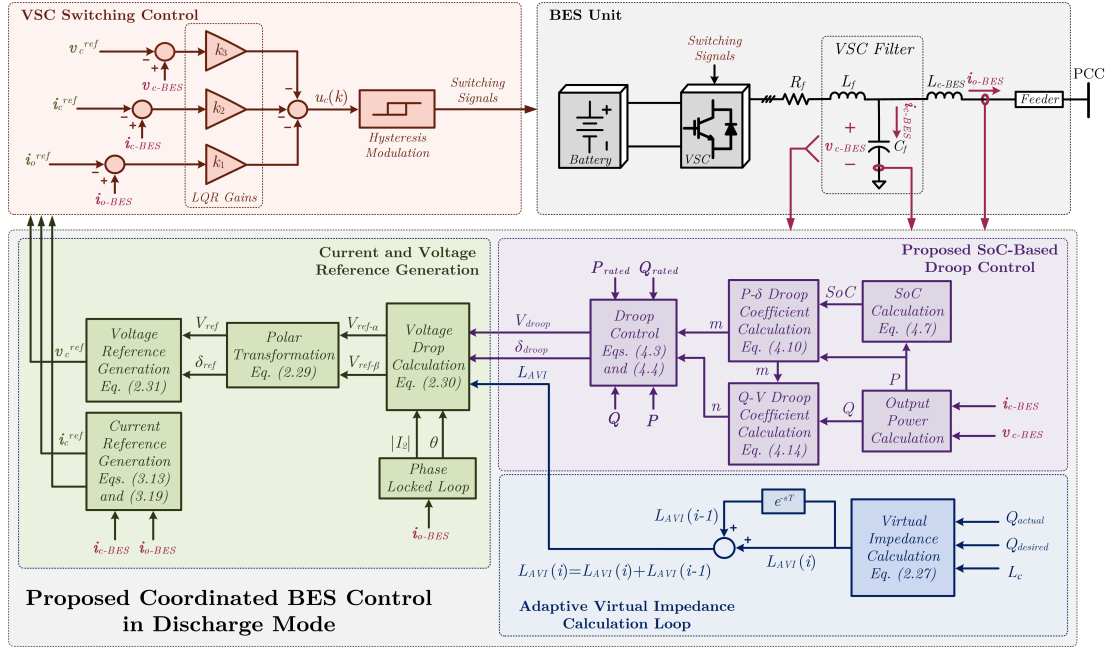


Figure 4.6: Proposed coordinated control of BES systems in discharge mode.

BES units in discharge and charge mode, respectively. Note that the reference generation for i_c and i_o also the VSC switching control, shown in Fig. 4.6 and Fig. 4.7, are described in Chapter 3 and are not repeated here. Also, the voltage reference generation in discharge mode is discussed in Chapter 2. It is worth mentioning that the BES performance when switching from one operation mode to another is smooth and seamless as will be shown in the simulation results of Section 5. Moreover, due to the employed voltage-control technique, the proposed modifications will not affect the system when the DERs supply unbalanced and harmonic loads [174, 175].

4.4 Determining BES Operation Mode

To determine the BES operation mode (charge/discharge), an algorithm is proposed here, which is shown in Fig. 4.8. The proposed algorithm continuously monitors the BES SoC level in order to choose its operation mode. If the estimated SoC value is within the nominal operation range ($SoC_{min} \leq SoC \leq SoC_{max}$) then the BES unit proceeds to discharge otherwise the algorithm investigates if the SoC is above the maximum limit or below the minimum limit. A value below the minimum limit ($SoC < SoC_{min}$) results into BES charge operation and a value above the maximum limit ($SoC > SoC_{max}$) results into either

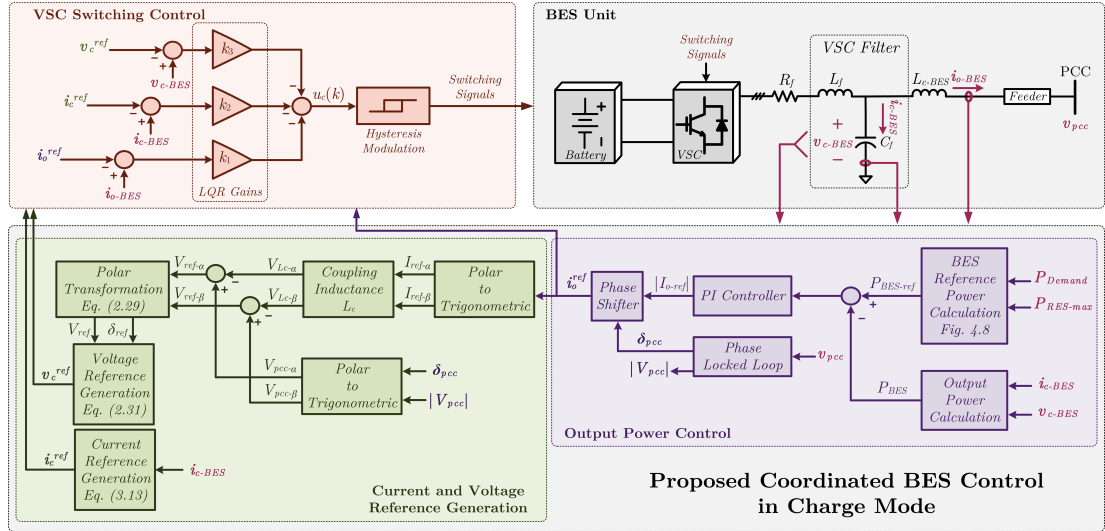


Figure 4.7: Proposed coordinated control of BES systems in charge mode.

BES disconnection or BES discharge operation. Thus, the proposed cooperative control of the BES units always respects their available capacity and power rating without causing any disturbance in the power balance of the MG.

4.5 Performance Evaluation

To evaluate the performance of the proposed control strategy, the MG of Fig. 4.9, with four DERs (including two BES units and two RES units), is simulated in PSCAD/EMTDC. The MG composes four local buses and one central bus. Each DER is connected to one of the local buses via its VSC, where the VSC output terminals are connected to the local bus through the coupling inductance and the feeder. Moreover, distributed loads are also connected to each local bus via their breakers. Technical data of the investigated system is shown in Appendix B Table B.1.

Several case studies are performed to investigate the performance of the proposed active power control. Moreover, to validate the performance of the proposed reactive power control which conducts the virtual impedance calculation loop, the reactive power ratio error between DER- k and DER- l is also calculated in these case studies as;

$$Q_{ratio-err} \% = \left(\frac{Q_{desired}^k}{Q_{desired}^l} - \frac{Q_{actual}^k}{Q_{actual}^l} \right) / \left(\frac{Q_{desired}^k}{Q_{desired}^l} \right) \times 100 \quad (4.15)$$

where, $Q_{actual}^{k/l}$ and $Q_{desired}^{k/l}$ are the measured and desired reactive power of DER-

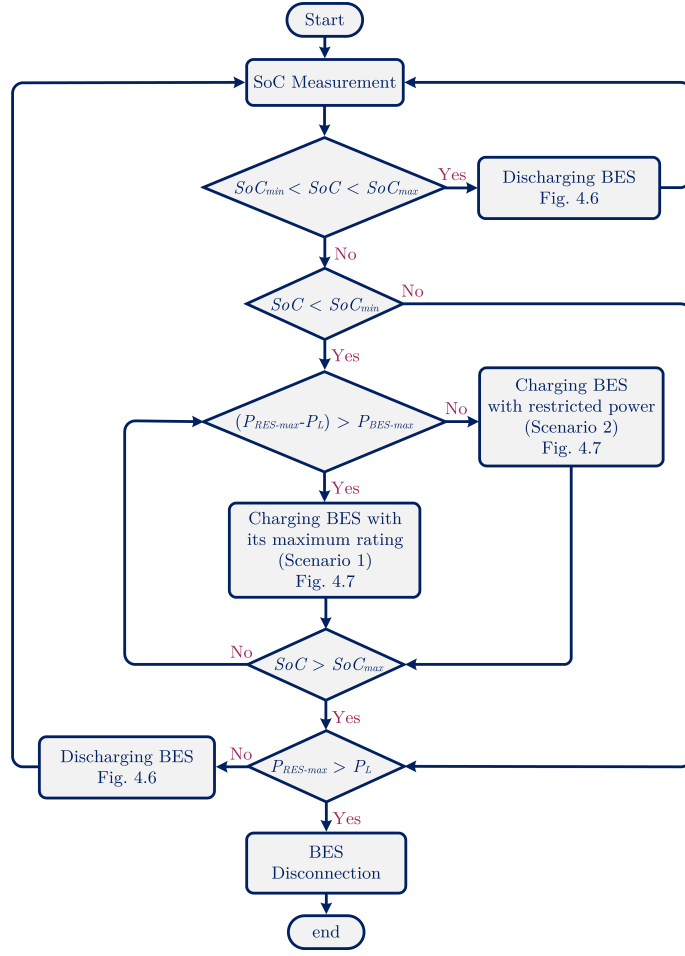


Figure 4.8: Proposed algorithm to decide the BES mode of operation.

k/l and are calculated based on (4.14) and the total demand.

4.5.1 Case-1: Normal Operation of the System

In this case study, the system performance in normal condition is evaluated (e.g. no load changes are applied to the system). Therefore, a constant load of 6.2 [kW] and 2 [kVar] is applied to bus-1, as shown in Fig. 4.10(a). Moreover, the virtual impedance loop is activated at $t = t_1$.

Fig. 4.10(b) shows the active power outputs of the RES and BES units. Where, P_1 and P_4 are the active powers of RES_1 and RES_2 , respectively and P_2 and P_3 are the active powers of BES_1 and BES_2 , respectively. From this figure, it is visible that the active power sharing ratio remains almost unchanged after activation of the virtual impedance loop at $t = t_1$. At $t = t_2$, the SoC level of BES_2 drops to 90%. Therefore, its discrete SoC level is changed to 80%.

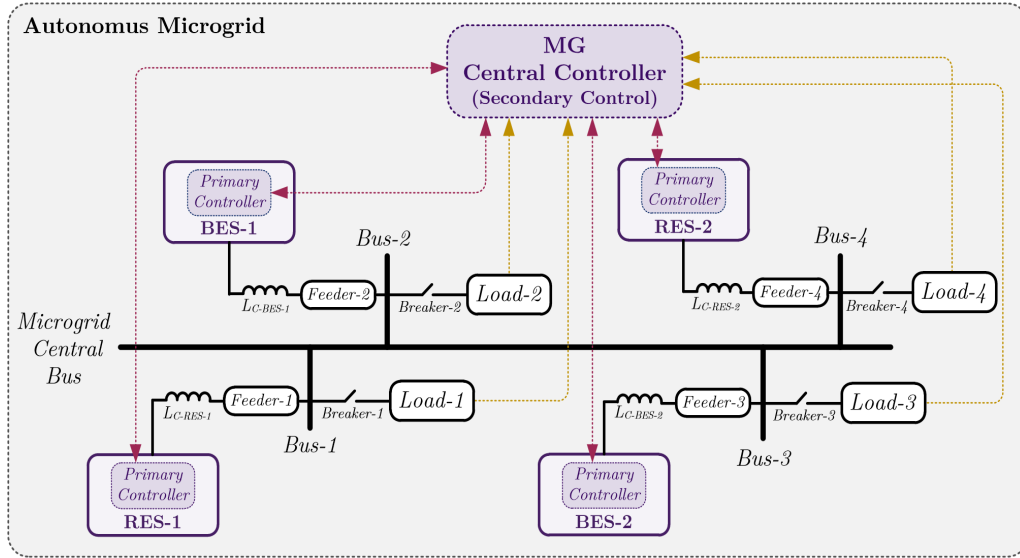


Figure 4.9: Schematic diagram of the investigated MG network.

Consequently, its output active power (P_3) is decreased according to the proposed active power control (see Fig. 4.4). At $t = t_3$, the SoC level of BES_1 drops below 60% and its discrete SoC level is changed to 50%. Hence, based on Fig. 4.4, BES_1 active power (P_2) is decreased as well. Therefore, with the proposed active power control both BES units can stay in the system as a back-up for longer time durations. Another aspect which is revealed here is that the output power reduction for each BES unit is only compensated by the RES units. This is confirmed in Fig. 4.10(b), where with the significant change of P_3 at $t = t_2$, P_2 (i.e. the output power of the other BES unit) remains almost unchanged. The same situation occurs at $t = t_3$, where P_2 drops significantly, and P_3 remains almost constant.

Fig. 4.10(c) shows the reactive power output of the RES and BES units. From this figure, at $t = t_1$, there is a remarkable variation in the reactive power sharing of the DERs as the adaptive virtual impedance (AVI) calculation loop is activated in the system. Moreover, with the proposed reactive power sharing approach, the reactive power of BES units increases when their active power output decreases with the SoC. For instance, at $t = t_2$, P_2 is decreased, and Q_2 is increased. The same trend can be seen for BES_1 at $t = t_3$. Hence, the reactive power control strategy ensures that the converters extra capacity is utilized without overloading the BES unit.

The batteries SoC level is shown in Fig. 4.12(d). Based on the proposed SoC-based droop control, the BES unit with a lower initial SoC level (SoC_{init})

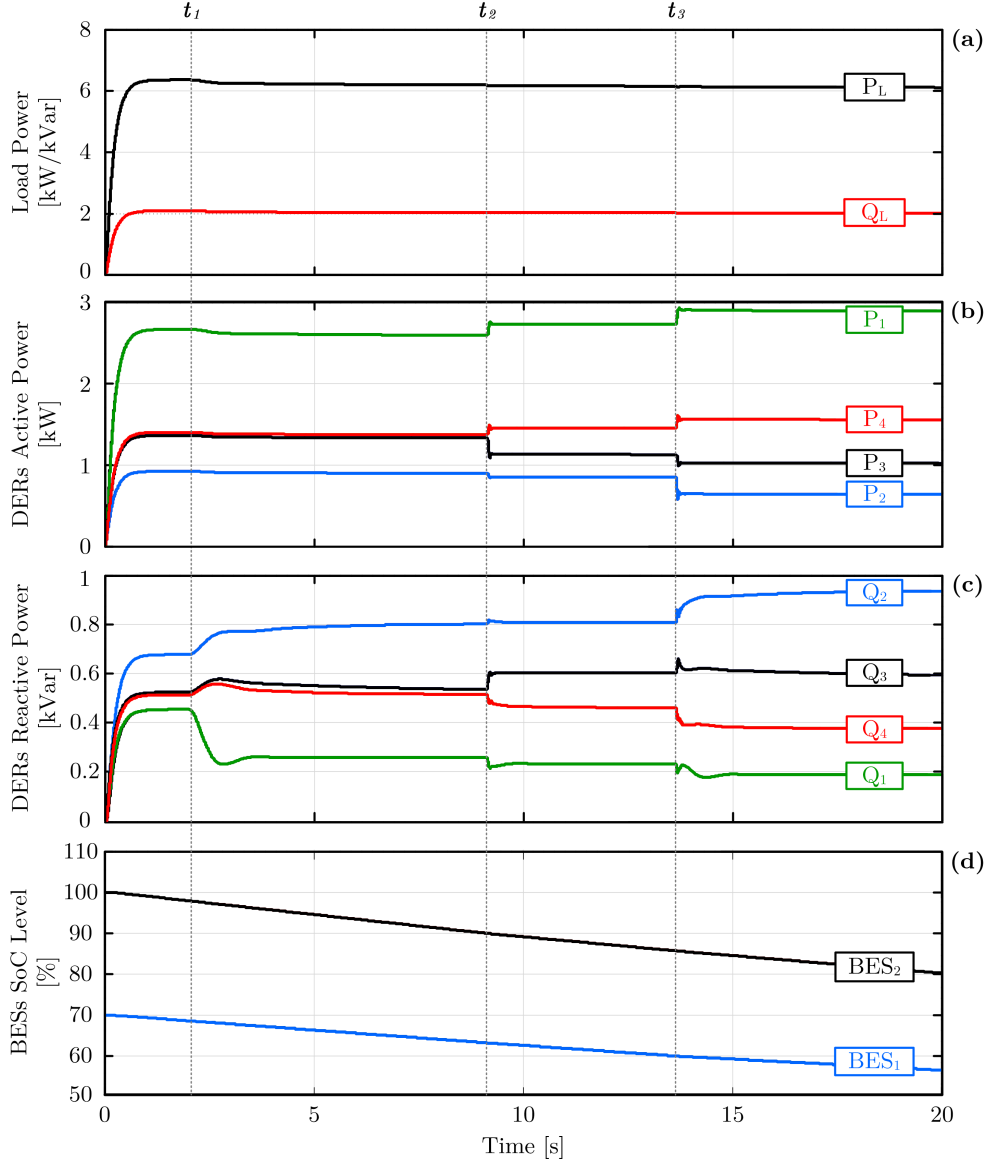


Figure 4.10: Simulation results of Case-1: normal operation of the system.

should be discharged with a lower rate. Table 4.1 verifies this fact revealing the percentage of SoC drop for both BES units in different time zones. As shown in Table 4.1, in all four time zones BES_2 discharges with a higher rate compared to BES_1 . Moreover, for the whole simulation period ($0 < t < 20$), BES_2 SoC level changes from 100% to 80% (i.e. drops 20%), while that of BES_1 varies from 70% to 56% (i.e. drops 14%). Therefore, BES_1 which has a lower SoC_{init} discharges with a lower rate compared to BES_2 to sustain its available charge for a longer time duration.

Table 4.2 and 4.3 summarize the active and reactive power ratio errors of Case-

Table 4.1: Percentage of SoC drop for Case-1.

Time Intervals	BES_1	BES_2
$0 < t < t_1$	1.4 %	2.1 %
$t_1 < t < t_2$	5.4 %	7.9 %
$t_2 < t < t_3$	3.2 %	4.3 %
$t_3 < t < 20 s$	3.4 %	5.4 %
$0 < t < 20 s$	20 %	14 %

Table 4.2: Active power ratio errors for Case-1.

Time Intervals	Active Power Ratios and Errors for Fig. 4.10(b)					
	P_1/P_2	Error [%]	P_1/P_3	Error [%]	P_1/P_4	Error [%]
$0 < t < t_1$	3.08	7.1	2.05	5.3	2	5.2
$t_1 < t < t_2$	3.08	7.1	2.05	5.7	2	5.6
$t_2 < t < t_3$	4.44	8.5	2.46	7.7	2	6.2
$t_2 < t < 20 s$	5	10	3.12	10	2	7.4

Table 4.3: Reactive power ratio errors for Case-1.

Time Intervals	Reactive Power Ratios and Errors for Fig. 4.10(c)					
	Q_1/Q_2	Error [%]	Q_1/Q_3	Error [%]	Q_1/Q_4	Error [%]
$0 < t < t_1$	0.324	106.5	0.486	78.1	0.5	76.7
$t_1 < t < t_2$	0.324	0.8	0.486	1.1	0.5	0.15
$t_2 < t < t_3$	0.225	0.8	0.405	0.4	0.5	0.01
$t_2 < t < 20 s$	0.20	0.15	0.32	1.2	0.5	0.12

1 in different time zones of the simulation. These tables indicate that the active power ratio errors are below 10% and are not affected by the adaptive virtual impedance (AVI) loop activation. However, the reactive power ratio errors are significantly mitigated with the activation of AVI at $t = t_1$. From Table 4.3 it can be observed that the reactive power ratio errors are kept below 3% and hence, are negligible when the AVI is activated in the system (i.e. for $t > t_1$), while the same errors are significantly high, without the AVI (i.e. for $t < t_1$).

4.5.2 Case-2: Comparison of SoC-based Droop and Conventional Droop

In this case study, the system performance with and without the proposed SoC-based droop control is investigated while two load variations are applied to the system. For $t < t_2$, breaker-1 and breaker-2 are closed, and the total load of the system is 7.4 [kW] and 2.4 [kVar]. For $t_2 < t < t_4$, breaker-2 is opened and the total load of the system decreases to 6 [kW] and 2 [kVar]. Finally, at $t = t_4$, breaker-3 is closed and the system total load increases to 7.2 [kW] and 2.4 [kVar]. The total load variations are shown in Fig. 4.11(a). Moreover, similar to Case-1, the virtual impedance loop is activated at $t = t_1$. Fig. 4.11(b), Fig. 4.11(c) and Fig. 4.11(d) reveal the DERs active and reactive powers and the SoC variations of the BES units, respectively. Furthermore, these figures also indicate the results for BES_1 when the simple droop control is applied to the system (shown with the dashed lines). From these figures, it is visible that with the proposed SoC-based droop control, the DERs active and reactive powers change accordingly with the load variations. At $t = t_3$, BES_1 SoC level drops to 50%; and therefore, the proposed control method compels this unit to deliver a lower amount of active power. This prevents the SoC level of BES_1 to drop to its minimum limit (SoC_{min}). Therefore, BES_1 remains connected to the system, even though, its initial SoC level (SoC_{init}) is close to SoC_{min} . Alternatively, as shown in Fig. 4.11(b), with simple droop control, BES_1 delivers higher amount of active power resulting in a higher rate of discharge (see Fig. 4.11(d)). Consequently, at $t = 13.6$ [s], the SoC level of BES_1 drops to SoC_{min} and therefore, it becomes disconnected.

Table 4.4 and Table 4.5 summarize the active and reactive power ratio errors of Case-2, respectively when SoC-based droop control is conducted in the system. The results indicate that the active power ratio errors are below 10%, similar to Case-1, and the reactive power ratio errors are lower than 3%, after activation of the AVI (i.e. $t > t_1$).

4.5.3 Case-3: BES Switching from Discharge to Charge

This case study investigates the performance of the BES charge controller when BES-1 SoC level drops to its minimum limit (SoC_{min}). Hence, its operation mode has to change from discharge to charge. To attain this, it is assumed that the initial SoC level of BES_1 is 42%, while SoC_{min} is 40%. Two load changes are

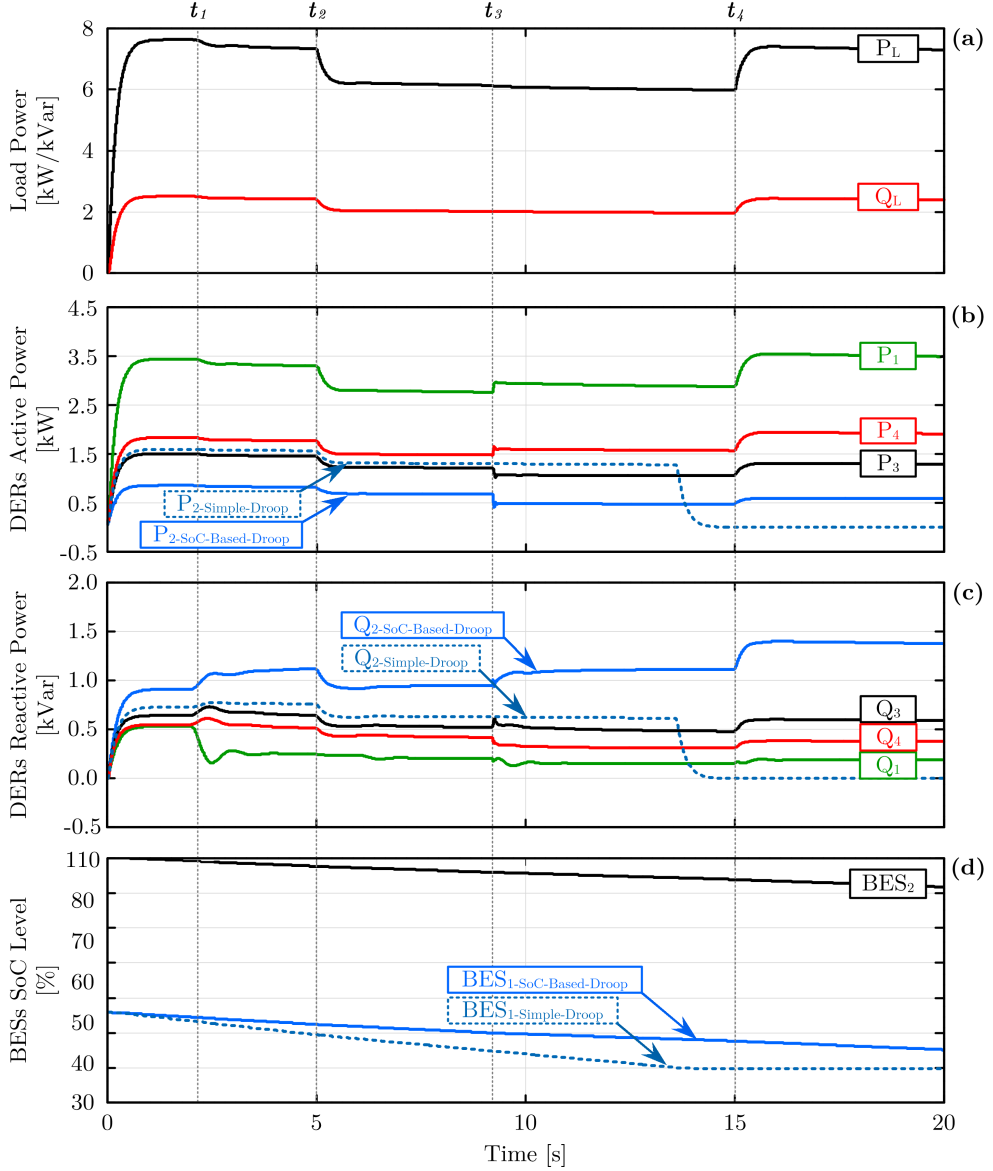


Figure 4.11: Simulation results of Case-2: comparison of SoC-based droop and conventional droop.

applied to the system as shown in Fig. 4.12(a). For $t < t_2$ breaker-2, breaker-3, and breaker-4 are closed, and the total load of 7 [kW] is applied to the system. At $t = t_2$, breaker-2 is opened and the total load decreases to 5 [kW]. At $t = t_3$, breaker-3 is also opened, and the total load decreases further to 3 [kW].

The active power variations of the DER units are shown in Fig. 4.12(b). Initially, BES_1 contributes in supplying the load as its SoC level is within the nominal operation range. For $t < t_1$, it can be seen that BES_1 is supplying the small amount of 0.55 [kW], due to its low SoC level. At $t = t_1$, BES_1 SoC level

Table 4.4: Active power ratio errors for Case-2 (SoC-based droop control).

Time Intervals	Active Power Ratios and Errors for Fig. 4.11(b)					
	P_1/P_2	Error [%]	P_1/P_3	Error [%]	P_1/P_4	Error [%]
$0 < t < t_1$	3.08	7.3	2.05	5.5	2	5.3
$t_1 < t < t_2$	3.08	7.3	2.05	5.9	2	5.7
$t_2 < t < t_3$	3.08	7.8	2.05	6.08	2	5.9
$t_2 < t < 20 s$	3.08	9.4	2.05	6.8	2	6.6

Table 4.5: Reactive power ratio errors for Case-2 (SoC-based droop control).

Time Intervals	Reactive Power Ratios and Errors for Fig. 4.11(c)					
	Q_1/Q_2	Error [%]	Q_1/Q_3	Error [%]	Q_1/Q_4	Error [%]
$0 < t < t_1$	0.324	93.9	0.486	67.6	0.5	66.3
$t_1 < t < t_2$	0.324	1.1	0.486	1.5	0.5	1.4
$t_2 < t < t_3$	0.324	2.8	0.486	1.4	0.5	1.3
$t_2 < t < 20 s$	0.324	2.2	0.486	1.01	0.5	0.9

drops to its minimum limit of 40%, and the proposed control strategy disconnects this unit from the MG. This is due to the insufficient surplus power from the RES units, for supplying the load and charging the BES at the same time (see Fig. 4.8). At $t = t_2$, as the load decreases to 5 [kW], BES_1 is reconnected to the MG and proceeds to charge based on the control strategy of Fig. 4.7. For $t_2 < t < t_3$, BES_1 power absorption is limited by the proposed charge controller to the available surplus power of 1 [kW]. At $t = t_3$, the proposed controller increases the charge rate of BES_1 since the load is decreased further and a surplus power of 2 [kW] is now available from the RES units.

Fig. 4.12(c) shows the SoC variations of both BES units. In addition, BES_1 SoC variations are separately shown in Fig. 4.12(d). From this figure, it is visible that at $t = t_1$, BES_1 SoC level drops to its minimum limit (40%). For $t_1 < t < t_2$, the SoC of BES_1 remains unchanged as this unit is disconnected. At $t = t_2$, BES_1 proceeds charging, and in turn, its SoC starts increasing. At $t = t_3$, the SoC continues to increase but with a higher rate due to the demand reduction.

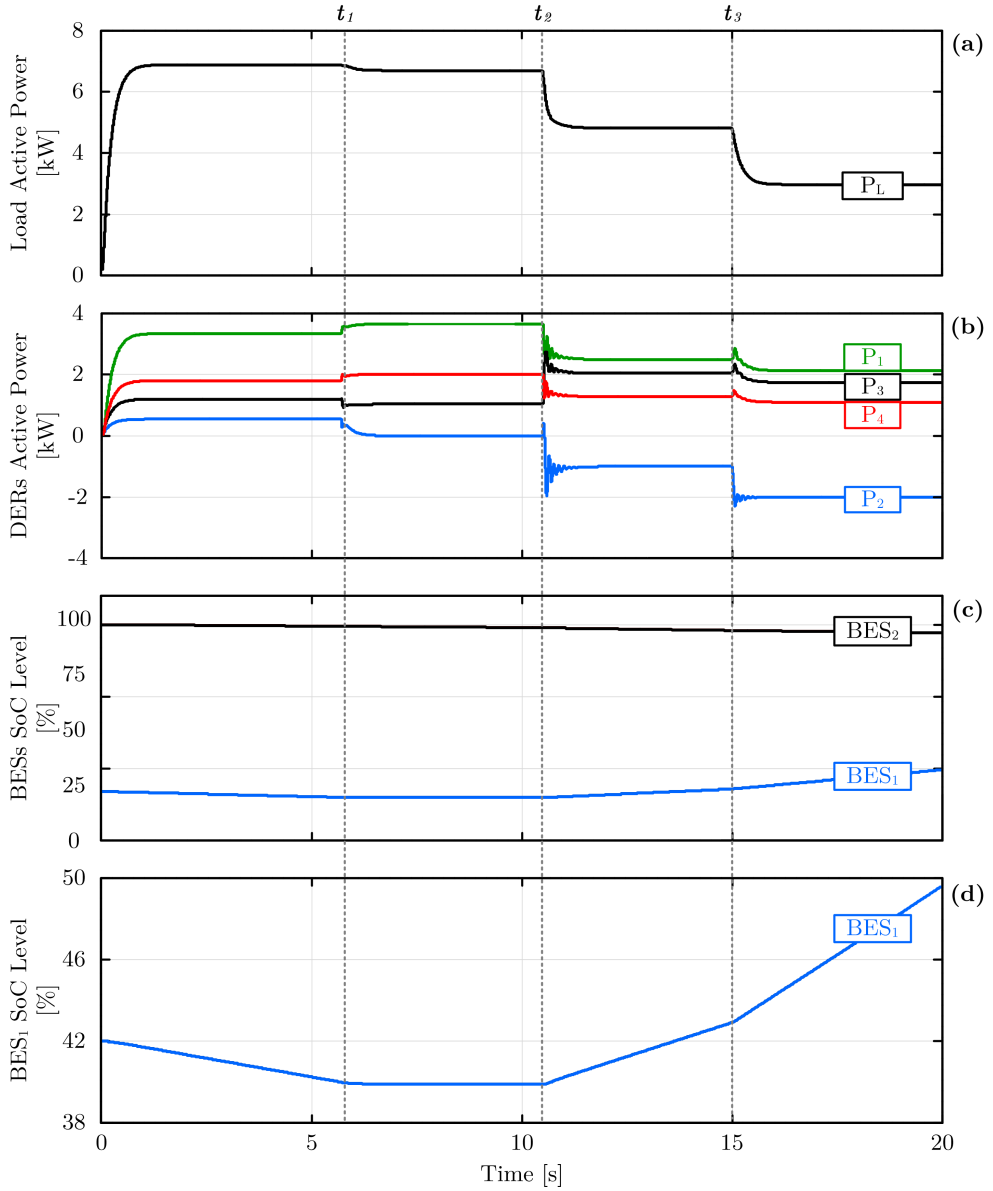


Figure 4.12: Simulation results of Case-3: BES switching from discharge to charge

4.5.4 Case-4: BES Switching from Charge to Discharge

This case study investigates the performance of the proposed control strategy when BES_1 SoC level reaches the maximum limit of the nominal operation range (SoC_{max}). For this, the initial SoC level of BES_1 is assumed to be 88.5%, and SoC_{max} is considered to be 90%. Two load changes are applied to the system, as shown in Fig. 4.13(a). For $t < t_1$, only breaker-1 is closed, and the total system demand is 3 [kW]. At $t = t_1$, breaker-2 is closed, and the overall demand becomes 5 [kW]. Finally, at $t = t_3$, breaker-4 is also closed, and the total load is further

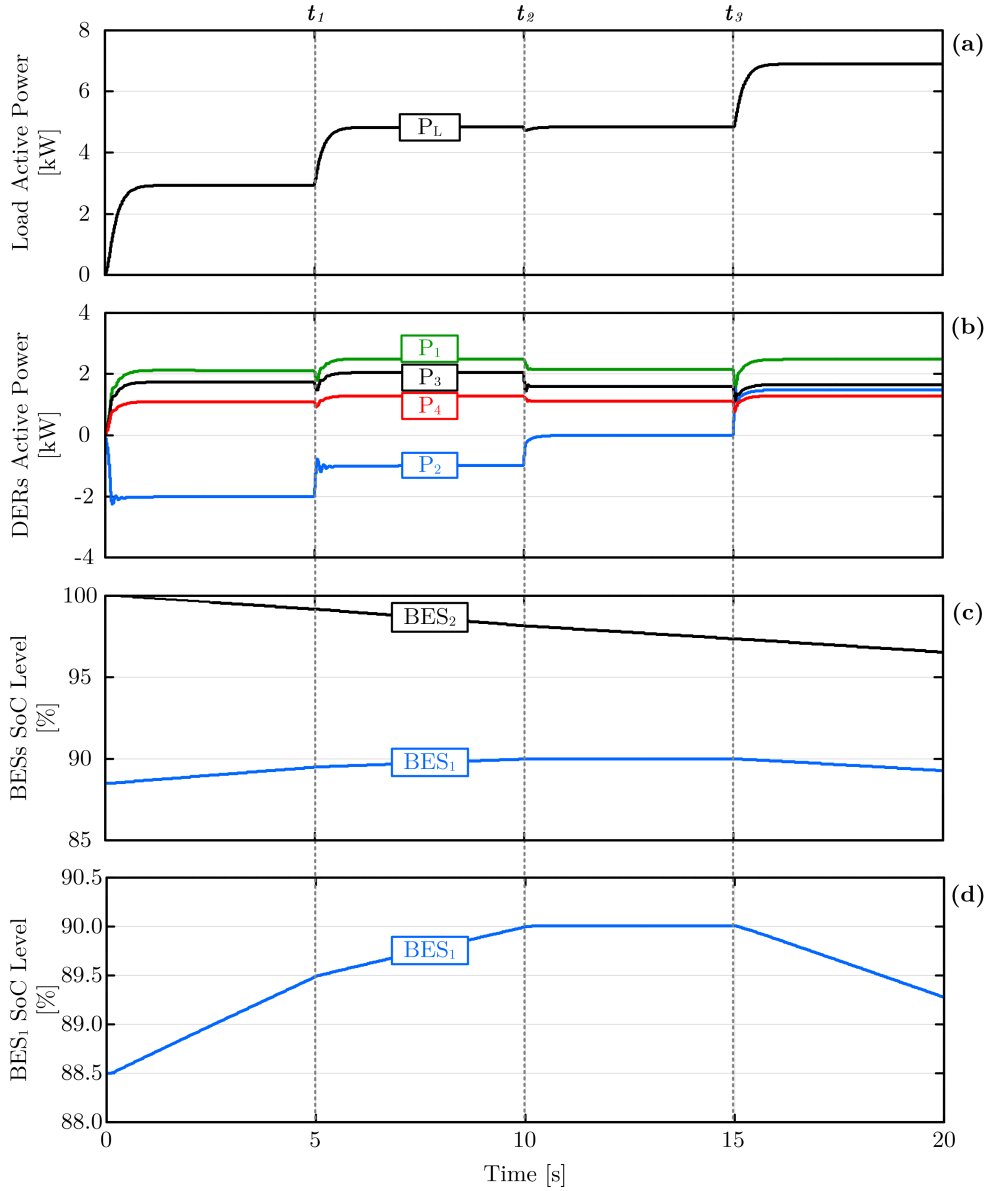


Figure 4.13: Simulation results of Case-4: BES switching from charge to discharge

increased to 7 [kW].

Fig. 4.13(b) depicts the active output power of the DERs. For $t < t_1$, BES_1 is charging with its maximum rating of 2 [kW], since the surplus power from the RES units is sufficient. At $t = t_1$, load increases to 5 [kW] and as a result BES_1 continues to charge with a lower rate (i.e. absorbing 1 [kW]). At $t = t_2$, the SoC level of BES_1 reaches SoC_{max} ; and based on the flowchart of Fig. 4.8, the control system disconnects BES_1 since the power from the RES units is sufficient for supplying the load. At $t = t_3$, the load is increased, and BES_1 is reconnected

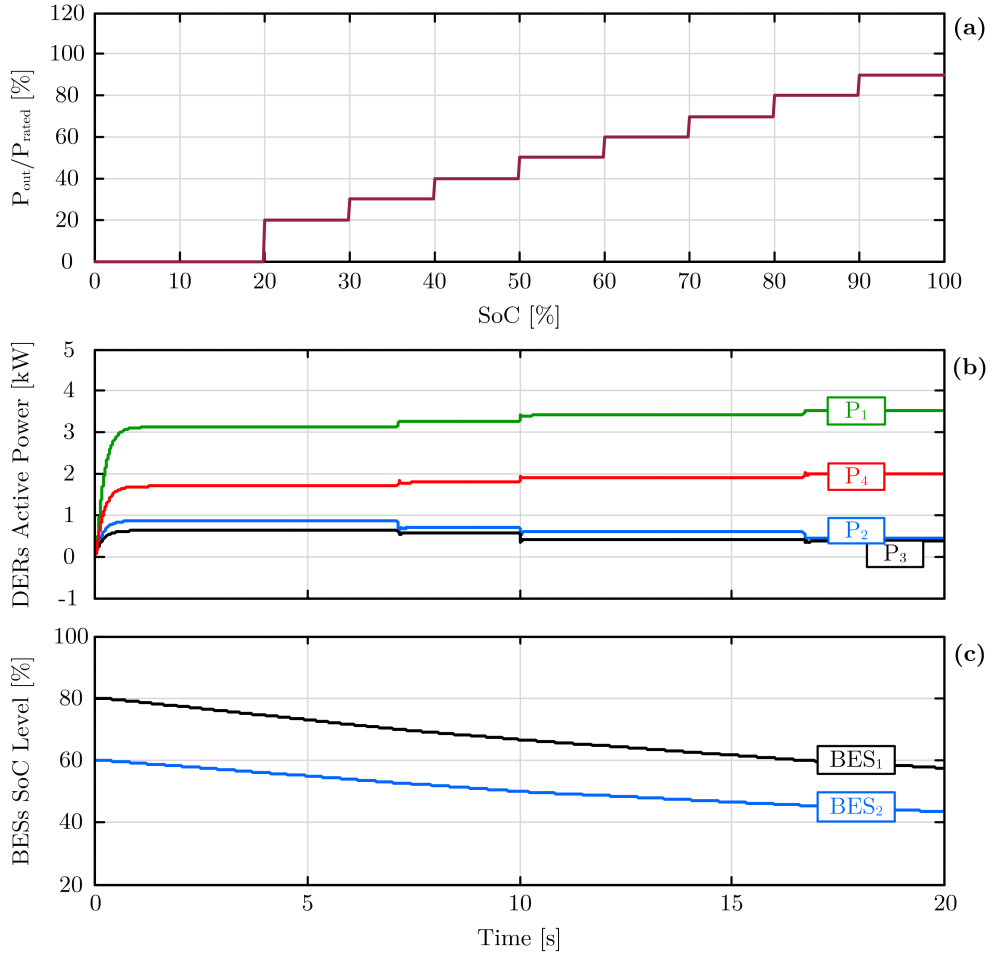


Figure 4.14: Simulation results of Case-5.1

while operating in discharge mode.

Fig. 4.13(c) shows the SoC variations of both BES units. Also, BES_1 SoC variations are shown in Fig. 4.13(d), separately. From this figure, for $0 < t < t_1$ and $t_1 < t < t_2$, BES_1 is charging. However, the rate of charge is lower for $t_1 < t < t_2$, as the SoC is about to reach SoC_{max} . For $t_2 < t < t_3$, SoC remains unchanged since BES_1 is disconnected. Finally, for $t > t_3$, BES_1 SoC level is decreasing as it switches to discharge mode.

4.5.5 Case-5: Comparison of Different Power-SoC characteristics

To evaluate different power-SoC characteristics for different types of BES units, another case study is designed and carried out here. Three different ac-

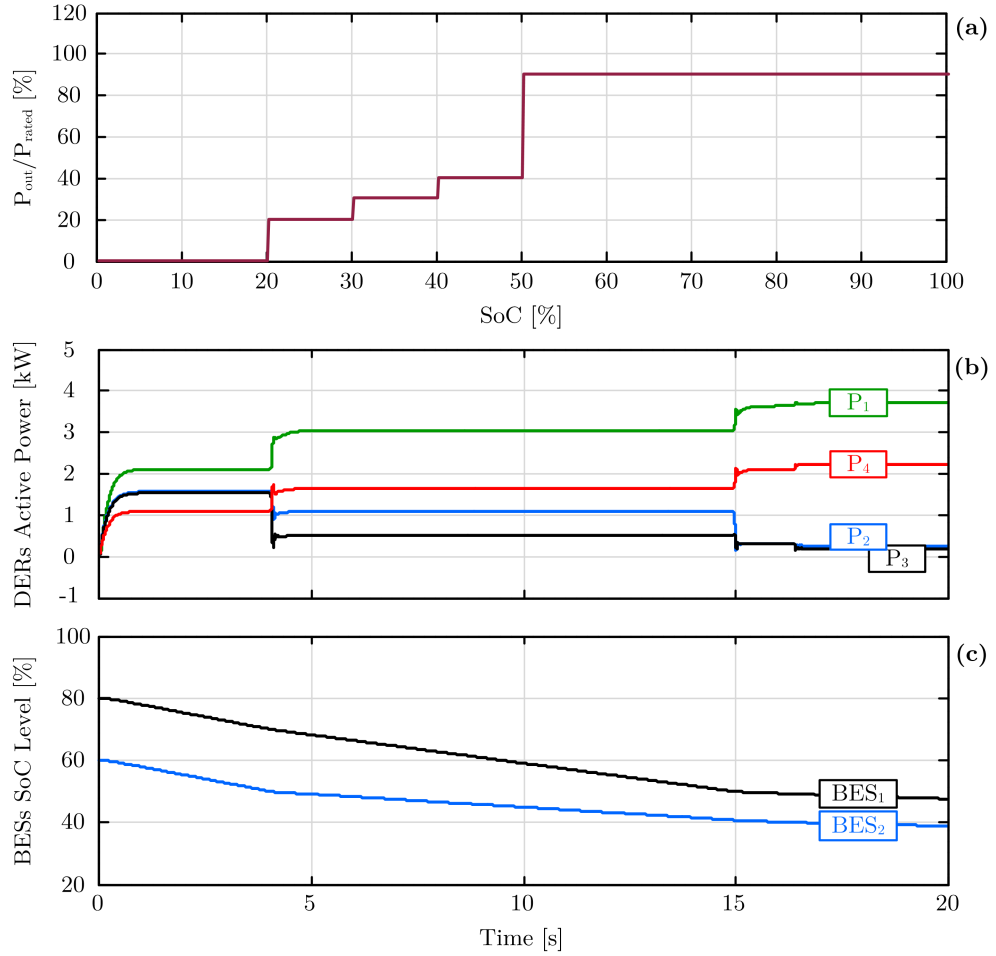


Figure 4.15: Simulation results of Case-5.2

tive power-SoC characteristics are considered in Case-5.1, Case-5.2, and Case-5.3 which are respectively illustrated in Figs. 4.14(a), 4.15(a) and 4.16(a). Note that the active power-SoC characteristic of Fig. 4.14(a) was conducted in all the aforementioned simulation studies (i.e. Case-1 to Case-4). Based on this characteristic, the discrete SoC variations are updated in steps of 10%.

From Figs. 4.14, 4.15, and 4.16, it can be seen that with the same load demand and for the same time interval, the SoC level of BES_1 drops to 57% in Case-5.1, while in Case-5.2 and Case-5.3 it drops to 47% and 35%, respectively. Also in Case-5.1 the SoC level of BES_2 drops to 43%, while in Case-5.2 and Case-5.3, it drops to 38% and 9%, respectively. This case study confirms that the BES units will be able to supply the load demand for a longer time duration if the proposed power-SoC characteristic of Fig. 4.14(a) is deployed in their control system.

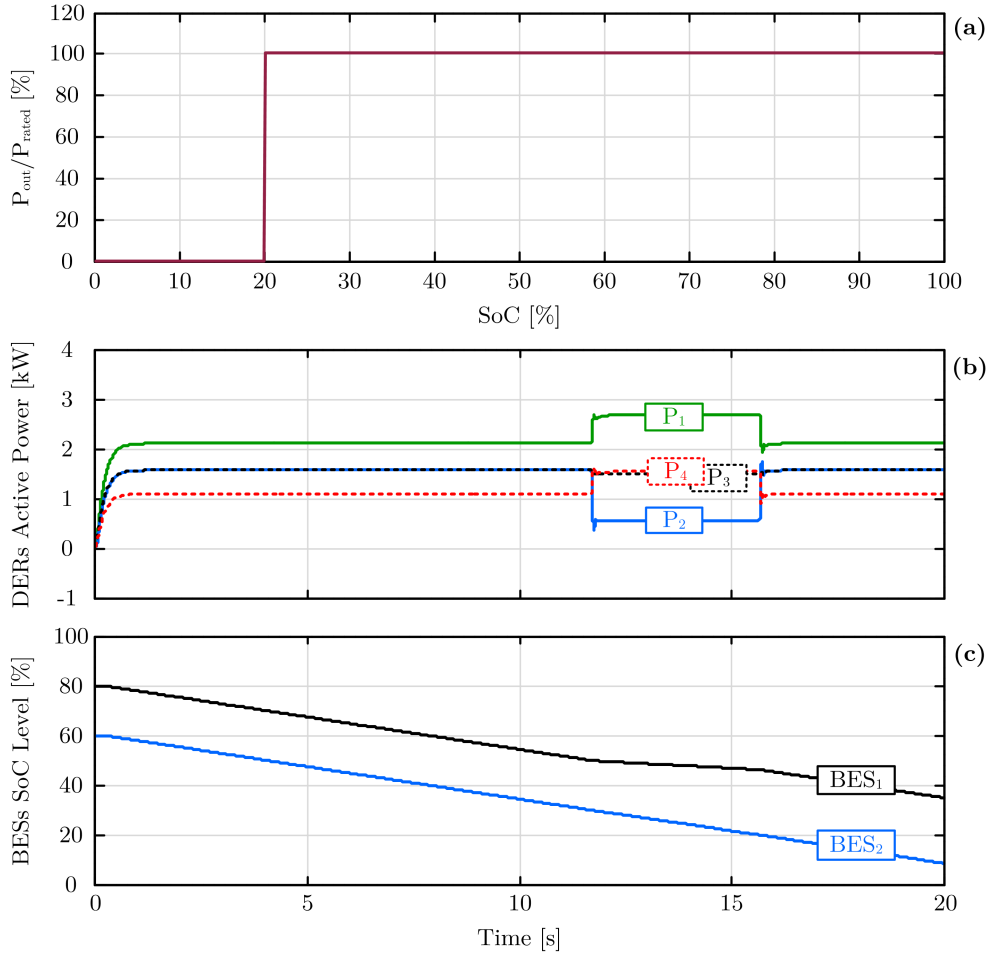


Figure 4.16: Simulation results of Case-5.3

4.6 Conclusions

A new hierarchical power management strategy for an autonomous MG with multiple DERs (i.e. including BES and RES units) is proposed in this chapter. The proposed strategy aims to coordinate the BES and RES units in a centralized manner. The comprehensive control structure of the BESs consists of two control subsystems where each subsystem is applied to the BES units depending on their operation mode, (i.e. charging or discharging mode). The main objective of the proposed comprehensive control of the BESs in discharge mode is to avoid premature depletion of the BES units as they contribute in supplying the load. Therefore, the BESs output active powers are modified accordingly as their SoC levels decrease. Another objective of the proposed SoC-based droop control is to modify the output power of each BES according to its own SoC level and regardless of the other units status. To achieve this, the SoC data of the BESs

is collected by the MGCC where the required modifications in the output power of the RESs are decided accordingly and transferred to their primary controllers. Additionally, in discharge mode, in order to use the BES converter capacity and to avoid overloading the RES units, a new reactive power sharing algorithm is employed for the DERs. Based on this algorithm, the BES units with lower SoC or higher unused converter capacity supply a higher amount of reactive power. To facilitate the desired active and reactive power sharing ratios, the virtual impedance-based approach introduced in Chapter 2 is included in the control structure of the BESs converters. Finally, the proposed comprehensive control of the BESs in charge mode aims to limit the power absorption of the BES units to the excess power of the system to ensure the system power balance. For this, the BES reference power in charge mode is decided by the MGCC considering the maximum available power from the RESs and the instantaneous demand. The proposed hierarchical power management strategy is designed and implemented for an autonomous MG with multiple BES and RES units, and the efficacy of the comprehensive control in both charge and discharge mode is verified.

Chapter 5

Autonomous Power Management of Islanded Microgrids with Multiple Energy Storage Systems

5.1 Introduction

Microgrids (MGs) are increasingly becoming popular due to the development of distributed generations (DGs) and power electronic technologies. MGs may operate in either grid-connected or autonomous mode [101],[158],[176]. The power mismatch between the generation and consumption in grid-connected mode is compensated by the grid. However, in the autonomous mode, a reliable power management strategy is required to coordinate all the associated units of the MG while ensuring efficient performance of each unit. From the control point of view, these strategies are categorized as centralized and decentralized depending on the presence or the absence of the microgrid central controller (MGCC).

In the case of centralized control strategies, the MGCC is responsible for collecting the measurements from the MG elements, analysing the received data and finally transferring the processed data through communication links. This requires the system to be equipped with several measurement and communication modules, which may result into system collapse in case of communication failures or even delays. In addition, for the MGs with distributed ESSs, centralized control strategies are not a suitable option due to the system reliability and costs [177, 178],[120].

In some decentralized power management strategies in the literature, the MGCC is replaced with the local controllers, which can communicate with one

another. However, in case of the MGs with multiple distributed units, these strategies become unsuitable. This is due to the complication of the system structure, scalability, and plug and play [179]-[180].

Some other decentralized power management strategies provide autonomous power control to the system. One of the most promising methods that avoids utilizing the MGCC and global/local communication links, is the droop control [181]-[186]. Droop control methods have been extensively employed in the MG power management strategies to enhance the system reliability. In these strategies, the required active power is shared among the DGs based on their capacities and frequency deviations. Therefore, a fixed power sharing ratio is considered for all the constituent units of the MG. However, in the case of renewable energy sources (RESs), the output power capacity is determined by the RES primary source (e.g. photovoltaic or wind generations). Thus, these units are preferably deployed in current control mode (CCM) to operate based on maximum power point tracking (MPPT) algorithms [93],[187]-[189]. Moreover, in the conventional droop control strategies the reference power of all the MG units is determined according to their maximum capacity. Therefore, droop control of the ESSs, which results into voltage control mode (VCM) integration of these units, leads to their premature depletion since their state of charge (SoC) (i.e. available capacity) is not taken into account. Consequently, the ESSs may promptly run out of energy and get disconnected, and in turn, the entire system may collapse due to the lack of back-up.

To overcome the aforementioned drawbacks, this chapter proposes a new decentralized power management strategy which is capable of maintaining the power balance of the MGs with multiple distributed ESSs. The proposed structure is independent from any global and/or local communication links and therefore, performs in an autonomous manner. Moreover, with the proposed power management strategy, the RESs operate in CCM and deliver their maximum available power, while the ESSs supply/absorb the generation and consumption mismatch. Furthermore, the proposed strategy always respects the ESS SoC level, when deciding its mode of operation in order to avoid ESS overcharge and over-discharge. Finally, the ESS control structure provides voltage regulation to the system in case of any voltage sag/swell.

Main features of the proposed power management strategy in this chapter are highlighted below;

- ESS mode of operation is determined based on its SoC level and the system

frequency. This implies that although the system frequency represents the generation and consumption mismatch, the priority is given to the ESS SoC level to decide its mode of operation while the amount of active power reference for each ESS is determined based on the system frequency.

- The system performance is smooth and seamless when the ESS mode of operation changes from charge to discharge or vice versa.
- ESS SoC level is kept within the reliable range while the RES units operate in CCM and deliver their maximum available power.
- The proposed strategy aims to charge the ESSs up to their maximum SoC limit (SoC_{max}) to avoid chattering between charge and discharge modes and to make them available as a backup for a longer time duration.
- The proposed power management strategy can be simply implemented on the existing ESSs of an MG without any need for significant changes in the inner loop control structures.

5.2 System Structure and Control

The stand-alone AC microgrid, shown in Fig. 5.1, consists of a PV system, a droop controlled DER, distributed ESSs, and loads. The PV system contains a unidirectional DC/DC converter and a voltage source converter (VSC), and the ESSs include a bidirectional DC/AC converter. The DER is also interfaced with the point of common coupling (PCC) through its VSC. The control structure of each MG element is explained in the following subsections.

5.2.1 Energy Storage System

The ESS configuration, shown in Fig. 5.2, consists of a battery bank, a bidirectional DC/AC converter and an LC filter. The ESS control structure includes two control loops, aiming to control the active output power and the PCC voltage. The SoC estimation block, estimates the SoC level based on an ampere counting algorithm as;

$$SoC(t) = SoC_{init} + \int_0^t \eta_{ESS} \frac{i_{ESS}(t)}{C_{ESS}} .dt \quad (5.1)$$

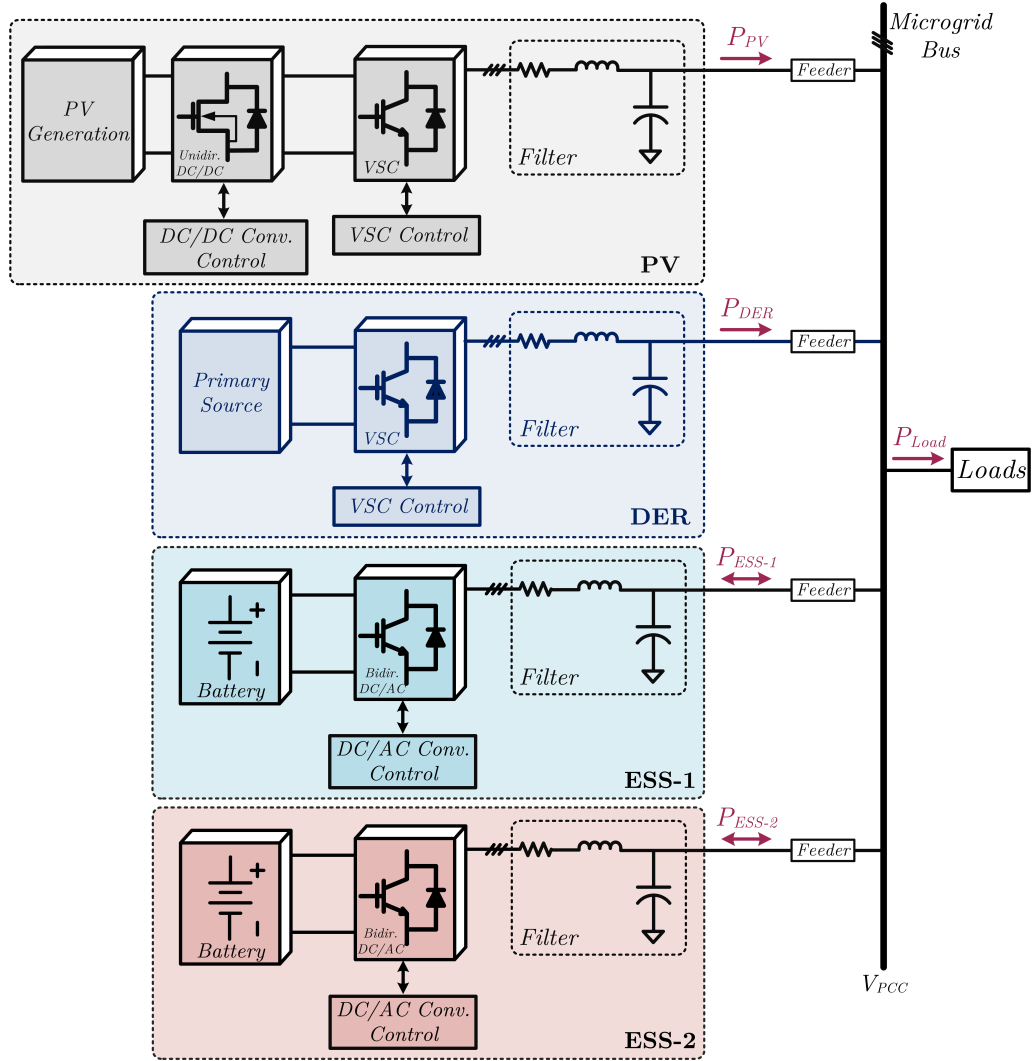


Figure 5.1: Stand-alone microgrid configuration with multiple ESSs, PV, DER and loads.

where, SoC_{init} is the initial SoC level, η_{ESS} is the charge/discharge efficiency, i_{ESS} is the ESS current, and C_{ESS} is the ESS capacity. More detailed algorithms can also be used as presented in [190, 191].

The reference power generation block, monitors the system frequency and the estimated SoC and determines the ESS mode of operation as well as the amount active power reference. This block performs based on the proposed algorithm which will be explained in detail in Section 3. A proportional-integral (PI) controller is used for both control loops in order to match the actual values of the ESS (i.e. output active power and the PCC voltage) with their references. Lastly, hysteresis modulation is utilized to generate the switching signals for the DC/AC

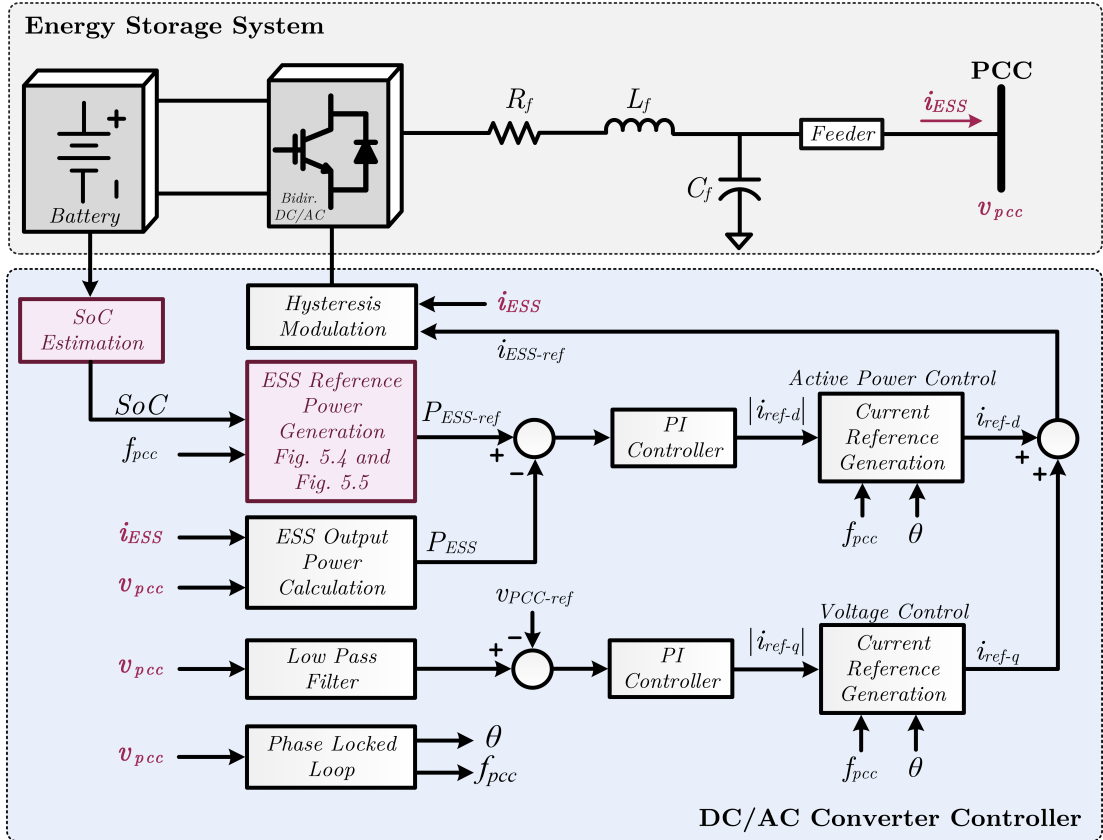


Figure 5.2: Energy storage system configuration and its control structure.

converter of the ESS system.

5.2.2 Photovoltaic System

The PV system including DC/DC and DC/AC converters, an LC filter, and its control structure is shown in Fig. 5.3. The PV system operates under CCM based on MPPT algorithm [192]. The Perturb and observation method is utilized for the MPPT block to extract the maximum power from the PV and to control the unidirectional DC/DC converter. A proportional-integral (PI) controller is utilized as a voltage controller to adjust the DC link voltage. Finally, the hysteresis modulation block generates the switching signals for the VSC.

5.2.3 Distributed Energy Resource

A droop controlled distributed energy resource (DER) is connected to the MG bus through a voltage source converter (VSC). It is worth noting that utilizing more than one DER would not affect the proposed power management strategy.

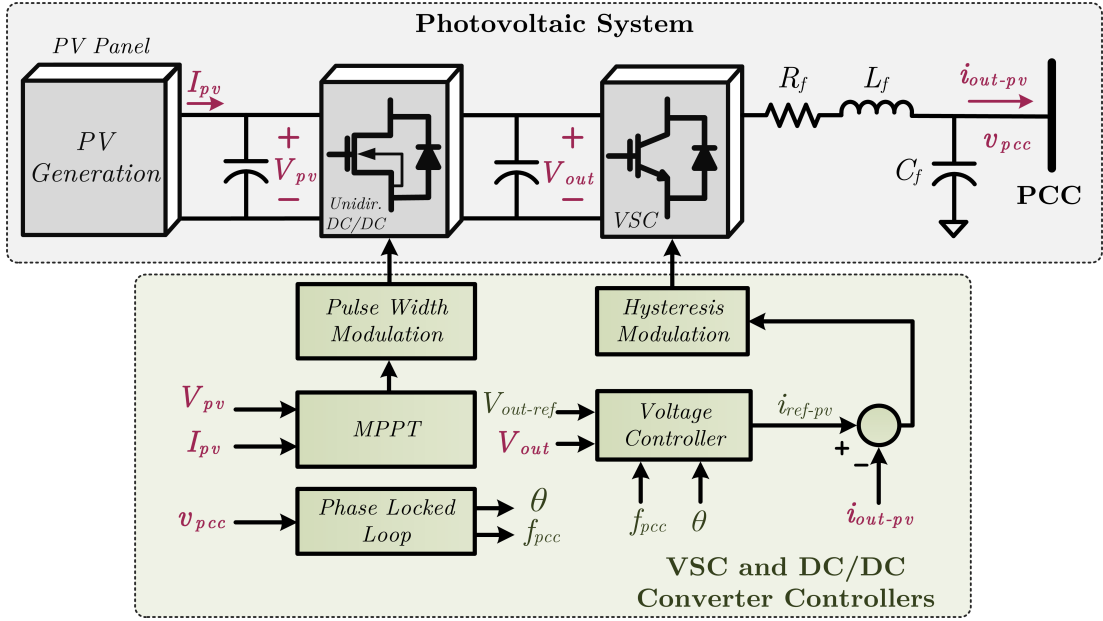


Figure 5.3: Photovoltaic system configuration and its control structure.

The VSC and its filter system are connected to the point of common coupling (PCC) through a coupling inductance of L_c (included in the feeder inductance shown in Fig. 5.1). Frequency and voltage droop equations for the DER unit are expressed as [148],

$$\begin{aligned} f &= f_{rat} - m(P - P_{rat}) \\ V &= V_{rat} - n(Q - Q_{rat}) \end{aligned} \quad (5.2)$$

where, f and f_{rat} are the PCC frequency and the rated frequency of the system. Also P and P_{rat} are the average and the rated active power of the DER. In the voltage droop equation, V and V_{rat} are the voltage of the filter capacitance (C_f) and the rated voltage of the DER. Also, Q and Q_{rat} are the average and the rated reactive power of the DER. Finally, m and n coefficients are calculated as,

$$\begin{aligned} m &= \frac{2\Delta f}{P_{rat}} \\ n &= \frac{\Delta V}{Q_{rat}} \end{aligned} \quad (5.3)$$

where, Δf and ΔV are the frequency and the voltage bands, respectively. In this study Δf is considered to be 0.5 Hz, and ΔV is 5% of the system rated voltage.

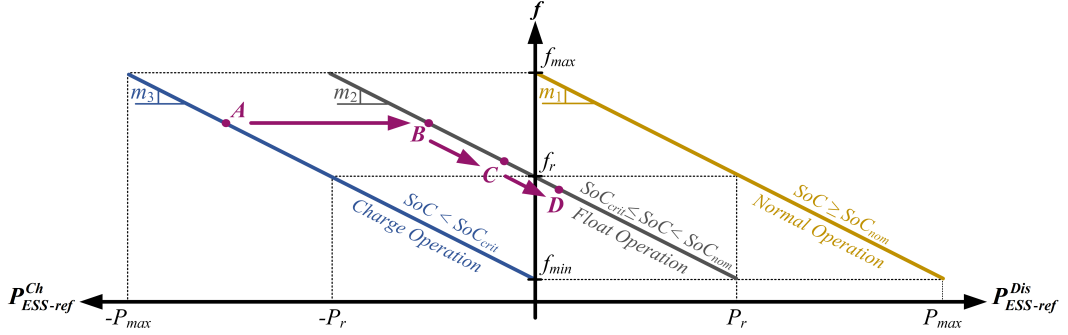


Figure 5.4: ESS reference power generation in association with the ESS SoC level and the system frequency.

5.3 Proposed Autonomous Power Management Strategy

The proposed autonomous power management strategy, which is included in the ESS reference power generation block of Fig. 5.2, determines the operation mode of the ESSs as well as the amount of active power reference for each ESS. This strategy aims to control the system power balance while utilizing all the MG constituent units effectively. For this, the reference power generation block gives the priority to the SoC level of the ESS to select its mode of operation. Then, the amount of reference power is determined based on the system frequency, which represents the power mismatch between the generation and consumption. Hence, the system power balance is always realized while ESS overcharge/over-discharge is avoided.

5.3.1 ESS Reference Power Generation

Based on the proposed power management strategy three different operating conditions are probable for the ESSs depending on their SoC level;

- **Normal Operation (force discharge):** This condition occurs when the ESS SoC level is above the nominal value ($SoC \geq SoC_{nom}$) indicating that the ESS has enough available charge to contribute in supplying the load. Therefore, the ESS reference power is calculated based on the right-hand side characteristic (normal operation characteristic) of Fig. 5.4. Note that the amount of reference power depends on the frequency. As an example, ESS discharges with its maximum capacity (P_{max}) when the system

frequency drops to its minimum limit (f_{min}) representing high levels of demand. Whereas, for $f = f_{max}$, the ESS active output power drops to zero due to low demand.

- **Float operation (charge/discharge):** This condition is for the SoC values between the critical and the nominal values ($SoC_{crit} \leq SoC < SoC_{nom}$) representing that the ESS can operate either in charge or in discharge mode. Thus, the ESS reference power is calculated based on the middle characteristic (float operation characteristic) of Fig. 5.4. From this characteristic, for the system frequencies lower than the rated value ($f < f_r$), which represent high levels of demand, the ESS operates in discharge mode. Whereas, for the frequencies higher than the rated frequency ($f > f_r$) the ESS switches to charge mode as the demand is low. Also, when the system frequency is equal to its rated value the ESS stops charging/discharging, since no power mismatch is detected between the generation and consumption. It is worth noting that the maximum charge and discharge reference power (P_r) in Fig. 5.4 is considered to be half of the ESS maximum capacity (P_{max}) to reduce the rate of charge/discharge and to avoid prompt depletion of the ESSs.
- **Charge operation (force charge):** This condition occurs when the ESS SoC level is below its critical value ($SoC < SoC_{crit}$) indicating that the ESS is in risk of over-discharge. To avoid this, the power management structure deliberately switches the ESS to charge mode while the reference power is calculated based on the left-hand side characteristic (charge operation characteristic) of Fig. 5.4. As shown in this characteristic, the reference power varies between zero and the maximum capacity of the ESS ($-P_{max}$) depending on the demand variations. Hence, the system power balance is never compromised as the ESS power absorption can be adjusted to zero in case of high demands.

The ESS reference power for the above conditions can be calculated as follows,

$$P_{ref-ESS} = \begin{cases} (f_r - f)/m_1 + P_r, & \text{if } SoC \geq SoC_{nom} \\ (f_r - f)/m_2, & \text{if } SoC_{crit} \leq SoC < SoC_{nom} \\ (f_r - f)/m_3 - P_r, & \text{if } SoC < SoC_{crit} \end{cases} \quad (5.4)$$

where,

$$m_1 = m_2 = m_3 = 2 \frac{\Delta f}{P_r}$$

According to [193], to protect the battery it is necessary to choose a higher value

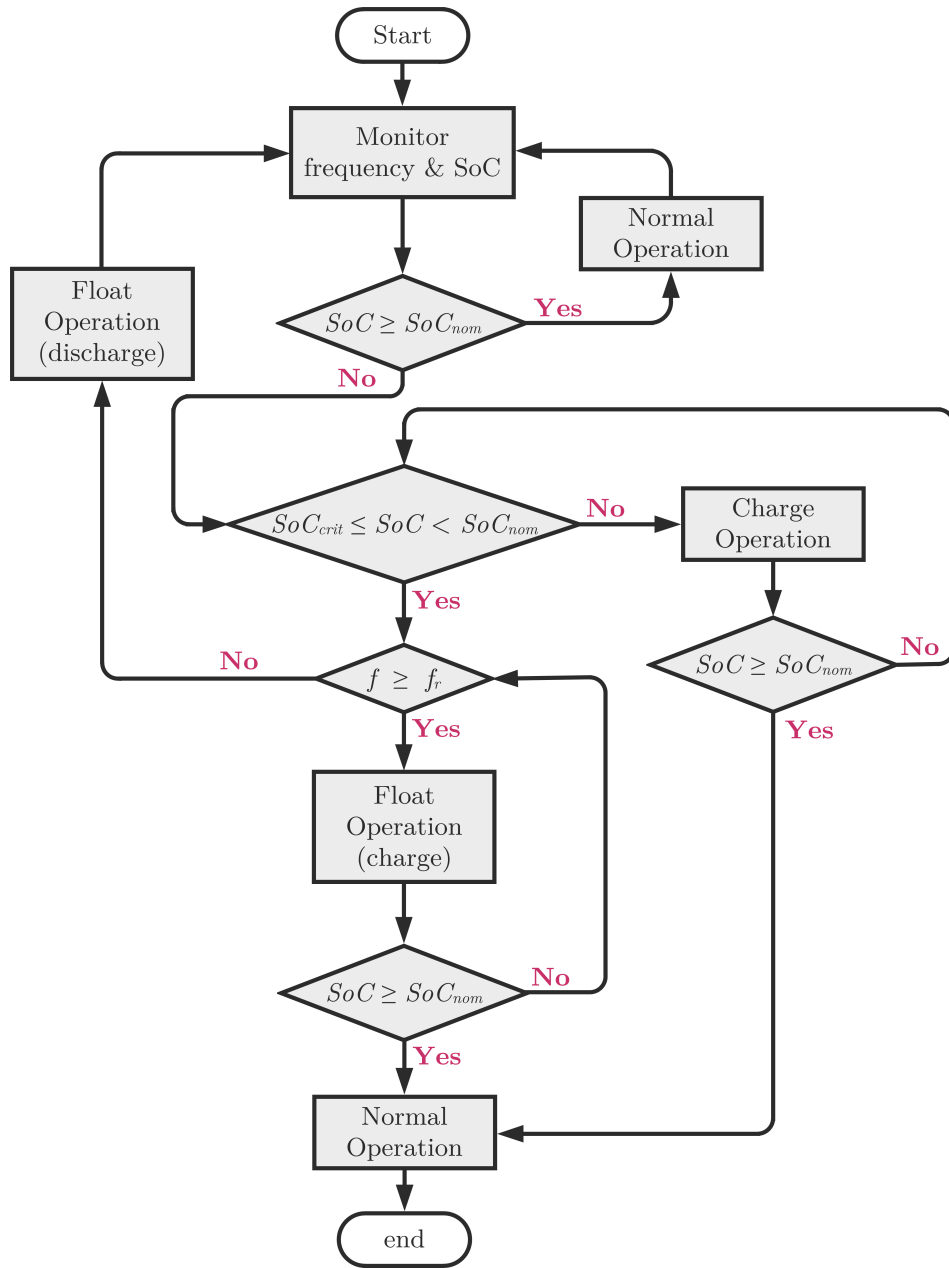


Figure 5.5: Proposed algorithm to decide the ESS operation mode.

for SoC_{crit} compared to the SoC value which reflects the batteries end-voltage. Moreover, the maximum and minimum margins (i.e. SoC_{max} and SoC_{crit}) should be determined based on specific applications of the batteries. A more detailed study on selection of batteries maximum and minimum SoC margins can be found in [194]. In this study, SoC_{nom} and SoC_{crit} are considered to be 50% and 30%, respectively. Note that variation of these SoC margins according to the system requirements would not affect the performance of the proposed strategy.

5.3.2 Proposed Algorithm to Decide the ESS Operation Mode

As mentioned previously the proposed power management strategy aims to charge the ESSs up to their maximum SoC limit (SoC_{max}) without interfering with the system power balance. This is to assure that the ESS is always available in the nominal condition and can operate as a backup in case of load increase. Another objective of this approach is to minimize the number of switching between the charge and discharge modes; and hence, to avoid chattering which may occur in some specific conditions. To achieve this, the proposed power management strategy employs an algorithm which can smoothly switch between the three defined characteristics of Fig. 5.4 without affecting the system performance.

Fig. 5.5 shows the proposed algorithm for deciding the ESS mode of operation. The system frequency and the SoC level of the related ESS are the only parameters which are monitored by this algorithm. This implies that the operation mode of each ESS is determined independent from the other ESSs status. Hence, no communication is required between the ESSs. The performance of the algorithm is described below.

Initially, the proposed algorithm, which is implemented in the control structure of the ESS converters, monitors the system frequency and the estimated SoC level of the related ESS. If the SoC is above the nominal value ($SoC \geq SoC_{nom}$), the ESS operates in normal condition and proceeds to discharge based on the normal characteristic of Fig. 5.4, represented as the first boundary of (5.4). In this case, the ESS active power reference varies between zero and the maximum capacity of the ESS (P_{max}) according to the load variations reflected by the system frequency.

If the SoC is not within the above range the algorithm checks whether the SoC is between the critical and nominal values ($SoC_{crit} \leq SoC < SoC_{nom}$). If this is the case, deciding the ESS mode of operation is assigned to the system frequency where two conditions may occur based on the normal characteristic of Fig. 4 (represented as the second boundary of (5.4));

- $f < f_r$: From this characteristic, it is visible that for the frequencies lower than the rated frequency ESS operates in discharge mode, and its reference power varies between zero and P_r (i.e. half of its maximum capacity) depending on the system frequency. The main objective of the control strategy in this mode is to limit the discharge rate of the ESS and to prevent

premature depletion. This condition is presented in the second equation of (5.4).

- $f > f_r$: For the frequencies higher than the rated value, the ESS operates in charge mode, and its absorbing power varies between $-P_r$ and zero according to the load variations. In this condition, based on the above algorithm, the ESS continues to be charged as long as its SoC level has not reached its maximum margin (SoC_{max}). Meanwhile, to avoid interfering with the system power balance the algorithm continuously monitors the system frequency to assure that the ESS is not required to switch to discharge mode. If at any stage, the system frequency reflects the load increase (i.e. $f < f_r$), the ESS is instantly switched to discharge mode but continues to operate based on the float characteristic of Fig. 5.4 as described above.

Finally, if the SoC is below the critical value ($SoC < SoC_{crit}$), the algorithm compels the ESS to switch to charge mode where the ESS reference power is decided based on the charge characteristic of Fig. 5.4 (represented as the third boundary of (5.4)). Similar to the previous case, the ESS continues to be charged until its SoC level reaches the maximum limit (SoC_{max}). Meanwhile, the algorithm continuously monitors the frequency and deliberately switches the ESS operation to discharge mode if the frequency variations represent a higher amount of consumption compared to the generation.

5.4 Simulation Results

To verify the efficacy of the proposed power management strategy, the stand-alone MG system of Fig. 5.1 is simulated for four different case studies. Each case study verifies the smooth and efficient performance of the proposed strategy while the ESSs switch from one operation condition to another based on the three predefined characteristics. Simulations are carried out in PSCAD/EMTDC and the data of the simulated system is given in the Appendix C Table C.1.

5.4.1 Case-1: Overall Performance of the System

In this case study five different scenarios are considered to investigate the overall performance of the proposed power management strategy as different operation conditions occur for each ESS. The PV system operates in CCM and delivers its maximum available power of 30 [kW].

Scenario S_1 : During this scenario, only the PV and the DER are supplying the load as the ESSs are inactive. A constant load of 40 [kW] and 10 [kVar] is applied to the system. As seen from Figs. 5.6(a) and 5.6(b), load active and reactive powers slightly deviate from the expected values since no voltage support is provided in the absence of the ESSs. This can be observed in Fig. 5.6(g) which shows that the PCC voltage is above the rated voltage of 239.6 [V]. Also, Fig. 5.6(f) indicates constant SoCs of both ESSs.

Scenario S_2 : In this scenario, the load remains the same as in S_1 , while both ESSs are activated with initial SoC levels of $SoC_{init-1}=15\%$ and $SoC_{init-2}=84\%$ (see Fig. 5.6(f)). This causes the proposed algorithm to deploy ESS-1 and ESS-2 in charge operation mode (based on charge characteristic of Fig. 5.4) and normal operation mode (based on normal characteristic of Fig. 5.4), respectively, as described in Section 3. This is confirmed by Figs. 5.6(d) and 5.6(e), where ESS-1 absorbs 11.8 [kW], and ESS-2 delivers 8.2 [kW] based on (5.4). Also, Fig. 5.6(f) shows the SoC levels of the ESSs, which both vary accordingly. Lastly, Fig. 5.6(g) indicates the PCC RMS voltage, which is regulated to its rated value of 239.6 [V] in the presence of ESSs. Moreover, the load active and reactive power deviations are also compensated as the voltage is restored (see Figs. 5.6(a) and 5.6(b)).

Scenario S_3 : In this scenario, the SoC level of ESS-1 hits its critical limit (SoC_{crit}) and therefore, its operating point is switched to the float characteristic of Fig. 5.4. To clarify this, an example of the operating point movement between two characteristics is shown in Fig. 5.4. As the frequency remains above the rated value ($f > f_r$), ESS-1 continues to charge but with a lower rate since its operating point moves from point A (i.e. operating point of S_2) to B (i.e. operating point of S_3). With the total decrease of the power consumption during S_3 , the DER output power reduces and the system frequency slightly steps up causing ESS-2 to reduce its rate of discharge while still operating based on the normal characteristic of Fig. 5.4. Fig. 5.6(f) indicates the SoC variations which concurs with the above statements. From Fig. 5.6(g), the PCC voltage remains constant as the ESSs provide the required voltage support.

Scenario S_4 : In this scenario, the load increases from 40 [kW] and 10 [kVar] to 50 [kW] and 12 [kVar]. With the total consumption increase, the system frequency decreases to 50.09 [Hz] and the DER output power steps up (see Figs. 5.6(a) and 5.6(c)). Thus, based on the proposed algorithm and considering the overall increase of the demand, ESS-1 continues to charge in float condition but with a lower charge rate. This procedure is shown in Fig. 5.4 by moving the operating point from B to C . Fig. 5.6(d) confirms the variations of the reference

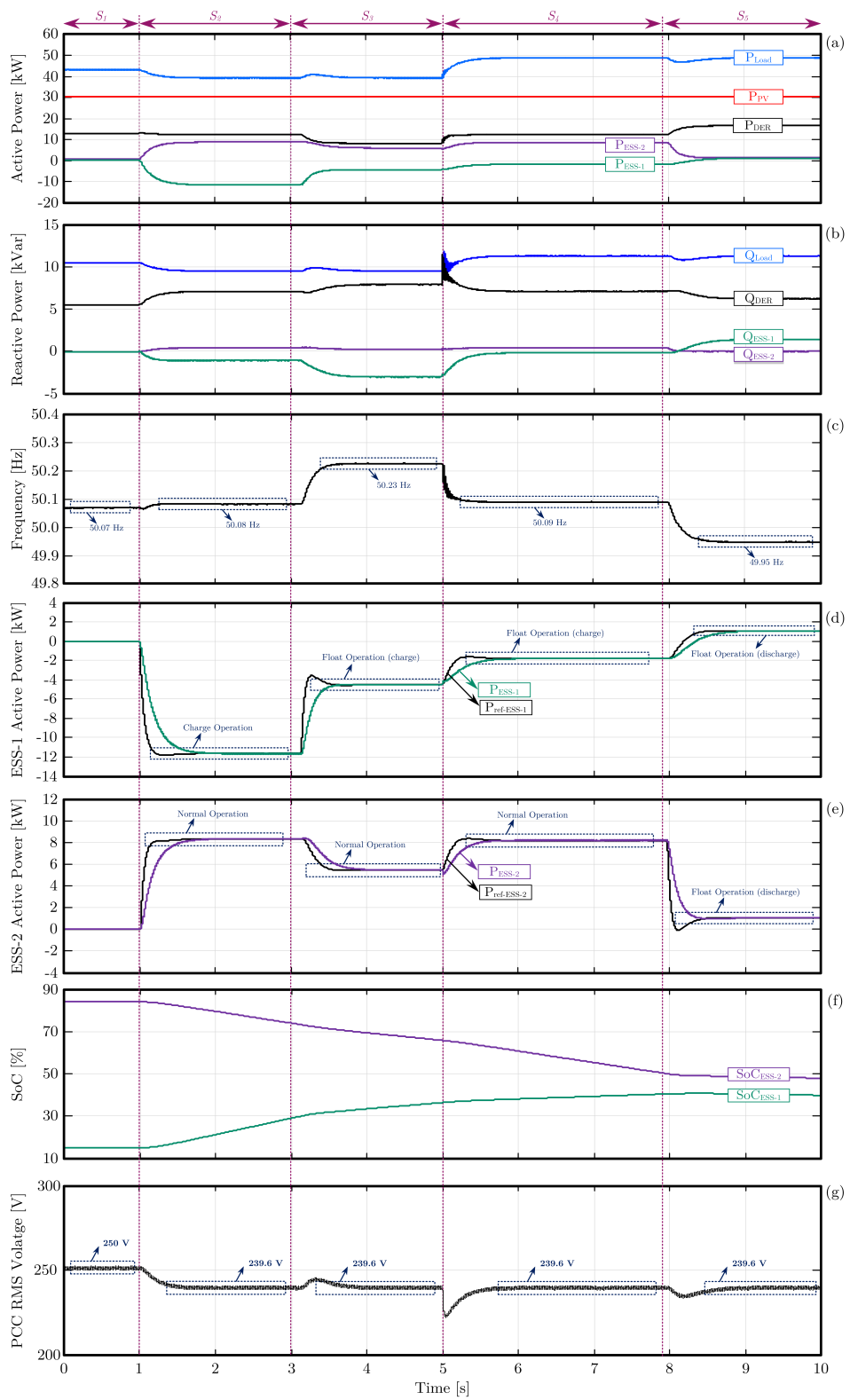


Figure 5.6: Case 1 results: overall performance of the system.

and actual active powers of ESS-1. Moreover, ESS-2 rate of discharge is increased while it continues to operate under normal condition as can be seen in Figs. 5.6(e) and 5.6(f).

Scenario S_5 : In this scenario, the SoC level of ESS-2 reduces to the values below its nominal value ($SoC_{nom}=50\%$) causing the total generation of the system to decrease. Thus, the system frequency becomes lower than the rated frequency ($f < f_r$) (see Figs. 5.6(c) and 5.6(f)). As a result, ESS-1 operating point moves further along with the middle characteristic of Fig. 5.4 (shown as point D), where it starts to operate in discharge mode (see Figs. 5.6(d)). Fig. 5.6(f) confirms that both ESSs are now discharging with a very slow rate.

5.4.2 Case-2: ESS Switching from Charge to Discharge

This case study, investigates the performance of the proposed strategy when the ESSs switch between charge and discharge modes. Same as Case 1, five different scenarios are considered and the PV system delivers its maximum available power of 30 [kW]. During the first scenario, the ESSs are inactive. Hence, the performance of the system in this scenario is similar to S_1 of the previous case and is not repeated here.

Scenario S_2 : During this scenario, both ESSs are activated with the initial SoC levels of $SoC_{init-1}=49\%$ and $SoC_{init-2}=61\%$ (see Fig. 5.7(f)). From Fig. 5.7(a), the load power steps up to 40 [kW], as the ESSs restore the voltage. Fig. 5.7(b) indicates that during S_2 , the system frequency is above the rated value ($f > f_r$) due to the low demand. Considering the above conditions and based on the proposed algorithm, ESS-1 proceeds to operate in float condition while absorbing 4.5 [kW] as shown in Fig. 5.7(c). Also, ESS-2 performs under normal condition delivering 5.5 [kW] to the system as indicated in Fig. 5.7(d). Fig 5.7(e) approves the above statements since the SoC levels vary accordingly.

Scenario S_3 : In this scenario, the load decreases to 30 [kW] which is equal to the maximum available power from the PV (P_{MPP}). Thus, the system frequency increases to 50.34 [Hz], and the DER unit generates less power. Consequently, ESS-1 rate of charge increases and absorbs 6.7 [kW]. Also, ESS-2 delivers less power of 3.2 [kW] since the overall consumption of the system is decreased. Lastly, Fig. 5.7(e) concurs the above statements showing the SoC variations of each unit.

Scenario S_4 : In this scenario, load suddenly increases from 30 [kW] to 58 [kW]. As a result, the system frequency drops below its rated value ($f < f_r$), and the DER power steps up. Thus, based on the algorithm of Fig. 5.5, ESS-

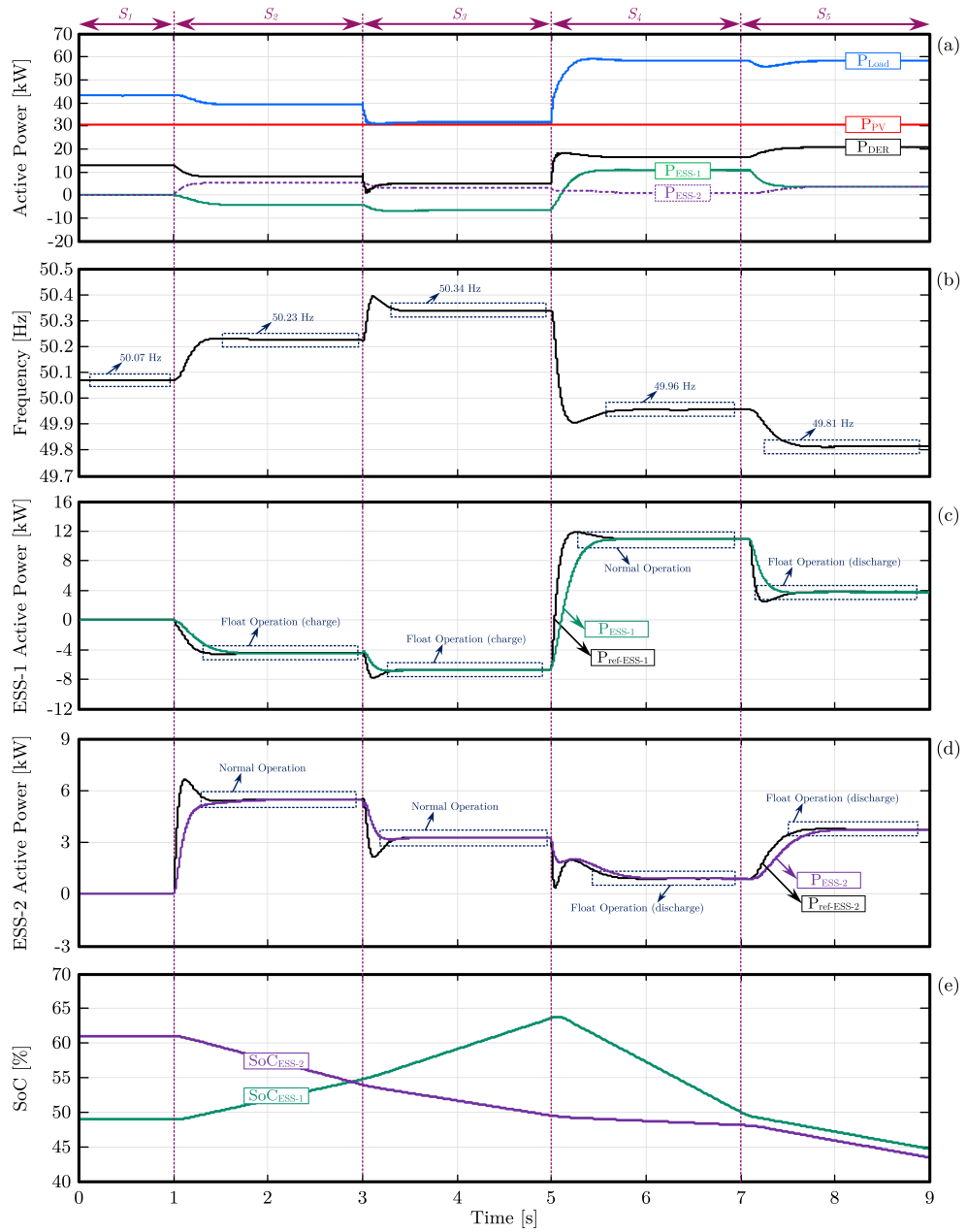


Figure 5.7: Case 2 results: switching from charge to discharge.

1 switches to normal operation mode, although its SoC level has not reached its maximum limit (SoC_{max}). This is visible in Fig. 5.7(b) as ESS-1 is now delivering 10.9 [kW]. From Fig. 5.7(e), ESS-2 SoC level becomes lower than its nominal value (SoC_{nom}). As a result, its operating point switches to the float characteristic of Fig. 5.4 which results into a lower discharge rate. The output power variations of the ESSs can also be confirmed by their SoC level changes shown in Fig. 5.5(e).

Scenario S_5 : In the last scenario, ESS-1 SoC level becomes lower than its nominal limit (SoC_{nom}), and its operating point switches to the float characteristic of Fig. 5.4. This results into reduction of the system total generation, which in turn, causes the system frequency to decrease. Accordingly, ESS-2 operating point moves along with the middle characteristic of Fig. 5.4 forcing this unit to deliver more power to the system. Furthermore, following the frequency drop, the DER unit delivers more power. Fig. 5.7(e) indicates that the rate of discharge for ESS-1 is decreased while that of ESS-2 is increased.

5.4.3 Case-3: Solar Radiation Mitigation

This case study investigates the system performance when the solar radiation mitigates. Among the five considered scenarios the first scenario is not explained as it is only presented to show the activation of the ESSs.

Scenario S_2 : In this scenario, the PV output power (P_{MPP}) is 30 [kW], and the ESSs are activated with the initial SoC levels of $SoC_{init-1}=70\%$ and $SoC_{init-2}=42\%$ (see Fig. 5.8(f)). With the constant load of 40 [kW], the system frequency is higher than the rated frequency ($f > f_r$). This causes ESS-1 to operate in normal condition (since $SoC_{init-1} > SoC_{nom}$) while ESS-2 operates in float condition absorbing 4.5 [kW] (since $SoC_{init-2} < SoC_{nom}$) as shown in Figs. 5.8(c) and 5.8(d).

Scenario S_3 : In this scenario, it is assumed that the solar radiation decreases by 50% resulting to P_{MPP} of 15 [kW]. With the total generation decrease, the system frequency drops to its rated value ($f = f_r$) as indicated in Fig. 5.8(b). Consequently, ESS-1 operating point moves along with the normal characteristic of Fig. 5.4 where it continues to discharge with a higher rate, as shown in Fig. 5.8(c). Also, the DER delivers more power to the system (see Fig 5.8(a)). Fig. 5.8(d) indicates that ESS-2 neither delivers nor absorbs power to/from the system as it is operating in float condition (the middle characteristic of Fig. 5.4), and the frequency is equal to the rated frequency. From Fig. 5.8(a), the load remains constant indicating that the voltage regulation is not affected, although ESS-2 active power output is reduced to zero.

Scenario S_4 : At the beginning of S_4 , ESS-1 SoC level becomes lower than SoC_{nom} (see Fig. 5.8(e)) causing its output power to reduce. With the total generation decrease, the system frequency drops below the rated frequency. Hence, ESS-2 switches to discharge mode while still operating on the float characteristic as shown in Fig. 5.8(d). Additionally, the DER generation increases with the

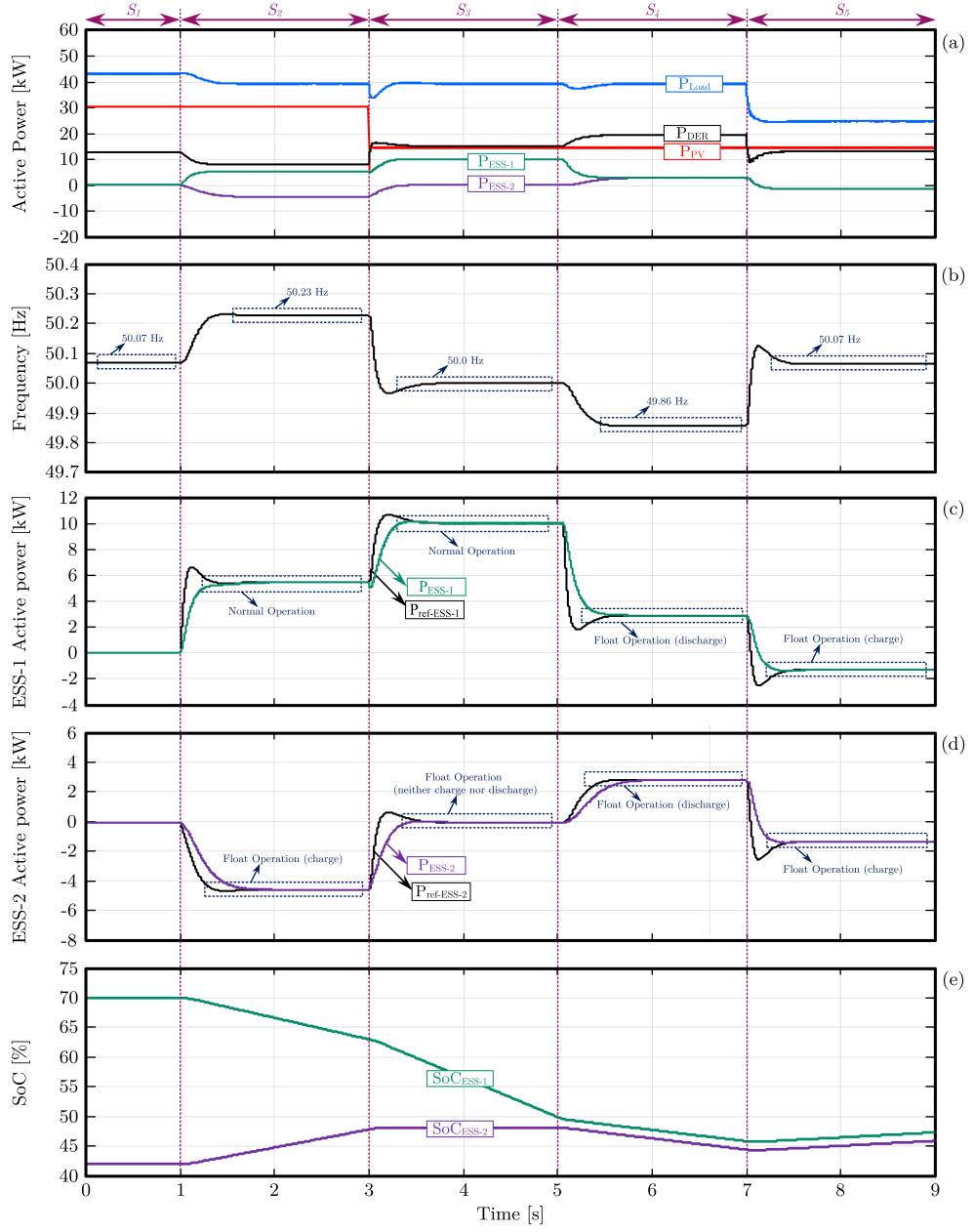


Figure 5.8: Case 3 results: solar radiation mitigation.

frequency decrease as shown in Fig. 5.8(a).

Scenario S_5 : In this scenario, it is assumed that the load is decreased from 40 [kW] to 25 [kW] causing the system frequency to go slightly above the rated frequency and the DER power to decrease. As a result, both ESSs operate based on the float characteristic of Fig. 5.4 and proceed to charge with the same rate since their SoC levels are both between the critical and the nominal margins ($SoC_{crit} < SoC_{ESS-2} < SoC_{ESS-1} < SoC_{nom}$).

5.4.4 Case-4: Demand Lower than the PV Generation and ESS Disruption

This case study investigates the system performance when the load power becomes lower than the maximum available power from the PV (P_{MPP}) and one of the ESSs gets disrupted. Note that the first scenario is similar to that of Case 1, and is not repeated here.

Scenario S_2 : In this scenario, a constant load of 40 [kW] is applied to the system and P_{MPP} is assumed to be 30 [kW]. Both batteries are activated with the initial SoC levels of $SoC_{init-1}=80\%$ and $SoC_{init-2}=31\%$ (see Fig. 5.9(e)). With the system frequency above the rated value, ESS-1 operates in normal condition and delivers 5.5 [kW] while ESS-2 performs in float condition and absorbs 4.5 [kW] as shown in Figs. 5.9(a), 5.9(c) and 5.9(d). Fig. 5.9(f) indicates that with the activation of the ESSs, the PCC voltage is regulated to its rated value.

Scenario S_3 : During S_3 , load power drops to 20 [kW] which is lower than P_{MPP} . Hence, the system frequency rises to its maximum limit ($f_{max}=50.5$ [Hz]). Following this, the output power of the DER and ESS-1 become zero while ESS-2 charge rate increases forcing this unit to absorb the power mismatch between the PV and the demand (10 [kW]). As shown in Fig. 5.9(e), ESS-1 is neither charged nor discharged since its SOC level remains constant. Whereas, ESS-2 charges with a higher rate during S_3 compared to S_2 .

Scenario S_4 : In this scenario, it is assumed that ESS-2 is disrupted; and hence, disconnected from the system. Meanwhile, the load power increases to 44 [kW]. Thereby, the total demand increases whereas the total generation is reduced. This causes the system frequency to drop to 50.22 [Hz]. As a result, DER and ESS-1 output powers increase from zero to 8.31 [kW] and 5.54 [kW], respectively. Moreover, ESS-2 output power drops to zero although its reference power is -4 [kW]. SoC variations shown in Fig 5.9(e), also confirm the above statements. Lastly, Fig. 5.9(f) illustrates that the PCC voltage remains constant since ESS-1 is still connected to the system.

Summary of the operation conditions for each of the ESSs in the above four case studies is given in Table 5.1 and Table 5.2.

5.5 Conclusions

A new decentralized power management strategy is proposed in this chapter which is specifically designed to maintain the power balance of the MGs

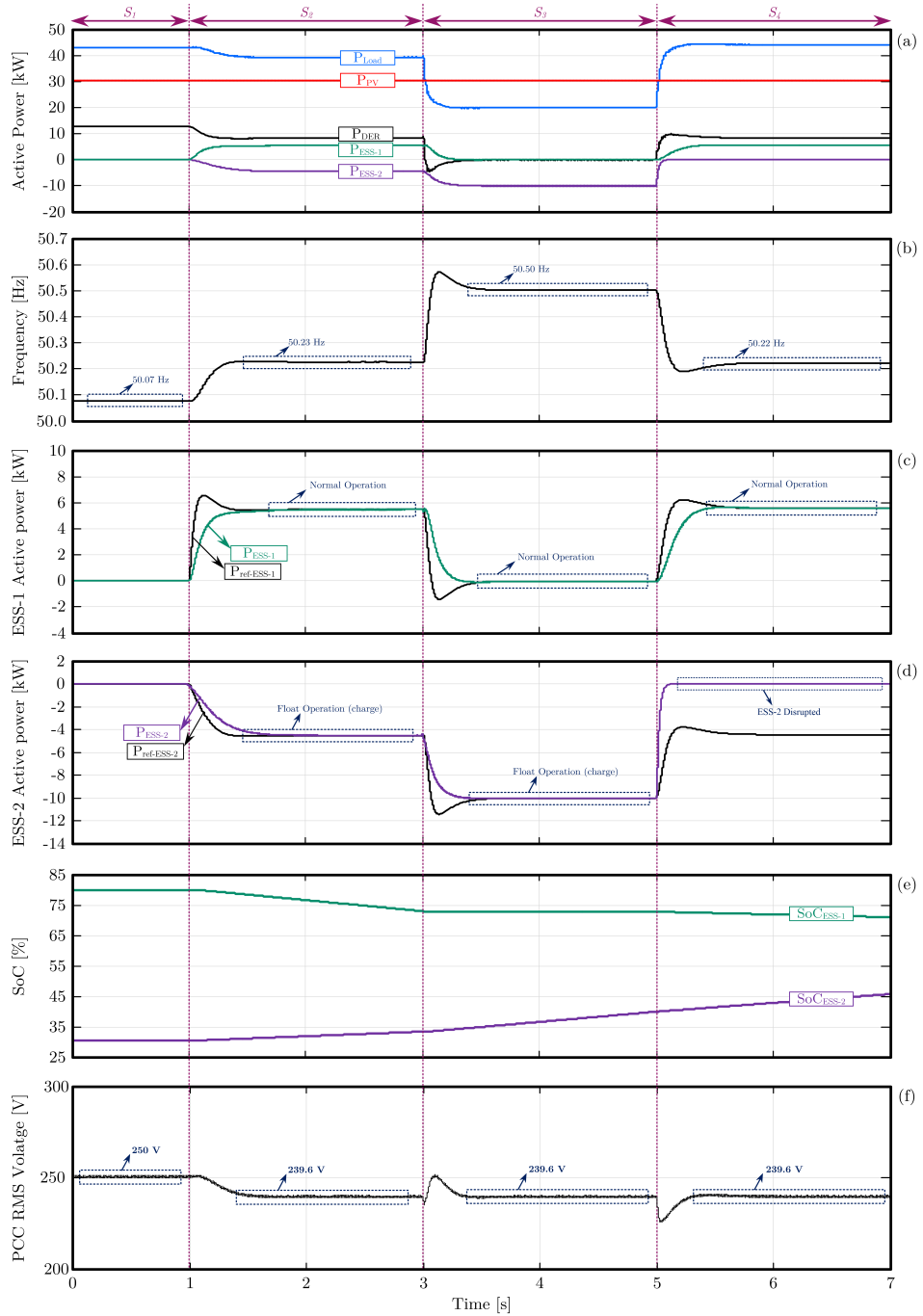


Figure 5.9: Case 4 results: demand lower than the PV generation and ESS disruption.

including multiple distributed ESSs. The proposed structure is independent from any global and/or local communication links; and therefore, performs in an autonomous manner. Based on the proposed power management strategy, the RES units operate in current control mode, and deliver their maximum available power while the ESSs supply/absorb the generation and consumption mismatch. Fur-

Table 5.1: ESSs operation conditions for Case 1 and Case 2

<i>Scenario</i>	<i>Operation Condition</i>			
	<i>Case 1</i>		<i>Case 2</i>	
	ESS-1	ESS-2	ESS-1	ESS-2
S_1	Inactive	Inactive	Inactive	Inactive
S_2	Charge	Normal	Float (charge)	Normal
S_3	Float (charge)	Normal	Float (charge)	Normal
S_4	Float (charge)	Normal	Normal	Float (discharge)
S_5	Float (discharge)	Float (discharge)	Float (discharge)	Float (discharge)

Table 5.2: ESSs operation conditions for Case 3 and Case 4

<i>Scenario</i>	<i>Operation Condition</i>			
	<i>Case 3</i>		<i>Case 4</i>	
	ESS-1	ESS-2	ESS-1	ESS-2
S_1	Inactive	Inactive	Inactive	Inactive
S_2	Normal	Float (charge)	Normal	Float (charge)
S_3	Normal	Float (-)	Normal	Float (charge)
S_4	Float (discharge)	Float (discharge)	Normal	Float (charge)
S_4	Float (charge)	Float (charge)	-	-

thermore, the proposed strategy always respects the ESS SoC level when deciding its mode of operation to avoid ESS overcharge and over-discharge. Also, the ESS control structure is designed to provide the required voltage support to the system in case of voltage deviations. Based on the proposed method, ESS operation mode is determined according to its SoC level and the system frequency. This implies that although the system frequency represents the generation and consumption mismatch, the priority is given to the ESS SoC level to decide its mode of opera-

tion while the amount of active power reference for each ESS is determined based on the system frequency. The simulation results verify the robust and reliable performance of the proposed strategy in different operation conditions.

Chapter 6

Decentralized Power Management of an Islanded PV-Diesel Microgrid with Battery Energy Storage

6.1 Introduction

Decentralized configurations in the form of standalone microgrids (MGs) are considered as an attractive solution for power generation of remote areas such as hilly regions or villages since they are more cost-effective in comparison to the extensions of the existing grid. MGs in general consist of several distributed generators (DGs), including dispatchable and non-dispatchable ones, energy storage systems (ESSs) and loads which may operate either in grid-connected mode or islanded mode [158]. Photovoltaic (PV) and wind turbine power generations are the most common renewable energy sources (RESs) utilized in MGs. Due to the intermittent nature of the power supplied by these RESs, it is mandatory to adopt a power management strategy that coordinates the ESSs such as battery energy storage (BES) systems with the RES units to avoid power imbalance [57]. To achieve this, it is crucial to control the state-of-charge of the BESs to assure that it is kept within the reliable range and batteries can operate as a back-up in charge/discharge mode whenever necessary [195].

Different power management strategies have been investigated in the literature. In the conventional strategies, the ESSs are designed to deliver/absorb the power mismatch (deficit/surplus) between the generation and consumption

during peak/off-peak periods [97],[196]. However, these strategies are not favorable if the batteries state of charge (SoC) is not considered. This is due to the frequent charge and discharge of the batteries which undeniably reduces the batteries life-time.

Centralized control structures are the most popular power management strategies which are widely used for the state of charge control of the batteries in the islanded MGs [178]. A centralized control method is proposed in [179] which controls the BES units by modifying their output powers according to their SoC level variations. The main disadvantage of this approach is that it is only feasible when dispatchable sources such as diesel generators are available in the system. However, these sources are not included in most of stand-alone MGs. In the stand-alone MGs with only non-dispatchable sources, where the micro-sources are controlled based on maximum power point tracking (MPPT) algorithms, the RESs may not be always able to deliver the required power of the BESs as dictated by their SoC variations. Another disadvantage of the proposed strategy in [179] is the requirement of the microgrid central controller (MGCC) for monitoring the BESs SoC level and transmitting the decided reference power commands to each unit (i.e. ESSs and RESs).

Altogether, the main drawback of centralized control strategies is that they are prone to failure if several distributed units are included in the MG. This is due to the communication network complexity, physical location problems, and plug and play limitations. Therefore, utilizing the centralized control methods may deteriorate the system reliability.

One of the most promising methods that avoids utilizing the central controller and communication links; and in turn, enhances the system reliability is the droop control [197],[153],[198, 199]. Droop control methods have been extensively employed in the MG power management strategies. In these strategies, the required active power is shared among DGs based on their capacities and frequency deviations. However, due to the fluctuations of wind and solar radiation, it is impossible for wind generators and PV systems to deliver a constant output power to the system at all times. In addition, the droop control methods determine the reference power of all the MG units based on their maximum capacity. Therefore, they may lead to premature depletion of the BES units as their available capacity (SoC) is not considered. Hence, droop based strategies are not suitable for control of the BES units.

To address this issue, decentralized control structures are introduced in the literature [200]. These structures combine the advantages of the above strategies,

as the microgrid central controller (MGCC) is removed and the required information is transmitted only among some optional DGs through low-bandwidth communications [201]. Hence, these strategies can avoid the communication network complexity and physical location problems. Thereby, they provide a robust power management to the stand-alone MGs without compromising the system reliability.

In this Chapter, a new decentralized power management strategy is proposed for efficient utilization of a BES unit in a PV-diesel stand-alone MG. Several features of the proposed strategy are highlighted below;

- The proposed strategy uses the system frequency as a signal to determine the operation mode of the MG units.
- In the absence of the diesel generator the proposed method operates in an autonomous manner without any needs for communication links. Whereas, in the presence of the diesel generator the low-bandwidth communication links are required to transfer the reference frequency from the BES to this unit. Hence, in either condition the power management of the MG is established in a decentralized manner.
- The BES system is controlled to be mainly charged by the PV aiming to limit the operation of the diesel generator. Thus, the diesel generator only contributes in charging the battery under a specific condition when the surplus power from the PV is insufficient and the BES unit is about to over-discharge.
- To ensure that the PV system is deployed efficiently, during normal operation of the BES, the PV operates in CCM and delivers its maximum available power.
- In case of BES overcharge, the PV system operates based on power curtailment strategy to adjust its output power with power demand to avoid overcharging of the BES unit.
- The system voltage is always regulated by the BES and in a specific condition when both BES and diesel generator are not present, the proposed power curtailment strategy allows the PV to provide the required voltage support to the system.

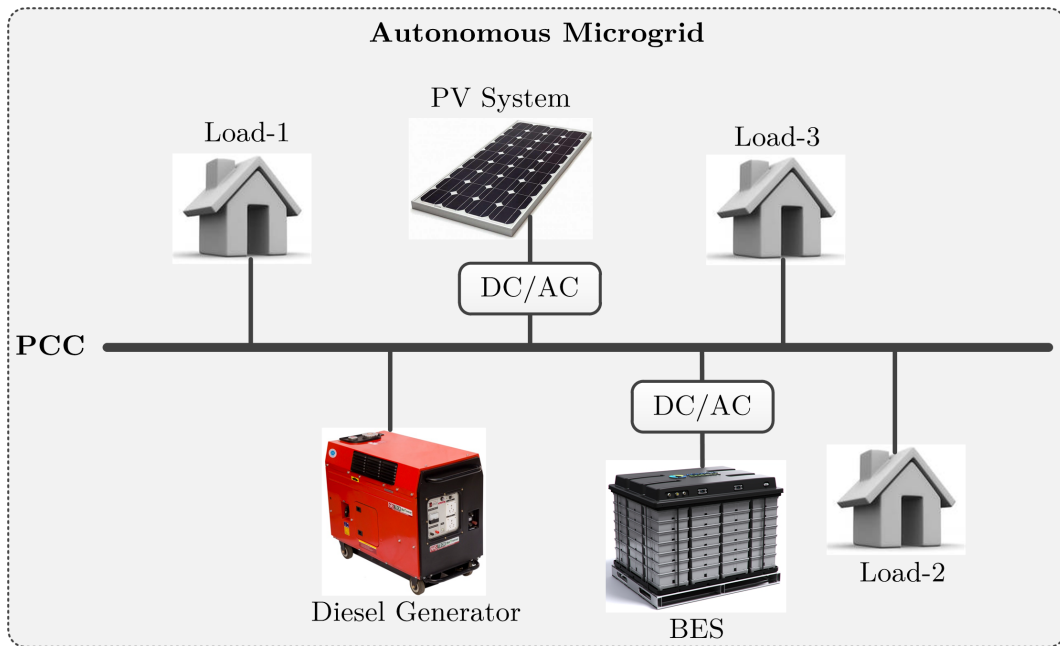


Figure 6.1: Stand-alone microgrid structure with BES, PV array, diesel generator and loads.

- The proposed strategy can be easily implemented on the existing PV-diesel MGs, since the BES and its control structure are coordinated in the MG as an additional distributed unit.
- Finally, the proposed BES control based on frequency bus-signaling does not interact with the smooth performance of the system as the imposed frequency variations by the BES unit are applied in a reliable manner and the overall frequency variations are within the acceptable range.

6.2 System Structure and Control

The stand-alone AC MG, shown in Fig. 6.1, consists of a PV system, a diesel generator, a BES unit and several distributed loads. The PV and BES systems include power electronic interfaces (i.e. DC/DC and DC/AC converters). The diesel generator operates as a back-up in the system only when the output power of the PV is lower than demand as in conventional PV-diesel MGs. BES is responsible for adjusting the system frequency and power balance in either the presence or absence of the diesel generator. Besides, BES is also designed to restore the PCC voltage. Moreover, the PV unit provides the required voltage

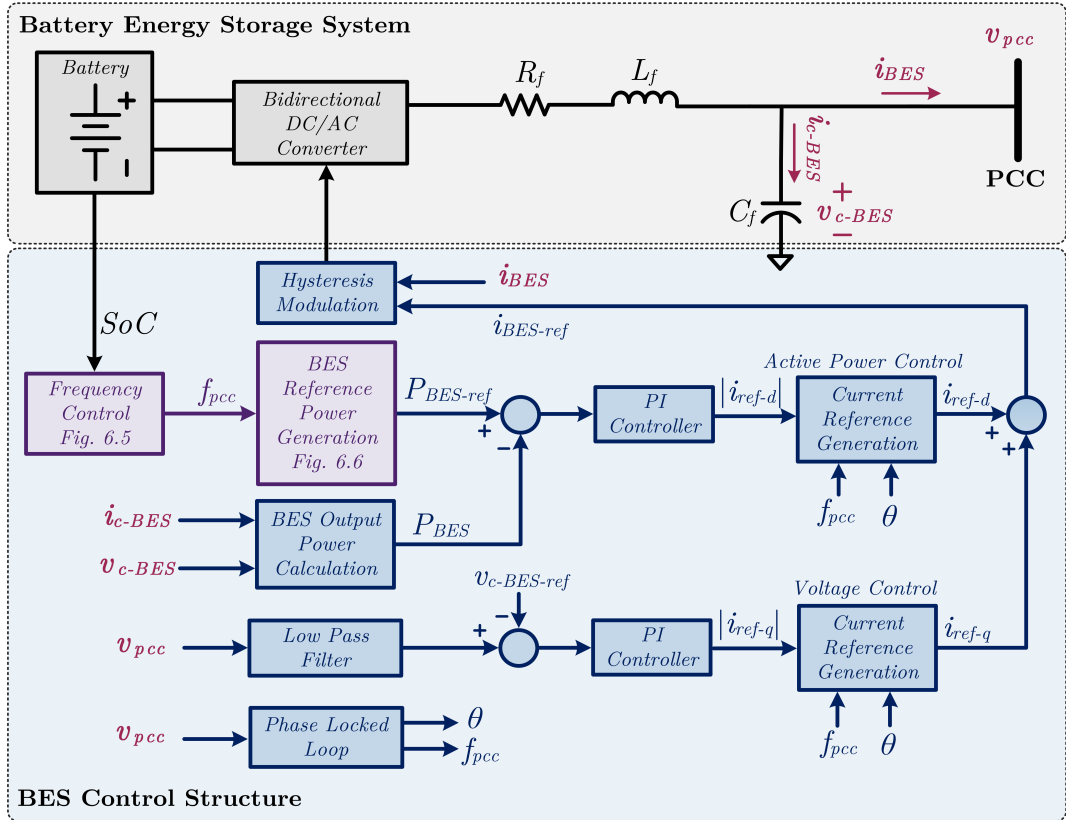


Figure 6.2: Battery energy storage system control structure.

support to the system when operating in power curtailment mode in the absence of both the BES unit and the diesel generator.

6.2.1 Battery Energy Storage System

The BES configuration, shown in Fig. 6.2, consists of a battery bank, a bidirectional DC/AC converter and an LC filter. The BES control system consists of two control loops to control the active power and the PCC voltage. The frequency determination block regulates the system frequency based on the SoC level of the BES. The BES reference power is then generated according to the system frequency which represents the BES status (i.e. SoC level). A proportional-integral (PI) controller is utilized in both control loops to ensure that the actual values of the BES active power output and the PCC voltage track their references properly. Finally, the hysteresis modulation block generates the switching signals of the converter.

The SoC estimation block, estimates the SoC level based on an ampere count-

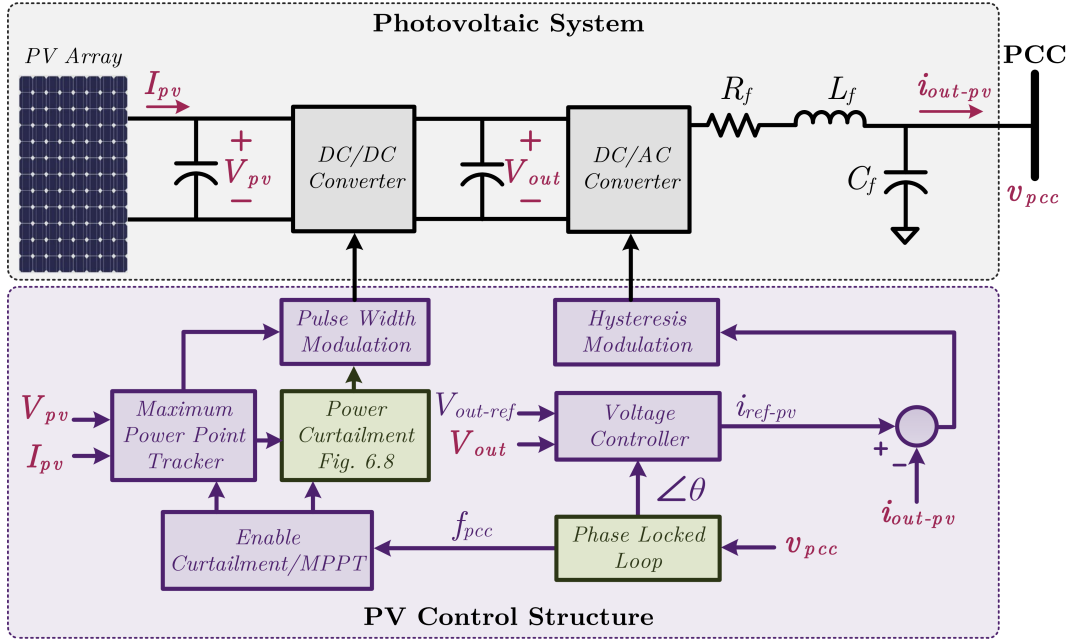


Figure 6.3: Photovoltaic system control structure.

ing algorithm as,

$$SoC_{init}(t) = SoC_{init} + \int_0^t \eta_{BES} \frac{i_{BES}(t)}{C_{BES}} dt \quad (6.1)$$

where, SoC_{init} is the initial SoC level, η_{BES} is the charge/discharge efficiency, i_{BES} is the BES current, and C_{BES} is the BES capacity [191]. More detailed algorithms can also be used as presented in [202].

6.2.2 Photovoltaic System

The PV system including DC/DC and DC/AC converters, an LC filter, and its control structure is shown in Fig. 6.3. The PV system may operate based on maximum power point tracking (MPPT) algorithm or power curtailment technique depending on the BES status reflected by the PCC frequency. Perturb and observation method or any other MPPT algorithms can be utilized to extract the maximum power from the PV unit [203]. Also, a new power curtailment technique will be presented in Section 3 which adjusts the PV output power with the variations of the demand while regulating the PCC voltage in the absence of the BES unit and the diesel generator. Finally, the voltage controller block adjusts the DC link voltage, and the hysteresis modulation block generates the switching signals for the DC/AC converter.

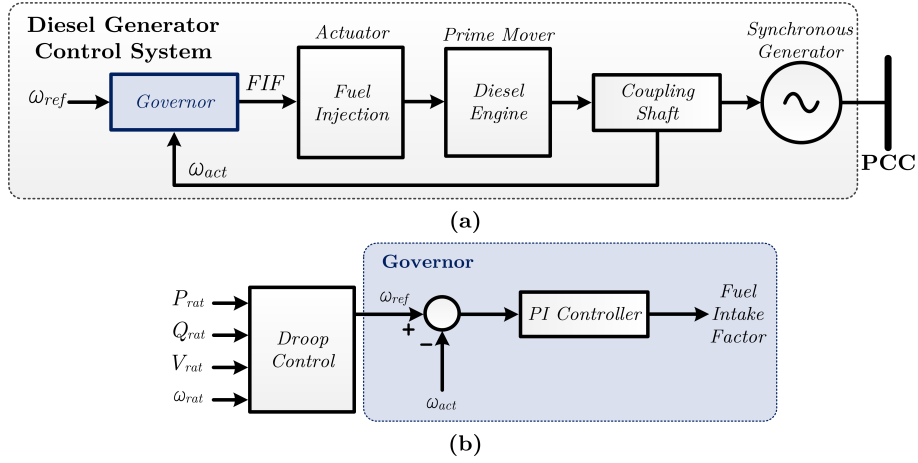


Figure 6.4: Diesel generator configuration; (a) speed control system, (b) droop control and governor control blocks.

6.2.3 Diesel Generator System

The main component of the diesel generator, as shown in Fig. 6.4(a), is the rotating synchronous generator which is driven by a diesel engine. The speed control diagram including the governor and the droop control is shown in Fig. 6.4(b). The diesel generator control system regulates the speed of the diesel engine against any disturbance that affects the system power balance. The speed error is processed through a PI controller. The fuel injection receives the control signal from the governor, and the fuel flow is changed, correspondingly. Finally, the interactions between the diesel engine and the synchronous generator through the coupling shaft sets the system frequency [204]. It is worth mentioning that the diesel generator gets disconnected whenever the load power is equal or lower than the PV generation and no backup is required in the system.

6.3 Proposed Power Management Strategy

A decentralized power management strategy is proposed in this section, which is essentially developed based on frequency regulation according to the SoC. The proposed strategy continuously monitors the SoC level of the BES unit and regulates the system frequency to alert the other units about the BES status. Consequently, the PV system can decide its mode of operation by solely measuring the local frequency. Hence, the proposed strategy provides a decentralized-autonomous control to the system independent from communication links when the diesel generator is disconnected. However, in the presence of the diesel gener-

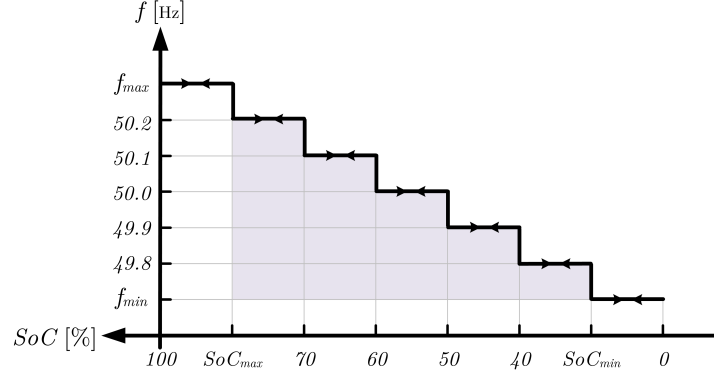


Figure 6.5: Frequency regulation based on SoC.

ator, low band-width communication links are used to transfer the BES reference frequency to this unit. Therefore, in either condition (i.e. presence or absence of the diesel generator), the power management of the MG is established in a decentralized manner and smooth performance of the system is ensured without compromising its reliability.

6.3.1 BES Comprehensive Charge and Discharge Control

As mentioned earlier, the BES unit is responsible for frequency regulation of the system based on its SoC level. Therefore, it is necessary to define a reliable range for both the SoC ($SoC_{min} < SoC < SoC_{max}$) and the system frequency ($f_{min} < f < f_{max}$). Also, since prompt and sudden frequency variations in the system may result into system instability, the proposed strategy applies small variations to the system frequency through the frequency determination block of Fig. 6.2 in every 10% of SoC variations. Moreover, when SoC reaches its upper/lower limits (SoC_{max}/SoC_{min}) the system frequency is retained on its maximum/minimum margins (f_{max}/f_{min}) to ensure that the frequency limits are not violated. Hence, the correlation between the SoC and the system frequency shown in Fig. 6.5 can be expressed as;

$$f = \begin{cases} f_{max} & SoC \geq SoC_{max} \\ 50.2 & 70\% \leq SoC < SoC_{max} \\ 50.1 & 60\% \leq SoC < 70\% \\ 50.0 & 50\% \leq SoC < 60\% \\ 49.9 & 40\% \leq SoC < 50\% \\ 49.8 & SoC_{min} \leq SoC < 40\% \\ f_{min} & SoC < SoC_{min} \end{cases} \quad (6.2)$$

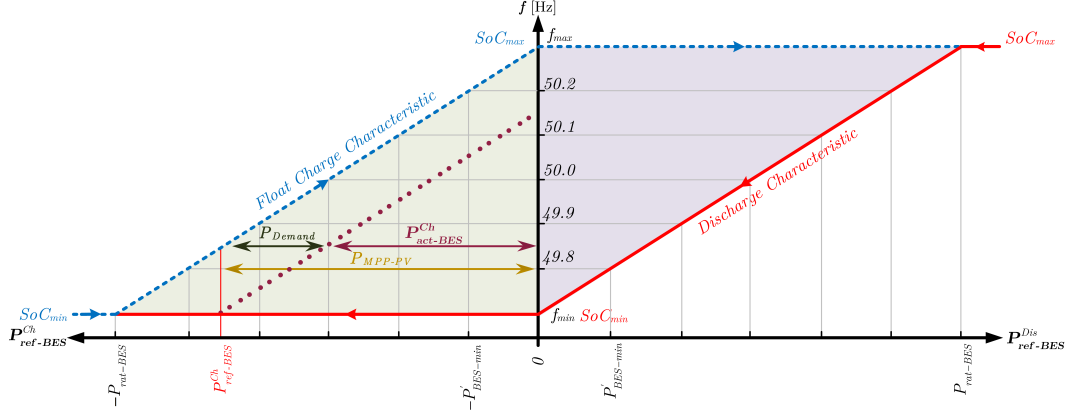


Figure 6.6: BES reference power generation in association with the system frequency and SoC.

where, SoC_{max}/SoC_{min} and f_{max}/f_{min} are the SoC and frequency maximum/minimum limits, respectively, and are specified in Appendix D Table D.1. Note that these parameters can be simply modified according to the system requirements.

Considering (6.2), the proposed BES reference power versus the system frequency is shown in Fig. 6.6. From the discharge graph (solid red line), it can be seen that the BES is designed to deliver power with its maximum capacity ($P_{rat-BES}$) when the system frequency is equal to its higher limit indicating that $SoC = SoC_{max}$, and BES is fully charged. Also, the BES reference power is set to zero when frequency is equal to its lower limit ($SoC = SoC_{min}$). From the charge graph (dashed blue line), it is visible that BES intends to draw power with its maximum capacity ($-P_{rat-BES}$) when the system frequency is equal to its lower limit representing that $SoC = SoC_{min}$, and BES is almost fully discharged. Also, the BES reference power is set to zero when $f = f_{max}$ (i.e. $SoC = SoC_{max}$) or when the BES is fully charged. Hence, in the discharge mode the BES power increases with the increase of frequency, whereas in the conventional droop strategies the inverter output active power decreases with the increase of the frequency. Moreover, in the charge mode the absolute of BES absorbing power decreases with the increase of frequency. To clarify the performance of the proposed strategy, three possible scenarios that might occur according to the SoC level are explained in Table 6.1.

From Table 6.1, it can be surmized that the BES is always able to match its output power with the discharge reference power ($P_{ref-BES}^{Dis}$) of Fig. 6.6 since in the discharge mode the diesel generator is presented in the system. However,

Table 6.1: Possible scenarios in the islanded MG of Fig. 6.1

Scenario	Case	PV Generation	Die-G Status	PV Status	BES Status
I	1	$P_{PV} < P_{Demand}$	C	C/MPPT	C/Discharge
	2	$P_{PV} > P_{Demand}$	D	C/MPPT	C/Charge
II	1	$P_{PV} < P_{Demand}$	C	C/MPPT	C/Discharge
	2	$P_{PV} > P_{Demand}$	D	C/Curtailment	D
III	1	$P_{PV} < P_{Demand}$	C	C/MPPT	D or C/Discharge
	2	$P_{PV} > P_{Demand}$	D	C/MPPT	C/Charge

I= $SoC_{min} < SoC < SoC_{max}$

C=Connected

II= $SoC > SoC_{max}$

D=Disconnected

III= $SoC < SoC_{min}$

during charge operation of the BES, the PV power is higher than demand, and the diesel generator is disconnected. Thus, due to the intermittency of the solar radiation, the PV system may not always be able to deliver the required fixed reference power of Fig. 6.6 ($P_{ref-BES}^{Ch}$). To address this issue, the algorithm of Fig. 6.7 is proposed here which provides a float charge characteristic for the BES unit to limit its power absorption to the surplus power of the PV by monitoring the PCC voltage. From this flowchart, as the BES switches to charge mode, initially, its active power reference is set to the minimum value of $P_{BES-min}$ then the algorithm monitors the PCC voltage where three possible conditions may occur as described below;

- Voltage drop: A voltage drop reflects that the consumption is higher than the PV generation; and therefore, the algorithm must reduce the BES absorbing power to restore the voltage. An example of this situation is shown in Fig. 6.6; the required power for charging BES based on the float charge characteristic is shown on the horizontal axis as $P_{ref-BES}^{Ch}$. Whereas, considering the load power (P_{Demand}) and the MPP power (P_{MPP}), PV is not able to deliver the overall demand (i.e. $P_{ref-BES}^{Ch} + P_{Demand}$). Therefore, based on the above algorithm, the float charge characteristic needs to be shifted toward the frequency axis (dotted line) such that BES draws less power of $P_{act-BES}^{Ch}$ from the PV and the system power balance is ensured.
- Voltage rise: A voltage rise denotes that some extra power is available within the system which needs to be absorbed by the BES. Thus, in this condition, the float charge characteristic moves away from the frequency

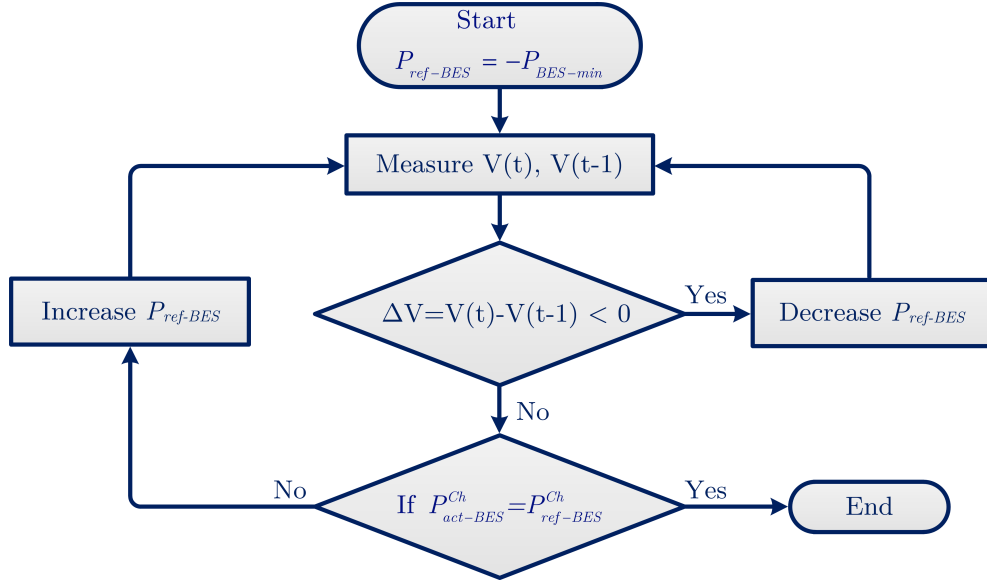


Figure 6.7: Active power reference modification to provide float charge characteristic for BES.

axis to increase the absorbing power of the BES.

- Voltage unchanged: Unchanged voltage represents that the MPP power from the PV is sufficient for charging the BES and supplying the load. Therefore, the BES can continue to absorb power as dictated by the float charge characteristic of Fig. 6.6.

The BES active power reference for charge mode (i.e. float characteristic), shown in Fig. 6.6, can be expressed as;

$$P_{ref-BES}^{Ch} = -P_{rat-BES} + \frac{P_{rat-BES}}{f_{max} - f_{min}}(f - f_{min}) \quad (6.3)$$

where, $P_{rat-BES}$ is the maximum capacity of BES and is specified in Appendix D Table D.1. Also, the BES reference power for the discharge mode, shown in Fig. 6.6, can be calculated as;

$$P_{ref-BES}^{Dis} = \frac{P_{rat-BES}}{f_{max} - f_{min}}(f - f_{min}) \quad (6.4)$$

Note that the BES actual active power in charge mode ($P_{act-BES}^{Ch}$) may differ from the reference charge power of ($P_{ref-BES}^{Ch}$) obtained by (6.3) since the charge characteristic is floated.

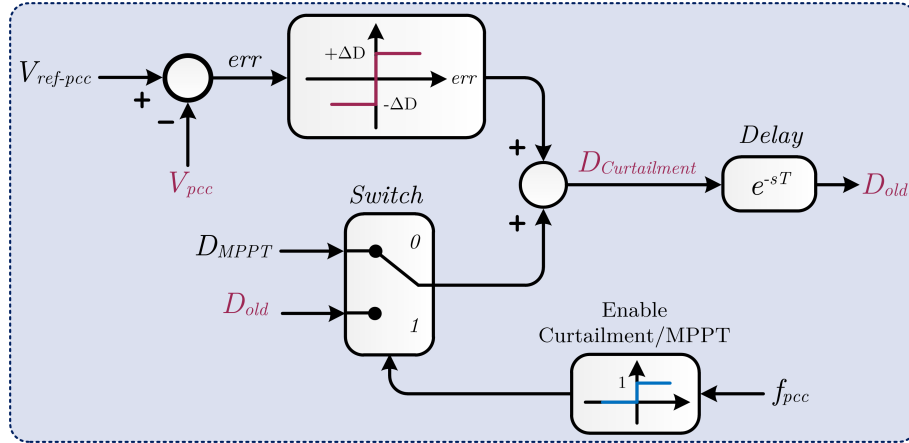


Figure 6.8: Proposed power curtailment technique for PV.

6.3.2 PV Power Curtailment Control

As mentioned in Section 2, the output power of the PV system requires to be adjusted with respect to the demand especially when the BES is fully charged and disconnected from the MG. For this reason, a new power curtailment technique is proposed and applied to the PV system, for $f > f_{max}$, which represents that $SoC = SoC_{max}$, and the BES is disconnected.

Based on the discussions of the previous section, any load increase/decrease, causes voltage drop/rise at the PCC if no voltage support is provided to the system. Thus, in the absence of the BES and the diesel generator, the PV system is responsible for providing the required voltage support. This can be achieved, by the proposed power curtailment technique which adjusts the duty ratio of the DC/DC converter to restore the PCC voltage according to the load variations.

To validate the proposed power curtailment technique shown in Fig. 6.8, the MG system of Fig. 6.1 is simulated when the BES and the diesel generator are both disconnected. The simulation results, with and without applying the proposed power curtailment technique, are shown in Fig. 6.9 where Figs. 6.9(a), 6.9(b) and 6.9(c) show the resulting active power, the PCC voltage, and the duty ratio for the DC/DC converter of the PV system, respectively. During this study, two load variations are applied to the system. At $t = 2$ [s], the load decreases from 15 [kW] to 10 [kW], and at $t = 4$ [s] the load increases to 12.5 [kW].

From the active power results shown in Fig. 6.9(a), it can be seen that for $t < 2$ [s], the load is 15 [kW] and PV is delivering its maximum available power of 15 [kW] while operating under MPPT. Fig. 6.9(b) also concurs that the system power balance is maintained during this time interval as the PCC voltage does

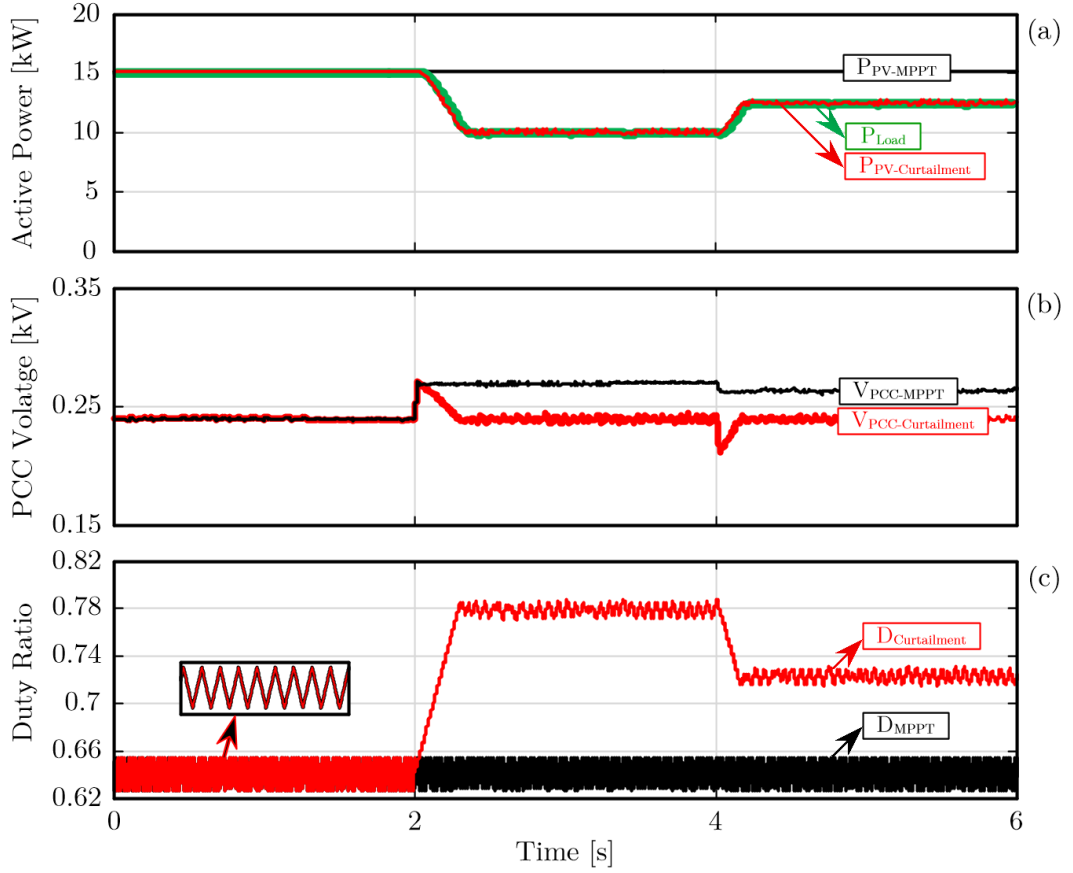


Figure 6.9: Simulation results of the proposed power curtailment technique.

not deviate from 0.239 [kV]. Moreover, the average duty ratio of the DC/DC converter during this time interval is 0.64 as shown in Fig. 6.9(c).

At $t = 2$ [s], the load decreases to 10 [kW] and remains constant till $t = 4$ [s]. In this time interval, initially, PV continues to operate under MPPT strategy. This causes a voltage rise at PCC since the generation becomes higher than the consumption. Consequently, the PV system is informed that its output power needs to be curtailed. As a result, the proposed power curtailment strategy comes to effect and modifies the duty ratio to bring the voltage inside the reliable range. From Fig. 6.9(a), it is visible that during this time interval the PV power is reduced from its MPP value to 10 [kW] to match the demand.

At $t = 4$ [s], the load increases to 12.5 [kW]. This load variation causes a voltage drop at PCC if PV continues to produce the same power as before (see Fig. 6.9(b)). Accordingly, the power curtailment strategy is notified and the PV power is increased by reducing the duty ratio. Fig. 6.9(b) also shows that the power curtailment strategy stops modifying the duty ratio when the PCC voltage

is within the acceptable range indicating that the generation and consumption are balanced.

6.4 Simulation results

Based on the anticipated scenarios introduced in Table 6.1, several case studies are considered here to evaluate the performance of the proposed power management strategy for the stand-alone MG system of Fig. 6.1. The simulations are carried out in PSCAD/EMTDC, and the technical data of the simulated system is given in Appendix D Table D.1. It is worth mentioning that two of the case studies (Cases 3 and 5) are specifically designed to examine the performance of the proposed strategy when the BES mode of operation changes from charge to discharge or vice versa. The system under study is run for the period of 6 [s], and three time intervals (i.e. TI-1, TI-2, and TI-3) are defined depending on different conditions occurring in each case study.

6.4.1 Scenario I: Normal Operation of BES

Case 1: BES Discharge Operation

In this case study, the BES operation in the discharge mode is investigated. For this, a constant load of 30 [kW] is applied to the system, and the PV unit delivers its maximum available power of 15 [kW]. As the PV power is lower than demand, based on the scenarios defined in Table 6.1, the diesel generator stays connected to the MG. Figs. 6.10(a), 6.10(b), 6.10(c), and 6.10(d) show the active powers, BES SoC level, system frequency, and PCC voltage, respectively.

As shown in Fig. 6.10(a), during TI-1, the BES unit is inactive and the load is supplied by the diesel generator and the PV system. At $t = 2$ [s], (i.e. the beginning of TI-2), BES is activated with the initial SoC (SoC_{init}) of 62.1%. Hence, the BES unit operates in the discharge mode and delivers the output power of 6.7 [kW] obtained by (6.4). Moreover, at $t = 2$ [s], the PCC voltage is restored as the BES becomes activated (see Fig. 6.10(d)). In TI-2, the PV system continues to operate under MPPT as the BES unit adjusts the frequency to $f = 50.1$ [Hz] $< f_{max}$, according to its SoC (based on (6.2)). At the beginning of TI-3, the SoC drops below 60%, and the BES sets the frequency to 50 [Hz]. As a result, the BES output power is reduced to 5 [kW]. Subsequently, the diesel generator picks up this lack of generation as shown in Fig. 6.10(a).

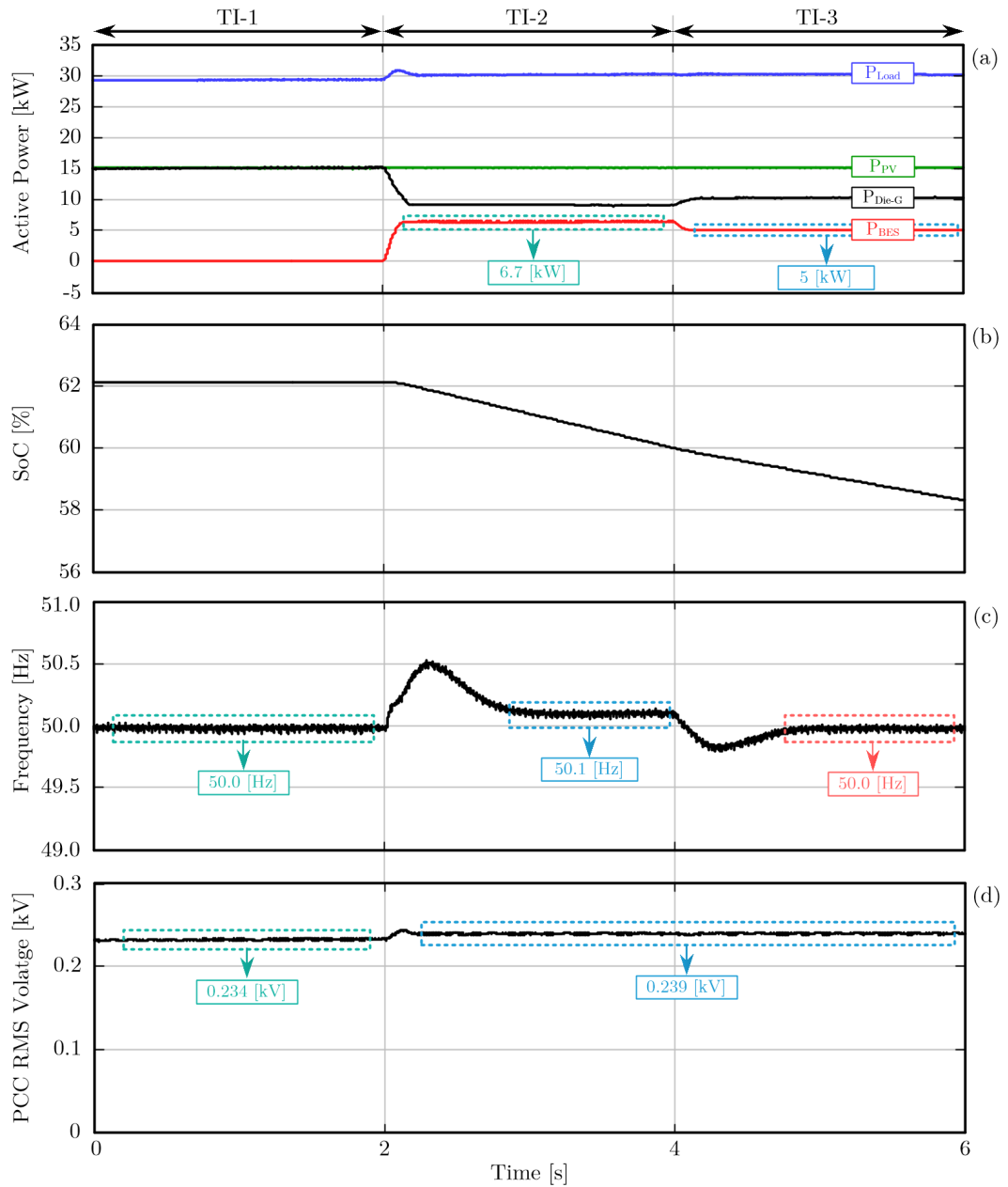


Figure 6.10: Case 1 results: BES discharge operation.

Case 2: BES Charge Operation

To investigate the BES operation in charge mode in this case study, it is assumed that the PV power is greater than demand and the BES initial SoC level (SoC_{init}) is 57.6%. Hence, based on Scenario I of Table 6.1, the diesel generator is disconnected and the BES unit operates in charge mode. Fig. 6.11 presents the related simulation results for this case study.

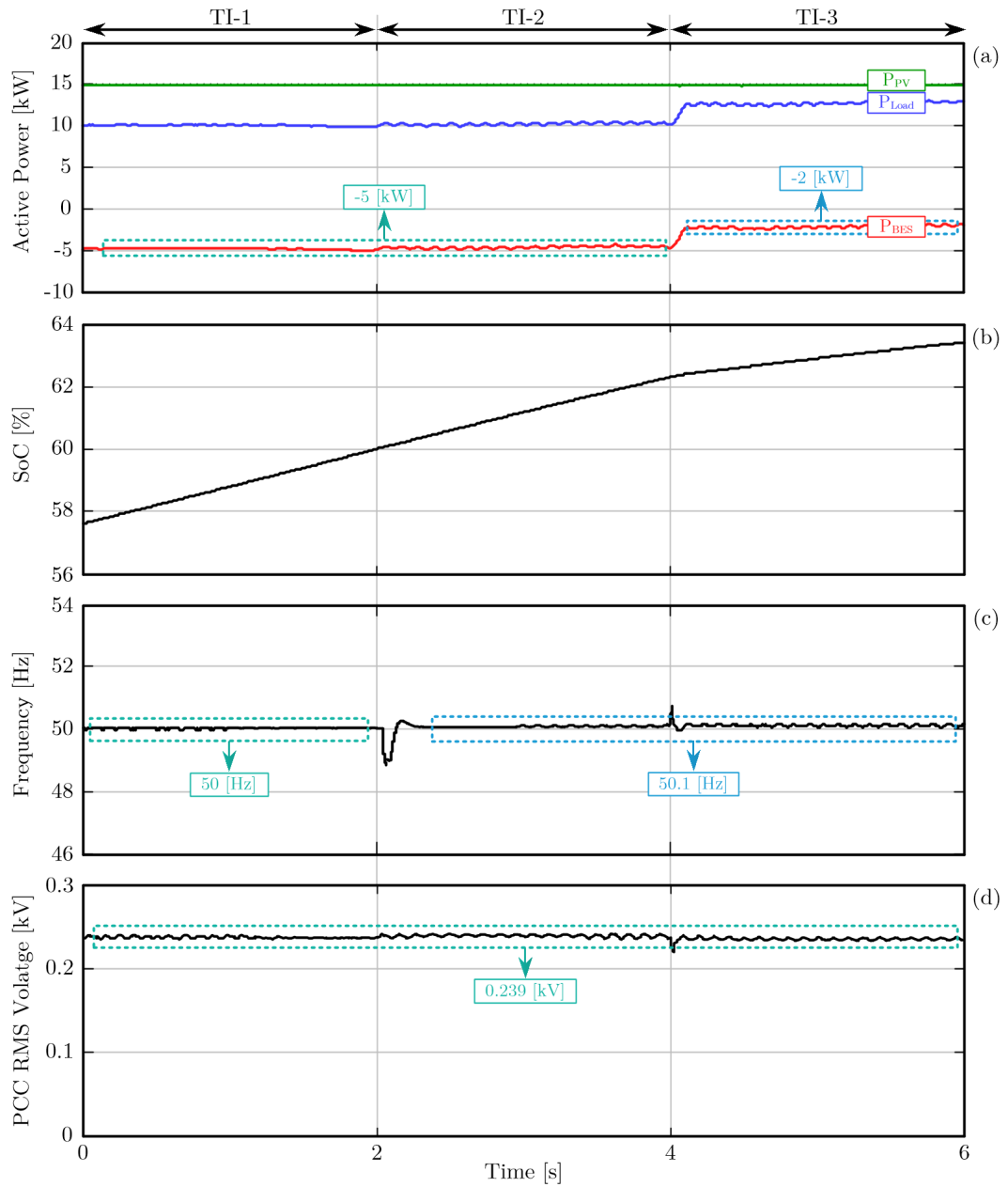


Figure 6.11: Case 2 results: BES charge operation.

In TI-1, the load consumes a constant power of 10 [kW]. From Fig. 6.11(b), BES SoC level is between 50% and 60%. Hence, based on the proposed strategy, BES sets the frequency to 50 [Hz] as shown in Fig. 6.11(c). With the system frequency of 50 [Hz] $< f_{max}$, PV operates under MPPT strategy and injects its maximum available power of 15 [kW] (see Fig. 6.11(a)). During this period, the control strategy aims to charge the BES unit with the available excess power in the system and without compromising the system stability. Thus, BES gradually

increases its power absorption and simultaneously monitors the PCC voltage based on the proposed algorithm of Fig. 6.7. This procedure continues till the equilibrium generation and consumption is reached.

During TI-2, $60\% < SoC < 70\%$, as a result, the system frequency is set to 50.1 [Hz]. From (6.3), BES is supposed to draw 3.3 [kW] whereas more surplus power is available from the PV. Thus, to avoid voltage rise at PCC, BES float charge characteristic is moved away from the frequency axis, and its absorbing power is gradually increased to balance the generation and consumption. Finally, the available excess power of 5 [kW] is absorbed by the BES as shown in Fig. 6.11(d) while the PCC voltage is remained within the reliable range.

In TI-3, the load increases to 13 [kW] as shown in Fig. 6.11(a) while $60\% < SoC < 70\%$ and $f = 50.1 \text{ [Hz]} < f_{max}$. Hence, the PV system continues to operate in MPPT mode and generates the same power as in TI-2. Considering the above conditions, the available excess power from PV is 2 [kW] whereas from (6.3) the BES reference power is -3.3 [kW]. Therefore, the BES float charge characteristic is moved toward the frequency axis. Finally, the BES power absorption is limited to 2 [kW] where the PCC voltage remains unaffected.

6.4.2 Scenario II: Overcharge Operation of BES

Case 3: BES Switching from Charge to Discharge

This case study investigates the system performance when BES switches from charge to discharge. For this, initially, the PV output power is assumed to be greater than demand ($P_{PV} > P_{Demand}$). Hence, the diesel generator is disconnected. The related simulation results for this case study are presented in Fig. 6.12. During TI-1, BES is inactive and the load is supplied by the PV as indicated in Fig. 6.12(a). At $t = 2$ [s], the BES unit is activated with SoC_{init} of 76.5%. Meanwhile, the load power decreases to 10 [kW]. Therefore, BES operates in charge mode and regulates the system frequency to 50.2 [Hz] (see Fig. 6.12(c)). During TI-2, the PV system still generates the same amount of power, and in turn, BES absorbs the surplus power of 5 [kW] to maintain the power balance of the system. At $t = 4$ [s], SoC reaches its maximum limit ($SoC_{max} = 80\%$) as shown in Fig. 6.12(b), and simultaneously the load increases to 34 [kW]. As a result, the diesel generator is reconnected to MG, and BES switches to the discharge mode by imposing the same frequency to the system as in TI-2. During TI-3, BES delivers 8.33 [kW] to the system as obtained by (6.4).

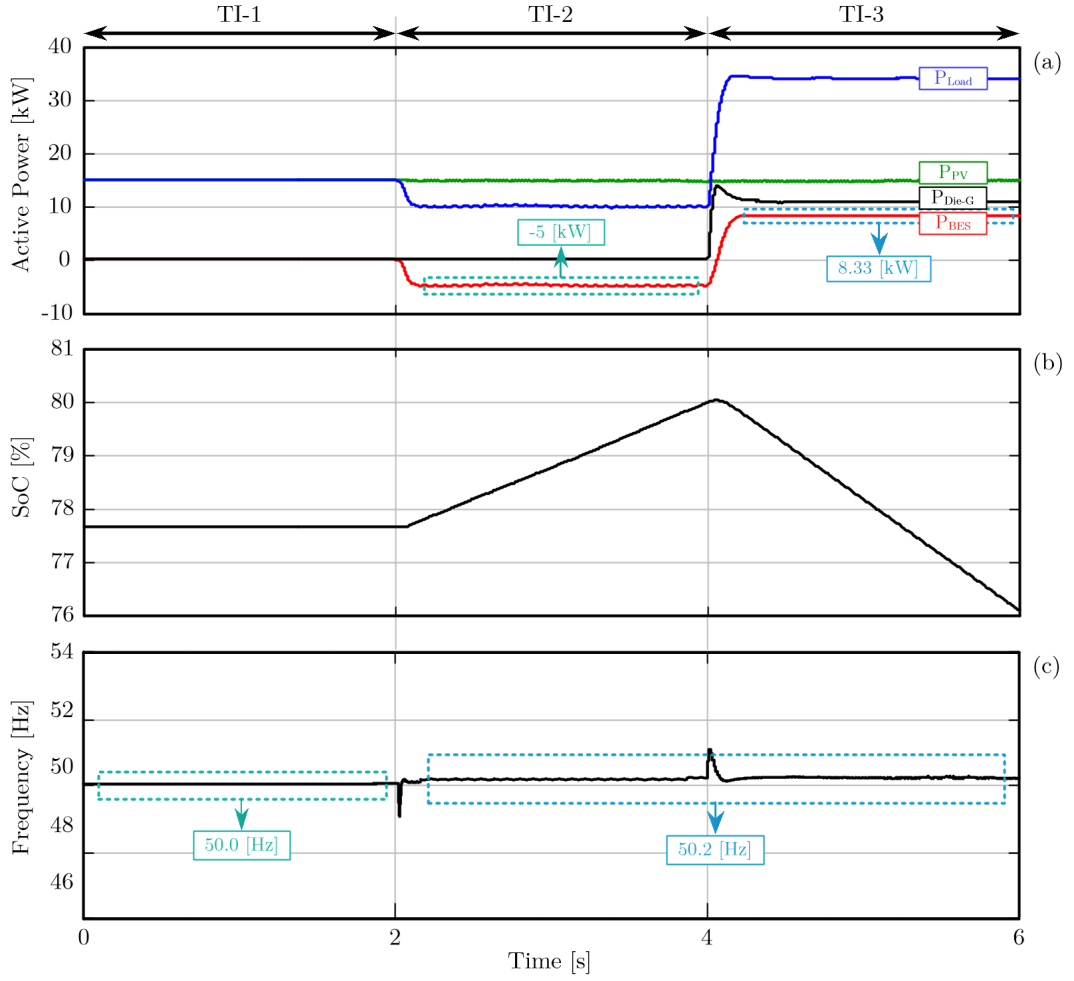


Figure 6.12: Case 3 results: BES switching from charge to discharge.

Case 4: PV Power Curtailment

In this case study, initially, $P_{PV} > P_{Demand}$ and $SoC_{init} = 77.6\%$. Hence, the diesel generator is disconnected, and the BES unit operates in the discharge mode. Fig. 6.13 presents the related simulation results. In TI-1, $f = 50$ [Hz] as shown in Fig. 6.13(c), and a constant load of 10 [kW] is applied to the system. From (6.3), the calculated reference power of BES is -1.7 [kW] while a surplus power of 5 [kW] is available from PV. Therefore, the BES absorbing power is adjusted to 5 [kW] to prevent voltage rise at PCC. This is achieved by moving the BES float charge characteristic away from the frequency axis. From Fig. 6.13(b), it is visible that at $t = 2$ [s], SoC reaches its maximum limit of SoC_{max} , and the BES gets disconnected. As a result, in TI-2, the proposed power curtailment strategy limits the PV output power to 10 [kW] by increasing its converter's duty ratio.

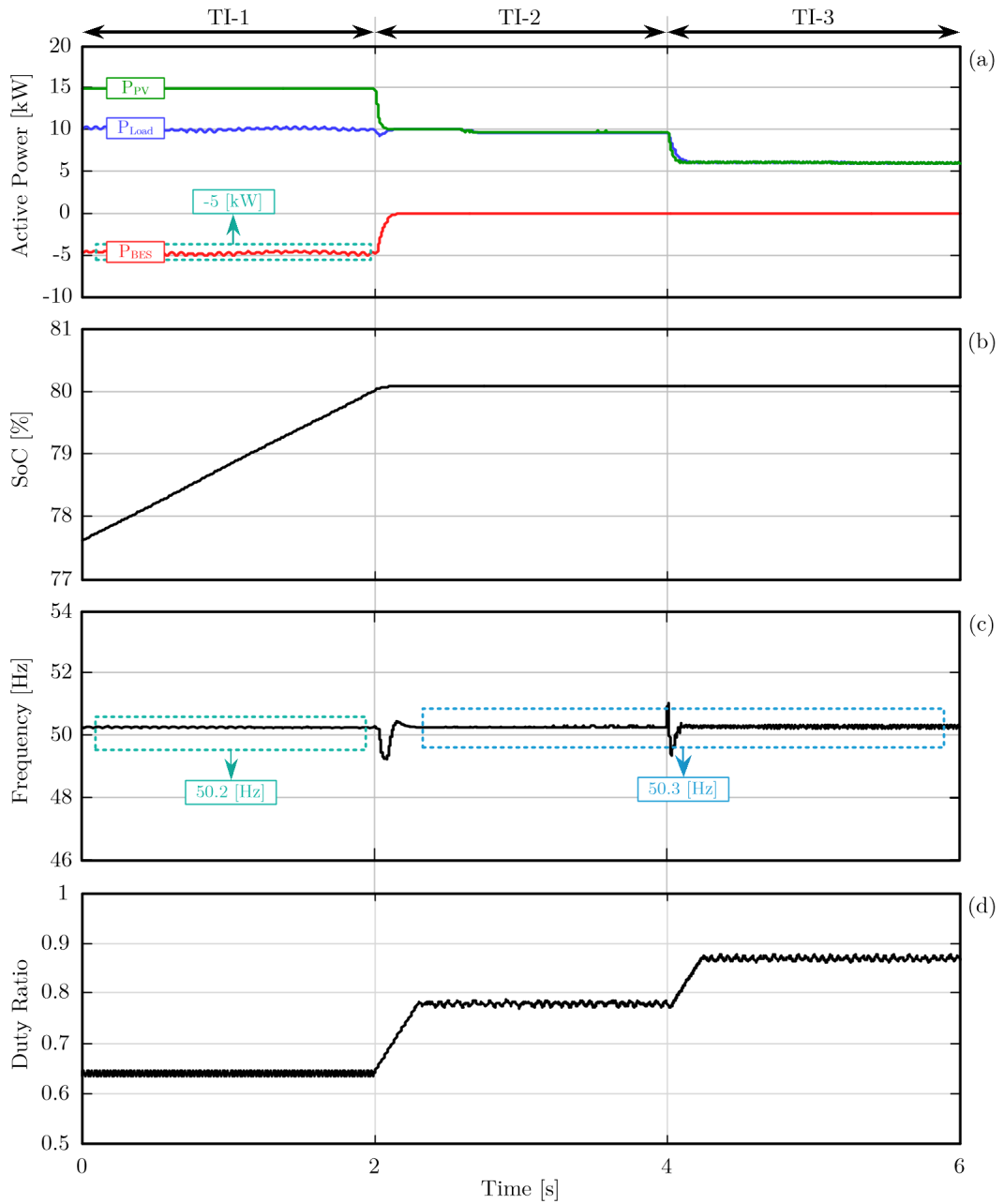


Figure 6.13: Case 4 results: PV power curtailment.

At $t = 4$ [s], the load is decreased to 6 [kW]. Hence, during TI-3, the PV output power is limited to 6 [kW] by further increasing of the duty ratio. Fig. 6.13(d) confirms the duty ratio variations as described.

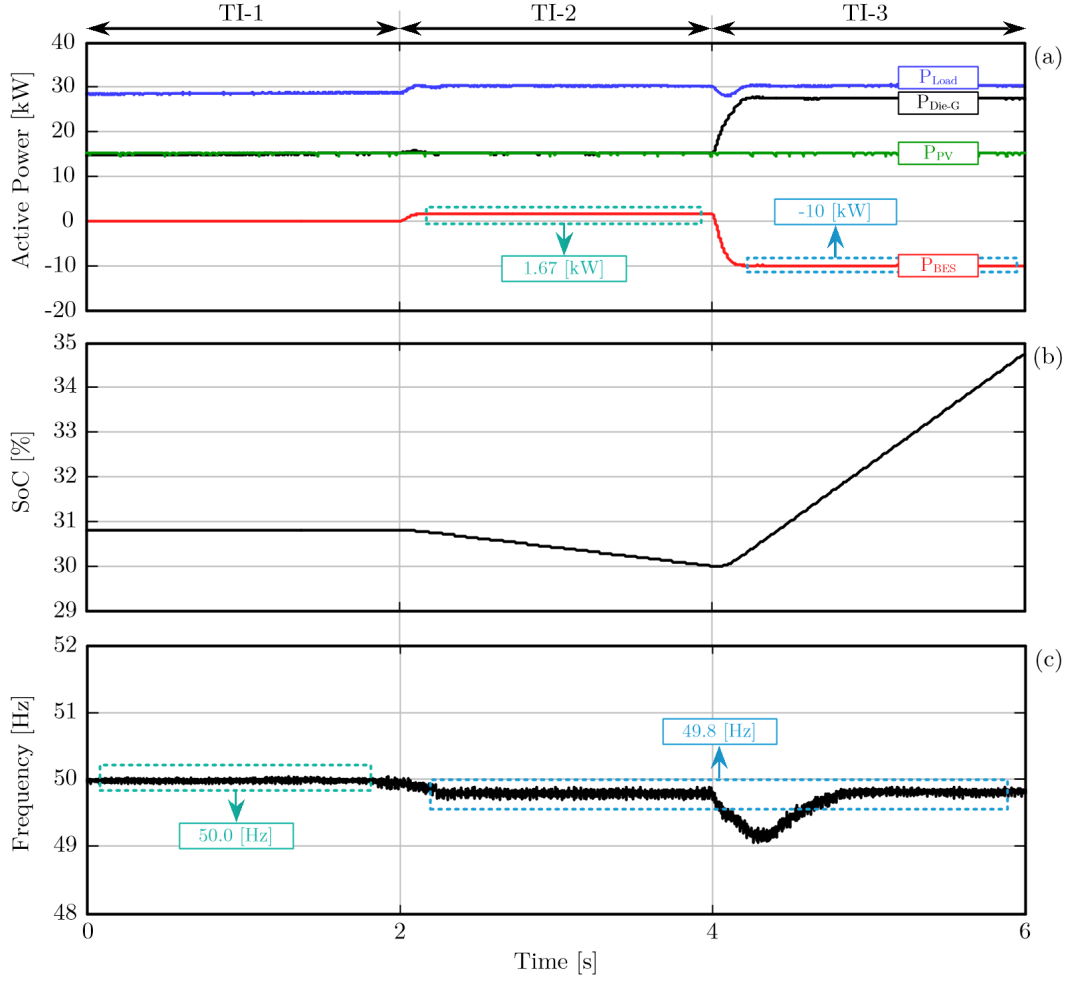


Figure 6.14: Case 5 results: BES switching from discharge to charge.

6.4.3 Scenario III: Over-discharge Operation of BES

Case 5: BES Switching from Discharge to Charge

In this case, the PV output power is lower than demand (i.e. $P_{PV} < P_{Demand}$). Hence, the diesel generator is connected to the MG. The related simulation results are depicted in Fig. 6.14. During TI-1, the BES unit is inactive and the load is supplied by the diesel generator and the PV unit. At $t = 2$ [s], the BES unit is activated with $SoC_{init} = 30.7\%$, and the system frequency is set to 49.8 [Hz] (see Fig. 6.14(c)). With the system frequency regulated at its minimum limit, other units are informed that the BES SoC level is close to SoC_{min} . Therefore, during TI-2, BES delivers the small output power of 1.67 [kW] to the system as dictated by (6.4) whereas the PV and the diesel generator both deliver 15 [kW]. This procedure continues until $t = 4$ [s] where BES switches to charge mode as

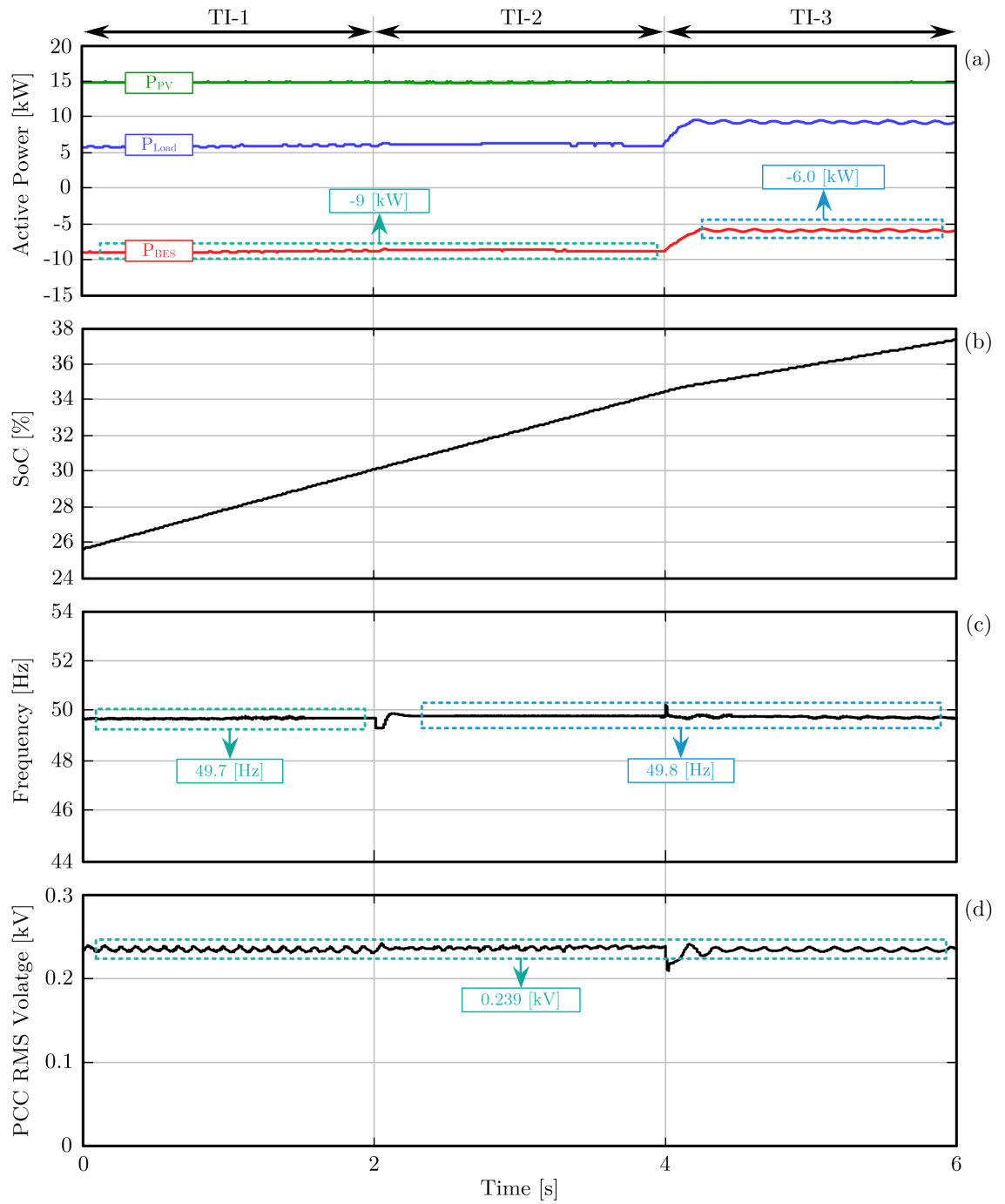


Figure 6.15: Case 6 results: Demand lower than the PV generation.

$SoC = SoC_{min}$, and it starts to absorb 10 [kW] from the system. As mentioned in Table 6.1, this is the only case where the diesel generator contributes in charging the BES. This is due to the lack of generation by the PV and the specific condition of the BES unit which is about to be over-discharged.

Case 6: Demand Lower than the PV Generation

In this condition, the diesel generator is disconnected from the MG, and the BES unit is operating in charge mode. Fig. 6.15 reveals the simulation results of this case study. During TI-1, a constant load of 6 [kW] is used and SoC_{init} is assumed to be 25.6%. Therefore, the proposed strategy regulates the system frequency to 49.7 [Hz] as shown in Fig. 6.15(c). Considering the above conditions, during TI-1, the BES unit operates in charge mode, and is supposed to draw 10 [kW], obtained by (6.2), from the system. However, the BES active power generation algorithm limits its absorbing power to 9 [kW], as shown in Fig. 6.15(a), to maintain the PCC voltage within the acceptable range. At $t = 2$ [s], the BES SoC level reaches SoC_{min} resulting in the system frequency of 49.8 [Hz]. Based on (6.2), during TI-2, the BES is supposed to draw 8.3 [kW]. However, an extra power of 10 [kW] is available within the system and therefore, the proposed strategy forces the BES to draw this amount of power. At $t = 4$ [s], the load increases to 9 [kW] and the proposed strategy limits the BES absorbing power to -6 [kW] to maintain the system power balance.

6.5 Conclusions

This chapter proposes a new decentralized power management strategy based on frequency bus-signalling approach for a PV-diesel MG with one BES unit. Based on the proposed strategy, the BES unit regulates the system frequency according to its SoC level to inform the other units about its status. Hence, in the absence of the diesel generator, the PV unit can decide its mode of operation based on local frequency measurements. Also, in the presence of the diesel generator low band-width communication links are adequate to receive the reference frequency from the BES unit. Thus, the MG power management is always realized in a decentralized manner without any need for central controller. Another advantage of the proposed comprehensive charge/discharge control is that it facilitates a float charge characteristic for the BES to ensure that the system power balance is always maintained. Moreover, the proposed control aims to limit the operation of the diesel generator. For this, the power management is designed to charge the BES unit mainly when some surplus power is available from the PV. Additionally, the PV unit is designed to operate in either maximum power point tracking (MPPT) mode or power curtailment mode according to the BES status. Lastly, the proposed power management, which is realized in a decen-

tralized manner, provides a robust voltage regulation to the system under any circumstances. Several case studies are designed and investigated to verify the effective performance of the proposed strategy in different operation scenarios.

Chapter 7

Conclusions

This thesis is mainly focused on developing reliable power management strategies for stand-alone microgrids (MGs) including dispatchable and non-dispatchable units. The main objective of the proposed power management strategies is to balance the power flow within the islanded MG while respecting the batteries available charge. Also, the proposed power sharing techniques aim to enhance reactive power sharing of the incorporated units of the MG by reducing reactive power ratio errors.

7.1 Thesis Summary and Conclusions

The general conclusions of the thesis are listed below.

1. Different power sharing techniques for parallel converter interfaced distributed energy resources (DERs) within an autonomous microgrid are studied in Chapter 2. The desired power sharing ratio is decided by the secondary controller of the distribution network and sent to the primary controllers of each DER via the microgrid central controller (MGCC). This chapter initially, discusses the limitations of the first two techniques. Then, a third technique is proposed and implemented in an example stand-alone MG which overcomes the limitations of the other two methods. The proposed method aims to enhance the reactive power sharing accuracy by imposing a virtual impedance at the output of the DERs. The imposed virtual impedance provides the required voltage drop at the converters terminals to facilitate the desired reactive power ratio among the DERs without modifying their coupling inductance. The amount of virtual impedance is adaptively changed with the system variations to guarantee that the power ratio

errors are kept below 5%. The simulation results verify the robust and reliable performance of the proposed technique compared to the existing ones.

2. Chapter 3 introduces an alternative power sharing technique based on virtual impedance concept. It is shown that the proposed technique in this chapter successfully decouples the active and reactive power outputs and provides an accurate reactive power sharing without compromising the system stability. To attain this, an algorithm is proposed which determines the optimum virtual impedance value based on the stability analysis of the MG. Hence, the proposed technique in this chapter considers the system transients and stability in addition to the steady state power ratio errors of the DERs. This strategy provides a more reliable response to the system in comparison to the method introduced in Chapter 2 since it is developed based on the small-signal model of the stand-alone microgrid. The control strategy has been simulated for an example MG. The time domain results verify the effective performance of the system in the enhancement of the reactive power ratios accuracy while the small-signal results confirm the system stability.
3. Chapter 4 proposes a new hierarchical power management strategy for multiple battery energy storage (BES) systems and renewable energy sources (RESs) of an autonomous MG. The proposed comprehensive control of the BES units is composed of two subsystems. Each subsystem is included in the BES control structure depending on its operation mode (i.e. charge or discharge mode). The main objective of the proposed control algorithm in discharge mode is to consider their state of charge (SoC) in the droop control characteristic aiming to avoid premature depletion of these units. Hence, in the proposed state of charge-based droop control, the active output powers of the BESs are modified dynamically according to their SoC level variations. Additionally, a new reactive power sharing algorithm is developed based on the proposed discharge control of BESs which aims to utilize the unused capacity of the BES converters and to avoid overloading the RES units. Based on this algorithm, the BES units with lower SoC which represents their higher available converter capacity, supply more reactive power. To achieve this, the virtual impedance method introduced in Chapter 2 is included in the control structure of the BES converters in discharge mode to facilitate the desired active and reactive power sharing

ratios. Another objective of the proposed SoC-based droop control is to modify the output power of each BES independent from the SoC level of the other units. For this, the proposed hierarchical control collects the SoC data of the BESs and transfers them to the RES units through the microgrid central controller (MGCC). Then, the MGCC decides the required modifications in the output power of the RESs considering the BES units status. Finally, the proposed control algorithm in charge mode ensures that the BES units power absorptions are limited to the surplus power of the system. To attain this, the BES reference power in charge mode is decided by the MGCC considering the maximum available power from the RESs and the instantaneous demand. Thus, the MG power balance is always ensured. The proposed hierarchical control strategy is designed and implemented for an autonomous MG with two BES and two RES units where the efficacy of the comprehensive control in both charge and discharge mode is verified.

4. Chapter 5 proposes a new decentralized power management strategy which is specifically designed for the control of stand-alone MGs with multiple distributed ESSs without requirement of global and/or local communication links. Hence, the proposed control structure performs in an autonomous manner. The considered MG consists of a PV unit, a droop controlled DER, and multiple BESs. The proposed strategy, allows the PV unit to operate in current control mode (CCM) and deliver its maximum available power based on the maximum power point tracking algorithms. Also, the ESSs supply/absorb the generation and consumption mismatch. Based on the proposed strategy, the operation mode of each ESS is decided according to its own SoC level (i.e. independent from the SoC level of the other ESSs) where three operation modes are defined; (1) normal operation, (2) float operation, and (3) force charge operation. In each operation mode, the ESS reference power is determined based on a predefined frequency-power characteristic, in which the system frequency distinguishes the generation/consumption mismatch. The proposed control strategy also aims to charge the ESSs up to their maximum SoC margin to enable them to operate in normal or float operation depending on the system demand. The proposed autonomous strategy has been deployed for an example MG with multiple ESSs. The simulation results confirm the seamless and efficient performance of the system as the ESSs switch from one operation mode to another.

5. Chapter 6 proposes a new decentralized power management strategy based on frequency bus-signalling for a PV-diesel islanded MG with one BES unit. Based on the proposed method the system frequency is regulated according to the BES SoC level. To achieve this, a comprehensive charge/discharge control strategy is applied to the BES which also facilitates a float charge characteristic for this unit. In discharge mode, a higher system frequency represents a higher SoC level. Hence, the BES is designed to vary its reference output power from its maximum rating to zero when the system frequency varies from its upper margin to its lower margin. Also, with the same frequency variations in charge mode, the BES reference absorbing power varies from zero to its maximum capacity. Note that this charge reference characteristic is floated in order to enable the proposed strategy to limit the BES power absorption to the excess power of the system. This is achieved by shifting this float characteristic along with the reference power axis. Hence, the BES reference power in charge mode is justified based on the PCC voltage measurement. Another objective of the proposed strategy is to control the BES unit to be mainly charged by the PV in order to limit the operation of the diesel generator. Moreover, PV may perform in maximum power point tracking (MPPT) or curtailment mode according to the BES status. The proposed power curtailment technique for the PV system, which is applied to the PV in the absence of the BES and the diesel generator, allows the PV unit to provide the required voltage support to the system in addition to justifying the PV output power with demand. Hence, the proposed power management provides a robust voltage regulation to the system under any circumstances. Note that in the absence of the diesel generator (i.e. when PV power is higher than demand), the MG power management operates autonomously without any communications. Also, in the presence of the diesel generator, local low bandwidth communication links are used to transfer the system reference frequency from the BES unit to the diesel generator. Hence, the proposed strategy still can operate without requiring a central controller. Several case studies have been designed and investigated to validate the efficient performance of the proposed decentralized power management strategy.

7.2 Future Work

Suggested future work is presented in the following:

- Investigating the effectiveness of the proposed reactive power sharing techniques to enhance harmonic power sharing in stand-alone microgrids.
- In the proposed hierarchical (centralized) control all the associated units in the MG are assumed to operate in voltage control mode. Next step is to consider RES units of the MG to operate in current control mode, and modify the droop characteristic of the BESs such that they share the power mismatch of the system by communicating with one another.
- Applying the proposed decentralized power management strategies to a wind based islanded MG. Wind generation has chaotic nature similar to the photovoltaic generation. However, the dynamics of wind turbines is a challenging issue compared to the PVs static nature and is introduced due to their power electronic converters.
- Modifying the proposed decentralized strategies to make them applicable for the islanded MGs with controllable resources, such as fuel cells or microturbines, in addition to the PV units. In this case, considering the slow dynamics of these sources becomes crucial as it may affect the power balance of the MG.
- The considered battery energy storage is included as a distributed unit. Next step could be considering this unit as a hybrid unit (i.e. incorporated with the renewable sources), and controlling the power management of the hybrid unit in collaboration with the whole MG.

Appendix A

Chapter 3 System Technical Data

Table A.1: Technical data of the considered MG in Chapter 3.

Parameter	Description
<i>Microgrid Parameters</i>	
Rated PCC Voltage	$V_{LL} = 400 V$
Frequency	$f = 50 Hz$
Feeder Resistance	$R = 0.2 \Omega$
Feeder Inductance	$L = 6.4 mH$
<i>Voltage Source Converters</i>	
Filter Resistance	$R_f = 0.1 \Omega$
Filter Inductance	$L_f = 38.5 mH$
Filter Capacitance	$C_f = 50 \mu$
DC Link Voltage	$V_{dc} = 350 V$
Rated Power	$P_{rat} = 20 kW, Q_{rat} = 18 kVar$
Coupling Inductance	$L_{c-1} = L_{c-2} = L_{c-3} = 10 mH$
LQR Gains	$k_1 = 8.3977, k_2 = 0.4338, k_3 = 0.8405$
<i>Objective Functions</i>	
OF_1	$\alpha = 50 \%, \beta = 50 \%$
OF_2	$\alpha = 75 \%, \beta = 25 \%$
OF_3	$\alpha = 25 \%, \beta = 75 \%$
OF_4	$\alpha = 0 \%, \beta = 100 \%$

Appendix B

Chapter 4 System Technical Data

Table B.1: Technical data of the investigated MG in Chapter 4.

Parameter	Description
<i>Microgrid Parameters</i>	
Rated PCC Voltage	$V_{LL} = 400 \text{ V}$
Frequency	$f = 50 \text{ Hz}$
Feeder Resistance	$R = 0.5 \Omega$
Feeder Inductance	$L = 3.2 \text{ mH}$
<i>Voltage Source Converters</i>	
Filter Resistance	$R_f = 0.1 \Omega$
Filter Inductance	$L_f = 0.36 \text{ mH}$
Filter Capacitance	$C_f = 50 \mu\text{F}$
DC Link Voltage	$V_{dc} = 350 \text{ V}$
LQR Gains	$k_1 = 6.1802, k_2 = 2.2968, k_3 = 22.968$
Coupling Inductance	$L_{c-1} = L_{c-2} = L_{c-3} = 0.30 \text{ mH}$
<i>Global Droop Parameters</i>	
Rated Active Power	$P_0 = 3 \text{ kW}$
Rated Reactive Power	$Q_0 = 1 \text{ kVar}$
Angle Droop Coefficient	$m_0 = 897.6$
Voltage Droop Coefficient	$n_0 = 24$
<i>Initial SoC Percentage</i>	
	Case-1 Case-2 Case-3 Case-4 Case-5
BES_1	70 70 42.5 88.5 80
BES_2	100 100 100 100 60

Appendix C

Chapter 5 System Technical Data

Table C.1: Technical Data of the MG Elements in Chapter 5.

Parameter	Description
<i>Energy Storage Systems:</i>	
Rated Voltage	$V_{LL} = 415 \text{ V}$
Rated Power	$P_{max} = 20 \text{ kW}, Q_{max} = 8 \text{ kVar}$
Filter Resistance	$P_r = 10 \text{ kW}$
Filter Inductance	$SoC_{max} = 80 \%$
<i>Distributed Energy Resource:</i>	
Rated Voltage	$V_{LL} = 415 \text{ V}$
Maximum Capacity	$P_{max} = 30 \text{ kW}, Q_{max} = 8 \text{ kVar}$
Droop Parameters	$m = 33.34, n = 3$
Coupling Inductance	$L_c = 1 \text{ mH}$
<i>Photovoltaic System:</i>	
Rated Voltage	$V_{LL} = 415 \text{ V}$
Rated Power	$P_{rat} = 30 \text{ kW}$
<i>Filter Elements for all Units:</i>	
Filter Resistance	$R_f = 0.025 \Omega$
Filter Inductance	$L_f = 5 \text{ mH}$
Filter Capacitance	$C_f = 50 \mu\text{F}$

Appendix D

Chapter 6 System Technical Data

Table D.1: Technical data of the investigated system in Chapter 6.

Parameter	Description
<i>Microgrid System:</i>	
Rated Voltage	$V_{LL} = 0.415$ kV
Frequency Maximum Limit	$f_{max} = 50.3$ Hz
Frequency Minimum Limit	$f_{min} = 49.7$ Hz
<i>Diesel Generator System:</i>	
Rated Power	$P_{rat} = 12$ kW, $Q_{rat} = 8$ kVar
Filter Resistance	$R_f = 0.025$ Ω
Filter Inductance	$L_f = 1$ mH
Drop Coefficients	$m = 209$, $n = 1.5$
<i>Photovoltaic System:</i>	
Rated Power	$P_{rat} = 15$ kW
Filter Resistance	$R_f = 0.025$ Ω
Filter Inductance	$L_f = 1$ mH
Filter Capacitance	$C_f = 50$ μ F
<i>Battery Storage System:</i>	
Rated Power	$P_{rat} = 10$ kW, $Q_{rat} = 5$ kVar
Filter Resistance	$R_f = 0.025$ Ω
Filter Inductance	$L_f = 1$ mH
Filter Capacitance	$C_f = 50$ μ F
SoC Maximum Limit	$SoC_{max} = 80\%$
SoC Minimum Limit	$SoC_{min} = 30\%$

Appendix E

Publications Incorporated in Thesis

1. Tahoura Hosseinimehr, Arindam Ghosh, and Sumedha Rajakaruna, “Decentralized Power Management of an Autonomous Microgrid Including Battery Energy Storage, PV and Diesel Generator,” *IET Generation, Transmission & Distribution Journal*, Submitted, GTD-2017-1003, 2017. [Chapter 6]
2. Tahoura Hosseinimehr, and Arindam Ghosh, “Autonomous Power Management Strategy for Stand-Alone Microgrids with Distributed Energy Storage Systems,” *Electric Power System Research Journal*, Under Revision, EPSR-D-17-01075, 2017. [Chapter 5]
3. Tahoura Hosseinimehr, Arindam Ghosh, and Farhad Shahnia, “Cooperative Control of Battery Energy Storage Systems in Microgrids,” *International Journal of Electrical Power and Energy Systems*, vol., 87, pp.109-120, 2017. [Chapters 2 & 4]
4. Tahoura Hosseinimehr, Farhad Shahnia, and Arindam Ghosh, “Power Sharing Control of Batteries within Autonomous Microgrids Based on Their State of Charge,” *Australasian Universities Power Engineering Conference*, Wollongong, NSW, Australia, September 27-September 30, 2015. [Chapter 4]
5. Tahoura Hosseinimehr, Farhad Shahnia, and Arindam Ghosh, “Dynamic Power Sharing Control Among Converter-Interfaced DERs in an Autonomous

Microgrid,” *Power Tech 2015 Conference*, Eindhoven, The Netherlands, June 29-July 2, 2015. [Chapter 3]

6. Tahoura Hosseinimehr, Farhad Shahnia, and Arindam Ghosh, “Different Power Sharing Techniques for Converter-Interfaced DERs in an Autonomous Microgrid,” *Asia-Pacific Power and Energy Engineering 2014 Conference*, Hong Kong, China, December 7-December 10, 2014. [Chapter 2]

Bibliography

- [1] R. H. Lasseter, “Microgrids,” vol. 1, pp. 305–308 vol.1, 2002.
- [2] C. Williams, “Chp systems,” pp. 57–59, March 2004.
- [3] R. H. Lasseter, “Microgrids and distributed generation,” *Journal of Energy Engineering*, vol. 133, no. 3, pp. 144–149, 2007.
- [4] T. S. e. a. J. Lopez, A. Pecas, “Management of microgrids,” pp. 62–68, October 2003.
- [5] S. M. Malik, X. Ai, Y. Sun, C. Zhengqi, and Z. Shupeng, “Voltage and frequency control strategies of hybrid ac/dc microgrid: a review,” *IET Generation, Transmission Distribution*, vol. 11, no. 2, pp. 303–313, 2017.
- [6] J. G. de Matos, F. S. F. e Silva, and L. A. d. S. Ribeiro, “Power control in ac isolated microgrids with renewable energy sources and energy storage systems,” *IEEE Transactions on Industrial Electronics*, vol. 62, no. 6, pp. 3490–3498, June 2015.
- [7] D. Wu, F. Tang, T. Dragicevic, J. C. Vasquez, and J. M. Guerrero, “A control architecture to coordinate renewable energy sources and energy storage systems in islanded microgrids,” *IEEE Transactions on Smart Grid*, vol. 6, no. 3, pp. 1156–1166, May 2015.
- [8] Y. W. Li and C. N. Kao, “An accurate power control strategy for power-electronics-interfaced distributed generation units operating in a low-voltage multibus microgrid,” *IEEE Transactions on Power Electronics*, vol. 24, no. 12, pp. 2977–2988, Dec 2009.
- [9] H. Nikkhajoei and R. H. Lasseter, “Distributed generation interface to the certs microgrid,” *IEEE Transactions on Power Delivery*, vol. 24, no. 3, pp. 1598–1608, July 2009.

- [10] C. Sao and P. Lehn, "Control and power management of converter fed microgrids," in *IEEE PES General Meeting*, July 2010, pp. 1–1.
- [11] M. Shahabi, M. R. Haghifam, M. Mohamadian, and S. A. Nabavi-Niaki, "Microgrid dynamic performance improvement using a doubly fed induction wind generator," *IEEE Transactions on Energy Conversion*, vol. 24, no. 1, pp. 137–145, March 2009.
- [12] M. Milosevic, P. Rosa, M. Portmann, and G. Andersson, "Generation control with modified maximum power point tracking in small isolated power network with photovoltaic source," in *2007 IEEE Power Engineering Society General Meeting*, June 2007, pp. 1–8.
- [13] I. S. Bae and J. O. Kim, "Reliability evaluation of distributed generation based on operation mode," *IEEE Transactions on Power Systems*, vol. 22, no. 2, pp. 785–790, May 2007.
- [14] H. A. Gil and G. Joos, "Models for quantifying the economic benefits of distributed generation," *IEEE Transactions on Power Systems*, vol. 23, no. 2, pp. 327–335, May 2008.
- [15] S. Haffner, L. F. A. Pereira, L. A. Pereira, and L. S. Barreto, "Multistage model for distribution expansion planning with distributed generation; part i: Problem formulation," *IEEE Transactions on Power Delivery*, vol. 23, no. 2, pp. 915–923, April 2008.
- [16] H. Farhangi, "The path of the smart grid," *IEEE Power and Energy Magazine*, vol. 8, no. 1, pp. 18–28, January 2010.
- [17] M. S. W. El-Khattam, "Distributed generation technologies, definitions and benefits," *Electric Power Systems Research*, vol. 71, no. 2, pp. 119 – 128, January 2004.
- [18] S. Grillo, S. Massucco, A. Morini, A. Pitto, and F. Silvestro, "Microturbine control modeling to investigate the effects of distributed generation in electric energy networks," *IEEE Systems Journal*, vol. 4, no. 3, pp. 303–312, Sept 2010.
- [19] M. Etezadi-Amoli and K. Choma, "Electrical performance characteristics of a new micro-turbine generator," in *2001 IEEE Power Engineering Soci-*

- ety Winter Meeting. Conference Proceedings (Cat. No.01CH37194)*, vol. 2, 2001, pp. 736–740 vol.2.
- [20] M. W. Davis, A. H. Gifford, and T. J. Krupa, “Microturbines-an economic and reliability evaluation for commercial, residential, and remote load applications,” in *IEEE Power Engineering Society. 1999 Winter Meeting (Cat. No.99CH36233)*, vol. 2, Jan 1999, pp. 888 vol.2–.
- [21] F. Blaabjerg, Z. Chen, and S. B. Kjaer, “Power electronics as efficient interface in dispersed power generation systems,” *IEEE Transactions on Power Electronics*, vol. 19, no. 5, pp. 1184–1194, Sept 2004.
- [22] T. Petru and T. Thiringer, “Modeling of wind turbines for power system studies,” *IEEE Transactions on Power Systems*, vol. 17, no. 4, pp. 1132–1139, Nov 2002.
- [23] B. C. Ummels, M. Gibescu, E. Pelgrum, W. L. Kling, and A. J. Brand, “Impacts of wind power on thermal generation unit commitment and dispatch,” *IEEE Transactions on Energy Conversion*, vol. 22, no. 1, pp. 44–51, March 2007.
- [24] E. Muljadi, C. P. Butterfield, B. Parsons, and A. Ellis, “Effect of variable speed wind turbine generator on stability of a weak grid,” *IEEE Transactions on Energy Conversion*, vol. 22, no. 1, pp. 29–36, March 2007.
- [25] D. Andersson, A. Petersson, E. Agneholm, and D. Karlsson, “Kriegers flak 640 mw off-shore wind power grid connection mdash;a real project case study,” *IEEE Transactions on Energy Conversion*, vol. 22, no. 1, pp. 79–85, March 2007.
- [26] R. Billinton and W. Wangdee, “Reliability-based transmission reinforcement planning associated with large-scale wind farms,” *IEEE Transactions on Power Systems*, vol. 22, no. 1, pp. 34–41, Feb 2007.
- [27] T. Thiringer, “Power quality measurements performed on a low-voltage grid equipped with two wind turbines,” *IEEE Transactions on Energy Conversion*, vol. 11, no. 3, pp. 601–606, Sep 1996.
- [28] J. Matevosyan and L. Soder, “Minimization of imbalance cost trading wind power on the short-term power market,” *IEEE Transactions on Power Systems*, vol. 21, no. 3, pp. 1396–1404, Aug 2006.

- [29] P. Suhane, S. Rangnekar, A. Mittal, and A. Khare, “Sizing and performance analysis of standalone wind-photovoltaic based hybrid energy system using ant colony optimisation,” *IET Renewable Power Generation*, vol. 10, no. 7, pp. 964–972, 2016.
- [30] T. Ackermann and J. W. Press, *Wind Power in Power Systems*. John Wiley, 2003.
- [31] “Alta wind energy center (awec), california, united states of america,” <http://www.power-technology.com/projects/alta-wind-energy-center-awec-california/>.
- [32] M. W. Ellis, M. R. V. Spakovsky, and D. J. Nelson, “Fuel cell systems: efficient, flexible energy conversion for the 21st century,” *Proceedings of the IEEE*, vol. 89, no. 12, pp. 1808–1818, Dec 2001.
- [33] L. H. Diaz-Saldierna, J. Leyva-Ramos, D. Langarica-Cordoba, and J. A. Morales-Saldae, “Control strategy of switching regulators for fuel-cell power applications,” *IET Renewable Power Generation*, vol. 11, no. 6, pp. 799–805, 2017.
- [34] —, “Control strategy of switching regulators for fuel-cell power applications,” *IET Renewable Power Generation*, vol. 11, no. 6, pp. 799–805, 2017.
- [35] F. Blaabjerg, R. Teodorescu, M. Liserre, and A. V. Timbus, “Overview of control and grid synchronization for distributed power generation systems,” *IEEE Transactions on Industrial Electronics*, vol. 53, no. 5, pp. 1398–1409, Oct 2006.
- [36] S. Moon, S. G. Yoon, and J. H. Park, “A new low-cost centralized mppt controller system for multiply distributed photovoltaic power conditioning modules,” *IEEE Transactions on Smart Grid*, vol. 6, no. 6, pp. 2649–2658, Nov 2015.
- [37] Y. Levron, D. R. Clement, B. Choi, C. Olalla, and D. Maksimovic, “Control of submodule integrated converters in the isolated-port differential power-processing photovoltaic architecture,” *IEEE Journal of Emerging and Selected Topics in Power Electronics*, vol. 2, no. 4, pp. 821–832, Dec 2014.

- [38] Y. Yu, G. Konstantinou, C. D. Townsend, and V. G. Agelidis, "Comparison of zero-sequence injection methods in cascaded h-bridge multilevel converters for large-scale photovoltaic integration," *IET Renewable Power Generation*, vol. 11, no. 5, pp. 603–613, 2016.
- [39] M. I. Hossain, R. Yan, and T. K. Saha, "Investigation of the interaction between step voltage regulators and large-scale photovoltaic systems regarding voltage regulation and unbalance," *IET Renewable Power Generation*, vol. 10, no. 3, pp. 299–309, 2016.
- [40] W. Xiao, W. G. Dunford, P. R. Palmer, and A. Capel, "Regulation of photovoltaic voltage," *IEEE Transactions on Industrial Electronics*, vol. 54, no. 3, pp. 1365–1374, June 2007.
- [41] M. Farhadi and O. Mohammed, "Energy storage technologies for high-power applications," *IEEE Transactions on Industry Applications*, vol. 52, no. 3, pp. 1953–1961, May 2016.
- [42] X. Xu, M. Bishop, D. G. Oikarinen, and C. Hao, "Application and modeling of battery energy storage in power systems," *CSEE Journal of Power and Energy Systems*, vol. 2, no. 3, pp. 82–90, Sept 2016.
- [43] J. A. McDowall, "Opportunities for electricity storage in distributed generation and renewables," in *2001 IEEE/PES Transmission and Distribution Conference and Exposition. Developing New Perspectives (Cat. No.01CH37294)*, vol. 2, 2001, pp. 1165–1168 vol.2.
- [44] H. Han, X. Hou, J. Yang, J. Wu, M. Su, and J. M. Guerrero, "Review of power sharing control strategies for islanding operation of ac microgrids," *IEEE Transactions on Smart Grid*, vol. 7, no. 1, pp. 200–215, Jan 2016.
- [45] M. H. Bollen and F. Hassan, *Measuring progress towards energy*. John Wiley, 2014.
- [46] T. Adefarati and R. C. Bansal, "Integration of renewable distributed generators into the distribution system: a review," *IET Renewable Power Generation*, vol. 10, no. 7, pp. 873–884, 2016.
- [47] H. Han, X. Hou, J. Yang, J. Wu, M. Su, and J. M. Guerrero, "Review of power sharing control strategies for islanding operation of ac microgrids," *IEEE Transactions on Smart Grid*, vol. 7, no. 1, pp. 200–215, Jan 2016.

- [48] L. Meng, Q. Shafiee, G. F. Trecate, H. Karimi, D. Fulwani, X. Lu, and J. M. Guerrero, “Review on control of dc microgrids,” *IEEE Journal of Emerging and Selected Topics in Power Electronics*, vol. PP, no. 99, pp. 1–1, 2017.
- [49] “Photovoltaic systems,” <http://www.yourhome.gov.au/energy/photovoltaic-systems>, accessed: 2017-06-02.
- [50] H. R., *Energy Storage*. Springer, 2010.
- [51] J. P. Barton and D. G. Infield, “Energy storage and its use with intermittent renewable energy,” *IEEE Transactions on Energy Conversion*, vol. 19, no. 2, pp. 441–448, June 2004.
- [52] , “Electrical energy storage,” IEC and Fraunhofer Institut fr Solare Energiesysteme, White Paper, 2011.
- [53] M. Montoya, R. Sherick, P. Haralson, R. Neal, and R. Yinger, “Islands in the storm: Integrating microgrids into the larger grid,” *IEEE Power and Energy Magazine*, vol. 11, no. 4, pp. 33–39, July 2013.
- [54] F. Katiraei, R. Iravani, N. Hatziargyriou, and A. Dimeas, “Microgrids management,” *IEEE Power and Energy Magazine*, vol. 6, no. 3, pp. 54–65, May 2008.
- [55] D. E. Olivares, A. Mehrizi-Sani, A. H. Etemadi, C. A. Caizares, R. Iravani, M. Kazerani, A. H. Hajimiragha, O. Gomis-Bellmunt, M. Saadifard, R. Palma-Behnke, G. A. Jimnez-Estvez, and N. D. Hatziargyriou, “Trends in microgrid control,” *IEEE Transactions on Smart Grid*, vol. 5, no. 4, pp. 1905–1919, July 2014.
- [56] F. A. Inthamoussou, J. Pegueroles-Queralt, and F. D. Bianchi, “Control of a supercapacitor energy storage system for microgrid applications,” *IEEE Transactions on Energy Conversion*, vol. 28, no. 3, pp. 690–697, Sept 2013.
- [57] M. Datta, T. Senjyu, A. Yona, T. Funabashi, and C. H. Kim, “A frequency-control approach by photovoltaic generator in a pv-diesel hybrid power system,” *IEEE Transactions on Energy Conversion*, vol. 26, no. 2, pp. 559–571, June 2011.
- [58] J. M. Guerrero, J. C. Vasquez, J. Matas, L. G. de Vicuna, and M. Castilla, “Hierarchical control of droop-controlled ac and dc microgrids -a general

- approach toward standardization,” *IEEE Transactions on Industrial Electronics*, vol. 58, no. 1, pp. 158–172, Jan 2011.
- [59] S. Anand, B. G. Fernandes, and J. Guerrero, “Distributed control to ensure proportional load sharing and improve voltage regulation in low-voltage dc microgrids,” *IEEE Transactions on Power Electronics*, vol. 28, no. 4, pp. 1900–1913, April 2013.
- [60] W. Jing, C. H. Lai, S. H. W. Wong, and M. L. D. Wong, “Battery-supercapacitor hybrid energy storage system in standalone dc microgrids: areview,” *IET Renewable Power Generation*, vol. 11, no. 4, pp. 461–469, 2016.
- [61] J. Rocabert, A. Luna, F. Blaabjerg, and P. Rodriguez, “Control of power converters in ac microgrids,” *IEEE Transactions on Power Electronics*, vol. 27, no. 11, pp. 4734–4749, Nov 2012.
- [62] J. A. P. Lopes, C. L. Moreira, and A. G. Madureira, “Defining control strategies for microgrids islanded operation,” *IEEE Transactions on Power Systems*, vol. 21, no. 2, pp. 916–924, May 2006.
- [63] A. Yazdani and R. Iravani, *Voltage-Sourced Converters in Power Systems*. Wiley, 2010.
- [64] H. Mahmood, D. Michaelson, and J. Jiang, “Strategies for independent deployment and autonomous control of pv and battery units in islanded microgrids,” *IEEE Journal of Emerging and Selected Topics in Power Electronics*, vol. 3, no. 3, pp. 742–755, Sept 2015.
- [65] N. L. Daz, A. C. Luna, J. C. Vasquez, and J. M. Guerrero, “Centralized control architecture for coordination of distributed renewable generation and energy storage in islanded ac microgrids,” *IEEE Transactions on Power Electronics*, vol. 32, no. 7, pp. 5202–5213, July 2017.
- [66] R. Yazdani, A. Iravani, *Voltage-sourced converters in power systems*. John Wiley, 2010.
- [67] M. B. Delghavi and A. Yazdani, “Islanded-mode control of electronically coupled distributed-resource units under unbalanced and nonlinear load conditions,” *IEEE Transactions on Power Delivery*, vol. 26, no. 2, pp. 661–673, April 2011.

- [68] —, “A unified control strategy for electronically interfaced distributed energy resources,” *IEEE Transactions on Power Delivery*, vol. 27, no. 2, pp. 803–812, April 2012.
- [69] A. J. W. B. F. Wollenberg, *Power Generation, Operation and Control*. John Wiley, 1984.
- [70] A. Haddadi, A. Yazdani, G. Jos, and B. Boulet, “A gain-scheduled decoupling control strategy for enhanced transient performance and stability of an islanded active distribution network,” *IEEE Transactions on Power Delivery*, vol. 29, no. 2, pp. 560–569, April 2014.
- [71] J. M. Guerrero, M. Chandorkar, T. L. Lee, and P. C. Loh, “Advanced control architectures for intelligent microgrids; part i: Decentralized and hierarchical control,” *IEEE Transactions on Industrial Electronics*, vol. 60, no. 4, pp. 1254–1262, April 2013.
- [72] M. N. Marwali, J.-W. Jung, and A. Keyhani, “Control of distributed generation systems - part ii: Load sharing control,” *IEEE Transactions on Power Electronics*, vol. 19, no. 6, pp. 1551–1561, Nov 2004.
- [73] J. C. Vasquez, J. M. Guerrero, M. Savaghebi, J. Eloy-Garcia, and R. Teodorescu, “Modeling, analysis, and design of stationary-reference-frame droop-controlled parallel three-phase voltage source inverters,” *IEEE Transactions on Industrial Electronics*, vol. 60, no. 4, pp. 1271–1280, April 2013.
- [74] M. Savaghebi, A. Jalilian, J. C. Vasquez, and J. M. Guerrero, “Secondary control scheme for voltage unbalance compensation in an islanded droop-controlled microgrid,” *IEEE Transactions on Smart Grid*, vol. 3, no. 2, pp. 797–807, June 2012.
- [75] J. He, C. Wang, Y. Pan, and B. Liang, “A simple decentralized islanding microgrid power sharing method without using droop control,” *IEEE Transactions on Smart Grid*, vol. PP, no. 99, pp. 1–1, 2017.
- [76] I. U. Nutkani, P. C. Loh, and F. Blaabjerg, “Droop scheme with consideration of operating costs,” *IEEE Transactions on Power Electronics*, vol. 29, no. 3, pp. 1047–1052, March 2014.

- [77] S. Kotra and M. K. Mishra, "A supervisory power management system for a hybrid microgrid with hess," *IEEE Transactions on Industrial Electronics*, vol. 64, no. 5, pp. 3640–3649, May 2017.
- [78] N. Korada and M. K. Mishra, "Grid adaptive power management strategy for an integrated microgrid with hybrid energy storage," *IEEE Transactions on Industrial Electronics*, vol. 64, no. 4, pp. 2884–2892, April 2017.
- [79] D. Salomonsson, L. Soder, and A. Sannino, "An adaptive control system for a dc microgrid for data centers," *IEEE Transactions on Industry Applications*, vol. 44, no. 6, pp. 1910–1917, Nov 2008.
- [80] D. E. Olivares, C. A. Caizares, and M. Kazerani, "A centralized energy management system for isolated microgrids," *IEEE Transactions on Smart Grid*, vol. 5, no. 4, pp. 1864–1875, July 2014.
- [81] D. E. Olivares, J. D. Lara, C. A. Caizares, and M. Kazerani, "Stochastic-predictive energy management system for isolated microgrids," *IEEE Transactions on Smart Grid*, vol. 6, no. 6, pp. 2681–2693, Nov 2015.
- [82] Q. Jiang, M. Xue, and G. Geng, "Energy management of microgrid in grid-connected and stand-alone modes," *IEEE Transactions on Power Systems*, vol. 28, no. 3, pp. 3380–3389, Aug 2013.
- [83] M. H. Nehrir, C. Wang, K. Strunz, H. Aki, R. Ramakumar, J. Bing, Z. Miao, and Z. Salameh, "A review of hybrid renewable/alternative energy systems for electric power generation: Configurations, control, and applications," *IEEE Transactions on Sustainable Energy*, vol. 2, no. 4, pp. 392–403, Oct 2011.
- [84] J. Y. Kim, J. H. Jeon, S. K. Kim, C. Cho, J. H. Park, H. M. Kim, and K. Y. Nam, "Cooperative control strategy of energy storage system and microsources for stabilizing the microgrid during islanded operation," *IEEE Transactions on Power Electronics*, vol. 25, no. 12, pp. 3037–3048, Dec 2010.
- [85] H. Kanchev, D. Lu, F. Colas, V. Lazarov, and B. Francois, "Energy management and operational planning of a microgrid with a pv-based active generator for smart grid applications," *IEEE Transactions on Industrial Electronics*, vol. 58, no. 10, pp. 4583–4592, Oct 2011.

- [86] F. Valenciaga and P. F. Puleston, "Supervisor control for a stand-alone hybrid generation system using wind and photovoltaic energy," *IEEE Transactions on Energy Conversion*, vol. 20, no. 2, pp. 398–405, June 2005.
- [87] T. Dragievi, J. M. Guerrero, J. C. Vasquez, and D. Krlec, "Supervisory control of an adaptive-droop regulated dc microgrid with battery management capability," *IEEE Transactions on Power Electronics*, vol. 29, no. 2, pp. 695–706, Feb 2014.
- [88] B. Wang, M. Sechilariu, and F. Locment, "Intelligent dc microgrid with smart grid communications: Control strategy consideration and design," *IEEE Transactions on Smart Grid*, vol. 3, no. 4, pp. 2148–2156, Dec 2012.
- [89] X. Lu, J. M. Guerrero, K. Sun, and J. C. Vasquez, "An improved droop control method for dc microgrids based on low bandwidth communication with dc bus voltage restoration and enhanced current sharing accuracy," *IEEE Transactions on Power Electronics*, vol. 29, no. 4, pp. 1800–1812, April 2014.
- [90] S. Anand, B. G. Fernandes, and J. Guerrero, "Distributed control to ensure proportional load sharing and improve voltage regulation in low-voltage dc microgrids," *IEEE Transactions on Power Electronics*, vol. 28, no. 4, pp. 1900–1913, April 2013.
- [91] W. Qiu and Z. Liang, "Practical design considerations of current sharing control for parallel vrm applications," in *Twentieth Annual IEEE Applied Power Electronics Conference and Exposition, 2005. APEC 2005.*, vol. 1, March 2005, pp. 281–286 Vol. 1.
- [92] T. Dragievi, J. M. Guerrero, and J. C. Vasquez, "A distributed control strategy for coordination of an autonomous lvdc microgrid based on power-line signaling," *IEEE Transactions on Industrial Electronics*, vol. 61, no. 7, pp. 3313–3326, July 2014.
- [93] D. Wu, F. Tang, T. Dragicevic, J. C. Vasquez, and J. M. Guerrero, "Autonomous active power control for islanded ac microgrids with photovoltaic generation and energy storage system," *IEEE Transactions on Energy Conversion*, vol. 29, no. 4, pp. 882–892, Dec 2014.

- [94] L. Zhang, T. Wu, Y. Xing, K. Sun, and J. M. Gurrero, "Power control of dc microgrid using dc bus signaling," in *2011 Twenty-Sixth Annual IEEE Applied Power Electronics Conference and Exposition (APEC)*, March 2011, pp. 1926–1932.
- [95] X. Sun, Z. Lian, B. Wang, and X. Li, "A hybrid renewable dc microgrid voltage control," in *2009 IEEE 6th International Power Electronics and Motion Control Conference*, May 2009, pp. 725–729.
- [96] X. Yu, A. Huang, R. Burgos, J. Li, and Y. Du, "A fully autonomous power management strategy for dc microgrid bus voltages," in *2013 Twenty-Eighth Annual IEEE Applied Power Electronics Conference and Exposition (APEC)*, March 2013, pp. 2876–2881.
- [97] E. Serban and H. Serban, "A control strategy for a distributed power generation microgrid application with voltage- and current-controlled source converter," *IEEE Transactions on Power Electronics*, vol. 25, no. 12, pp. 2981–2992, Dec 2010.
- [98] S. Bae and A. Kwasinski, "Dynamic modeling and operation strategy for a microgrid with wind and photovoltaic resources," *IEEE Transactions on Smart Grid*, vol. 3, no. 4, pp. 1867–1876, Dec 2012.
- [99] L. Valverde, F. Rosa, and C. Bordons, "Design, planning and management of a hydrogen-based microgrid," *IEEE Transactions on Industrial Informatics*, vol. 9, no. 3, pp. 1398–1404, Aug 2013.
- [100] S. Adhikari and F. Li, "Coordinated v-f and p-q control of solar photovoltaic generators with mppt and battery storage in microgrids," *IEEE Transactions on Smart Grid*, vol. 5, no. 3, pp. 1270–1281, May 2014.
- [101] B. Kroposki, C. Pink, R. DeBlasio, H. Thomas, M. Simes, and P. K. Sen, "Benefits of power electronic interfaces for distributed energy systems," *IEEE Transactions on Energy Conversion*, vol. 25, no. 3, pp. 901–908, Sept 2010.
- [102] T. Senjyu, T. Nakaji, K. Uezato, and T. Funabashi, "A hybrid power system using alternative energy facilities in isolated island," *IEEE Transactions on Energy Conversion*, vol. 20, no. 2, pp. 406–414, June 2005.

- [103] A. A. Hamad, M. A. Azzouz, and E. F. El-Saadany, "Multiagent supervisory control for power management in dc microgrids," vol. 7, no. 2, March 2016, pp. 1057–1068.
- [104] I. Y. Chung, W. Liu, D. A. Cartes, E. G. Collins, and S. I. Moon, "Control methods of inverter-interfaced distributed generators in a microgrid system," vol. 46, no. 3, May 2010, pp. 1078–1088.
- [105] C. Sao and P. Lehn, "Control and power management of converter fed microgrids," pp. 1–1, July 2010.
- [106] H. Xin, R. Zhao, L. Zhang, Z. Wang, K. P. Wong, and W. Wei, "A decentralized hierarchical control structure and self-optimizing control strategy for f-p type dgs in islanded microgrids," *IEEE Transactions on Smart Grid*, vol. 7, no. 1, pp. 3–5, Jan 2016.
- [107] S. J. Ahn, J. W. Park, I. Y. Chung, S. I. Moon, S. H. Kang, and S. R. Nam, "Power-sharing method of multiple distributed generators considering control modes and configurations of a microgrid," vol. 25, no. 3, July 2010, pp. 2007–2016.
- [108] H. Karimi, H. Nikkhajoei, and R. Iravani, "Control of an electronically-coupled distributed resource unit subsequent to an islanding event," pp. 1–1, July 2008.
- [109] X. Yu, A. M. Khambadkone, H. Wang, and S. T. S. Terence, "Control of parallel-connected power converters for low-voltage microgrid; part i: A hybrid control architecture," *IEEE Transactions on Power Electronics*, vol. 25, no. 12, pp. 2962–2970, Dec 2010.
- [110] M. Hamzeh, H. Karimi, and H. Mokhtari, "A new control strategy for a multi-bus mv microgrid under unbalanced conditions," *IEEE Transactions on Power Systems*, vol. 27, no. 4, pp. 2225–2232, Nov 2012.
- [111] F. Zhang, Y. Yang, C. Ji, W. Wei, Y. Chen, C. Meng, Z. Jin, and G. Zhang, "Power management strategy research for dc microgrid with hybrid storage system," pp. 62–68, June 2015.
- [112] A. G. Madureira and J. A. P. Lopes, "Coordinated voltage support in distribution networks with distributed generation and microgrids," *IET Renewable Power Generation*, vol. 3, no. 4, pp. 439–454, December 2009.

- [113] K. Pandiaraj, P. Taylor, N. Jenkins, and C. Robb, "Distributed load control of autonomous renewable energy systems," *IEEE Transactions on Energy Conversion*, vol. 16, no. 1, pp. 14–19, Mar 2001.
- [114] R. Majumder, G. Ledwich, A. Ghosh, S. Chakrabarti, and F. Zare, "Droop control of converter-interfaced microsources in rural distributed generation," vol. 25, no. 4, Oct 2010, pp. 2768–2778.
- [115] S. J. Ahn, J. W. Park, I. Y. Chung, S. I. Moon, S. H. Kang, and S. R. Nam, "Power-sharing method of multiple distributed generators considering control modes and configurations of a microgrid," *IEEE Transactions on Power Delivery*, vol. 25, no. 3, pp. 2007–2016, July 2010.
- [116] M. J. Sanjari and G. B. Gharehpetian, "Small signal stability based fuzzy potential function proposal for secondary frequency and voltage control of islanded microgrid," *Electric Power Components and Systems*, vol. 41, no. 5, pp. 485–499, 2013.
- [117] F. Katiraei, R. Iravani, N. Hatziargyriou, and A. Dimeas, "Microgrids management," *IEEE Power and Energy Magazine*, vol. 6, no. 3, pp. 54–65, May 2008.
- [118] T. Hosseinimehr, F. Shahnia, R. P. S. Chandrasena, and A. Ghosh, "Different power sharing techniques for converter-interfaced ders in an autonomous microgrid," in *2014 IEEE PES Asia-Pacific Power and Energy Engineering Conference (APPEEC)*, Dec 2014, pp. 1–6.
- [119] R. P. S. Chandrasena, F. Shahnia, A. Ghosh, and S. Rajakaruna, "Secondary control in microgrids for dynamic power sharing and voltage/frequency adjustment," in *2014 Australasian Universities Power Engineering Conference (AUPEC)*, Sept 2014, pp. 1–8.
- [120] T. Hosseinimehr, A. Ghosh, and F. Shahnia, "Cooperative control of battery energy storage systems in microgrids," *International Journal of Electrical Power and Energy Systems*, vol. 87, pp. 109 – 120, Dec 2016.
- [121] J. M. Carrasco, L. G. Franquelo, J. T. Bialasiewicz, E. Galvan, R. C. PortilloGuisado, M. A. M. Prats, J. I. Leon, and N. Moreno-Alfonso, "Power-electronic systems for the grid integration of renewable energy sources: A survey," *IEEE Transactions on Industrial Electronics*, vol. 53, no. 4, pp. 1002–1016, June 2006.

- [122] F. Blaabjerg, Z. Chen, and S. B. Kjaer, "Power electronics as efficient interface in dispersed power generation systems," *IEEE Transactions on Power Electronics*, vol. 19, no. 5, pp. 1184–1194, Sept 2004.
- [123] Y. Li, D. M. Vilathgamuwa, and P. C. Loh, "Design, analysis, and real-time testing of a controller for multibus microgrid system," *IEEE Transactions on Power Electronics*, vol. 19, no. 5, pp. 1195–1204, Sept 2004.
- [124] F. Katiraei and M. R. Iravani, "Power management strategies for a microgrid with multiple distributed generation units," *IEEE Transactions on Power Systems*, vol. 21, no. 4, pp. 1821–1831, Nov 2006.
- [125] F. Z. Peng, Y. W. Li, and L. M. Tolbert, "Control and protection of power electronics interfaced distributed generation systems in a customer-driven microgrid," in *2009 IEEE Power Energy Society General Meeting*, July 2009, pp. 1–8.
- [126] B. Shi and G. Venkataramanan, "Parallel operation of voltage source inverters with minimal intermodule reactors," in *Conference Record of the 2004 IEEE Industry Applications Conference, 2004. 39th IAS Annual Meeting.*, vol. 1, Oct 2004, p. 162.
- [127] Y. W. Li and C. N. Kao, "An accurate power control strategy for power-electronics-interfaced distributed generation units operating in a low-voltage multibus microgrid," *IEEE Transactions on Power Electronics*, vol. 24, no. 12, pp. 2977–2988, Dec 2009.
- [128] A. Hasanzadeh, O. C. Onar, H. Mokhtari, and A. Khaligh, "A proportional-resonant controller-based wireless control strategy with a reduced number of sensors for parallel-operated upss," *IEEE Transactions on Power Delivery*, vol. 25, no. 1, pp. 468–478, Jan 2010.
- [129] Y. A. R. I. Mohamed and E. F. El-Saadany, "Adaptive decentralized droop controller to preserve power sharing stability of paralleled inverters in distributed generation microgrids," *IEEE Transactions on Power Electronics*, vol. 23, no. 6, pp. 2806–2816, Nov 2008.
- [130] N. Pogaku, M. Prodanovic, and T. C. Green, "Modeling, analysis and testing of autonomous operation of an inverter-based microgrid," *IEEE Transactions on Power Electronics*, vol. 22, no. 2, pp. 613–625, March 2007.

- [131] K. D. Brabandere, B. Bolsens, J. V. den Keybus, A. Woyte, J. Driesen, and R. Belmans, “A voltage and frequency droop control method for parallel inverters,” *IEEE Transactions on Power Electronics*, vol. 22, no. 4, pp. 1107–1115, July 2007.
- [132] A. Tuladhar, H. Jin, T. Unger, and K. Mauch, “Control of parallel inverters in distributed ac power systems with consideration of the line impedance effect,” in *Applied Power Electronics Conference and Exposition, 1998. APEC '98. Conference Proceedings 1998., Thirteenth Annual*, vol. 1, Feb 1998, pp. 321–328 vol.1.
- [133] J. M. Guerrero, L. G. de Vicuna, J. Matas, M. Castilla, and J. Miret, “Output impedance design of parallel-connected ups inverters with wireless load-sharing control,” *IEEE Transactions on Industrial Electronics*, vol. 52, no. 4, pp. 1126–1135, Aug 2005.
- [134] —, “A wireless controller to enhance dynamic performance of parallel inverters in distributed generation systems,” *IEEE Transactions on Power Electronics*, vol. 19, no. 5, pp. 1205–1213, Sept 2004.
- [135] E. A. A. Coelho, P. C. Cortizo, and P. F. D. Garcia, “Small signal stability for single phase inverter connected to stiff ac system,” in *Conference Record of the 1999 IEEE Industry Applications Conference. Thirty-Forth IAS Annual Meeting (Cat. No.99CH36370)*, vol. 4, 1999, pp. 2180–2187 vol.4.
- [136] —, “Small-signal stability for parallel-connected inverters in stand-alone ac supply systems,” *IEEE Transactions on Industry Applications*, vol. 38, no. 2, pp. 533–542, Mar 2002.
- [137] D. N. Zmood and D. G. Holmes, “Stationary frame current regulation of pwm inverters with zero steady-state error,” *IEEE Transactions on Power Electronics*, vol. 18, no. 3, pp. 814–822, May 2003.
- [138] L. Corradini, P. Mattavelli, M. Corradin, and F. Polo, “Analysis of parallel operation of uninterruptible power supplies loaded through long wiring cables,” *IEEE Transactions on Power Electronics*, vol. 25, no. 4, pp. 1046–1054, April 2010.

- [139] J. M. Guerrero, L. Hang, and J. Uceda, "Control of distributed uninterruptible power supply systems," *IEEE Transactions on Industrial Electronics*, vol. 55, no. 8, pp. 2845–2859, Aug 2008.
- [140] J. C. Vasquez, R. A. Mastromauro, J. M. Guerrero, and M. Liserre, "Voltage support provided by a droop-controlled multifunctional inverter," *IEEE Transactions on Industrial Electronics*, vol. 56, no. 11, pp. 4510–4519, Nov 2009.
- [141] J. M. Guerrero, J. C. Vasquez, J. Matas, L. G. de Vicuna, and M. Castilla, "Hierarchical control of droop-controlled ac and dc microgrids; a general approach toward standardization," *IEEE Transactions on Industrial Electronics*, vol. 58, no. 1, pp. 158–172, Jan 2011.
- [142] H. Tao, J. L. Duarte, and M. A. M. Hendrix, "Line-interactive ups using a fuel cell as the primary source," *IEEE Transactions on Industrial Electronics*, vol. 55, no. 8, pp. 3012–3021, Aug 2008.
- [143] F. Briz, M. W. Degner, and R. D. Lorenz, "Analysis and design of current regulators using complex vectors," *IEEE Transactions on Industry Applications*, vol. 36, no. 3, pp. 817–825, May 2000.
- [144] D. De and V. Ramanarayanan, "Decentralized parallel operation of inverters sharing unbalanced and nonlinear loads," *IEEE Transactions on Power Electronics*, vol. 25, no. 12, pp. 3015–3025, Dec 2010.
- [145] P. T. Cheng, C. A. Chen, T. L. Lee, and S. Y. Kuo, "A cooperative imbalance compensation method for distributed-generation interface converters," *IEEE Transactions on Industry Applications*, vol. 45, no. 2, pp. 805–815, March 2009.
- [146] J. M. Guerrero, J. C. Vasquez, J. Matas, M. Castilla, and L. G. de Vicuna, "Control strategy for flexible microgrid based on parallel line-interactive ups systems," *IEEE Transactions on Industrial Electronics*, vol. 56, no. 3, pp. 726–736, March 2009.
- [147] Y. Li and Y. W. Li, "Power management of inverter interfaced autonomous microgrid based on virtual frequency-voltage frame," *IEEE Transactions on Smart Grid*, vol. 2, no. 1, pp. 30–40, March 2011.

- [148] T. Hosseinimehr, F. Shahnia, and A. Ghosh, “Dynamic power sharing control among converter-interfaced ders in an autonomous microgrid,” in *2015 IEEE Eindhoven PowerTech*, June 2015, pp. 1–6.
- [149] R. Majumder, G. Ledwich, A. Ghosh, S. Chakrabarti, and F. Zare, “Droop control of converter-interfaced microsources in rural distributed generation,” *IEEE Transactions on Power Delivery*, vol. 25, no. 4, pp. 2768–2778, Oct 2010.
- [150] M. Gopal, *Digital Control and State Variable Methods*. Tata McDraw Hill, 2009.
- [151] A. Tewari, *Modern Control Design with Matlab and Simulink*. Wiley, 2002.
- [152] A. Ghosh and G. Ledwich, *Power Quality Enhancement Using Custom Power Devices*. Springer, 2002.
- [153] R. Majumder, B. Chaudhuri, A. Ghosh, R. Majumder, G. Ledwich, and F. Zare, “Improvement of stability and load sharing in an autonomous microgrid using supplementary droop control loop,” *IEEE Transactions on Power Systems*, vol. 25, no. 2, pp. 796–808, May 2010.
- [154] N. Kroutikova, C. a. Hernandez-Aramburo, and T. C. Green, “State-space model of grid-connected inverters under current control mode,” *IET Electric Power Applications*, vol. 1, no. 3, pp. 329–338, May 2007.
- [155] N. Pogaku, M. Prodanovic, and T. C. Green, “Modeling, analysis and testing of autonomous operation of an inverter-based microgrid,” *IEEE Transactions on Power Electronics*, vol. 22, no. 2, pp. 613–625, March 2007.
- [156] R. Majumder, B. Chaudhuri, A. Ghosh, R. Majumder, G. Ledwich, and F. Zare, “Improvement of stability and load sharing in an autonomous microgrid using supplementary droop control loop,” in *IEEE PES General Meeting*, July 2010, pp. 1–1.
- [157] R. H. Lasseter, “Smart distribution: Coupled microgrids,” *Proceedings of the IEEE*, vol. 99, no. 6, pp. 1074–1082, June 2011.
- [158] A. Tani, M. B. Camara, and B. Dakyo, “Energy management in the decentralized generation systems based on renewable energy; ultracapacitors and battery to compensate the wind/load power fluctuations,” *IEEE Transactions on Industry Applications*, vol. 51, no. 2, pp. 1817–1827, March 2015.

- [159] L. Miao, J. Wen, H. Xie, C. Yue, and W. J. Lee, “Coordinated control strategy of wind turbine generator and energy storage equipment for frequency support,” *IEEE Transactions on Industry Applications*, vol. 51, no. 4, pp. 2732–2742, July 2015.
- [160] M. A. Abdullah, K. M. Muttaqi, D. Sutanto, and A. P. Agalgaonkar, “An effective power dispatch control strategy to improve generation schedulability and supply reliability of a wind farm using a battery energy storage system,” *IEEE Transactions on Sustainable Energy*, vol. 6, no. 3, pp. 1093–1102, July 2015.
- [161] “Ieee recommended practice for sizing lead-acid batteries for stand-alone photovoltaic (pv) systems - redline,” *IEEE Std 1013-2007 (Revision of IEEE Std 1013-2000) - Redline*, pp. 1–58, July 2007.
- [162] M. Gholizadeh and F. R. Salmasi, “Estimation of state of charge, unknown nonlinearities, and state of health of a lithium-ion battery based on a comprehensive unobservable model,” *IEEE Transactions on Industrial Electronics*, vol. 61, no. 3, pp. 1335–1344, March 2014.
- [163] J. Xu, C. C. Mi, B. Cao, J. Deng, Z. Chen, and S. Li, “The state of charge estimation of lithium-ion batteries based on a proportional-integral observer,” *IEEE Transactions on Vehicular Technology*, vol. 63, no. 4, pp. 1614–1621, May 2014.
- [164] D. I. Stroe, M. wierczycki, A. I. Stan, R. Teodorescu, and S. J. Andreasen, “Accelerated lifetime testing methodology for lifetime estimation of lithium-ion batteries used in augmented wind power plants,” *IEEE Transactions on Industry Applications*, vol. 50, no. 6, pp. 4006–4017, Nov 2014.
- [165] M. Datta and T. Senjyu, “Fuzzy control of distributed pv inverters/energy storage systems/electric vehicles for frequency regulation in a large power system,” *IEEE Transactions on Smart Grid*, vol. 4, no. 1, pp. 479–488, March 2013.
- [166] I. Serban and C. Marinescu, “Control strategy of three-phase battery energy storage systems for frequency support in microgrids and with uninterrupted supply of local loads,” *IEEE Transactions on Power Electronics*, vol. 29, no. 9, pp. 5010–5020, Sept 2014.

- [167] Y. Han, P. M. Young, A. Jain, and D. Zimmerle, “Robust control for microgrid frequency deviation reduction with attached storage system,” *IEEE Transactions on Smart Grid*, vol. 6, no. 2, pp. 557–565, March 2015.
- [168] T. Morstyn, B. Hredzak, and V. G. Agelidis, “Distributed cooperative control of microgrid storage,” *IEEE Transactions on Power Systems*, vol. 30, no. 5, pp. 2780–2789, Sept 2015.
- [169] R. Majumder, A. Ghosh, G. Ledwich, and F. Zare, “Angle droop versus frequency droop in a voltage source converter based autonomous microgrid,” in *2009 IEEE Power Energy Society General Meeting*, July 2009, pp. 1–8.
- [170] J. He, Y. W. Li, and F. Blaabjerg, “An enhanced islanding microgrid reactive power, imbalance power, and harmonic power sharing scheme,” *IEEE Transactions on Power Electronics*, vol. 30, no. 6, pp. 3389–3401, June 2015.
- [171] M. A. Mahmud, M. J. Hossain, H. R. Pota, and A. M. T. Oo, “Robust nonlinear distributed controller design for active and reactive power sharing in islanded microgrids,” *IEEE Transactions on Energy Conversion*, vol. 29, no. 4, pp. 893–903, Dec 2014.
- [172] A. Micallef, M. Apap, C. Spiteri-Staines, J. M. Guerrero, and J. C. Vasquez, “Reactive power sharing and voltage harmonic distortion compensation of droop controlled single phase islanded microgrids,” *IEEE Transactions on Smart Grid*, vol. 5, no. 3, pp. 1149–1158, May 2014.
- [173] J. Kim, J. M. Guerrero, P. Rodriguez, R. Teodorescu, and K. Nam, “Mode adaptive droop control with virtual output impedances for an inverter-based flexible ac microgrid,” *IEEE Transactions on Power Electronics*, vol. 26, no. 3, pp. 689–701, March 2011.
- [174] R. Majumder, F. Shahnia, A. Ghosh, G. Ledwich, M. Wishart, and F. Zare, “Operation and control of a microgrid containing inertial and non-inertial micro sources,” in *TENCON 2009 - 2009 IEEE Region 10 Conference*, Jan 2009, pp. 1–6.
- [175] R. P. S. Chandrasena, F. Shahnia, S. Rajakaruna, and A. Ghosh, “Control, operation and power sharing among parallel converter-interfaced ders in a microgrid in the presence of unbalanced and harmonic loads,” in *2013*

Australasian Universities Power Engineering Conference (AUPEC), Sept 2013, pp. 1–6.

- [176] B. Kroposki, C. Pink, R. DeBlasio, H. Thomas, M. Simes, and P. K. Sen, “Benefits of power electronic interfaces for distributed energy systems,” *IEEE Transactions on Energy Conversion*, vol. 25, no. 3, pp. 901–908, Sept 2010.
- [177] M. Karimi, P. Wall, H. Mokhlis, and V. Terzija, “A new centralized adaptive underfrequency load shedding controller for microgrids based on a distribution state estimator,” *IEEE Transactions on Power Delivery*, vol. 32, no. 1, pp. 370–380, Feb 2017.
- [178] T. Dragicevic, J. M. Guerrero, J. C. Vasquez, and D. Krlec, “Supervisory control of an adaptive-droop regulated dc microgrid with battery management capability,” *IEEE Transactions on Power Electronics*, vol. 29, no. 2, pp. 695–706, Feb. 2014.
- [179] T. Hosseinimehr, F. Shahnia, and A. Ghosh, “Power sharing control of batteries within autonomous microgrids based on their state of charge,” pp. 1–6, Sept 2015.
- [180] T. Dragicevic, J. M. Guerrero, and J. C. Vasquez, “A distributed control strategy for coordination of an autonomous lvdc microgrid based on power-line signaling,” *IEEE Transactions on Industrial Electronics*, vol. 61, no. 7, pp. 3313–3326, July 2014.
- [181] D. Wu, J. M. Guerrero, J. C. Vasquez, T. Dragicevic, and F. Tang, “Coordinated power control strategy based on primary-frequency-signaling for islanded microgrids,” pp. 1033–1038, Sept 2013.
- [182] W. Liu, W. Gu, Y. Xu, Y. Wang, and K. Zhang, “General distributed secondary control for multi-microgrids with both pq-controlled and droop-controlled distributed generators,” *IET Generation, Transmission Distribution*, vol. 11, no. 3, pp. 707–718, 2017.
- [183] K. J. Bunker and W. W. Weaver, “Multidimensional droop control for wind resources in dc microgrids,” *IET Generation, Transmission Distribution*, vol. 11, no. 3, pp. 657–664, 2017.

- [184] X. Zhao, J. M. Guerrero, M. Savaghebi, J. C. Vasquez, X. Wu, and K. Sun, “Low-voltage ride-through operation of power converters in grid-interactive microgrids by using negative-sequence droop control,” *IEEE Transactions on Power Electronics*, vol. 32, no. 4, pp. 3128–3142, April 2017.
- [185] J. Xiang, Y. Wang, Y. Li, and W. Wei, “Stability and steady-state analysis of distributed cooperative droop controlled dc microgrids,” *IET Control Theory Applications*, vol. 10, no. 18, pp. 2490–2496, 2016.
- [186] F. Gao, S. Bozhko, A. Costabeber, C. Patel, P. Wheeler, C. I. Hill, and G. Asher, “Comparative stability analysis of droop control approaches in voltage-source-converter-based dc microgrids,” *IEEE Transactions on Power Electronics*, vol. 32, no. 3, pp. 2395–2415, March 2017.
- [187] Z. Li, C. Zang, P. Zeng, H. Yu, and S. Li, “Agent-based distributed and economic automatic generation control for droop-controlled ac microgrids,” *IET Generation, Transmission Distribution*, vol. 10, no. 14, pp. 3622–3630, 2016.
- [188] H. Mahmood, D. Michaelson, and J. Jiang, “Decentralized power management of a pv/battery hybrid unit in a droop-controlled islanded microgrid,” *IEEE Transactions on Power Electronics*, vol. 30, no. 12, pp. 7215–7229, Dec 2015.
- [189] —, “A power management strategy for pv/battery hybrid systems in islanded microgrids,” *IEEE Journal of Emerging and Selected Topics in Power Electronics*, vol. 2, no. 4, pp. 870–882, Dec 2014.
- [190] H. Chaoui and H. Gualous, “Adaptive state of charge estimation of lithium-ion batteries with parameter and thermal uncertainties,” *IEEE Transactions on Control Systems Technology*, vol. 25, no. 2, pp. 752–759, March 2017.
- [191] M. Partovibakhsh and G. Liu, “An adaptive unscented kalman filtering approach for online estimation of model parameters and state-of-charge of lithium-ion batteries for autonomous mobile robots,” *IEEE Transactions on Control Systems Technology*, vol. 23, no. 1, pp. 357–363, Jan 2015.
- [192] L. Piegari and R. Rizzo, “Adaptive perturb and observe algorithm for photovoltaic maximum power point tracking,” *IET Renewable Power Generation*, vol. 4, no. 4, pp. 317–328, July 2010.

- [193] D. Linden and T. B. Reddy, *Handbook of Batteries*. McGraw-Hill, 2002.
- [194] B. Xiao, Y. Shi, and L. He, “A universal state-of-charge algorithm for batteries,” in *Design Automation Conference*, June 2010, pp. 687–692.
- [195] J. W. Choi, S. Y. Heo, and M. K. Kim, “Hybrid operation strategy of wind energy storage system for power grid frequency regulation,” *IET Generation, Transmission Distribution*, vol. 10, no. 3, pp. 736–749, 2016.
- [196] E. Serban and H. Serban, “A control strategy for a distributed power generation microgrid application with voltage- and current-controlled source converter,” *IEEE Transactions on Power Electronics*, vol. 25, no. 12, pp. 2981–2992, Dec. 2010.
- [197] H. Liu, P. C. Loh, X. Wang, Y. Yang, W. Wang, and D. Xu, “Droop control with improved disturbance adaption for a pv system with two power conversion stages,” *IEEE Transactions on Industrial Electronics*, vol. 63, no. 10, pp. 6073–6085, Oct. 2016.
- [198] X. Lu, K. Sun, J. M. Guerrero, J. C. Vasquez, and L. Huang, “State-of-charge balance using adaptive droop control for distributed energy storage systems in dc microgrid applications,” *IEEE Transactions on Industrial Electronics*, vol. 61, no. 6, pp. 2804–2815, June 2014.
- [199] D. Sha, Z. Guo, and X. Liao, “Control strategy for input-parallel-output-parallel connected high-frequency isolated inverter modules,” *IEEE Transactions on Power Electronics*, vol. 26, no. 8, pp. 2237–2248, Aug. 2011.
- [200] A. H. Etemadi, E. J. Davison, and R. Iravani, “A decentralized robust control strategy for multi-der microgrids-part i: Fundamental concepts,” *IEEE Transactions on Power Delivery*, vol. 27, no. 4, pp. 1843–1853, Oct. 2012.
- [201] J. H. Jeon, J. Y. Kim, H. M. Kim, S. K. Kim, C. Cho, J. M. Kim, J. B. Ahn, and K. Y. Nam, “Development of hardware in-the-loop simulation system for testing operation and control functions of microgrid,” *IEEE Transactions on Power Electronics*, vol. 25, no. 12, pp. 2919–2929, Dec. 2010.
- [202] M. Partovibakhsh and G. Liu, “An adaptive unscented kalman filtering approach for online estimation of model parameters and state-of-charge of

- lithium-ion batteries for autonomous mobile robots,” *IEEE Transactions on Control Systems Technology*, vol. 23, no. 1, pp. 357–363, Jan 2015.
- [203] R. Tonkoski, L. A. C. Lopes, and T. H. M. El-Fouly, “Coordinated active power curtailment of grid connected pv inverters for overvoltage prevention,” *IEEE Transactions on Sustainable Energy*, vol. 2, no. 2, pp. 139–147, April 2011.
- [204] M. Torres and L. Lopez, “Inverter-based diesel generator emulator for the study of frequency variations in a laboratory-scale autonomous power system,” *Energy and Power Engineering*, vol. 5, no. 3, pp. 274–283, Dec 2013.

Every reasonable effort has been made to acknowledge the owners of copyright material. I would be pleased to hear from any copyright owner who has been omitted or incorrectly acknowledged.

Tahoura Hosseinimehr
07/08/2017